Escaping atmospheres
of hot extrasolar gas planets

**Dissertation with the aim of achieving a doctoral degree
at the Faculty of Mathematics, Informatics and Natural Sciences**

**Department of Physics
Universität Hamburg**

submitted by

Michael Salz

Hamburg, 2015

Day of oral defense: 11.12.2015

The following evaluators recommend the admission of the dissertation:
Prof. Dr. J. H. M. M. Schmitt
Dr. A. Mignone
Prof. Dr. J. L. Linsky

Abstract

Gas planets in close proximity to their host stars endure high levels of irradiation. Extreme ultraviolet radiation and X-rays are absorbed in the planets' upper atmospheres, the so-called thermospheres. The absorption of this radiation ionizes the atmospheric gas and causes substantial heating rates, leading to temperatures of up to 20 000 K. Such high temperatures likely result in a continuous expansion of the planetary thermosphere, taking the form of a planetary wind. In the most extreme cases, the permanent mass loss resulting from such a wind might be large enough to completely evaporate smaller gas planets or the atmospheres of terrestrial planets over their lifetime.

The goal of my dissertation is to improve our understanding of the escaping thermospheres via a twofold approach: I simulated planetary atmospheres to study their behavior in detail and, furthermore, I initiated a comprehensive observational campaign to determine crucial system parameters and identify promising candidates for follow-up transit observations.

For the numerical approach, I designed a new interface between the MHD code PLUTO and the photoionization and microphysics solver CLOUDY, "the PLUTO-CLOUDY Interface" (TPCI). The use of an equilibrium microphysics solver is a new feature in dynamical simulations of the escaping atmospheres. I applied TPCI to study the atmospheres of transiting hot gas planets in the solar neighborhood. The simulations revealed substantial radiative cooling in the atmospheres of the most massive hot Jupiters. This cooling is strong enough to balance the enormous irradiation and, thus, leads to stable and compact thermospheres. These results support the existence of a transition in planetary atmospheres, from a regime of strong escape in smaller hot gas planets to stable atmospheres in massive planets. Based on the simulations, I derived a correction factor, which incorporates this new transition into the energy-limited escape model, which is a widely used concept to derive estimates for the mass-loss rates of strongly irradiated planets that was developed more than 30 years ago. The simulated atmospheres were also used to derive theoretical Lyα absorption signals for the 18 systems studied here. Today, such absorption signals have been measured in four transiting systems and, for the first time, it was possible to reproduce the observed trend in the absorption depth in the four systems.

Furthermore, I have observed seven systems in the vicinity of the Sun with the X-ray telescopes XMM-Newton and Chandra. These observations revealed the high-energy irradiation level of the planetary thermospheres and, thus, the current planetary mass-loss rates. The measured irradiation levels are also used in my simulations of the planetary atmospheres. Additionally, I have observed three targets of the X-ray sample in snapshot observations with the Hubble Space Telescope to determine the host stars' Lyα flux at Earth. Two of the three targets were detected and are bright enough to study the planetary atmospheres in future transit campaigns.

The presented work is the first comprehensive study of escaping atmospheres in hot gas planets in the solar neighborhood. Based on the observations and simulations, I have identified the system WASP-80 as the most promising candidate for transit spectroscopy in terms of the host stars' Lyα flux and the planetary absorption signal. Based on my simulations, the revised energy-limited escape formula allows viable estimates of the mass-loss rates from small terrestrial planets up to the most massive hot Jupiters.

Zusammenfassung

Gasplaneten, die sich in extremer Nähe zu ihrem Zentralstern befinden, sind hohen Bestrahlungsstärken ausgesetzt. Extrem ultraviolette Strahlung und Röntgenstrahlung werden in der oberen Atmosphäre von Planeten absorbiert, in der sogenannten Thermosphäre. Die Absorption dieser Strahlung ionisiert das atmosphärische Gas und führt zu erhebliche Heizraten, sodass Temperaturen von bis zu 20 000 K erreicht werden können. Solch hohe Temperaturen führen höchstwahrscheinlich zu einer kontinuierlichen Ausdehnung der planetaren Thermosphäre, die sich dann in der Form eines planetaren Windes zeigt. Im Extremfall kann dieser Wind einen so starken Massenverlust verursachen, dass kleinere Gasplaneten oder die Atmosphären von terrestrischen Planeten während deren Lebensdauer komplett verdampfen können.

Das Ziel meiner Dissertation ist ein besseres Verständnis der entweichenden Thermosphären mittels zweier Ansätze: Erstens habe ich die planetaren Atmosphären simuliert um deren Verhalten im Detail studieren zu können, und zweitens habe ich eine umfassende Beobachtungskampagne angestoßen, um wichtige Systemparameter zu bestimmen, und um die besten Kandidaten für zukünftige Transitbeobachtungen zu identifizieren.

Für den numerischen Ansatz habe ich ein neues Interface zwischen dem MHD-Programm PLUTO und dem Photoionisations- und Mikrophysik-Simulationsprogramm CLOUDY geschrieben, „the PLUTO-CLOUDY Interface" (TPCI). Die Anwendung eines Simulationsprogrammes, das den mikrophysikalischen Gleichgewichtszustand innerhalb der entweichenden Atmosphären bestimmt, ist ein komplett neuer Ansatz. Ich habe TPCI verwendet, um die Atmosphären von heißen Transitplaneten im nächsten Umfeld der Sonne zu studieren. Die Simulationen zeigen erhebliche Kühlung in den Atmosphären der schwersten heißen Jupiter durch Abstrahlung. Diese Kühlung ist stark genug um die enorme Einstrahlung auszugleichen, und führt daher zu stabilen und kompakten Thermosphären. Diese Ergebnisse belegen somit einen Übergang in den plantaren Atmosphären: Kleinere heiße Gasplaneten erfahren einen starken Atmosphärenverlust, während massivere Planeten eine stabile Atmosphäre beherbergen. Beruhend auf den Simulationen habe ich einen Korrekturfaktor bestimmt, der diesen neuen Übergang in das Model des energielimitierten Massenverlustes einbindet. Dieses vor mehr als 30 Jahren entwickelt Modell ist weitverbreitet zur Abschätzung des Massenverlustes von stark bestrahlten Planeten. Für die hier studierten 18 Systeme wurden außerdem theoretische $Ly\alpha$-Absorptionssignale anhand der simulierten Atmosphären berechnet. Bisher wurden solche Absorptionssignale bei vier Transitplaneten gemessen. Zum ersten Mal ist es mit meiner Methode gelungen, den beobachteten Trend in den gemessenen Absorptionstiefen der vier Systeme zu reproduzieren.

Ferner habe ich sieben Systeme in der Umgebung der Sonne mit den Röntgenteleskopen XMM-Newton und Chandra beobachtet. Anhand der Beobachtung konnten wir die hochenergetische Bestrahlungsstärke der planetaren Thermosphären und somit den momentanen Massenverlust bestimmen. Die gemessenen Bestrahlungsstärken wurden auch in meine Simulationen integriert. Zusätzlich habe ich in kurzen Beobachtungen mit dem Hubble Space Telescope die $Ly\alpha$-Flüsse von Dreien dieser Zentralsterne gemessen. Zwei der Zentralsterne wurden detektiert und sind hell genug um eine planetare Atmosphäre in einer zukünftigen Transitbeobachtung studieren zu können.

Die hier präsentierte Arbeit ist die erste umfassende Studie über verdampfende Atmosphären heißer Gasplaneten in der näheren Umgebung der Sonne. Sowohl in den Beobachtungen als auch in den Simulationen hat sich WASP-80 als vielversprechendster Kandidat für zukünftige Transitspektroskopie herausgestellt, einmal in Hinsicht auf den $Ly\alpha$-Fluss des Zentralsternes aber auch in Bezug auf das berechnete Absorptionssignal des Planeten. Basierend auf meinen Simulationen ermöglicht die verbesserte, energielimitierte Massenverlustformel brauchbare Abschätzungen der Massenverlustraten von kleinen terrestrischen Planeten bis hin zu den schwersten heißen Jupitern.

Contents

List of Figures

planetary absorption atmosphere planets Lyman simulations wind hydrogen alpha line absorption simulation cooling heating radiative hot escape HD209458b mass-loss TPCI temperature thermosphere stars planet mass stellar host energy density rate rates signals neutral emission irradiation thermosphere gas hydrodynamic simulated flux observations transit loss X-ray EUV source solver radiation atmospheric photoionization signal velocity pressure strong lower energy-limited Rpl XUV CLOUDY targets results region upper factor estimates code level system used based range depth derive potential expansion Roche-lobe detection fraction shows WASP-80 systems advection structure expanded cm case et individual total ionization solar spectral use processes models metals large excess time boundary winds interstellar HD189733b detected acceleration PLUTO number model included measured equilibrium escaping star Jupiters page efficiency paper strength distance rst al ionized three times small larger rotation show input layer point absorbed example transition gravitational high luminosity result stable given radius close found HD important Jupiter compared

1 Overview

The detection of numerous extrasolar planets in the past two decades has altered our view into the night sky, because today we know that the stars that we see most likely also harbor planetary systems similar to the solar system. Although planet detection surveys remain too incomplete to allow a definite assessment, the general picture emerges that planetary systems around stars are rather the rule than the exception. For example, the Kepler mission detected 0.17 planets per star with periods less than 50 d (Howard et al. 2012). Mercury, the closest planet in the Solar System, has a period of 88 d, which means that Solar System-like planets are not even included in this number. Therefore, it is reasonable to assume that a large fraction of the stars in the Milky Way do host at least one planet. Beyond the knowledge that there are billions of planets in our galaxy, the diversity of the discovered planetary systems comes as a surprise and is still revolutionizing our understanding of the formation of planets.

1.1 The origin of hot Jupiters

The first planet that was detected around a solar-like star already came as a surprise. 51 Peg b is a Jupiter-sized planet at a distance of 0.05 AU from its host star (Mayor & Queloz 1995), which corresponds to only 8.5 stellar radii above the stellar photosphere. At the time of the discovery, it was not clear how a gas planet can exist at such a small distance from a star. Under certain circumstances, giant planets can form in close orbits (Bodenheimer et al. 2000), but corresponding to standard planet formation theory, a gas giant is not thought to form in such proximity (Mizuno 1980). According to our understanding, planet formation starts with an accumulation of rocks and ices, which form a planet core. This occurs beyond the so-called ice line at a couple AU from the host star, where temperatures are low enough to allow the formation of ice grains. The planetary core forms within a protoplanetary disk; when a critical mass of about 10 Earth-masses is reached, the surrounding disk material is rapidly accreted forming a proto-gas giant. Subsequently such a protoplanet further accretes gas from the disk. The accretion process is too slow to form giant planets beyond 20 to 30 AU, because the orbital periods become too long compared to the expected disk lifetimes of < 10 Ma (Close 2010).

Alternatively, gas giants can form via a second major formation mechanism based on disk instabilities. This involves a fragmentation of the protoplanetary disk with the gravitational collapse of dense clumps (Cameron 1978). However, this channel is confined to regions of the disk beyond 50 AU, even more distant from the host star (Meru & Bate 2012). Both formation mechanisms can coexist, but are spatially separate in protoplanetary disks (Close 2010).

Today, 51 Peg b-like planets are called hot Jupiters, and we know that 1.2 % of the FGK stars in the solar neighborhood harbor such hot Jupiters (Marcy et al. 2005). Before the

detection of these planets it was already known that the orbits of the Solar System planets are not necessarily identical to their formation radius. The standard formation picture within a protoplanetary disk causes migration of gas giants (Goldreich & Tremaine 1980), because a protoplanet induces spiral arms in the disk and hence transfers angular momentum causing an inward or outward migration. Also accretion of disk material onto the host star causes a planet to be dragged toward the central star. These processes are called disk migration, but did not attract much attention before the detection of hot Jupiters, because the gas planets in the Solar System are all found beyond the ice line. Consequently, shortly after the detection of 51 Peg b, its close orbit was explained in terms of disk migration by Lin et al. (1996).

Disk migration is not the only theory for the origin of close-in gas planets. Scattering of multiple planets after the dissipation of the protoplanetary disk can also contribute to the population of hot Jupiters (Nagasawa et al. 2008). Such planet-planet interactions are, for example, used to explain the distribution of eccentricities in exoplanetary systems (Marcy et al. 2005). The origin of these eccentric planetary orbits is not easily explained through the formation in a protoplanetary disk, which rotates uniformly. Furthermore, also a large fraction of hot Jupiters are found in inclined or eccentric orbits (e.g., Triaud et al. 2010; Bakos et al. 2007), others, like WASP-8 b, even reside in retrograde orbits (Queloz et al. 2010). Therefore, scattering of planets may well be important to understand the formation of hot Jupiters.

This short introduction to the puzzle that the first discovered exoplanet already poses for our understanding of planet formation demonstrates what we can learn from the detection and characterization of extrasolar planets. Besides the search for a second Earth, one major goal of exoplanet science is the construction of a unified planet formation theory, which can explain the presence of hot Jupiters as well as our own Solar System (e.g., Ida & Lin 2010; Alibert et al. 2011).

1.2 Atmospheric stability

The discovery of 51 Peg b raises yet another question: How can a gas planet survive the extreme environment in such close proximity to the host star? Certainly the detection of many hot Jupiters and hot Neptunes speaks for itself: The majority of these gas planets must be stable over a significant fraction of their lifetime. However, their atmospheres are most likely not stable, but undergo a persistent evaporation.

1.2.1 Formation of a planetary wind

Evaporating atmospheres were first studied for the atmospheres of Earth and Venus under the extreme ultraviolet (EUV) irradiation of the Sun by Watson et al. (1981). The authors found hydrodynamically escaping atmospheres for both planets if hydrogen was the major constituent. This process is also called a planetary wind[1] in analogy to the solar wind. Such a planetary wind should not be confused with weather phenomena in

---

[1]Throughout this dissertation I refer to the process either as planetary wind, as escaping atmosphere or as (photo-) evaporation. The terms are used interchangeably without distinction.
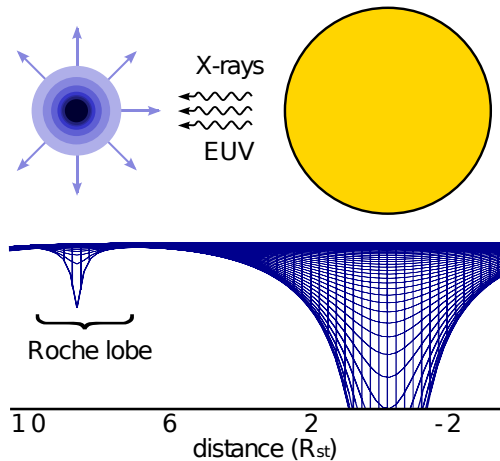
Fig. 1.1. Sketch of a hot Jupiter hosting system. High-energy emission of the host star heats the planetary atmosphere to several thousand Kelvin. The continuous energy supply causes atmospheric evaporation. A side view of the effective gravitational potential is plotted below with the size of the Roche lobe indicated.

the lower atmosphere of Earth, but it is more or less a radial gas outflow from the planet into interplanetary space, which involves a persistent mass loss. Figure 1.1 shows a sketch of the formation of a planetary wind for the case of a hot Jupiter in combination with the effective gravitational potential.

The analogy to the Sun is chosen intentionally, because a planetary wind is not unlike the solar wind as described by the early Parker models (Parker 1958). The solar corona has a temperature of about 2×10^6 K. Thermal conductivity is high in the hot plasma (Spitzer 1978) and the temperature decays slowly in the radial direction. Parker showed that in respect of the high temperatures a hydrostatic solar atmosphere leads to a finite pressure at infinity. This pressure is not balanced by the interstellar medium, thus, the solar corona most undergo a persistent expansion leading to the transonic solar wind.

In the case of hot Jupiters, stellar high-energy irradiation sufficiently heats the planetary atmospheres to drive a similar continuous expansion, resulting in a planetary wind. In contrast to the solar wind, we precisely know the heat source for the planetary wind, as long as the EUV emission of the host star is known; for the solar corona the energy source is still an ongoing topic of research (e.g., Testa et al. 2014). Furthermore, the absorption of EUV radiation occurs throughout the planetary thermosphere and thermal conduction is not required to distribute the energy. Unlike the solar wind, the planetary wind does not expand into the interstellar medium, but is surrounded by the stellar wind, which can provide the outer pressure to stabilize a planetary atmosphere at least partially (Chassefière 1996; Murray-Clay et al. 2009). I will go into more details about the outer influences on the escaping atmospheres in Sect. 1.4.

1.2.2 History of the Martian atmosphere

Today, photoevaporation is believed to have affected planets and even moons in the Solar System (e.g., Lammer et al. 2008). The escape processes in the atmospheres of Earth and Venus are actually more complex than initially described by Watson et al. (1981). Recently, an overview of the evolution of the Martian atmosphere was given by Lammer et al. (2013); I shortly outline the review to assess the importance of hydrodynamic escape for Solar System objects. It shall be noted that not much is truly certain about

the evolution of the atmospheres of Mars, Earth, and Venus. Lammer et al. outline the important processes including uncertainties and the reader is referred to the review for references to the original studies.

The late stages of the formation of the inner planets is thought to involve growth through collisions of planetesimals. These objects contained a certain fraction of volatiles (e.g., $\sim 0.1\%$ water), which were inserted into the newly formed planets. Planets with at least the size of Mars can accrete gas from the protoplanetary disk, which dissolves after about 10 Ma. The protoatmosphere of Mars was hydrogen dominated and contained up to ~ 55 times the amount of hydrogen contained in all oceans on Earth. The activity level of the young Sun was close to the saturation limit, and EUV emission was about 100 times stronger than today (Ribas et al. 2005). At this irradiation level, the atmospheres of the inner planets were unstable. Mars lost its protoatmosphere during the first ~ 100 Ma as a result of photoevaporation; likely, heavier elements like carbon and oxygen were also lost in the process. Continuous impacts of planetesimals supplied further volatiles to the protoatmosphere, but did not compensate the hydrodynamic mass loss.

After the loss of the initial atmosphere, Mars obtained a secondary atmosphere mostly through outgassing of volatiles, which were contained in the initial planetesimals that formed the planet. The secondary atmosphere may have been exposed to continued hydrodynamic escape, depending on the time needed to evaporate the initial protoatmosphere and on the decline in solar activity. After hydrodynamic escape stopped, the secondary atmosphere stabilized, likely with a pressure 100 times higher than todays pressure in the Martian atmosphere (7 mbar). A greenhouse effect heated the atmosphere, which allowed liquid water on the surface, and the late heavy bombardment probably inserted further volatiles into the Martian atmosphere. Since then, the secondary atmosphere has mostly been absorbed into the Martian crust and lost through non-thermal escape processes.

It is no simple task to study any of the processes, which affected the evolution of the planetary atmospheres in the Solar System. In particular, hydrodynamic escape of a hydrogen dominated atmosphere does not persist on any Solar System planet today. Hot gaseous extrasolar planets offer the possibility to gather observational evidence for a process that was likely strongly involved in shaping the atmosphere of the Solar System planets as we know them today.

1.2.3 Atmospheric stability of hot gas giants

At a distance of 0.05 AU from a solar-like host star a hot gas planet endures 400 times the irradiation level of Earth. The strong irradiation leads to temperatures of more than 1000 K at the planetary photosphere[2] (e.g., 1300 K for 51 Peg b, Mayor & Queloz 1995). Naively, this temperature would only be expected on the planetary dayside, because hot gas planets are most likely tidally locked, so that always the same side is irradiated (Goldreich & Soter 1966). However, observations of Knutson et al. (2007) with the Spitzer space telescope have shown that hot Jupiters efficiently transport energy from the dayside

---

[2] The photosphere is defined as the atmospheric layer with an optical depth of $\tau = 2/3$. Its height approximately corresponds with the planetary radius measured in the optical range. I always refer to the planetary photosphere, because a gas planet has no surface.
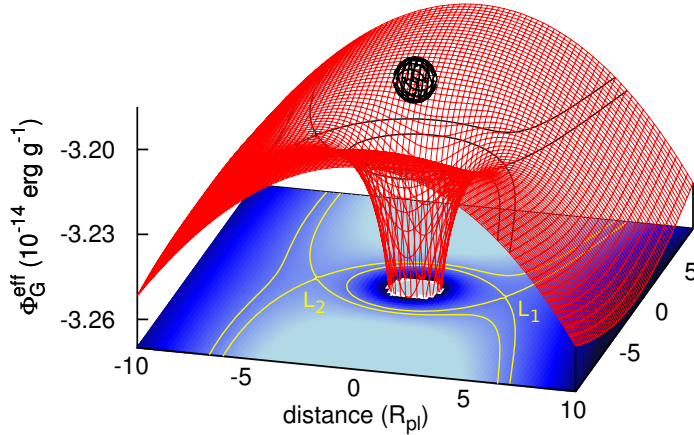
Fig. 1.2. Effective gravitation potential in the vicinity of HD 209458 b. The size of the planet is depicted by the black sphere. The position of the host star is located toward the right-hand side. L_1 and L_2 denote the first and second Lagrange points; L_1 is found at a height of 4.2 R_{pl}.

to the nightside. For one of the most studied hot Jupiters, HD 209458 b, observations even indicate a strong wind of about 2 km s^{-1} in the lower atmosphere, which can distribute the energy irradiated on the dayside more homogeneously over the planetary photosphere (Snellen et al. 2010).

High-energy emission from the host star, capable of ionizing hydrogen, is absorbed in the upper planetary atmosphere, also referred to as thermosphere. The absorption of EUV emission and X-rays produces temperatures on the order of 10 000 K (Schneider et al. 1998). An atmosphere with this temperature is strongly expanded, however, the effective gravitational potential in the rotating two-body system, forms a finite area where material remains bound to the planet. This region is called the Roche lobe (see Fig. 1.2). Schneider et al. (1998) argue that once the atmosphere expands beyond the Roche lobe the planet loses mass, possibly in a cometary-tail like structure.

The argument of Schneider et al. does not solve the dynamics of an overflowing atmosphere. Lammer et al. (2003) was one of the first authors to apply the atmospheric escape study of Watson et al. (1981) to the newly found hot Jupiters. The authors found that stellar high-energy irradiation sufficiently heats the planetary atmospheres to drive a continuous expansion resulting in a planetary mass loss. Although many hot gas planets likely experience a strong hydrodynamic wind, the fractional mass loss remains small. More recent studies conclude that most detected systems are stable over more than 10 Ga, hence, atmospheric escape typically will not evaporate a complete gas planet (Ehrenreich & Désert 2011). This is certainly consistent with the detection of these planets. However, the problem becomes more severe for smaller gas planets with masses less than a Neptune-mass. In these planets the atmospheres are more weakly bound and for example a complete escape of volatile elements in the planet 55 Cnc e is possible (Ehrenreich et al. 2012).

1.3 Observations of expanded planetary atmospheres

Today, signals of planetary atmospheres have been detected most successfully via transit observations (Burrows 2014). This requires that our view of the system is almost aligned with the planetary orbital plane, so that the planet passes in front and behind the host
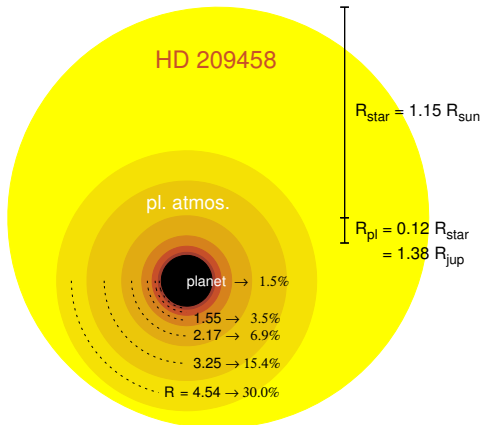
Fig. 1.3. Sketch of the hot Jupiter HD 209458 b in transit. The size of the planetary atmosphere is given in planetary radii (R_{pl}). In this system, the atmosphere must be expanded more than 3 R_{pl} to cover 15 % of the stellar disk.

star from our point of view. There are two possible configurations for transit observations: First, the planet transits behind the host star and a comparison of in-transit and out-of-transit observations yields a signal from the planet either by emission or reflection. The second possibility is the orbital phase, where the planet transits in front of the host star. Here, stellar radiation passes through the planetary atmosphere allowing the characterization of absorption in molecular or atomic lines. In this respect, 51 Peg b is not an ideal candidate to test the theory of escaping planetary atmospheres, because transits were not detected and also the search for a partial transit of an expanded escaping atmosphere with the Hubble Space Telescope (HST) remained futile (observations from Basri 1999, unpublished).

In the following, I discuss detected absorption signals of expanded atmospheres. An overview of observations of the systems HD 209458 and HD 189733 is given in Table 1.1. I focus on detected absorption signals, but also nondetections provide useful information. For example, line absorption by the ion Si III but no absorption by Si IV confines the temperatures in the planetary thermospheres. This is important for models of the planetary thermospheres, but it is beyond the short overview presented here.

1.3.1 HD 209458 b – the prototype of planets with expanded atmospheres

The first transiting planet, HD 209458 b, was found simultaneously by Henry et al. (2000) and by Charbonneau et al. (2000). Remarkably, this discovery was soon followed by the detection of the planetary atmosphere in lines of atomic sodium (Charbonneau et al. 2002). The unresolved excess absorption signal in sodium of 0.023 % was confirmed by Snellen et al. (2008) who found 0.135 % absorption in an observation with a higher resolution. Both observations indicate that neutral sodium is confined to the lower atmosphere of this planet. However, only one year after the detection of the first planetary atmosphere, Vidal-Madjar et al. (2003) published a detection of absorption[3] on the level of 15 ± 4 % in the Lyman α (Lyα) line of neutral hydrogen for this planet measured over three individual transits with the Space Telescope Imaging Spectrograph (STIS) on board

---

[3] Atmospheric absorption signals are not consistently defined in literature. I use the term *excess* absorption signals, if the optical transit depth is subtracted and a purely atmospheric signal is provided.

7

Tab. 1.1. Absorption signals from observations.

Element	Wavelength (Å)	Signal (%)	Instrument	Res.[A]	Reference
HD 209458 b − 1.6% opt. transit depth − Henry et al. (2000); Charbonneau et al. (2000)					
Na I	5893	0.023 ± 0.006[B]	HST/STIS	✗	Charbonneau et al. (2002)
H (Lyα)	1216	15 ± 4	HST/STIS	✓	Vidal-Madjar et al. (2003)
H (Lyα)	1216	5 ± 2			
O I	1306	13 ± 4.5	HST/STIS	✗	Vidal-Madjar et al. (2004)
C II	1335	7.5 ± 3.5			
H[C]	3000−4000	0.030 ± 0.006[B]	HST/STIS	✗	Ballester et al. (2007)
H (Lyα)	1216	8.0 ± 5.7	HST/ACS	✗	Ehrenreich et al. (2008)
Na I	5893	0.135 ± 0.017[B]	Subaro/HDS	✓	Snellen et al. (2008)
C II	1335	7.8 ± 1.3	HST/COS	✓	Linsky et al. (2010)
Si III	1207	8.2 ± 1.4			
H (Hα)[D]	6563	—	HET	✓	Jensen et al. (2012)
Mg I	2852	6.2 ± 2.9	HST/STIS	✗	Vidal-Madjar et al. (2013)
HD 189733 b − 2.4% opt. transit depth − Bouchy et al. (2005)					
Na I	5893	0.067 ± 0.021[B]	HET	✓	Redfield et al. (2008)
H (Lyα)	1216	5.1 ± 0.8	HST/ACS	✗	Lecavelier des Etangs et al. (2010)
H (Hα)	6563	0.087 ± 0.015[B]	HET	✓	Jensen et al. (2012)
H (Lyα)[E]	1216	2.9 ± 1.4 / 5.0 ± 1.3	HST/STIS	✓	Lecavelier des Etangs et al. (2012)
O I	1306	6.4 ± 1.8	HST/COS	✗	Ben-Jaffel & Ballester (2013)
H + metals	X-rays	7 ± 1	CXO/XMM[F]	✗	Poppenhaeger et al. (2013)

[A]Indicates if the absorption signal is spectrally resolved.
[B]Excess absorption signal.
[C]Absorption in the Balmer continuum.
[D]Clear transit signal with unexplained spectral shape.
[E]Two individual transit observations in 2010 and 2011.
[F]Chandra X-ray Observatory and XMM-Newton.

the HST (see Fig. 13 in paper 3). The transit depth[4] measured in the optical range is only 1.6 %. Figure 1.3 relates the size of the planet to the size of the atmosphere in front of the host star. The authors concluded that the neutral hydrogen atmosphere extends beyond the Roche lobe and, thus, material must be lost continuously from the planet. This discovery led to a discussion about the true absorption depth and about the mass-loss rate (Ben-Jaffel 2007, 2008; Vidal-Madjar et al. 2008); in particular, the question of the mass-loss rate is still debated (see Sect. 1.5).

For a validation of the absorption signal the target was re-observed with the HST/STIS at a lower resolution, but with a wider spectral range. Vidal-Madjar et al. (2004) measured 5 % absorption over the unresolved Lyα line, which is consistent with the previous results. The credibility of the detection of the expanded atmosphere was further strengthened by the detection of excess absorption in O I and C II lines. Most importantly, the presence of metals with a higher molecular weight in the upper thermosphere can be seen as a proof of the escape process. In a static atmosphere heavy elements are homoge-

---

[4] The transit depth is defined as the fraction of the stellar disk, which is covered by the planetary disk during a transit. I always refer to the transit depth measured in the *optical* range unless otherwise stated. The transit depth has been measured to be wavelength dependent.

neously mixed only up to a certain height, the homo- or turbopause. Above this layer the atmosphere is stratified with the lightest elements hydrogen and helium at the top (heterosphere). In the atmosphere of Earth the homopause occurs at a height of approximately 100 km (measured by 107 rocket flights over a period of 20 years, Pokhunkov et al. 2009). The presence of heavy metals more than 2 R_{pl} above the planetary photosphere requires strong winds to sustain a homogeneous mixing in this region. Most likely the escaping atmosphere itself is the source for these strong winds (Vidal-Madjar et al. 2004).

Several additional observations of the system HD 209458 have been conducted until today. Ballester et al. (2007) detected excess absorption in the hydrogen Balmer continuum, which is associated with a dense, 5000 K hot atmospheric layer at an intermediate height between the lower atmosphere and the thermosphere. Unfortunately, shortly after the detection of the expanded atmosphere in HD 209458 b, the STIS instrument failed in 2004 and was not repaired until 2009 by the Servicing Mission 4. Nevertheless, Ehrenreich et al. (2008) again confirmed the Lyα absorption signal with the Advanced Camera for Surveys (ACS) on board the HST. The low resolution spectrum resulted in 8.0 % absorption measured over two transits of the hot Jupiter. In 2010, Linsky et al. reported 7.8 ± 1.3 % and 8.2 ± 1.4 % absorption in C II and Si III lines in spectrally resolved observations with the Cosmic Origins Spectrograph (COS) on the HST. The carbon signal agrees with the earlier result from Vidal-Madjar et al., but the Si III signal was absent in the earlier data, which is attributed to temporal variability of the escaping atmosphere. Most importantly, the velocity structure of the spectrally resolved absorption reveals 2σ signals at -10 and $+15$ km s^{-1} and less significant absorption features at larger velocity offsets. Since 10 km s^{-1} is a typical expansion velocity for a planetary wind (e.g., Koskinen et al. 2013a), this is the first indication of a direct measurement of the planetary wind velocity. Until today, these measurements were not confirmed. Jensen et al. (2012) measured a transit signal in the Hα line of HD 209458 with the Hobby-Eberly-Telescope (HET), but the unusual spectral shape of the absorption and emission feature has not been fully understood. Finally, Vidal-Madjar et al. (2013) also detected an absorption signal of neutral magnesium. Most recently the HST/COS observations were re-evaluated and the detection absorption from Si III was challenged (Ballester & Ben-Jaffel 2015).

HD 209458 b is a keystone in the study of expanded planetary atmospheres. Some of the listed observation techniques have since been applied to further systems, but almost all of them were first tested on HD 209458. Although the individual signals are weak, the wealth of measurements leaves little doubt today: HD 209458 b does host an expanded atmosphere. There are strong indications that this expanded atmosphere is indeed evaporating, however, the problem is highly complex and a conclusive proof that the signals cannot be produced by a stable thermosphere has not been but forward (see Sect. 1.4).

1.3.2 HD 189733 b and WASP-12 b

Besides HD 209458 b, an expanded atmosphere has only been detected conclusively in the hot Jupiter HD 189733 b (see Table 1.1) and in WASP-12 b. HD 189733 b was discovered by Bouchy et al. (2005). With a distance of only 19.3 pc, this system is closer to the Sun than HD 209458 with 47 pc. Its Lyα flux is almost ten times stronger than that of HD 209458 (see paper 2), thus, the system is more easily accessible for transit observations.

The atmosphere of the planet was discovered by Redfield et al. (2008) in sodium lines with the HET. The absorption level is two to three times larger than in HD 209458 b, nevertheless, neutral sodium is confined to the lower atmosphere of the planet. An expanded atmosphere was detected by Lecavelier des Etangs et al. (2010), who found 5.1 % absorption in the Lyα line in a spectrally unresolved observation with the ACS on the HST. Jensen et al. (2012) detected clear excess absorption in the Hα line of 0.087 ± 0.015 % over a 16 Å bandpass with the HET. In the line center the excess absorption depth is even 2 %.

The Lyα absorption signal was confirmed by Lecavelier des Etangs et al. (2012), who detected 5% absorption in an observation, which occurred in 2011. An earlier observation in 2010 did not show any excess absorption, thus, the absorption signal is time variable in this system. The spectrally resolved signal in this observation shows a maximal absorption depth of 14.4 ± 3.6 % in the blue line wing at a line shift around -180 km s^{-1}. In 2013, Ben-Jaffel & Ballester report on 6.4 ± 1.8 % absorption in a neutral oxygen line. Interestingly, excess absorption was also detected via X-ray observations, which possibly opens a new channel for the characterization of expanded planetary atmospheres (Poppenhaeger et al. 2013). The target was again observed in 2013 with the HST/STIS (Wheatley, unpublished). A preliminary analysis of one transit observation again reveals little absorption over the complete Lyα line, but 7.1 ± 2.8 % absorption in the blue line wing.

The expanded atmosphere of WASP-12 b was detected by Fossati et al. (2010) through broad band excess absorption in the NUV range with the HST/COS and significant absorption in several metal lines. The detection was confirmed in two more observations with similar setups (Haswell et al. 2012; Nichols et al. 2015). At a distance of 300 pc this system, discovered by Hebb et al. (2009), is too faint for Lyα transit observations.

1.3.3 Further systems with indications for expanded thermospheres

There are two further systems where excess absorption was measured in individual observations. These generally provide evidence for expanded planetary thermospheres, but all of these observations are prone to stellar variability especially in the ultraviolet wavelength range (see Sect. 1.3.5). For an unambiguous detection, a confirmation of these signals is essential.

- Ehrenreich et al. (2012) report a 7.5 ± 1.8 % absorption feature in the Lyα line of 55 Cnc during the conjunction of the hot Jupiter 55 Cnc b, while no significant signal was detected during the transit of the super-Earth 55 Cnc e. Interestingly, the hot Jupiter does not transit the host star in the optical range, only the expanded atmosphere seems to undergo a grazing transit.

- Kulow et al. (2014) find 8.8 ± 4.5 % absorption in the Lyα line during the transit of the hot Neptune GJ 436 b, but an astonishing 22.9 ± 3.9 % absorption 2 h after the transit. This may well be the first detection of a cometary tail-like evaporation structure as originally proposed by Schneider et al. (1998).

The study of planetary atmospheres is still a young research field. If the absorption signals can be confirmed in these two systems, expanded atmospheres can likely be seen as a common feature of hot gas planets.

1.3.4 Detecting planets around the brightest stars

The detected signals of expanded planetary atmospheres are on the edge of feasibility with today's instrumentation. The thermospheres mostly absorb in the UV range, because the thin and hot gas is weakly excited and only atomic transitions close to the ground state can be detected in absorption. These transitions are often in the UV range for neutral or weakly ionized atoms, for example for O I or C II (NIST Atomic Spectra Database Lines Data, Kramida et al. 2014). Two exceptions are the Hα absorption measured by Jensen et al. (2012), which is caused by hydrogen in the excited second state, and the absorption in the sodium doublet at 589.3 nm detected by Charbonneau et al. (2002), which is in the visual range.

In the UV range, stellar line fluxes are two to four orders of magnitude fainter than the blackbody emission in the visual range (see Fig. 1 in paper 3). The line flux of the strongest emission line (hydrogen Lyα) is further diminished by interstellar absorption. Therefore, the characterization of expanded planetary atmospheres is limited to close-by systems, which are bright enough for the measurements. A brighter host star allows an easier detection of a planetary atmosphere, because a high signal-to-noise ratio is achieved with shorter observations. However, the detection of transiting planets around the brightest stars is also difficult. Current transit surveys are limited to stars with visual magnitudes > 7 (e.g., Pollacco et al. 2006). Actually, 55 Cnc is the only known star visible to the naked eye that hosts a transiting planet (Winn et al. 2011).

The two most important systems for the science of expanded planetary atmospheres, HD 209458 and HD 189733, are the second and third brightest host stars with transiting planets at the time of writing (exoplanets.org, Han et al. 2014). Even brighter systems are highly desirable for atmospheric science. The SIMBAD database lists 1600 FGK main sequence or slightly evolved stars with $V < 7$ mag and still 550 visible to the naked eye ($V < 6$ mag). The occurrence rate of hot Jupiters with 1.2 % in FGK stars coupled with the probability for orbital alignment of about 10 % indicates that a few additional transiting hot Jupiters could be found around the very brightest stars (Marcy et al. 2005; Beatty & Seager 2010). Furthermore, hot super-Earth type planets are six times more frequent than hot Jupiters (Howard et al. 2012), indicating an even larger discovery potential.

Some of these hypothetical planets will hopefully be detected in the near future. The GAIA mission, which will map about one billion stars in our Galaxy (Perryman et al. 2001), has the potential to detect thousands of transiting planets around stars up to a brightness of $V > 5.7$ mag (Voss et al. 2013; Martín-Fleitas et al. 2014); this mission has just entered its operational phase. More importantly, the Transiting Exoplanet Survey Satellite (TESS), planned to launch in 2017, is designed to find transits for stars as bright as $V = 4$ (Ricker et al. 2014). Furthermore, the CHEOPS ESA mission, also with a planned launch in 2017, will detect smaller additional planets around bright host stars, which are known to host a Neptune-sized planet (Broeg et al. 2013). Finally, the PLATO
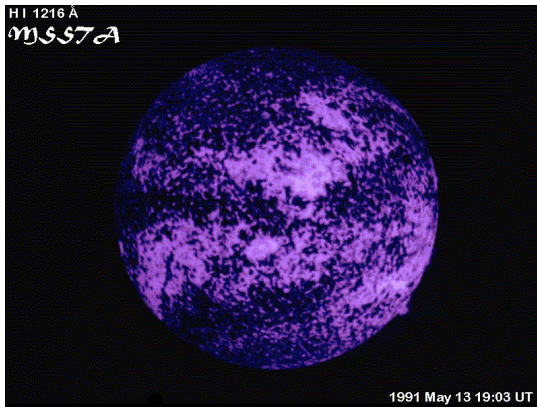
Fig. 1.4. Solar Lyα emission recorded by The Multi-Spectral Solar Telescope Array (MSSTA), which was a telescope carried by a sounding rocket (NASA). The solar Lyα emission is connected to active regions, which occur in activity belts.

mission from ESA will observe one million bright stars and detect and characterize hundreds of planets starting in 2022/24 (Rauer et al. 2014).

1.3.5 Inhomogeneity and variability of host stars

One major detection challenge is the variability of the host stars. This was studied by Ben-Jaffel (2007), who performed a detailed analysis of the transit observations of HD 209458 b. In their Fig. 2 they show that the Lyα line flux of this inactive target in the out-of-transit observations is stable to about 1 %, but with a statistical error of 3 % and on a rather short time scale of about 5 h. In general, one could expect that the Lyα emission of host stars is highly time variable and also inhomogeneously distributed over the stellar disk. Figure 1.4 shows the Sun's emission in the Lyα line; the emission emerges from active regions, which form active belts. If the stellar emission is concentrated onto 50 % of the stellar surface and an exoplanet traverses in front of an active belt, the resulting transit depth would be increased by a factor of two, without any atmospheric absorption. However, to reproduce a transit depth of 10 %, the emission must also be concentrated on a smaller fraction of the stellar disk and the planet would have to transit directly in front of the emission. This geometric configuration is unlikely, especially if excess absorption is detected in several observations. This topic was most recently covered by Llama & Shkolnik (2015), who simulated transits of hot Jupiters with resolved images of the Sun. The authors found that in the EUV and X-ray range transit depths can be enhanced by up to a factor of two. However, absorption features with a strength of about 10 % are unlikely to be mimicked by an inhomogeneous emission pattern if the planet covers only 1 to 2 % of the stellar disk.

Especially for the Lyα line the problem is actually not as bad as suggested by Fig. 1.4, because the image shows emission dominated by the line center, which is produced at high temperatures around 20 000 K in the solar chromosphere (Vernazza et al. 1981). However, the line center is extinguished by interstellar absorption and the planetary Lyα absorption features are detected in the line wings with shifts of 0.2 to 1.0 Å (see Fig. 13 in paper 3). These line wings are formed deeper in the solar chromosphere, where pressure broadening increases the line width and photons emitted in the line wings can escape due to a higher escape probability of emission shifted from the central wavelength. A typical temperature
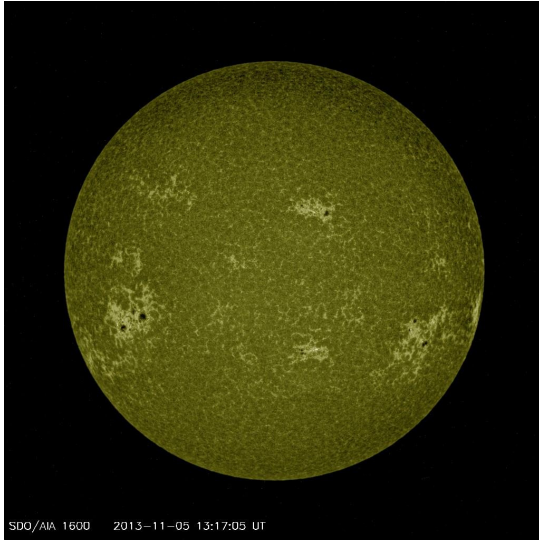
Fig. 1.5. Solar emission at about 6 000 K (C IV at 1600 Å). The emission shows a web-like structure, is bright around active regions, but generally more homogeneous than emission at higher temperatures. Courtesy of NASA/SDO and the AIA, EVE, and HMI science teams.

is about 6000 K for emission shifted 1 Å from the line center (Vernazza et al. 1981). Figure 1.5 shows carbon emission that originates from regions with this temperature. The emission is more homogeneously distributed than the Lyα peak emission. Thus, it is less likely that a transit feature can be produced by inhomogeneous emission at this temperature at least for solar-like stars.

## 1.4 A more complete picture of planetary winds

The escaping atmosphere as described in Sect. 1.2.3 certainly provides a strongly simplified picture of the actual processes affecting the atmospheres of hot gas planets. Figure 1.6 visualizes the major processes that have been neglected in the simple planetary wind model. Each of them can affect the planetary mass-loss rate and the absorption signal in transit observations.

1.4.1 The planetary nightside

The nightside of the planet is thought to be less than 500 K cooler than the dayside, due to strong winds that redistribute energy in the lower atmosphere of the planet (e.g., Knutson et al. 2007). Nevertheless, in the shadow of the planet the temperature of the thermosphere is reduced, leading to a possible inflow of material onto the nightside (Stone & Proga 2009, also see Sect. 1.5.1).

1.4.2 Radiative cooling

Radiative cooling re-emits a fraction of the absorbed energy. In models of planetary winds this is often included by assuming a certain heating efficiency for the absorption of EUV radiation. Individual authors used widely different heating efficiencies ranging from 0.1 to 1.0 as elaborated by Shematovich et al. (2014). A few authors also included individual additional cooling agents like Lyα cooling (e.g., Murray-Clay et al. 2009).
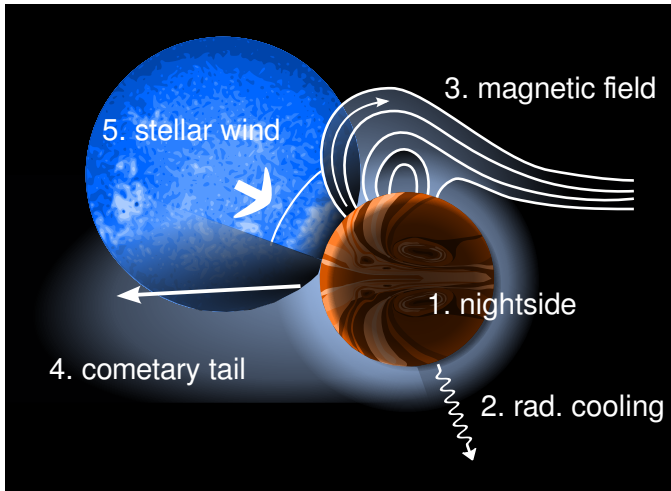
Fig. 1.6. Sketch of the major influences on the planetary wind. The figure depicts a hot Jupiter in transit as seen in Lyα emission (except of the planetary photosphere). The planetary wind is shown in absorption in front of the star and as scattering source next to star (scattering is exaggerated). The figure is split into individual parts, which are explained in the main text.

Effects of radiative cooling are discussed in detail in paper 3. In previous studies radiative cooling was underestimated especially in compact and massive planets, where the heating efficiency approaches zero.

1.4.3 Magnetic fields

Strong magnetic fields can affect the partially ionized outflow from gas planets. However, the magnetic fields of hot Jupiters have not been measured with certainty (Sirothia et al. 2014). For the radio emission of HD 209458 b and HD 189733 b Lecavelier des Etangs et al. (2011) present upper limits, which can be converted into upper limits for the planetary magnetic field strength with certain assumptions. This results in magnetic fields that should be weaker than a few times the field strength of Jupiter, which has an equatorial field strength of $B = 4.3$ G (Trammell et al. 2011), but these are no strict upper limits. For WASP-12 b Vidotto et al. (2010) derive an upper limit for the magnetic field strength of 24 G.

Unfortunately, also theoretical approaches do not constrain the magnetic field strength. As pointed out by Trammell et al. (2011) estimates for hot Jupiter magnetic fields range from 0.1 to 10 times Jupiter's field strength. Dynamo models typically involve rotation and convection to generate magnetic fields (Parker 1955). Since hot Jupiters are most likely tidally locked, their rotation period is equal to the orbital period. They rotate more slowly than Jupiter itself and one would expect weak magnetic fields. However, Christensen et al. (2009) argue that the generated field strength is independent of the rotation rate in planets under certain conditions. Especially hot Jupiters with low mean densities must experience a high thermal heat flux in the interior, which drives a strong thermal convection. This results in high estimates for the magnetic field strength.

Most often planetary magnetic fields are neglected, but Trammell et al. (2014) found that strong magnetic fields can stabilize a planetary thermosphere over large fractions of the planetary surface. Without constraints for the magnetic field strength of hot Jupiters, it is difficult to assess their impact, however.

1.4.4 3D structure

Deviations from spherical symmetry in the planetary wind are certain, therefore, I depict the freely escaping atmosphere as a cometary tail-like structure in Fig. 1.6. Close to the planet a spherical shape of the wind is likely valid. However, above the Roche lobe the effective gravitational potential strongly favors flows toward and away from the host star (see Fig. 1.2). Furthermore, the stellar wind will deflect the planetary wind, as for example shown by the simulations of Tremblin & Chiang (2013). Stellar rotation causes a spiral structure of the stellar wind (Parker 1958), thus, it collides with a certain angle from the head-on direction of the orbital motion of the planet. Due to the gravitational potential, the orbital velocity of the planet, and the interaction with the stellar wind the escaping atmosphere should be deflected into a cometary tail-like structure above the planetary Roche lobe (Schneider et al. 1998).

The detectability of a cometary tail depends on the strength of the planetary wind and the irradiation level. A moderately irradiated small gas planet can produce a mostly neutral planetary wind, where the cometary shape can be detected. This is exactly the case for GJ 436 b, where indications of such a structure were detected (Kulow et al. 2014). Strongly irradiated high-mass planets produce weak but highly ionized winds, which are invisible for Lyα transit observations (see paper 3).

Previous authors have argued that the planetary wind is also affected by radiation pressure (Vidal-Madjar et al. 2003; Bourrier & Lecavelier des Etangs 2013). In paper 3 we show that the planetary wind is collisional in agreement with the analysis of, for example, Murray-Clay et al. (2009). In combination with the high degree of ionization of the planetary wind above the Roche lobe, this reduces the radiation pressure to negligible values.

1.4.5 Stellar wind pressure

Finally, an escaping planetary atmosphere can be stabilized by an outer pressure, which is provided by a stellar wind from the host star (Murray-Clay et al. 2009). If the stellar wind pressure is high enough, it can suppress the planetary wind at least around the head-on collision point. Moving away from this point, the angle between the colliding winds increases, hence the pressure exerted by the stellar wind decreases until the planetary wind is strong enough to escape against the outer pressure. Again, the stable part of the atmosphere will be hotter and more strongly ionized, and the expected contribution to the absorption signal is small (see Fig. 1.6).

Naturally, there are further questions regarding the photoevaporation of hot gas planets. How strongly are they affected by the activity of the host star? What happens during the impact of a coronal mass ejection? How much do metals affect the wind through additional cooling and which metals are dragged along into the thermosphere? At which irradiation does the outflow become molecular as already mentioned by Watson et al. (1981) for Earth and Venus, and how much do molecules affect the wind through additional absorption and emission? Some of these questions have been partially addressed, but in general one has to conclude that the process of a planetary wind driven by high energy irradiation is not yet thoroughly understood.
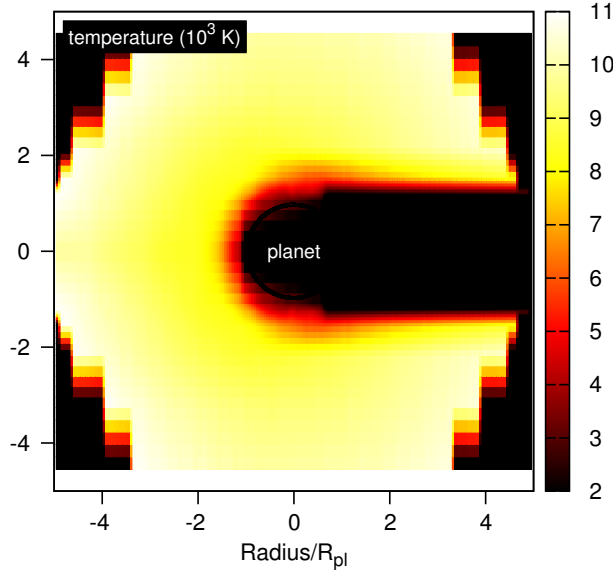
Fig. 1.7. Temperature structure in a planetary atmosphere, which is irradiated from the left-hand side. This is a result of a pseudo-2D radiative transfer simulation through a static atmosphere. Only in the shadow of the planet the spherical symmetry is broken.

1.5 Modeling the atmospheres

The complexity of the environment of hot Jupiter atmospheres is also reflected in a continuing disagreement regarding the interpretation of the measured absorption signals. In the discovery paper of the expanded atmosphere of HD 209458 b, Vidal-Madjar et al. (2003) provided only a brief explanation that radiation pressure in the Lyα line could accelerate neutral hydrogen above the Roche lobe away from the planet forming a cometary tail-like structure. The authors neglected the photo-evaporation process as noted shorty after the detection by Lammer et al. (2003). Since the discovery, at least four different models have been used to explain the absorption signal of HD 209458 b. In principle, each of the following models can reproduce the observations individually.

1.5.1 Spherically symmetric planetary wind

A number of authors have constructed 1D models of the escaping atmospheres, simulating the formation of the wind including a consistent EUV absorption scheme (Yelle 2004; Tian et al. 2005; García Muñoz 2007; Penz et al. 2008; Murray-Clay et al. 2009; Koskinen et al. 2013a).

The models result in spherically symmetric escaping thermospheres. This approach is more than just a simple toy model; for the thermosphere below the Roche lobe a spherical approximation is a reasonable assumption. While 50% of the photosphere lies in the shadow of the planet, the impact becomes less important with increasing height. At 2 $R_{\rm pl}$ the planetary shadow covers only 1/16 of the atmospheric layer. This is illustrated in Fig. 1.7, which depicts the temperature structure in an atmosphere with a spherical density structure due to the one-sided irradiation of a hot Jupiter. The pseudo-2D irradiation simulation indicates that only the shadow region deviates from spherical symmetry. In dynamical simulations bulk flows into the shadow region would mitigate the strong temperature deviations that are found in this static irradiation simulation. For example

Stone & Proga (2009) showed that the mass-loss rate in an axis-symmetric 2D simulation is a factor four weaker than in the spherically symmetric case. However, 75% of this change is induced by a higher energy input in their spherically symmetric simulations. Thus, if the energy input is handled correctly in a 1D simulation, the resulting mass-loss rate is a valid estimate.

Generally the 1D models produce comparable results. Koskinen et al. (2013a) invested some effort in explaining differences in the atmospheric structures from previous authors and concluded that these are caused by different numerical schemes, different boundary conditions, or varying irradiation assumptions. The biggest advantage of 1D simulations is that they can be used to study the impact of individual physical process on the escaping atmosphere. For example Murray-Clay et al. (2009) found that Lyα cooling is a strong energy sink in the atmosphere of HD 209458 b. Today, such details have only been studied in 1D models. None of the published multidimensional models solve the escaping atmosphere with a consistent photoionization scheme (e.g., Stone & Proga 2009; Trammell et al. 2011, 2014).

In spite of similar atmospheric structures, the authors of the 1D simulations disagree whether a spherical atmosphere can reproduce the absorption signals of HD 209458 b. However, as pointed out in paper 3, an undisturbed spherically expanding atmosphere cannot explain the absorption signal of HD 189733 b.

1.5.2 Colliding winds and charge exchange

Holmström et al. (2008) were the first to acknowledge that charge exchange between the neutral planetary atmosphere and the ionized stellar wind must be an important process. Hot and fast protons from the stellar wind interact with neutral hydrogen from the planetary atmosphere. Through exchange of electrons a hot neutral hydrogen population with a large velocity offset is created (energetic neutral atoms, ENA). This ENA cloud can be responsible for significant absorption also in the wings of the Lyα line, where the absorption of HD 189733 b was observed.

The model was further developed by Ekenbäck et al. (2010), who preformed meta-particle simulations (direct simulation Monte Carlo method, DSMC) starting at the exobase, which is the height above which the atmosphere of a planet becomes collisionless. The assumption of a collisionless regime is not valid for the thermospheres of hot Jupiters, as shown by the 1D simulations (see paper 3). The interaction with the stellar wind occurs before the atmospheres become collisionless (Murray-Clay et al. 2009). However, the DSMC model of Ekenbäck et al. explicitly includes collisions and should produce results similar to hydrodynamic simulations, if a sufficient number of meta-particles is included. Nevertheless, hydrodynamic (HD) simulations of the colliding winds including charge exchange in a turbulent interaction region as presented by Tremblin & Chiang (2013) are likely more appropriate for the conditions in this region. Although charge exchange is probably required to explain the absorption signals measured at high velocity offsets, none of the colliding wind simulations solves the problem of the underlying planetary wind formation by photoevaporation. Furthermore, the HD and the DSMC particle simulations of the colliding winds produce different results, for example regarding the shape of the interaction region.

1.5.3 Radiation pressure

The stellar radiation pressure model introduced by Vidal-Madjar et al. (2003) was further developed by Bourrier & Lecavelier des Etangs (2013). They also performed Monte-Carlo particle simulations starting at the exobase similar to the models from Ekenbäck et al.. The authors neglect collisions and remove ionized particles of the planetary wind in the simulations. Charge exchange between the stellar and the planetary wind is included. However, the assumption of a collisionless regime is inappropriate; removing ionized planetary wind particles from the simulation neglects that neutrals and ions are coupled by charge exchange throughout the planetary wind. Although the simulations can explain the blue shifted absorption signals partially, they are most likely not valid for the conditions in planetary thermospheres (see paper 3).

1.5.4 Magnetically stabilized atmosphere

Recent MHD simulations of Trammell et al. (2014) show that stronger planetary magnetic fields can stabilize the escaping atmosphere over parts of the planetary surface. In the presented model the resulting planetary mass-loss rate is reduced by a factor of three. The authors argue that the magnetically stabilized parts of the planetary atmospheres contribute significantly to the measured absorption signals. However, as pointed out in paper 3, their reasoning is based on isothermal simulations, which do not account for the fact that stable parts of an atmosphere are hotter than the freely escaping atmosphere due to the lack of adiabatic cooling (Watson et al. 1981). Furthermore, it is challenging to reconcile a stable atmosphere with the detection of metals in the expanded thermosphere (see Sect.1.3).

1.6 Current and future progress in the field

Here, I outline some ideas of how the study of escaping atmospheres in hot gas planets can proceed in the future, which puts our approaches, followed by my collaborators and me (see Sect. 2), into a broader context.

1.6.1 Improved numerical models

The models presented in the previous section depend on partially contradicting assumptions and include different physical processes. The ideal numerical model would include all important processes. Such a hypothetical simulation can start in the lower atmosphere, because the planetary wind is to a large extent decoupled from these regions (see paper 3). The photoionization and the produced radiative heating and cooling must be solved in detail as discussed in paper 3. For modestly irradiated planets the wind is molecular, which requires a photochemistry solver. The model would also have to include a multi-species approach with diffusion to solve the advection of heavy metals into the thermosphere. Above the Roche lobe, the problem has a strongly asymmetric nature and 3D simulations are required for realistic solutions. The gravitational potential of the rotating two-body system is one of the dominating forces. The interaction with the stellar

wind must be included and certainly the charge exchange process. Radiation pressure should also be included to further study its effects.

Finally, magnetic fields are crucial, at least for the interaction with the stellar wind. The example of Venus shows that even if a planet does not host a strong intrinsic magnetic field, the atmosphere is partially shielded from the stellar wind through a magnetic barrier above the ionosphere (Zhang et al. 1991, 2006). In the transition to stable atmospheres of either weakly irradiated or massive planets, the thermospheres become collisionless and a realistic simulation is dominated by non-thermal mass loss processes (e.g., Lammer et al. 2008; Johnson et al. 2008; Lammer et al. 2013). This ideal simulation does not exist at the moment and a construction of such a model is challenging to adapt to available computational resources today.

1.6.2 Observational approach

In principle, the ambiguity in the interpretation of the observations can be solved by further observations. There are two possible approaches. The first one involves further observations of the known targets with a high resolution spectrograph (COS on HST) to resolve the spectral components of the absorption signal. This approach is promising for the system GJ 436, where a large absorption signal has been measured. A new transit study of the system should not only aim at a confirmation of the absorption signal, but could be used to detect individual velocity components of the expanding atmosphere and the interaction region with the stellar wind similar to the observations of HD 209458 b by Linsky et al. (2010). This observation has the potential to prove the atmospheric escape via the photoevaporation process. For HD 209458 b an improvement of the existing observations is expensive regarding the required exposure time. The observations from Linsky et al. (2010) with COS used 20 HST orbits, corresponding to about 32 h allocated time. An improvement of the signal-to-noise ratio by a factor of two requires a four times longer exposure duration resulting in more than 5 d allocated spacecraft time.

The second approach is based on a comparison of absorption signals from different systems. Among others (Fossati et al. 2015; Bourrier et al. 2015), it is being pursued by my collaborators and me. The absorption signals of HD 209458 b and HD 189733 b show pronounced differences in the spectral structure. These are connected to system parameters via the underlying physical processes. Each of the models explained above depends on individual system parameters as explained in paper 2. Therefore, it should be possible to distinguish the dominating processes in the planetary atmospheres by comparing absorption signals of different system.

Only few detected planetary systems are amenable to Lyα transit observations with current facilities. In principle, these systems can be scanned for absorption signals with the HST over the next few years, creating a uniform database of absorption signals. However, also this approach leads to a high demand of spacecraft time, because fainter targets require a stacking of several transit observations. This increases the required time for a single detection sometimes to more than 20 HST orbits. Certainly only the most promising targets can be chosen for this approach. Unfortunately, the situation is unlikely to improve in the near future. For the post-HST era only one large scale UV space telescope is planned, the World Space Observatory-Ultraviolet with a launch date

in 2018 (Shustov et al. 2011). The telescope and instruments will have a similar sensibility as current instruments on the HST, but the observing time is exclusively dedicated to the UV spectral range, which at least partially relieves the high demand for observing time compared to the HST (Fossati et al. 2014).

2 Results

Here, I summarize the results presented in the publications and point out their impact on the research field. My approach is twofold: On the one hand I simulate the atmospheres of hot gas giants to gain a better understanding of the involved processes and on the other hand I work on improving the observational basis to better confine atmospheric models. Throughout this chapter I repeatedly refer to *our* work, because the results were produced in collaboration with colleagues (see Sect. Publications).

2.1 Simulating the escaping atmospheres of hot gas planets

In this dissertation, individual aspects of the planetary atmospheres are investigated in 1D simulations. I focus on a detailed study of the heating and cooling processes in atmospheres consisting of hydrogen and helium.

2.1.1 Motivation

Our study was inspired by CoRoT-2 b, a hot Jupiter orbiting one of the most active host stars detected so far (Alonso et al. 2008; Schröter et al. 2011). The high-energy irradiation of this planet is about 10^5 times stronger than the irradiation of Earth, and X-rays contribute about 60% of the hydrogen ionizing irradiation (see paper 3). In similar 1D simulations, the absorption of EUV radiation is solved by a simple absorption scheme using a wavelength dependent absorption cross-section for the photoionization of hydrogen. These models assume an average heating efficiency for photons of all energies (e.g., Tian et al. 2005; Penz et al. 2008; Murray-Clay et al. 2009). The heating efficiency accounts for the fraction of the photon energy used to ionize hydrogen, but also for unspecified cooling agents. Only the remaining energy is available to heat the atmosphere and drive the planetary wind. This approach is bound to fail for X-rays, however. The absorption of an X-ray photon causes a large number of secondary ionizations and only a small fraction of the photon energy is available for atmospheric heating. Thus, the heating efficiency in the absorption of X-rays is smaller than that of EUV radiation. For example, Cecchi-Pestellini et al. (2006) presented a study of the absorption of high-energy radiation in atmospheric gas and provided wavelength dependent heating efficiencies, which have been used in the atmospheric evaporation study of Koskinen et al. (2013a).

I opted for a different approach, in particular, the use of a self-consistent photoionization solver for the absorption of high-energy radiation. The chosen photoionization solver computes the absorption of EUV radiation and X-rays, including radiative cooling of the gas, secondary ionizations, and many more processes affecting the microphysical state of the gas. Hence, a heating efficiency is not specified, but is the result of the detailed solution of the microphysical equilibrium state.

However, few available photoionization solvers include hydrodynamical effects, which are of course crucial for simulating the escaping atmospheres. The most advanced codes are only available for static density structures, because they have to cope with two computationally demanding problems. First, radiative transfer is especially demanding in multidimensional simulations, because all cells can mutually interact and convergence of the radiative solution can require many iterations. The computational load further depends linearly on the chosen spectral resolution. Second, solving the microphysical state of a gas can be computationally demanding, depending on how many interactions are included, thus, depending on the chosen complexity of the microphysical model. Both tasks are coupled, because radiative transfer is affected by the microphysical state of the gas via the source function, and the microphysical state, for example the degree of ionization, certainly depends on the local mean radiation field.

2.1.2 A new photoionization hydrodynamics solver

To model the escaping atmospheres of hot gas planets, a new simulation tool "the PLUTO-CLOUDY Interface" (TPCI) has been constructed. The numerical scheme and the verification of this code is the topic of the first publication (paper 1, see Sect. Publications). It is an interface between the photoionization solver CLOUDY and the magnetohydrodynamics (MHD) code PLUTO. It follows a simple scheme: The dynamical evolution of a gas is advanced by PLUTO and between (magneto-) hydrodynamic steps CLOUDY is called to solve the microphysical equilibrium state under the given irradiation. It returns the radiative heating and cooling, which is included in the MHD code.

In paper 1 the interface is tested in 1D simulations, but it is also capable of parallel 3D simulations on a Cartesian grid with pseudo-3D radiative transfer[1]. Paper 1 is a method paper, which focuses on the verification of the code. Although the code was designed to solve the atmospheres of hot Jupiters, the result is a versatile code, which can be used to compute dynamical photoevaporative flows in many environments. For the verification in paper 1 four problems were drawn from different astrophysical fields, which demonstrates the range of applications for the interface.

One of the test problems is the escaping atmosphere of HD 209458 b. The results of TPCI are comparable to the most recent simulations of Koskinen et al. (2013a). Besides the possibility to include many metals and also molecules, especially the improved radiative cooling rates for Lyα and free-free emission show where TPCI can be used to improve previous results. While Murray-Clay et al. (2009) and Koskinen et al. (2013a) included Lyα emission based on certain estimates, TPCI directly solves the emission from first principles by balancing the level populations in a large hydrogen model atom[2], accounting for the local photon escape probabilities. While paper 1 focuses on technical aspects, applications and physical results are presented in the following publications.

---

[1]Radiative transfer is computed along 1D slices of the computational domain.
[2]The standard setup for the hydrogen atom has 10 resolved levels and additionally 15 levels with l-mixing according to statistical weights.

2.1.3 Escaping planetary atmospheres in the solar neighborhood

The importance of the detection of further expanded planetary atmospheres has been outlined in Sect. 1.5. The considerable observational effort for such detections can only be undertaken for a small number of targets in the next few years. Thus, it is crucial to the select systems, with the highest probability to detect an expanded atmosphere. In the third paper, TPCI simulations of the atmospheres of 18 hot gas giants with stellar distances < 120 pc are presented (paper 3, see Sect. Publications). These comprise the most promising targets in the search for yet undetected expanded planetary atmospheres (in terms of measurable Lyα flux at Earth). The simulations include accurately reconstructed irradiation levels of X-rays, EUV, and Lyα emission, which are to a large extent based on our new X-ray measurements (see Sect. 2.2.1).

Based on the simulations, we found a transition from strong planetary winds in small hot Neptunes, to stable thermospheres in compact and massive hot Jupiters. The use of the microphysics solver was most important for this result, because it resulted in strong radiative cooling throughout the hot thermospheres of compact exoplanets. In the most extreme cases, like HAT-P-2 b or HAT-P-20 b, the cooling was sufficient to balance the high level of irradiation. The atmospheres are in radiative equilibrium and no acceleration of a planetary wind takes place.

The simulated spherical atmospheres are used to predict Lyα absorption signals. In the four systems with HST/STIS observations, we compare our results to the measured absorption signals. Table 4 in paper 3 shows that the general trend in the detected signals is reproduced: Large absorption signals are calculated for HD 209458 b and GJ 436 b, where large signals were measured. In agreement with the observations, the signal of HD 189733 b is smaller and also the nondetection of 55 Cnc e is reproduced by the model atmosphere.

The computed absorption signals of all systems in the solar neighborhood with transiting hot gas planets are provided in Table 3 in paper 3 and visualized in Figs. 15 & 16. The strength of the absorption signals depends on the strength of the planetary wind, on the degree of ionization in the wind, and on the planet to star size ratio. The analysis reveals that WASP-80 b is the most promising candidate to search for expanded atmospheres in respect of the predicted absorption signal.

2.1.4 Energy-limited escape revised

Watson et al. (1981) showed that under certain conditions escaping atmospheres approach an energy-limited escape flux. In this case, the mass-loss rate of a planet can be estimated by simple reasoning: The complete absorbed radiative energy (corrected for the heating efficiency) is converted into gravitational potential energy by lifting atmospheric material out of the planetary gravitational potential. For example Erkaev et al. (2007) presented a concise derivation of the concept. While the resulting mass-loss rate is an upper limit, energy-limited escape is a widely used concept and has been applied to all detected hot gas planets to estimate their lifetimes due to photoevaporation (e.g., Ehrenreich et al. 2012). However, in paper 3 we found stable thermospheres in compact and massive hot Jupiters,

which contradicts the predictions of energy-limited escape. The differences result from three inherent weaknesses of the energy-limited model, which I discuss below.

1. Range of validity

The concept of energy-limited escape is based on hydrodynamically escaping atmospheres. The hydrodynamic description is only valid if the thermosphere is collisional. The height of the exobase depends on the atmospheric density, and the stronger the planetary wind, the higher is the density in the thermosphere. Thus, only planets with a high mass-loss rate truly host a hydrodynamically escaping atmosphere, and only for these planets the energy-limited model can be used. However, there is no simple rule to decide, which planets actually host hydrodynamically escaping atmospheres.

2. Heating efficiency

If a close-in planet hosts no hydrodynamical wind, the radiative energy input must be disposed of otherwise. This is achieved through emission – the planetary atmosphere is in radiative equilibrium[3]. Hence, the heating efficiency for the absorption of high-energy radiation cannot be identical for all planets. In small, hot gas planets, a large fraction of the energy input is consumed to drive the planetary wind, but in massive and compact hot Jupiters this energy input is re-emitted, thus, the heating efficiency approaches zero.

3. Atmospheric expansion radius

The larger the extent of the planetary atmosphere, the more radiation is absorbed, which results in a stronger planetary wind. The expansion is negligible for massive hot Jupiters, because their thermospheres are rather compact. In contrast, smaller gas planets host more strongly expanded atmospheres with expansion radii exceeding $3\,R_{\mathrm{pl}}$.

Correcting the energy-limited escape model

All three weaknesses of the energy-limited escape model are addressed in the fourth publication (paper 4, see Sect. Publications); the most important point is the heating efficiency. It is shown that the heating efficiency depends on the gravitational potential energy per unit mass of the planet. A planet with a high potential has a hotter atmosphere, which re-emits a larger fraction of the radiative energy input, thus, the resulting planetary wind is weaker. A correction for the heating efficiency is provided. The transition from a hydrodynamic planetary wind to stable atmospheres occurs at a gravitational potential of $\log -\Phi_{\mathrm{G}} \approx 13.6\ \mathrm{erg\,g^{-1}}$; planets with a higher gravitational potential have stable thermospheres.

The atmospheric expansion radius with respect to the absorption of XUV radiation can be computed directly from the simulations (see Table A.1 in paper 4). It depends on the gravitational potential and on the irradiation level; a scaling law to derive the expansion radius is provided.

The presented new energy-limited escape is important for the study of exoplanetary atmospheres and for considerations regarding the stability of close-in gas planets. For the first time, it is now possible to decide, which planets host stable thermospheres based on

---

[3] For this argument, the complexity of stable thermospheres is neglected and no other energy sinks are considered.

their radius and mass alone. The new heating efficiency corrects errors of several orders of magnitude in the mass loss estimates for hot gas planets. This affects mass loss studies as presented, for example, by Sanz-Forcada et al. (2011) or Ehrenreich & Désert (2011)

2.2 Observational approach

The observational approach chosen by my collaborators and me involves two distinct advances. On the one hand, it is important to find further exoplanets with expanded atmospheres, to reveal the dominating influences on the planetary thermospheres. On the other hand, the conditions in the planetary thermospheres crucially depend on the high-energy irradiation level of the planets, which can be revealed by X-ray observations.

In any case, it is essential to first select the best targets. The second paper describes our target selection (paper 2, see Sect. Publications), which is based on a prediction of the measurable Lyα line flux at Earth, because four of the five detections so far were achieved by Lyα transit spectroscopy. In total we find 19 systems, for which Lyα transit spectroscopy seems promising[4].

2.2.1 Irradiation level

Knowledge about the irradiation level is crucial for determining the mass-loss rates of hot gas planets (e.g., Sanz-Forcada et al. 2011) and also for every model of the planetary thermospheres. Irradiation shortward of 912 Å is capable of ionizing hydrogen and contributes to the heating of the thermospheres. However, stellar emission from 400 to 912 Å is completely extinguished by interstellar absorption (e.g., Linsky et al. 2014). Only shortward of 400 Å, emission of the closest stars becomes detectable as observed for example by the Extreme Ultraviolet Explorer (Craig et al. 1997). To determine the irradiation level of hot extrasolar gas planets, the spectrum in the EUV range must be reconstructed. There are several approaches for this purpose of which three were compared in paper 2. The different approaches agree at best within a factor of 2.5 for inactive stars, but differ by up to a factor of 10 for active stars. Hence, we argue in paper 2 that the EUV irradiation level of extrasolar planets cannot be accurately determined at the moment. Note that this situation has been slightly improved, because one of the three approaches was recently revised leading to a better agreement for active stars (Chadney et al. 2015).

X-rays contribute to the high-energy irradiation level from active stars, furthermore, they provide the most direct method to reconstruct the stellar EUV emission (Sanz-Forcada et al. 2011; Chadney et al. 2015). In paper 2, we use X-ray observations with the Chandra and XMM-Newton X-ray observatories of seven exoplanetary systems with hot gas planets to determine the high-energy emission of the host stars and reconstruct the planetary irradiation level. Additionally, X-rays can be used to derive estimates of the Lyα emission of host stars (Linsky et al. 2013). The relation is used to predict the best targets for future Lyα transit spectroscopy including estimates of the interstellar

---

[4] In paper 2 we neglected smaller planets; the full list of systems is given in paper 3.

absorption in the line center. As a result, we confirm that the closest target, WASP-80, is likely also the best target to search for an expanded atmosphere in terms of the predicted measurable Lyα flux at Earth.

2.2.2 Lyα snapshots of close-by host stars

The first detection of an expanded atmosphere in the hot Jupiter HD 209458 b by Vidal-Madjar et al. (2003) required data from three individual transits over a total of 12 HST orbits. Most of the host stars that appear suited for Lyα transit spectroscopy likely have smaller line fluxes at Earth than HD 209458 (see paper 2 and paper 3). Furthermore, Table 4 in paper 2 reveals the uncertainty in the process of estimating the Lyα line fluxes of the host stars at Earth. Despite our careful target selection, a nondetection of individual targets is a relevant risk. This becomes evident in the nondetection of GJ 1214 in an HST Lyα snapshot observation (France et al. 2013). GJ 1214 is the third closest exoplanetary system with a transiting planet at the time of writing (exoplanets.org, Han et al. 2014), and according to our predictions the star should be similarly bright as HD 209458 in the Lyα line flux. Short snapshots are therefore valuable to determine the Lyα line flux of the host stars, which then allows a precise planning of a transit campaign.

We conducted an exploratory snapshot program of hot Jupiter hosts with HST/STIS, where planetary atmospheres are likely detectable through Lyα transit spectroscopy. The target list is identical with that of our X-ray observations (see paper 2). In the frame of the snapshot program[5] three targets were observed; a publication is in preparation. Two out of three targets were detected. The data were analyzed following the standard procedure. A crucial step in the analysis is the removal of geocoronal contamination. The exosphere of Earth consists mainly of hydrogen, which scatters solar Lyα emission and contaminates stellar Lyα signals observed with the STIS. The geocoronal contamination varies along the slit direction of the instrument and is time variable. We extracted 25 spectra above and below the spectral trace and subtracted the mean geocoronal spectrum from the target spectrum. The standard deviation of the 50 geocoronal spectra is added to the noise of the target spectrum.

Figure 2.1 shows the spectra of HAT-P-20, WASP-38, and WASP-80. HAT-P-20 is clearly detected and the flux in the blue line wing is comparable to that of HD 209458 ($F_{\mathrm{Ly}\alpha} = 8.6 \pm 0.2 \times 10^{-15}$ erg cm^{-2} s^{-1}). WASP-38 was not detected ($F_{\mathrm{Ly}\alpha} < 2 \times 10^{-15}$ erg cm^{-2} s^{-1}), which is consistent with the nondetection in our X-ray exposure (see paper 2). As the X-ray observations were unavailable at the time of the scheduling of the HST observations, we could not avoid the double nondetection. Emission of WASP-80 is detected in the red line wing in agreement with interstellar absorption in this direction (Redfield & Linsky 2008). The total line flux is $F_{\mathrm{Ly}\alpha} = 6.6 \pm 0.3 \times 10^{-15}$ erg cm^{-2} s^{-1}. The observation occurred partially during the transit of the hot Jupiter, thus, an absorption signal of the planet could be present in the data, but cannot be extracted without reference spectra.

The line flux of WASP-80 is sufficient to detect an expanded atmosphere. An invariable absorption signal of 10% would be detected (three-sigma) by adding five transit obser-

---

[5] Snapshot programs are used to optimize the HST observation scheduling. They do not yield guaranteed observations of individual targets.

vations. The system is highly suited for transit observations, because the simulation of WASP-80 b reveals a potentially larger absorption signal than that of GJ 436 b where 23% absorption was detected (Kulow et al. 2014). An absorption signal of this strength could be detected in a single transit observation.
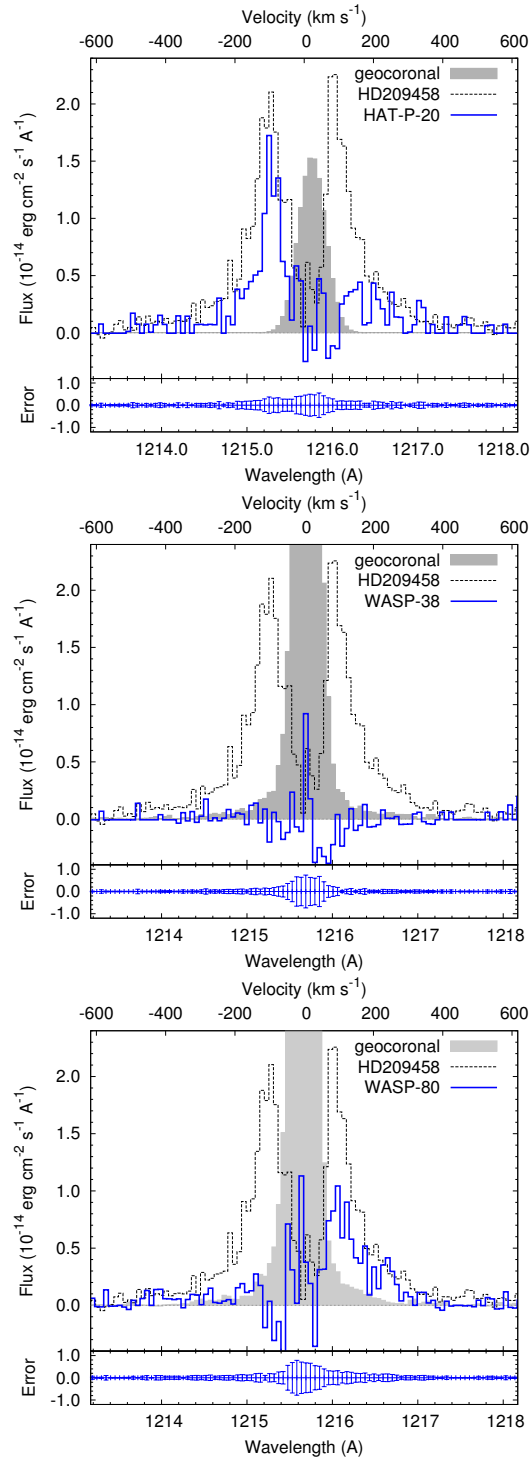
Fig. 2.1. Lyα spectra of HAT-P-20, WASP-38, and WASP-80. Geocoronal contamination is shown by gray histograms, a comparison spectrum of HD 209458 is given by the dashed line; the blue solid lines show the spectra of the targets. The lower panels depict the noise level (on a smaller scale).

3 Outlook

In the following, I outline future perspectives for the theoretical and observational approaches, which have arisen from my work.

3.1 Simulations

The problem of escaping atmospheres of hot gas planets comprises many unsolved issues that have to be studied in the future. In particular, TPCI can be used to study the effects of metals in an escaping atmosphere. The carbon, oxygen, silicon, and magnesium absorption signals prove that metals are present in the upper atmosphere. In general, metals act as strong cooling agents for example in H II regions (e.g., Osterbrock & Ferland 2006) and, hence, could reduce the mass-loss rates. However, metals strongly absorb X-rays (Morrison & McCammon 1983) and can also increase the mass-loss rates of hot gas planets in the vicinity of active host stars. Furthermore, the detected absorption signals of metals can be used to constrain our model atmosphere in addition to the Lyα signals. Koskinen et al. (2013b) performed such a study for HD 209458 b. The authors speculate that the weak absorption signals in the Na I lines (Charbonneau et al. 2002) are caused by ionization of sodium in the lower atmosphere, which disagrees with earlier assumptions that sodium precipitates in low lying clouds. This aspect can be studied with TPCI.

TPCI can further be used to simulate molecular outflows from moderately irradiated smaller planets. This extends Fig. 3 in paper 4 toward lower irradiation levels. Such a study of weakly irradiated planets could also include the exoplanet 55 Cnc b, where indications for a grazing transit of an expanded atmosphere exist (Ehrenreich et al. 2012). Finally, the suggested simulation regime extends toward the evaporation of the protoatmospheres of Earth, Venus, and Mars around a young and active Sun (see Sect. 1.2.1).

Besides the investigation of individual aspects, like the impact of metals or molecules in 1D simulations, TPCI can be used to simulate the 3D picture of an escaping atmosphere with some restrictions. Naturally, a multidimensional TPCI simulation requires a larger investment of computational effort. Thus, only the most interesting system can be chosen. At the moment this is GJ 436 with the possible detection of a cometary tail. The convergence of the 1D simulation in this system took 6 month on a single 3.1 GHz CPU. The atmosphere underwent a series of strong shock waves, which can be circumvented in a multidimensional simulation by initializing with the converged spherically symmetric atmosphere. However, flows into the shadow region will again cause shocks and possible inflow on the nightside. There is further potential for reducing the computation effort. For example, is suffices to set the boundary in the lower atmosphere at a density of 10^{13} cm^{-3} instead of the standard 10^{14} cm^{-3}, which has been used for the simulations in paper 3. This has proven to increase the simulation speed by as much as a factor of

10, because the lower atmosphere is the region with the highest resolution. Most importantly, in multidimensional simulations TPCI is capable of parallel simulations and can be run on clusters. If an individual CPU is available for every y/z-grid-point, the total computational time would be similar to a 1D simulation. Communication is not a major issue, because most of the computational time is spent in the microphysics solver, which requires no communication at all.

The proposed simulation would be the first simulation to comprise the formation of the planetary wind by photoevaporation in combination with the interaction with the stellar wind. There are a few restrictions of TPCI. Charge exchange with the stellar wind cannot be simulated self-consistently, but would have to be approximated in the post-processing stage. Advection of species is unavailable in multidimensional simulations within TPCI. This has a minor effect on the total mass-loss rate of the planet ($\sim 10\%$), but it certainly affects the resulting absorption signal, thus, we will also have to account for the advection of neutrals in the post-processing phase. While the proposed simulation is highly interesting, the feasibility regarding computation effort remains to be proven.

3.2 Observations

We will further aim at increasing the observational basis. Our X-ray observations presented in paper 2 were focused on large planets, which potentially produce strong absorption signals. However, the detection of a 23 % absorption signal by the hot Neptune GJ 436 b has proven that small planets can also produce large absorption signals (Kulow et al. 2014). The simulations presented in paper 3 support this conclusion: small and moderately irradiated planets produce the largest absorption signals. Therefore, we have successfully proposed to extend the X-ray observations to smaller planets. Observations of the brightest four hot Neptune hosts have been approved, and the targets will be observed during the upcoming cycle of XMM-Newton[1]. We will use these observations to determine the high-energy irradiation level for the hot Neptunes following the procedure of paper 2.

Further snapshots with HST/STIS of promising targets are needed to reveal, which host stars are bright enough for the detection of a planetary atmosphere. Our work has yielded a list of the most promising targets in terms of the estimated Lyα luminosity. Furthermore, only systems, in which the planet hosts a sufficiently expanded neutral atmosphere in our simulations, will be proposed. For example, the detection of the stable thermosphere of HAT-P-20 appears implausible with today's instrumentation according to our simulations.

Currently the best target for a Lyα transit campaign is WASP-80, which we will propose to observe with HST/STIS in the upcoming cycle. Further host stars, which reveal sufficient Lyα line flux in snapshot observations, can be proposed for Lyα transit spectroscopy campaigns in the future. Increasing the number of detected expanded planetary atmospheres is a long term plan. A broader observational basis in combination with improved models for the planetary thermospheres will lead to a more complete picture of the escaping atmospheres.

---

[1] Two targets will be observed for us, two for a different group.

Bibliography

Alibert, Y., Mordasini, C., & Benz, W. 2011, A&A, 526, A63

Alonso, R., Auvergne, M., Baglin, A., et al. 2008, A&A, 482, L21

Bakos, G. Á., Kovács, G., Torres, G., et al. 2007, ApJ, 670, 826

Ballester, G. E. & Ben-Jaffel, L. 2015, ArXiv e-prints [`arXiv:1503.01621`]

Ballester, G. E., Sing, D. K., & Herbert, F. 2007, Nature, 445, 511

Beatty, T. G. & Seager, S. 2010, ApJ, 712, 1433

Ben-Jaffel, L. 2007, ApJ, 671, L61

Ben-Jaffel, L. 2008, ApJ, 688, 1352

Ben-Jaffel, L. & Ballester, G. E. 2013, A&A, 553, A52

Bodenheimer, P., Hubickyj, O., & Lissauer, J. J. 2000, Icarus, 143, 2

Bouchy, F., Udry, S., Mayor, M., et al. 2005, A&A, 444, L15

Bourrier, V. & Lecavelier des Etangs, A. 2013, A&A, 557, A124

Bourrier, V., Lecavelier des Etangs, A., & Vidal-Madjar, A. 2015, A&A, 573, A11

Broeg, C., Fortier, A., Ehrenreich, D., et al. 2013, in European Physical Journal Web of
   Conferences, Vol. 47, European Physical Journal Web of Conferences, 3005

Burrows, A. S. 2014, Nature, 513, 345

Cameron, A. G. W. 1978, Moon and Planets, 18, 5

Cecchi-Pestellini, C., Ciaravella, A., & Micela, G. 2006, A&A, 458, L13

Chadney, J. M., Galand, M., Unruh, Y. C., Koskinen, T. T., & Sanz-Forcada, J. 2015,
   Icarus, 250, 357

Charbonneau, D., Brown, T. M., Latham, D. W., & Mayor, M. 2000, ApJ, 529, L45

Charbonneau, D., Brown, T. M., Noyes, R. W., & Gilliland, R. L. 2002, ApJ, 568, 377

Chassefière, E. 1996, J. Geophys. Res., 101, 26039

Christensen, U. R., Holzwarth, V., & Reiners, A. 2009, Nature, 457, 167

Close, L. 2010, Nature, 468, 1048

Craig, N., Abbott, M., Finley, D., et al. 1997, ApJS, 113, 131

Ehrenreich, D., Bourrier, V., Bonfils, X., et al. 2012, A&A, 547, A18

Ehrenreich, D. & Désert, J.-M. 2011, A&A, 529, A136+

Ehrenreich, D., Lecavelier des Etangs, A., Hébrard, G., et al. 2008, A&A, 483, 933

Ekenbäck, A., Holmström, M., Wurz, P., et al. 2010, ApJ, 709, 670

Erkaev, N. V., Kulikov, Y. N., Lammer, H., et al. 2007, A&A, 472, 329

Fossati, L., Bisikalo, D., Lammer, H., Shustov, B., & Sachkov, M. 2014, Ap&SS, 354, 9

Fossati, L., Bourrier, V., Ehrenreich, D., et al. 2015, ArXiv e-prints [`arXiv:1503.01278`]

Fossati, L., Haswell, C. A., Froning, C. S., et al. 2010, ApJ, 714, L222

France, K., Froning, C. S., Linsky, J. L., et al. 2013, ApJ, 763, 149

García Muñoz, A. 2007, Planet. Space Sci., 55, 1426

Goldreich, P. & Soter, S. 1966, Icarus, 5, 375

Goldreich, P. & Tremaine, S. 1980, ApJ, 241, 425

Han, E., Wang, S. X., Wright, J. T., et al. 2014, PASP, 126, 827

Haswell, C. A., Fossati, L., Ayres, T., et al. 2012, ApJ, 760, 79

Hebb, L., Collier-Cameron, A., Loeillet, B., et al. 2009, ApJ, 693, 1920

Henry, G. W., Marcy, G. W., Butler, R. P., & Vogt, S. S. 2000, ApJ, 529, L41

Holmström, M., Ekenbäck, A., Selsis, F., et al. 2008, Nature, 451, 970

Howard, A. W., Marcy, G. W., Bryson, S. T., et al. 2012, ApJS, 201, 15

Ida, S. & Lin, D. N. C. 2010, ApJ, 719, 810

Jensen, A. G., Redfield, S., Endl, M., et al. 2012, ApJ, 751, 86

Johnson, R. E., Combi, M. R., Fox, J. L., et al. 2008, Space Sci. Rev., 139, 355

Knutson, H. A., Charbonneau, D., Allen, L. E., et al. 2007, Nature, 447, 183

Koskinen, T. T., Harris, M. J., Yelle, R. V., & Lavvas, P. 2013a, Icarus, 226, 1678

Koskinen, T. T., Yelle, R. V., Harris, M. J., & Lavvas, P. 2013b, Icarus, 226, 1695

Kramida, A., Yu. Ralchenko, Reader, J., & and NIST ASD Team. 2014, NIST Atomic Spectra Database (ver. 5.2), [Online]. Available: `http://physics.nist.gov/asd` [2015, January 22]. National Institute of Standards and Technology, Gaithersburg, MD.

Kulow, J. R., France, K., Linsky, J., & Loyd, R. O. P. 2014, ApJ, 786, 132

Lammer, H., Chassefière, E., Karatekin, Ö., et al. 2013, Space Sci. Rev., 174, 113

Lammer, H., Kasting, J. F., Chassefière, E., et al. 2008, Space Sci. Rev., 139, 399

Lammer, H., Selsis, F., Ribas, I., et al. 2003, ApJ, 598, L121

Lecavelier des Etangs, A., Bourrier, V., Wheatley, P. J., et al. 2012, A&A, 543, L4

Lecavelier des Etangs, A., Ehrenreich, D., Vidal-Madjar, A., et al. 2010, A&A, 514, A72+

Lecavelier des Etangs, A., Sirothia, S. K., Gopal-Krishna, & Zarka, P. 2011, A&A, 533, A50

Lin, D. N. C., Bodenheimer, P., & Richardson, D. C. 1996, Nature, 380, 606

Linsky, J. L., Fontenla, J., & France, K. 2014, ApJ, 780, 61

Linsky, J. L., France, K., & Ayres, T. 2013, ApJ, 766, 69

Linsky, J. L., Yang, H., France, K., et al. 2010, ApJ, 717, 1291

Llama, J. & Shkolnik, E. L. 2015, ArXiv e-prints [`arXiv:1501.04963`]

Marcy, G., Butler, R. P., Fischer, D., et al. 2005, Progress of Theoretical Physics Supplement, 158, 24

Martín-Fleitas, J., Sahlmann, J., Mora, A., et al. 2014, in Society of Photo-Optical Instrumentation Engineers (SPIE) Conference Series, Vol. 9143, Society of Photo-Optical Instrumentation Engineers (SPIE) Conference Series, 0

Mayor, M. & Queloz, D. 1995, Nature, 378, 355

Meru, F. & Bate, M. R. 2012, MNRAS, 427, 2022

Mizuno, H. 1980, Progress of Theoretical Physics, 64, 544

Morrison, R. & McCammon, D. 1983, ApJ, 270, 119

Murray-Clay, R. A., Chiang, E. I., & Murray, N. 2009, ApJ, 693, 23

Nagasawa, M., Ida, S., & Bessho, T. 2008, ApJ, 678, 498

Nichols, J. D., Wynn, G. A., Goad, M., et al. 2015, ArXiv e-prints [`arXiv:1502.07489`]

Osterbrock, D. E. & Ferland, G. J. 2006, Astrophysics of gaseous nebulae and active galactic nuclei, ed. Osterbrock, D. E. & Ferland, G. J.

Parker, E. N. 1955, ApJ, 122, 293

Parker, E. N. 1958, ApJ, 128, 664

Penz, T., Erkaev, N. V., Kulikov, Y. N., et al. 2008, Planet. Space Sci., 56, 1260

Perryman, M. A. C., de Boer, K. S., Gilmore, G., et al. 2001, A&A, 369, 339

Pokhunkov, A. A., Rybin, V. V., & Tulinov, G. F. 2009, Cosmic Research, 47, 480

Pollacco, D. L., Skillen, I., Collier Cameron, A., et al. 2006, PASP, 118, 1407

Poppenhaeger, K., Schmitt, J. H. M. M., & Wolk, S. J. 2013, ApJ, 773, 62

Queloz, D., Anderson, D. R., Collier Cameron, A., et al. 2010, A&A, 517, L1

Rauer, H., Catala, C., Aerts, C., et al. 2014, Experimental Astronomy, 38, 249

Redfield, S., Endl, M., Cochran, W. D., & Koesterke, L. 2008, ApJ, 673, L87

Redfield, S. & Linsky, J. L. 2008, ApJ, 673, 283

Ribas, I., Guinan, E. F., Güdel, M., & Audard, M. 2005, ApJ, 622, 680

Ricker, G. R., Winn, J. N., Vanderspek, R., et al. 2014, in Society of Photo-Optical In-strumentation Engineers (SPIE) Conference Series, Vol. 9143, Society of Photo-Optical Instrumentation Engineers (SPIE) Conference Series, 20

Salz, M., Banerjee, R., Mignone, A., et al. 2015a, ArXiv e-prints [`arXiv:1502.06517`]

Salz, M., Schneider, P. C., Czesla, S., & Schmitt, J. H. M. M. 2015b, ArXiv e-prints [`arXiv:1502.00576`]

Sanz-Forcada, J., Micela, G., Ribas, I., et al. 2011, A&A, 532, A6+

Schneider, J., Rauer, H., Lasota, J. P., Bonazzola, S., & Chassefiere, E. 1998, in Astro-nomical Society of the Pacific Conference Series, Vol. 134, Brown Dwarfs and Extrasolar Planets, ed. R. Rebolo, E. L. Martin, & M. R. Zapatero Osorio, 241–+

Schröter, S., Czesla, S., Wolter, U., et al. 2011, A&A, 532, A3+

Shematovich, V. I., Ionov, D. E., & Lammer, H. 2014, A&A, 571, A94

Shustov, B., Sachkov, M., Gómez de Castro, A. I., et al. 2011, Ap&SS, 335, 273

Sirothia, S. K., Lecavelier des Etangs, A., Gopal-Krishna, Kantharia, N. G., & Ishwar-Chandra, C. H. 2014, A&A, 562, A108

Snellen, I. A. G., Albrecht, S., de Mooij, E. J. W., & Le Poole, R. S. 2008, A&A, 487, 357

Snellen, I. A. G., de Kok, R. J., de Mooij, E. J. W., & Albrecht, S. 2010, Nature, 465, 1049

Spitzer, L. 1978, Physical processes in the interstellar medium, ed. Spitzer, L.

Stone, J. M. & Proga, D. 2009, ApJ, 694, 205

Testa, P., De Pontieu, B., Allred, J., et al. 2014, Science, 346

Tian, F., Toon, O. B., Pavlov, A. A., & De Sterck, H. 2005, ApJ, 621, 1049

Trammell, G. B., Arras, P., & Li, Z.-Y. 2011, ApJ, 728, 152

Trammell, G. B., Li, Z.-Y., & Arras, P. 2014, ApJ, 788, 161

Tremblin, P. & Chiang, E. 2013, MNRAS, 428, 2565

Triaud, A. H. M. J., Collier Cameron, A., Queloz, D., et al. 2010, A&A, 524, A25

Vernazza, J. E., Avrett, E. H., & Loeser, R. 1981, ApJS, 45, 635

Vidal-Madjar, A., Désert, J.-M., Lecavelier des Etangs, A., et al. 2004, ApJ, 604, L69

Vidal-Madjar, A., Huitson, C. M., Bourrier, V., et al. 2013, A&A, 560, A54

Vidal-Madjar, A., Lecavelier des Etangs, A., Désert, J.-M., et al. 2003, Nature, 422, 143

Vidal-Madjar, A., Lecavelier des Etangs, A., Désert, J.-M., et al. 2008, ApJ, 676, L57

Vidotto, A. A., Jardine, M., & Helling, C. 2010, ApJ, 722, L168

Voss, H., Jordi, C., Fabricius, C., et al. 2013, in Highlights of Spanish Astrophysics VII, ed. J. C. Guirado, L. M. Lara, V. Quilis, & J. Gorgas, 738–743

Watson, A. J., Donahue, T. M., & Walker, J. C. G. 1981, Icarus, 48, 150

Winn, J. N., Matthews, J. M., Dawson, R. I., et al. 2011, ApJ, 737, L18

Yelle, R. V. 2004, Icarus, 170, 167

Zhang, T. L., Baumjohann, W., Delva, M., et al. 2006, Planet. Space Sci., 54, 1336

Zhang, T. L., Luhmann, J. G., & Russell, C. T. 1991, J. Geophys. Res., 96, 11145

Publications

Paper 1, 2, 3 & 4 are reproduced on the following pages. Here, I give an overview of my contributions. I am the leading author on all publications. While I produced the main text, I also benefited from significant input from all of my coauthors.

The idea of studying the atmospheres of hot gas planets traces back to my supervisor J. H. M. M. Schmitt. While I was familiar with the PLUTO code, P. H. Hauschildt introduced the idea of using the CLOUDY code for solving the photoionization. The development of TPCI evolved in collaboration with all authors of paper 1. However, I was responsible for the coding work, carrying out the simulations, and designing and evaluating the test problems.

The investigation of the high-energy irradiation of close-by hot Jupiters was a collective idea. I proposed the Chandra and XMM-Newton observations in cooperation with all authors and performed the main data analysis.

The numerical exploration of close-by exoplanetary systems in the third and fourth publication was my idea. I supervised the simulations over several month; the computational resources were supplied by the Hamburger Sternwarte. While I analyzed the simulations, many aspects were clarified in discussions with my coauthors.

Publication status

The first two papers are accepted for publication in Astronomy & Astrophysics (Salz et al. 2015a,b). The third publication has been submitted to Astronomy & Astrophysics. The fourth publication is in preparation and will be submitted to Astronomy & Astrophysics. The analysis and the interpretation are complete, however, to increase clarity, I have started the simulations of the atmosphere of WASP-10 b changing only the planetary mass (see Fig. 1 of the publication). These simulations are not fully converged and changes of the mass-loss rates and the atmospheric structure of up to $30\,\%$ are still possible. The simulations will converge within less than two month, at which point I will submit the publication.

TPCI: The PLUTO-CLOUDY Interface

A versatile coupled photoionization hydrodynamics code

M. Salz[1], R. Banerjee[1], A. Mignone[2], P. C. Schneider[1], S. Czesla[1], J. H. M. M. Schmitt[1]

[1] Hamburger Sternwarte, Universität Hamburg, Gojenbergsweg 112, 21029 Hamburg, Germany
e-mail: `msalz@hs.uni-hamburg.de`
[2] Dipartimento di Fisica Generale, Universitá di Torino, via Pietro Giuria 1, 10125 Torino, Italy

ABSTRACT

We present an interface between the (magneto-) hydrodynamics code PLUTO and the plasma simulation and spectral synthesis code CLOUDY. By combining these codes, we constructed a new photoionization hydrodynamics solver: The PLUTO-CLOUDY Interface (TPCI), which is well suited to simulate photoevaporative flows under strong irradiation. The code includes the electromagnetic spectrum from X-rays to the radio range and solves the photoionization and chemical network of the 30 lightest elements. TPCI follows an iterative numerical scheme: First, the equilibrium state of the medium is solved for a given radiation field by CLOUDY, resulting in a net radiative heating or cooling. In the second step, the latter influences the (magneto-) hydrodynamic evolution calculated by PLUTO. Here, we validated the one-dimensional version of the code on the basis of four test problems: Photoevaporation of a cool hydrogen cloud, cooling of coronal plasma, formation of a Strömgren sphere, and the evaporating atmosphere of a hot Jupiter. This combination of an equilibrium photoionization solver with a general MHD code provides an advanced simulation tool applicable to a variety of astrophysical problems.

Key words. Methods: numerical, Hydrodynamics, Radiation: dynamics, Planets and satellites: atmospheres

1. Introduction

Hydrodynamic flows powered by strong irradiation (photoevaporation) can be found throughout the Universe from the evaporation of cosmological minihaloes (Shapiro et al. 2004) and the formation and evolution of H ɪɪ regions (O'Dell 2001) to the evaporation of circumstellar disks (Owen et al. 2010). The discovery of expanding hot-Jupiter atmospheres (Vidal-Madjar et al. 2003) has added another environment possibly dominated by photoevaporative mass loss (Lammer et al. 2003). Although photoevaporative phenomena occur on widely different spacial scales, the essential physical processes are similar: the absorption of ionizing radiation causes an increase in temperature and pressure, which results in a hydrodynamic wind.

Coupled photoionization and hydrodynamic simulations are essential for the progress of research in these fields. We created a new interface between an extensive equilibrium solver for the state of a gas or plasma under strong irradiation (CLOUDY) and a 3D (magneto-) hydrodynamics simulation code (PLUTO), the PLUTO-CLOUDY Interface (TPCI). The codes and the interface are publicly available[1][2][3]. The interface can be used to study photoevaporative processes under a wide range of conditions. However, we designed the code to study the environment of hot-Jupiter atmospheres, and a short introduction provides an idea of our requirements for the new simulation tool.

The photoevaporation of hot-Jupiter atmospheres is the result of a complex interplay of various physical processes. The ab-

sorption of extreme ultraviolet radiation (EUV, $\lambda = 100 - 912$ Å) heats the upper atmosphere of planets and in extreme cases triggers expansion and evaporation (Watson et al. 1981). Our focus lies on active host stars such as Corot-2 (Schröter et al. 2011), where the effect of X-rays ($\lambda < 100$ Å) on the mass-loss rate cannot be neglected (Cecchi-Pestellini et al. 2006). With standard abundances, metals dominate the absorption of X-rays (Morrison & McCammon 1983) and are in many cases important for the cooling of gases that are devoid of molecules and dust (e.g., in H ɪɪ regions, see Osterbrock & Ferland 2006). Thermal conduction can be a major heat source if strong temperature gradients occur in the atmospheres (Watson et al. 1981). Furthermore, hot Jupiters are most likely tidally locked, and eventually multidimensional simulations are needed to solve the disparate flows from the day and night side of the planets. Finally, planetary magnetic fields (Trammell et al. 2011) or the interaction with the stellar wind (Tremblin & Chiang 2013) also affect the evaporation process.

In this paper, we describe and validate the one-dimensional version of our numerical scheme without focusing on a particular science application. We start by describing our new coupled photoionization hydrodynamics simulation scheme (Sect. 2.1) and comparing it to available numerical codes (Sect. 2.2). The theoretical background and additional aspects of the interface are explained in Sects. 2.3 to 2.8. To verify the results of the code and demonstrate the range of applications, four problems were drawn from different fields and were solved with TPCI (Sect. 3). Our last test case is a simplified simulation of the escaping atmosphere of the hot Jupiter HD 209458 b, which we compare to

---

[1] http://www.nublado.org/
[2] http://plutocode.ph.unito.it/
[3] http://www.hs.uni-hamburg.de/DE/Ins/Per/Salz/

previous studies of the same system (Sect. 3.4). In Sect. 4 we discuss the results and indicate future applications for TPCI.

2. The PLUTO-CLOUDY Interface – TPCI

2.1. Overview

We introduce an interface between two popular codes: the (magneto-) hydrodynamics code PLUTO (Mignone et al. 2012) and the photoionization simulation code CLOUDY (Ferland et al. 2013). The interface allows studying steady-state and slowly evolving photoevaporative flows, in which the medium is in ionization and chemical equilibrium at all times during the simulation.

The numerical scheme follows a clear division between the solution of the (magneto-) hydrodynamic equations in PLUTO and the solution of the ionization and chemical equilibrium in CLOUDY (see Fig. 1). Basically, the photoionization solver is called by the hydrodynamic code with the density and temperature distributions and solves the microphysical state of the gas under the given conditions and with the specified irradiation. It returns the radiative heating or cooling distribution, which then affects the hydrodynamic evolution. The two steps are alternated during the simulation.

PLUTO is a freely distributed modular code for solving HD/MHD equations (Mignone et al. 2007, 2012). It is a Godunov-type code that computes intercellular fluxes by solving the Riemann problem at cell interfaces. Parabolic terms in the differential equations such as viscosity or conductivity can be included by operator splitting, which is also the case for source terms such as optically thin cooling or gravity. For TPCI we used the static grid version of the code.

CLOUDY is a photoionization and microphysics equilibrium solver for static structures, irradiated by an arbitrary source (Ferland et al. 1998, 2013). It accounts for the electromagnetic spectrum from hard X-rays to the radio regime. The 30 lightest elements, from hydrogen to zinc, are included, and the solver balances radiative and collisional ionization and recombination, but also more complicated physical processes such as inner shell ionization or charge exchange[4]. In TPCI CLOUDY is called with a fixed temperature and density structure and solves the ionization and chemical equilibrium for the given conditions, which results in an imbalance of radiative heating and cooling. The program has been thoroughly tested to approach LTE at high densities and can be used within the temperature range from 3 K to 10^{10} K and for number densities of up to 10^{15} cm^{-3}. In cold regions CLOUDY approaches the fully molecular limit, including about 10^3 chemical reactions mostly from the UMIST database (Le Teuff et al. 2000). The ionization and chemical network is solved completely within CLOUDY, and only the mean molecular weight of the medium is passed to PLUTO. Since CLOUDY is a static equilibrium solver, advection of species is in general not included in TPCI. However, in 1D simulations with with a bulk flow antiparallel to the direction of irradiation, advective effects on the ionization equilibrium can be included via a CLOUDY internal iterative solver. Diffusion of elements is not included in this approach.

The coupled simulation codes use independent grid structures, and communication is achieved by linear interpolation on tabulated structures. TPCI is capable of performing true 3D

MHD simulations coupled to pseudo-3D photoionization simulations along 1D parallel slices through the computational domain. One-dimensional simulations with the interface are serial, while 2D or 3D simulations are parallelized through the message passing interface (MPI). Here, we restrict the verification to 1D problems without magnetic fields. However, multidimensional simulations are not treated differently in the interface.

In the design of the interface we followed the paradigm to apply only minimal changes to both programs so as not to interfere with the well-tested numerical schemes while exploiting most of the capabilities of both codes. To this end, CLOUDY was used as an external library for solving the equilibrium state of the gas. Several input and output extensions were necessary to enable the use of CLOUDY within TPCI: we adapted the code to accept tabulated density, temperature, and velocity structures, and the methods for retrieving the results from CLOUDY were expanded to include all necessary data in the communication with PLUTO.

The setup of TPCI follows the setup of the individual codes. While the usual input script for CLOUDY simulations is specified directly in the interface, the input files for the PLUTO code have not been changed. For the output of the hydrodynamic variables the standard PLUTO output options are available. Through the CLOUDY output much additional information is available, such as the number densities of all ions and molecules, the important radiative heating and cooling agents with contribution to the total heating or cooling rate, and the irradiating, transmitted, and reflected spectra. In general, anybody who is familiar with the two simulation programs individually will be able to use the interface with only little additional introduction.

### 2.2. Other photoionization hydrodynamics simulation codes

For reference, we provide a short overview of some available radiation hydrodynamics codes and compare individual aspects of the numerical schemes with our new interface.

For instance, Owen et al. (2010) coupled the 3D photoionization and radiative transfer code MOCASSIN (Ercolano et al. 2003) with the hydrodynamic code ZEUS-2D (Stone & Norman 1992). MOCASSIN and CLOUDY are similarly extensive equilibrium photoionization solvers, but the temperature parameterization used by Owen et al. is only valid for X-ray heating.

Another example for coupling a microphysical equilibrium solver to a hydrodynamic simulation is the ionization module for the FLASH code (Fryxell et al. 2000) presented by Rijkhorst et al. (2006) and further improved by Peters et al. (2010). The 3D radiative transfer method is highly efficient in simulations with adaptive mesh refinement on distributed systems, but is computationally more demanding than the pseudo-3D scheme used here. A similarly advanced parallel radiative transfer method was introduced by Wise & Abel (2011) into the ENZO code (Bryan & Norman 1997; O'Shea et al. 2004); it is called MORRAY. The non-equilibrium chemistry solver is restricted to hydrogen and helium, however (The Enzo Collaboration et al. 2013).

Shapiro et al. (2004) and predating publications have extended the hydrodynamics code CORAL (Raga et al. 1995) to include radiative transfer and non-equilibrium photoionization of hydrogen, helium, and metals. The scheme uses a similar pseudo-multidimensional radiative transfer method, but neglects X-rays, which is one of our main interests. X-rays are also mostly neglected in the numerical schemes, which have been specifically designed to simulate escaping hot-Jupiter atmospheres, and the authors focus exclusively on 1D simulations

---

[4] We sometimes us the generic term microphysics, meaning all processes that affect the equilibrium state in CLOUDY. For a full list we refer to the CLOUDY publications.
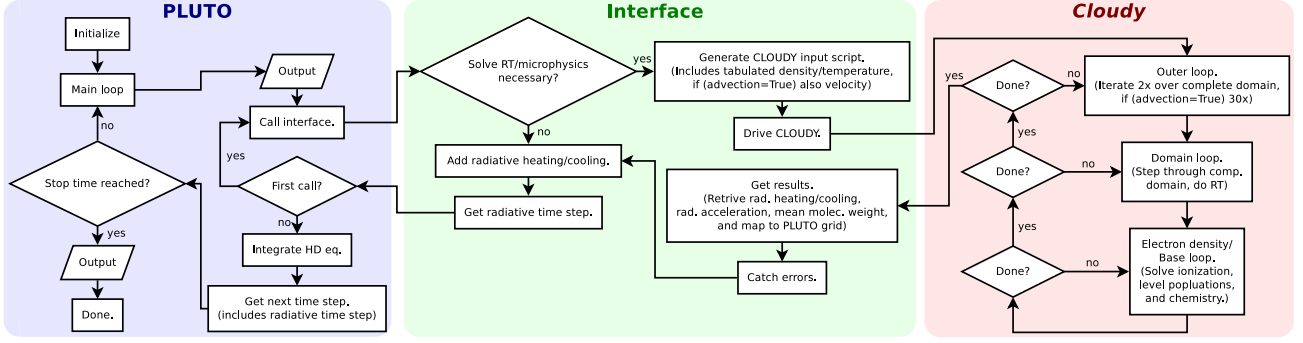
Fig. 1. Flowchart of the PLUTO-CLOUDY Interface. Affiliation of modules is indicated by colored boxes. PLUTO solves the hydrodynamic evolution and CLOUDY the ionization and chemical equilibrium state of the gas under strong irradiation. Communication is achieved through the interface, which also handles the interpolation between the two different grid structures.

(e.g., Yelle 2004; Tian et al. 2005; García Muñoz 2007; Penz et al. 2008; Murray-Clay et al. 2009; Koskinen et al. 2013).

In comparison, only TPCI solves our need for a photoionization hydrodynamics solver including hydrogen, helium, and metals as well as the absorption of EUV and X-ray emission.

2.3. Hydrodynamic simulation — PLUTO

In the following we present only the equations that are most relevant for the theoretical background of TPCI. The hydrodynamic simulation part is solved by the code PLUTO (Mignone et al. 2007, 2012). For a single fluid with mass density ρ, pressure p, and velocity $\mathbf{v}$, the hydrodynamic equations in the quasi-conservative form are given by

$$\frac{\partial \mathbf{U}}{\partial t} + \nabla \cdot \mathbf{F} = \nabla \cdot \Pi + \mathbf{S_p} . \tag{1}$$

Here $\mathbf{U} = (\rho, \rho \mathbf{v}, \mathcal{E})$ denotes the vector of conserved variables: mass, momentum, and total energy density, which is given by $\mathcal{E} = p/(\Gamma - 1) + 1/2 \rho v^2$, where Γ $(= 5/3)$ is the specific heat ratio of a monatomic gas. $\mathbf{F} = (\rho \mathbf{v}, \rho \mathbf{vv} + p, (\mathcal{E} + p)\mathbf{v})$ is the hyperbolic flux tensor, and Π is the parabolic flux tensor, which in our case only contains the conductive energy flux $\mathbf{F_c}$. $\mathbf{S_p}$ represents source terms such as gravity $\mathbf{S_G} = (0, \rho \mathbf{a_G}, \rho \mathbf{v} \cdot \mathbf{a_G})$ with the gravitational acceleration $\mathbf{a_G}$, and the radiative source term $\mathbf{S_R} = (0, 0, (G_R - L_R))$, where G_R and L_R are the radiative heating and cooling rates.

We follow a standard operator split scheme and include the radiative heating or cooling rate between the hydrodynamic integration steps. First, the homogeneous left-hand side of Eq. 1, namely the Euler equations, are solved. Second, PLUTO computes the included parabolic and source terms. Third, CLOUDY is called to compute the radiative source term (see Sect. 2.4), which subsequently affects the internal energy through the thermal pressure:

$$p^{n+1} = p^n + \Delta t^n (\Gamma - 1) S_R^n , \tag{2}$$

where Δt^n denotes the explicit time step at integration step n.

To minimize the computational effort, the radiative source term is not updated at every time step, but only if a change in either pressure or density by more than a user defined `change factor` triggers a call to the photoionization solver. A value of 1% for the `change factor` is a good compromise between accuracy and convergence speed for an initial settling phase of steady-state solutions. The accuracy can be increased by restarting the code with a smaller `change factor`.

2.4. Photoionization solver — CLOUDY

TPCI uses CLOUDY to solve the photoionization and the equilibrium state of the medium. We provide a compact overview of the most important processes for our applications in CLOUDY; for a more general introduction see Ferland et al. (1998, 2013). The code steps through a one-dimensional slice of the computational domain with an adaptive step width using linear interpolation on the tabulated density and temperature structures passed by PLUTO. In each cell it solves the local equilibrium state by taking into account ionization and recombination processes, chemical reactions, and atomic level transitions of all included elements.

CLOUDY separates the radiative transfer of continuum and line radiation. The continuum is diminished by absorption,

$$I = I_0 \exp\left(-d\tau_{\text{abs}}\right), \tag{3}$$

where I is the intensity after the initial intensity I_0 passes a slab of gas with the total optical depth $d\tau_{\text{abs}}$. The total optical depth contains all continuous opacity sources included in CLOUDY, but in the EUV range it is dominated by ionization processes of neutral hydrogen. The continuum is furthermore diminished by scattering (Lightman & White 1988):

$$I = I_0 \left(1 + \frac{1}{2} d\tau_{\text{scat}}\right)^{-1} . \tag{4}$$

The total scattering optical depth τ_{scat} also contains the opacities of several processes, of which Rayleigh scattering in the Lyman line wings dominates in the UV range.

The escape probability mechanism (Castor 1970; Elitzur 1982) is used to approximate radiative transfer effects. The local mean intensity J, needed to solve the rate equations, is then given by

$$J = S (1 - P_{\text{esc}}) . \tag{5}$$

Here S is the source function and P_{esc} the escape probability, which only depends on the optical depth. Solving the local equilibrium state is thereby decoupled from the radiative transfer equation. This approximation is exact in a single cell, where the source function is constant (Elitzur 1992). CLOUDY ensures this by choosing the adaptive grid resolution so that neither density, temperature, heating, or other properties change strongly within one cell. However, it is necessary to step through the computational domain at least twice to obtain a reasonable estimate

for the optical depth in the computation of the escape probability. This iteration is needed because radiation can escape in both directions, that is, away and toward the source.

CLOUDY can include the 30 lightest elements with any abundances. These species are only present in the photoionization solver, only the mean molecular weight is passed to the hydrodynamic single fluid simulation. The ionization ladder of every element is computed by balancing the rate equations

$$\frac{\partial n(X^i)}{\partial t} = n_e n(X^{i+1}) \alpha(X^i, T) - n(X^i)\left(\Gamma(X^i) + n_e \alpha(X^{i-1}, T)\right) = 0 \tag{6}$$

for each ionization stage. Here $n(X^i)$ is the number density of the element X in the ionization stage i, n_e is the electron number density, $\alpha(X^i, T)$ is the temperature-dependent recombination rate from X^{i+1} to X^i summed over all levels, and $\Gamma(X^i)$ is the photoionization rate given by

$$\Gamma(X^i) = \int_{\nu_{0,i}}^{\infty} \frac{4\pi J_\nu}{h\nu} a_\nu(X^i)\, d\nu. \tag{7}$$

Here J_ν is the mean intensity at frequency ν, $a_\nu(X^i)$ is the photoionization cross-section, and $\nu_{0,i}$ is the threshold frequency above which photoionization is possible. For simplicity we do not show more complex physical processes such as secondary ionizations or charge exchange in Eq. 6, which are also solved by CLOUDY, however.

For the hydrodynamic part of the simulation we need the radiative heating or cooling rates. While the heating rate G_R is a sum of many processes, the main heat source is usually given by photoionization:

$$G_\Gamma = \sum_{X^i} n(X^i) \int_{\nu_{0,i}}^{\infty} \frac{4\pi J_\nu}{h\nu} h\left(\nu - \nu_{0,i}\right) a_\nu(X^i)\, d\nu; \tag{8}$$

the sum includes all species. Locally other heat sources such as line absorption, charge exchange, and chemical reactions can dominate the heating rate.

Many processes contribute to the cooling rate L_R of a gas: recombination processes, free-free emission of electrons in the field of ions, line radiation, free-bound transition of H^-, and chemical reactions, to name a few. Cooling due to recombinations is given by

$$L_L = n_e n(X^{i+1}) kT \beta(X^i, T) P_{esc}, \tag{9}$$

where $\beta(X^i, T)$ stands for the effective recombination coefficient, averaged over the kinetic energy of the electron gas. The escape probability P_{esc} ensures that recombinations only contribute to the cooling rate if the emitted photon escapes the medium. Another main cooling agent is line radiation of collisionaly excited elements:

$$L_L = n_e \left(n_l c_{lu} - n_u c_{ul}\right) h\nu_{lu}. \tag{10}$$

Here c_{lu} denotes the collision rate between the lower and upper levels of the atom. The difference of collisional excitation and de-excitation is emitted radiatively and leads to cooling. The level populations of each ionization stage of every element are solved by balancing the equilibrium radiative and collisional transition rates in model atoms of differing complexity. Thus, CLOUDY includes a large number of lines ($10^5 - 10^6$, Ferland et al. 2013).

2.5. Time step control and relevant timescales

In TPCI simulations, restrictions due to hydrodynamic and microphysical timescales must be observed. PLUTO chooses the next hydrodynamic time step based on the Courant-Friedrichs-Levy (CFL) condition (Courant et al. 1928), which basically restricts disturbances in the medium to propagate by less than one cell width per time step. Radiative heating and cooling additionally limits the hydrodynamic time step in TPCI, meaning that the energy loss due to radiative cooling cannot exceed the internal energy. It is efficient to limit the next time step depending on the fraction of the energy content and the radiative source term (Frank & Mellema 1994):

$$\Delta t_{TPCI}^{n+1} = \epsilon_R \frac{p^n}{(\Gamma - 1) S_R^n}, \tag{11}$$

and the next hydrodynamic time step is then given by

$$\Delta t^{n+1} = \min\left[\Delta t_{PLUTO}^{n+1}, \Delta t_{TPCI}^{n+1}\right]. \tag{12}$$

Here ϵ_R is the user-defined maximum fractional variation parameter. The default value is $\epsilon_R = 0.1$, which restricts the change in internal energy due to radiative heating or cooling to be lower than 10% in every time step.

CLOUDY solves the equilibrium state of the medium based on a diversity of processes, each with a characteristic timescale, and the use of TPCI implies that the microphysical timescales are shorter than the hydrodynamic timescale. In gases with a temperature of about 10 000 K, hydrogen recombination usually is the microphysical process with the longest timescale (Ferland 1979):

$$T_{rec} = \frac{1}{\alpha_A(T_e) n_e} \approx 1.5 \times 10^9\, T_e^{0.8} n_e^{-1}. \tag{13}$$

TPCI locally checks whether recombination is slower than advection and issues a warning. Equation 13 holds only for ionized regions; especially molecular reactions occur on longer timescales. The CLOUDY output provides a manual method to control the longest timescales and, thus, check the validity of the approach.

In 1D simulations, the advection of species can be included through a steady-state solver in CLOUDY (see Sect. 2.6). With this scheme, steady flows can be simulated in which the advective timescales are shorter than microphysical timescales. Nevertheless, the assumption of photoionization and chemical equilibrium is a strong simplification, and the validity must be considered for every application.

2.6. Advection of species

The impact of advection due to a bulk flow of the medium can be included in the simulation by using an iterative steady state solver included in CLOUDY (Henney et al. 2005). The solver is available for simulations in which the medium flows toward the source of ionizing radiation. The solution of the equilibrium state then includes source and sink terms of all species, induced by material flows:

$$\nabla \cdot \left(n(X^i)\mathbf{v}\right) = n\mathbf{v} \cdot \nabla \left(n(X^i)/n\right). \tag{14}$$

In this case, PLUTO passes the velocity in addition to the density and temperature to the photoionization solver. CLOUDY computes the advective source terms using the relative density (Henney et al. 2005), which is an advective scalar.

The steady-state solver in CLOUDY includes advection in an iterative manner, and the user must control the convergence of the solution. The module defines the advection length Δz, a measure for the resolution of advection processes. It is refined if the advective solution has converged for the current advection length. The progress is controlled by following the discretization error and the convergence error (see Henney et al. 2005, for a detailed description). The convergence error is given by

$$\epsilon_1^2 = \sum_{X^i,j} \left(\frac{n_j^m(X^i) - n_j^{m-1}(X^i)}{\Delta z/v} \right)^2 , \qquad (15)$$

where m is the iteration number and j is the zone number; the sum extends over all elements and ionization stages as well as over all zones. The error approaches zero as the changes in number densities of consecutive iterations decreases. The discretization error is defined as

$$\epsilon_2^2 = \sum_{X^i,j} \left(\frac{n_j^m(X^i) - n_{(j-\Delta z)}^{m-1}(X^i)}{\Delta z/v} - \frac{n_j^m(X^i) - n_{(j-0.5\Delta z)}^{m-1}(X^i)}{\Delta z/2v} \right)^2 . \quad (16)$$

$(j - \Delta z)$ is a symbolic index referencing the density of the species at the distance of the advection length. The error describes the differences of the local, advective source or sink terms to the value if the advection length is refined by a factor of two. The sum again runs over all species and zones.

The discretization error depends on the resolution in the photoionization solver. This resolution can be up to ten times higher than in the hydrodynamic part of the simulation. For TPCI it is more important to check the advection length than the actual value of the discretization error. The advection length is refined if $\epsilon_1^2 < 0.1\epsilon_2^2$. It should generally be decreased to the hydrodynamic grid spacing, so that advective effects have the same accuracy as the rest of the simulation.

The described procedure does not follow our split scheme to solve hydrodynamic effects exclusively in PLUTO. However, at the moment we cannot solve the advection of species in PLUTO. It is possible to include advective scalars for the relative density of all species in PLUTO, but then CLOUDY would have to be called with the densities of all 30 elements and ionization stages, which is not implemented. The steady-state solver in CLOUDY is computationally demanding. One advection solution may need up to 100 iterations to converge because advective effects must be swept through the computational domain (Henney et al. 2005). Thus, including advection slows simulations down, and when searching for advective steady-state solutions, it is advisable to use the non-advective code for an initial settling of the hydrodynamic structure and then restart the simulation including advection to let the structure evolve to the final steady state. This procedure has been followed in the two test problems, which include advection of species (see Sects. 3.1 and 3.4).

2.7. Radiative acceleration

In addition to affecting the temperature of the gas, the absorption of radiation also exerts a pressure on the medium. CLOUDY records the radiative pressure produced by the absorption of radiation from the central source. The local radiative acceleration can be directly accessed after a CLOUDY call. This acceleration is handled like any external force by the PLUTO code (see Eq. 1).

2.8. Pseudo-multidimensional simulations

Although here we focus on 1D simulations, TPCI can be used in two or three dimensions on a Cartesian grid with irradiation along the x-axis. The radiative solution is then simply split into parallel 1D simulations, which is called a pseudo-3D radiative transfer. There is no true 3D radiative transfer in CLOUDY, but the coupling of 3D radiative transfer to hydrodynamics simulations is in many cases still computationally prohibitive today (e.g., Owen et al. 2010). In problems with a strong directionality in the radiative field, the pseudo-3D approximation is valid, unless there are shadow-casting objects (Morisset et al. 2005). However, in the case of strong shadows, the induced error can also be neglected if the energy transfer into the shadow region is hydrodynamically dominated.

The 1D version of the interface is a serial code because CLOUDY requires the complete density structure to solve the plane-parallel radiative transfer through the computational domain. PLUTO is, however, capable of 3D parallel computations, which is also enabled in TPCI by not decomposing the domain along the x-axis. Each thread then deals with the full 1D structure along the x-axis for a given number of y/z-grid-points. After the complete domain has been processed, the hydrodynamic evolution continues until the next call to CLOUDY is necessary. For this approach the computational domain should be decomposed so that the available processors have the same number of y/z-points to minimize idle times.

This pseudo-3D scheme provides a convenient possibility to allow parallel simulations with low complexity. In the best case, a multidimensional simulation will have a similar execution time as a 1D simulation if every y/z-grid-point uses an individual processor. The communication overhead is small, since the main computational load usually comes from the independent CLOUDY calls.

3. Verification

In the following we present TPCI simulations of four test problems. The first two simulations verify the implementation of our numerical scheme, each with a different focus. The third test problem is included to clarify the limits of validity of TPCI. The fourth test case is a simplified simulation of a hot-Jupiter atmosphere, which already demonstrates the capabilities of TPCI in this field. The setup of each simulation is given in Table 1.

3.1. Weak D-type ionization front

For the initial verification, we investigated the effects of steady-state flows in 1D simulations of ionization fronts. Such flows appear when molecular clouds are evaporated by the ionizing emission of newly formed stellar clusters. The gas is heated through ionization processes, and the cloud slowly evaporates. If the evaporation proceeds as a subsonic wind from a dense region, it is called a weak D-type ionization front, in contrast to strong ionization fronts, which involve transonic flows. (For rarefied R-type ionization fronts see Sect. 3.3.)

The results from our TPCI simulation are compared with an independent CLOUDY simulation, using the included steady-state solver, which was specifically designed to solve these photoevaporative flows (see Henney et al. (2005))[5]. This is a powerful test for TPCI because both simulations rely on the same

---

[5] The CLOUDY internal, iterative, steady-state hydrodynamics solver is restricted to specific flows and geometries. TPCI is more versatile and solves the dynamic evolution of the studied flows.

Table 1. Simulations for the verification of TPCI

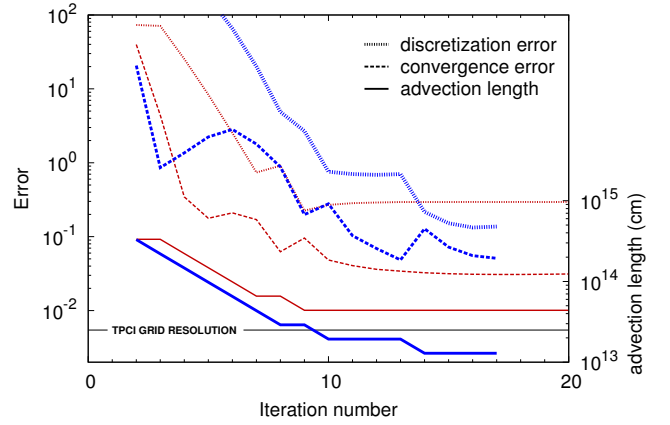| Name	Numerical setup (time stepping, interpolation, Riemann solver)	BC left $\rho\,v\,p$	right $\rho\,v\,p$	Grid geometry	grid points	Irradiation SED shape	ioniz. radiation field ($\lambda < 912$ Å)
D-front	RK3, WENO3, hllc +advection	f f o	o f o	Cartesian	200 uni.	50 000 K BB	$\Phi_H = 10^{11}$ cm^{-2} s^{-1}
c-shock	RK3, LINEAR, two_shock	o o o	o o o	Cartesian	400 uni.	—	—
R-front	RK3, LINEAR, hllc	o o o	o o o	Cartesian	400 uni.	50 000 K BB	$Q_H = 10^{49}$ s^{-1}
hJupiter	RK3, WENO3, hllc +gravity, +thermal cond. +advection	f o f	o o o	Spherical	240 stretch.	solar min.	$4\pi J = 1315$ erg cm^{-2} s^{-1}

Notes. Abbreviations: (BC) boundary condition, (f) fixed boundary condition, (o) outflow boundary condition, (SED) spectral energy distribution, (uni.) uniform grid spacing, (stretch.) stretched grid spacing, (BB) blackbody spectrum, (solar min.) solar minimum spectrum (Woods & Rottman 2002), $\Phi_H = Q_H/4\pi r_0^2$, $Q_H = \int_{\nu_0}^{\infty} L_\nu/h\nu\,d\nu$, $4\pi J = \int_{\nu_0}^{\infty} 4\pi J_\nu\,d\nu$, (RK3) third-order Runge-Kutta scheme (Gottlieb & Shu 1996), (WENO3) weighted essentially non-oscillatory finite difference scheme (Jiang & Shu 1996), (hllc) Harten, Lax and van Leer approximate Riemann solver with contact discontinuity (Toro et al. 1994), (two_shock) nonlinear Riemann solver based on the two-shock approximation (Colella & Woodward 1984; Fryxell et al. 2000).
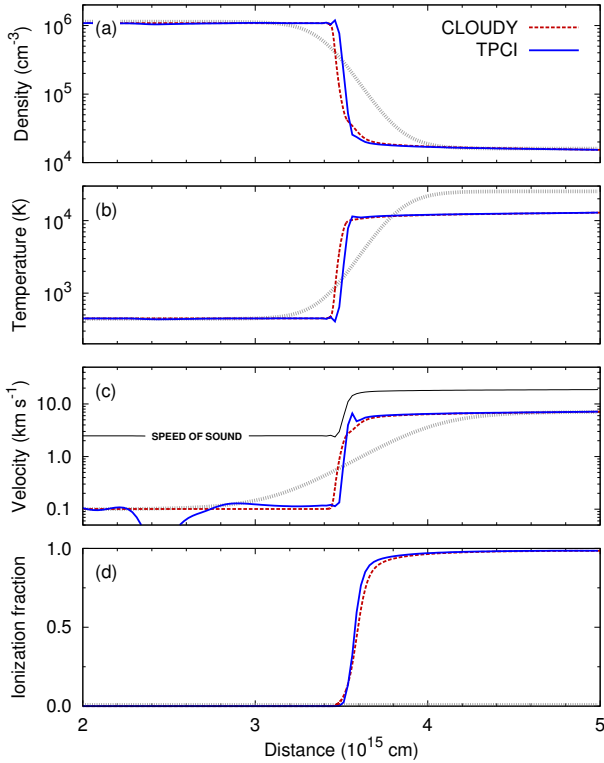
Fig. 2. Pure hydrogen weak D-type ionization front. Density (a), temperature (b), velocity (c), and degree of ionization (d) are depicted. A CLOUDY simulation (red dashed lines) is compared with a TPCI simulation (blue solid lines). Initial conditions are given by the gray dotted lines. In panel (c) the speed of sound is shown by the black solid line. The TPCI simulation agrees well with the independent CLOUDY simulation. Small oscillations in the high-density region that can be seen in panel (c) do not affect the solution significantly.


Fig. 3. Convergence of the models of the weak D-type ionization front. The CLOUDY simulation is shown by red, thin lines, the advective TPCI simulation by thick, blue lines. The discretization error (dotted), the convergence error (dashed), and the advection length (solid) are plotted against the iteration number of the steady-state solver in CLOUDY. The grid resolution of the TPCI simulation is indicated by the thin, black line. In both simulations the advection length is reduced to within a factor of 2 of the grid resolution in the hydrodynamic simulation part.

photoionization solver, thus, any differences in the results can only be caused by the interaction of the hydrodynamics and the photoionization solver through the interface.

Figure 2 shows the simulation of a weak D-type ionization front in a pure hydrogen gas in the rest frame of the front to-gether with the initial conditions. Cold, neutral gas (400 K) with a density of 10^6 cm^{-3} is irradiated from the right-hand side by a hot O-star with a 50 000 K blackbody spectrum. The gas shows a steady-state flow toward the source of ionizing radiation. The evaporation process is subsonic, starting with 0.1 km s^{-1} and reaching 7.1 km s^{-1} behind the ionization front. The temperature increases to 12 000 K and the density drops to 2×10^4 cm^{-3}.

We used TPCI without the advection of species for the initial settling of the simulation and subsequently restarted the simulation including the advection as described in Sect. 2.6. The settling phase of the dynamical simulation took 3×10^4 a, after which oscillations of the ionization front were reduced to about 1% of the depth of the ionized region. These oscillations in the denser gas are caused by the reflection of waves at the left-hand boundary and at the ionization front. The depth of the ionized region in the steady-state CLOUDY simulation agrees with the *dynamic* TPCI simulation within the errors produced by the re-
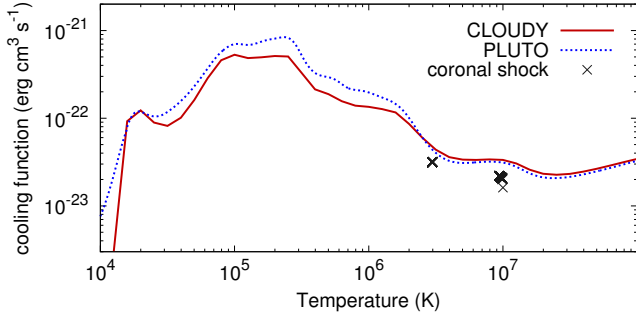
Fig. 4. Optically thin cooling function of PLUTO (blue, dotted) and CLOUDY (red, solid). The crosses depict the actual cooling in the coronal shock simulation with TPCI. These are a factor of 1.5 lower because the simulation shows significant optical-depth effects.

maining oscillations (see Fig. 2 (d)). The width of the ionization front is reduced by 25% in the dynamic simulation, which does not affect the overall structure, however.

The convergence of the steady-state solver in the advective TPCI and the CLOUDY simulations is shown in Fig. 3. The advection length has been iteratively refined whenever the solution converged for the current length (see Sect. 2.6). Every refinement temporarily increases the convergence error, which is then reduced over the following iterations until further refinement. The final discretization error is on the order of 10%, computed on the fine grid of the photoionization solver. This is sufficient because the advection length is similar to the coarser resolution of the hydrodynamical simulation part. Higher refinement is impossible because in this case the steady-state solver does not proceed beyond this level (see Sect. 4 for a discussion of this problem).

The comparison of the two simulations demonstrates that the interface works correctly and is capable of simulating photoevaporative flows. While the independent CLOUDY simulation with the internal steady-state solver produces smoother profiles, TPCI allows studying the dynamical evolution of the phenomenon.

3.2. Coronal flare - chromospheric evaporation wave

TPCI can also make use of CLOUDY to compute the cooling of collisional plasmas instead of strongly irradiated plasmas. This provides the possibility of testing the interface in the optically thin limit, where radiative losses only depend on the electron number density n_e and the cooling function Λ_R (e.g., Sutherland & Dopita 1993):

$$L_R = n_e^2 \Lambda_R(T, A). \tag{17}$$

The cooling function depends on temperature T and metal abundance A. A radiative transfer solver is not necessary for the simulation as long as the optical depth is negligible. Cooling in this regime is dominated by emission from ionized metals, in which case CLOUDY mostly uses transitions from the CHIANTI database (Dere et al. 1997; Landi et al. 2012). The resulting cooling function with solar abundances in CLOUDY is similar to standard optically thin cooling functions; see Fig. 4 for a comparison with the tabulated cooling function that is included in the PLUTO code.

We can thus compare a TPCI simulation with the radiative transfer and microphysics solver with a PLUTO simulation using the included cooling function. In contrast to the ionization front
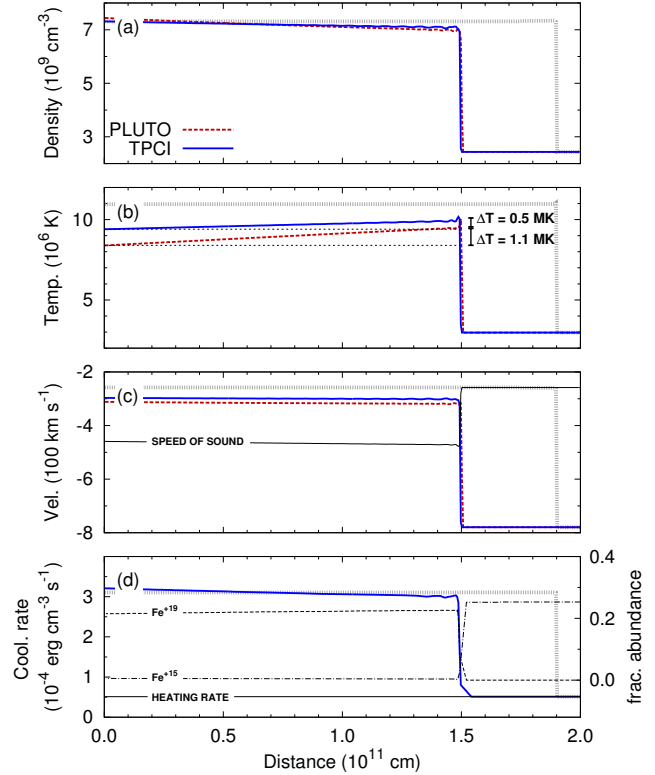
Fig. 5. Hydrodynamic evaporation wave in a flaring coronal loop. The red dashed lines show a simulation with PLUTO assuming optically thin cooling. The blue lines depict the results of TPCI, and the initial conditions are given by the gray dotted lines. The density is shown in panel (a), the temperature in (b), the velocity in (c), and the cooling of TPCI is plotted in panel (d) together with the constant heating rate. Panel (d) shows the fractional abundance of the two iron ions with the strongest individual contribution to the total cooling rate. In panel (b) the temperature decrement in the after-shock evolution is indicated. The sound speed is shown by the solid black line in panel (c). Both simulations show the same behavior, except that in the PLUTO simulation the cooling rate is twice as strong as in the TPCI simulation, which is due to optical-depth effects and small differences of the electron density.

simulation in the previous section, we now used the same hydrodynamics solver (i.e., PLUTO), but different solvers for the radiative cooling. Differences in the results of the test simulations can only result from the implementation of the radiative cooling from CLOUDY in PLUTO. In this simulation we included all 30 elements available in CLOUDY, which additionally tests the implementation of metals in the inteface.

We used a setup that was adapted to a strong chromospheric evaporation wave in a 1D magnetically confined coronal loop. Such evaporation fronts appear when a magnetic reconnection event releases a large amount of energy in the solar atmosphere, which leads to a solar flare (e.g., Reale & Orlando 2008). Evaporation of chromospheric plasma into the corona causes a wave that propagates at speeds of ~ 400 km s^{-1} through a coronal loop, increasing the density by up to one order of magnitude. Since optically thin cooling depends on the density squared, the cooling rate is increased and, in the long term, the evaporated plasma cools down and falls back onto the chromosphere. The magnetic loop structure usually survives the flare event.

For the simulation we went into the quasi-rest frame of the propagating evaporation wave (see Fig. 5 for the initial condi-

tions). The wave front is stable at the start of the simulation, but the strength of the wave weakens as a result of cooling. This reduces the propagation speed so that during the simulation the wave front starts trailing toward the left-hand boundary. This proceeds faster in the PLUTO simulation because of the stronger cooling rate. Therefore, we do not compare contemporaneous states in both simulations but states with the same displacement from the initial shock position. There is no irradiation in this simulation.

In the test, coronal material flows in from the right-hand side of the domain with a temperature of 3×10^6 K, a hydrogen number density of 2.4×10^9 cm^{-3}, and a velocity of -780 km s^{-1}. The plasma is compressed to a density of 7.1×10^9 cm^{-3} with a temperature of 10^7 K and a velocity of -300 km s^{-1}. The domain length was chosen deliberately longer than a typical magnetic loop to emphasize the cooling of the dense gas behind the shock.

To stabilize a coronal loop model, a constant mechanical coronal heating rate has to be applied (Rosner et al. 1978). This heating of unspecified source balances radiative and conductive losses throughout the loop. We applied a heating rate of $5.1/9.8 \times 10^{-5}$ erg cm^{-3} s^{-1} in the TPCI/PLUTO simulations, which exactly equals the cooling rates in the pre-shock region (see Fig. 5 (d)). Advection of species can affect the ionization stage of metals behind the shock, which in turn has a weak influence (factor < 1.5) on the value of the cooling function. The increased density affects the cooling rate with a factor of $\sim 3^2$, however, which is why we neglected advection of species in this simulation.

Both simulations show the same behavior (see Fig. 5). The plasma is heated in the wave front and slowly cools down in the post-shock region. The cooling efficiency is a factor of two higher in the PLUTO simulation than with TPCI. This has two reasons: first, the actual cooling rate in the TPCI simulation is lower by a factor of 1.5 than in the optically thin case because CLOUDY includes optical-depth effects along the coronal loop (see Fig. 4). For example, one of the strongest emission lines of the hot plasma is a Fe xx line at 12.9 Å, which has an optical depth of 3.9 and does not escape freely. Fe^{+19} and Fe^{+18} are the most abundant iron ions in the hot gas, while Fe^{+16} and Fe^{+15} dominate in the cooler gas. Second, the PLUTO simulation computes the electron density on a simple "hydrogen-only" approximation, which in this case overestimates the electron density by a factor of 1.2. Both factors combined result in the total difference of the cooling rates ($1.2^2 \times 1.5 = 2.2$).

A comparison of the two simulations shows that TPCI can also be used for collisional plasmas, especially if optical-depth effects are relevant. One drawback is the increase in computational effort by a factor of 10^5 compared to the much simpler, optically thin PLUTO simulation. The strong increase in computational effort results from solving the equilibrium state including all metals (see Sect.4). For future applications the gain in accuracy by using the radiative transfer and microphysics solver must be weighed against the increased computational effort.

3.3. Formation of a Strömgren sphere

In a third setup, we used the interface to follow the heating of cool interstellar hydrogen gas after the ignition of a strong central source. This test problem demonstrates the limits of TPCI that are due to the underlying assumption of ionization and chemical equilibrium. The sudden impact of ionizing photons after ignition of the source heats the surrounding gas, and a supersonic ionization front develops (R-type). The propagation of
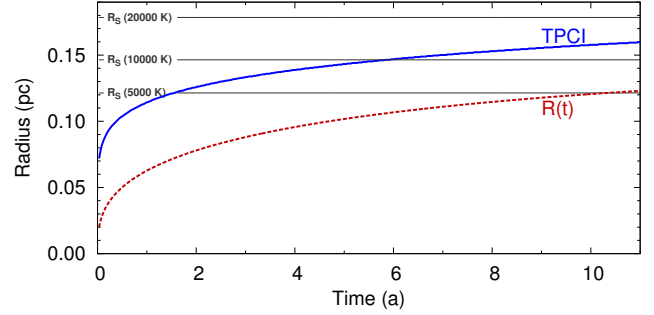
Fig. 6. Expansion of an R-type ionization front. The TPCI simulation (blue solid) is compared with the theoretical evolution of Eq. 19. Three Strömgren radii for different temperatures are indicated by labeled thin black lines. The expansion of the ionized region proceeds faster in the TPCI simulation because the equilibrium solutions of the photoionization solver at each integration step are not restricted by the time since ignition of the central source.

the ionization front is only restricted by the rate of new ionizing photons emitted by the central source. The rapid expansion comes to a rest after recombinations in the ionized sphere balance the production rate of ionizing photons; the resulting sphere is called a Strömgren sphere, and the radius is given by (e.g., Osterbrock & Ferland 2006):

$$R_S = \left(\frac{3Q_H}{4\pi n_0^2 \alpha_B} \right)^{1/3} . \tag{18}$$

Here, $Q_H = \int_{\nu_0}^{\infty} L_\nu / h\nu \, d\nu$ is the number of ionizing photons emitted by the central source per second, and L_ν is the stellar luminosity per unit frequency interval. n_0 is the initial density and $\alpha_B = 2.59 \times 10^{-13}$ cm^{3}s^{-1} is the hydrogen B recombination rate for a 10 000 K plasma. This rate includes recombination to all levels but the ground state because recombination to the ground state produces an ionizing photon that does not escape locally. The R-type ionization front does not raise significant bulk motion because it proceeds too fast through the interstellar medium to cause significant acceleration.

We started with an initial constant density of 10^4 cm^{-3}, a temperature of 100 K, and zero velocity. The emission rate of ionizing photons is $Q_H = 10^{49}$ s^{-1}, which is typical for a 50 000 K hot O-star. For the CLOUDY calls we used a spherical grid with the source in the center because geometric dilution of the radiation field must be included. Since no significant bulk flows develop throughout the simulation, we simply used a Cartesian grid in PLUTO (irradiation from the center in a spherical grid has not been implemented in TPCI yet), and we also did not need to include the advection of species. We only followed the time-dependent heating of the initially cool interstellar gas.

Numerically, R-type fronts have been studied for example by Dale et al. (2007). The authors derived a simple phenomenological solution for the expansion of the ionized region after ignition of the central source, which can be used to compare the results of our code:

$$R(t) = R_S \left(1 - \exp\left(-n_0 \alpha_B t \right) \right)^{1/3} . \tag{19}$$

This formula is derived by noting that the radius increment per time is restricted by the production rate of ionizing photons minus the recombination rate inside the already ionized region.

Figure 6 shows the propagation of the R-type ionization front in TPCI compared with the solution in Eq. 19. Especially the beginning of the simulation shows a faster expansion of the ionized
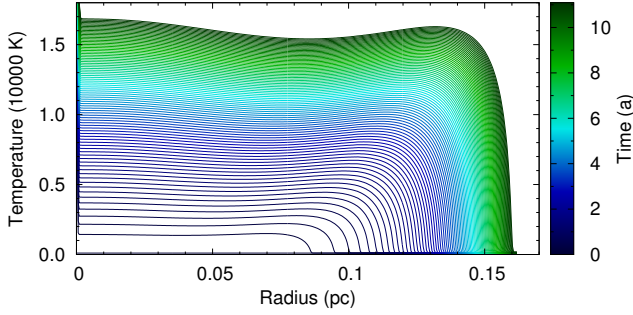
Fig. 7. Temperature evolution during expansion of the R-type ionization front. The temperature versus radius is plotted at various times. The time step between consecutive lines is constant, the time is referenced by the color scheme. The temperature increases from 1000 K to 17 000 K, being nearly constant throughout the ionized region. The expansion radius of the ionized region at a given time is marked by the steep temperature decline and increases from 0.085 to 0.16 pc. The distance between consecutive lines decreases, indicating the approach to the final Strömgren radius.

Fig. 8. Thermal conductivity coefficient. The coefficient for electron conductivity is depicted by the red dashed line, for neutral hydrogen by the green dotted line, and the blue solid line is the sum. The black dash-dotted line shows the more accurate weighted sum (Eq. 26) derived with the actual densities of neutral hydrogen and electrons in a CLOUDY simulation without irradiation. In the temperature region below 10 000 K the simple sum is accurate to within a factor of two.
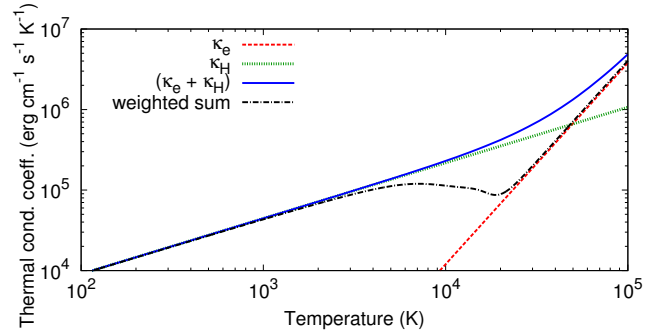
region than the theoretical prediction. To understand the differences, we have to remember that CLOUDY seeks equilibrium states. Although the evolution seems to be similar to the theoretical model, the simulation is based on a different physical mechanism.

Physically, the number of ionized hydrogen atoms cannot exceed the number of emitted ionizing photons since the central source has been switched on. This is not the case in the TPCI simulation because the equilibrium photoionization solver assumes that the source already existed for an infinite amount of time. The reason that we can nevertheless follow an expansion of the ionized region is based on the fact that recombinations in the cold gas are more frequent than in an almost fully ionized 10 000 K hot region. Therefore, CLOUDY actually computes an equilibrium Strömgren sphere at every time step, but with the temperature structure that is passed from PLUTO (see Fig. 7). The Strömgren sphere increases because recombination becomes less efficient with increasing temperature. In Fig. 6 the Strömgren radii for 5000 K, 10 000 K, and 20 000 K are displayed. At the times when the TPCI simulation reaches the first two indicated Strömgren radii, the mean temperatures in the ionized region are 5600 K and 11 400 K (compare Figs. 6 and 7). The photoionization solver does not assume the simple B recombination rate as in Eq. 18, but allows photons to escape based on the optical depth. Hence, recombination in the simulation is more efficient, which causes the mean temperatures to be slightly higher at the given Strömgren radii.

This simulation clearly shows that the user must be aware of the restrictions of TPCI and what is actually simulated. The interface cannot be used to correctly simulate the expansion of an ionized region after ignition of a central source because this is an effect of a time-dependent radiation field. It could, however, be used to follow the subsequent expansion of the hot gas in the Strömgren sphere into the surrounding cool interstellar gas under unchanged irradiation by the O-star because this can be approximated by equilibrium states.

3.4. Simulation of the atmosphere of HD 209458 b

The intention of the design of TPCI was simulating hot-Jupiter atmospheres, and here we present a first test case by solving a pure hydrogen atmosphere of HD 209458 b as our fourth test

case. The expanded atmosphere around HD 209458 b was discovered by Vidal-Madjar et al. (2003), and several studies investigated the system numerically (e.g., Yelle 2004; Tian et al. 2005; García Muñoz 2007; Penz et al. 2008; Murray-Clay et al. 2009; Koskinen et al. 2013). These studies provide a solid basis for comparing the results from TPCI.

For the simulation, we made use of two more modules of PLUTO: gravitational acceleration and thermal conductivity.

3.4.1. Gravity

The simulation of the escaping hot-Jupiter atmosphere incorporates the gravitational and centrifugal acceleration in the two-body system, also referred to as tidal forces. With the planet in the center, we derive for the effective potential

$$\Phi(r) = -\frac{GM_{\rm pl}}{r} - \frac{GM_{\rm st}}{a-r} - \frac{1}{2}\omega^2(l_{\rm cm} - r)^2 . \qquad (20)$$

Here r denotes the radial distance on the axis toward the star, $M_{\rm pl}$ and $M_{\rm st}$ are the planetary and stellar mass, a is the semi-major axis, $l_{\rm cm}$ is the distance to the center of mass, and G is the gravitational constant. The angular frequency ω is given by Kepler's third law

$$\left(\frac{2\pi}{T}\right)^2 = \omega^2 = \frac{G(M_{\rm st} + M_{\rm pl})}{a^3} . \qquad (21)$$

In PLUTO we include the acceleration:

$$a_{\rm G} = -\frac{\partial\Phi}{\partial r} = -\frac{GM_{\rm pl}}{r^2} + \frac{GM_{\rm st}}{(a-r)^2} - \frac{G(M_{\rm st} + M_{\rm pl})}{a^3}(l_{\rm cm} - r) . \quad (22)$$

By plotting the equation with the values of the system HD 209458 (Wright et al. 2011), we find that on the star-planet axis material can be bound to the planet up to 4.18 $R_{\rm pl}$, which is the size of the planet's Roche lobe on this axis.

3.4.2. Thermal conductivity

We used a simplified approach to include thermal conductivity by adding the conductivity of an electron proton plasma and of a neutral hydrogen gas. The first dominates for temperatures in excess of 50 000 K, the latter below this.

The following coefficients are taken from Banks & Kockarts (1973). The heat flux is given by

$$\mathbf{F_c} = -\kappa \, \nabla(T) \, . \tag{23}$$

For highly ionized gases, thermal conductivity is dominated by electron-ion collisions (Spitzer 1978). The conductivity coefficient is given by

$$\kappa_{\mathrm{ei}} = 1.2 \times 10^{-6} T_{\mathrm{e}}^{5/2} \, . \tag{24}$$

The thermal conductivity coefficient of neutral hydrogen is parameterized as

$$\kappa_{\mathrm{HH}} = 379 \, T^{0.69} \, , \tag{25}$$

and the total coefficient is given by the weighted sum

$$\kappa = \frac{1}{n} \sum n_s \kappa_s = \frac{1}{n} \left(n_{\mathrm{e}} \kappa_{\mathrm{e}} + n_{\mathrm{H}} \kappa_{\mathrm{H}} \right) \, . \tag{26}$$

In our simulations we used the direct sum of the two coefficients:

$$\kappa = \kappa_{\mathrm{e}} + \kappa_{\mathrm{H}} \, . \tag{27}$$

In the relevant temperature range below 10 000 K the approximation is correct to within a factor of two (see Fig. 8). Since we do not expect thermal conductivity to have a significant impact on the results (García Muñoz 2007), the procedure is sufficient to verify this claim in our simulation.

3.4.3. Simulation

We used a pure hydrogen atmosphere, irradiated from the top by the host star, and simulated the escape at the substellar point. With a stretched grid the cell size is increased from $0.0005 \, R_{\mathrm{pl}}$ in the lower atmosphere to $0.087 \, R_{\mathrm{pl}}$ at the top. The temperature in the lower atmospheres was fixed at the planet facing boundary to 1000 K, which is approximately the average dayside brightness temperature of HD 209458 b (Crossfield et al. 2012). In the simulation this was implemented by fixing the lower boundary density to $10^{15} \, \mathrm{cm}^{-3}$ and the pressure to $140 \, \mathrm{dyn \, cm}^{-2}$, which is equivalent to 0.14 mbar. The gas is heated by ionizing radiation with a solar minimum EUV spectral energy distribution (Woods & Rottman 2002), which is a good approximation for an inactive G0-type dwarf (Sanz-Forcada et al. 2011; Montes et al. 2001). In the spectral range below 912 Å (XUV), the planetary atmosphere at the distance of 0.047 AU from the host star is irradiated with a flux of $F_{\mathrm{XUV}} = 1315 \, \mathrm{erg \, cm}^{-2} \, \mathrm{s}^{-1}$. The derived value is similar to previous estimates, for instance, $1800 \, \mathrm{erg \, cm}^{-2} \, \mathrm{s}^{-1}$ in Koskinen et al. (2013). For this inactive host star (Sanz-Forcada et al. 2011), X-rays (< 100 Å) contribute only 3% of the energy in the XUV spectral range. In contrast to active host stars, X-rays have no strong impact on the mass loss of HD 209458 b. The initial conditions of the simulation are shown together with the results in Fig. 9. A comparable setup can be found in the simulations of Penz et al. (2008), Murray-Clay et al. (2009) or Koskinen et al. (2013).

In the expanding atmosphere neutral hydrogen is transported from the lower to the upper atmosphere, which means that advection of species is essential for the results in this simulation. To save computational time, we ran the simulation without the advection of species until a steady-state planetary wind was found and all shock waves had subsided. The resulting atmosphere was used as initial atmosphere for the final simulation including the advection of species. The convergence of the advective scheme
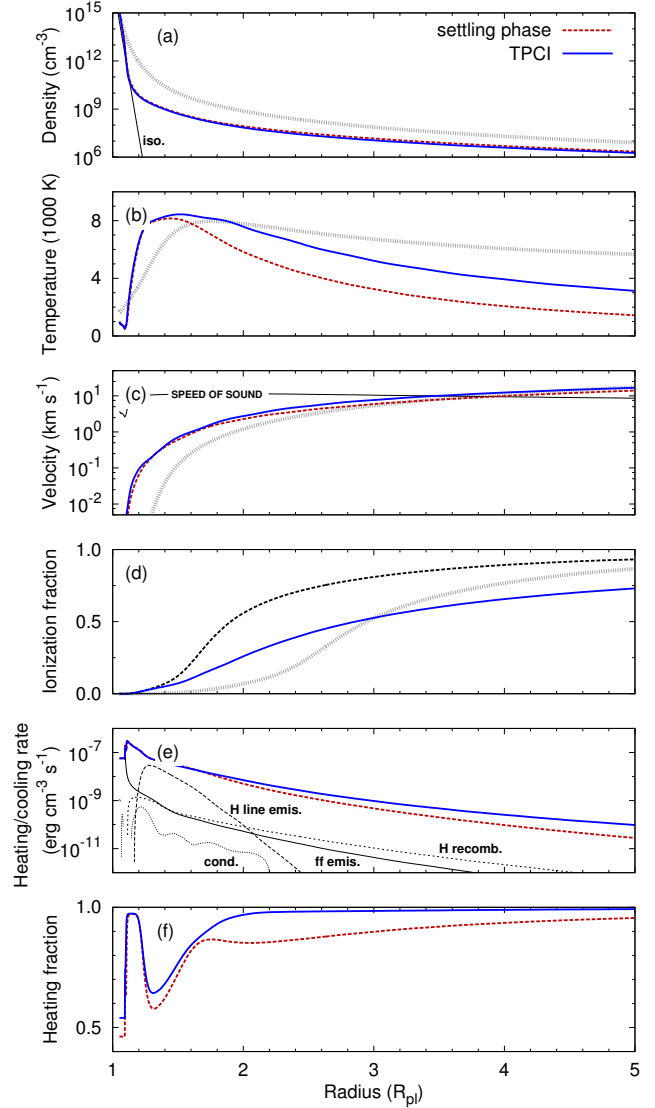
Fig. 9. Evaporating hydrogen atmosphere of HD 209458 b. Density (a), temperature (b), velocity (c), ionization fraction (d), heating and cooling rate (e), and the heating fraction (f) are plotted versus the planetary radius. The red dashed lines depict the initial settling phase, the blue solid lines the final TPCI simulation including advection of species. The initial conditions are given by the gray dotted lines. Panel (a) also shows the density structure of an isothermal atmosphere with 500 K (black solid line). In panel (c) the speed of sound is indicated (black solid line), and in panel (e) the three main cooling agents in the atmosphere are shown by black thin lines. "H line emis." is cooling due to line emission from hydrogen atoms (mainly Lyα), "ff emis." is cooling by free-free emission of electrons, and "H recomb." is recombination cooling of hydrogen. Additionally, thermal conductive cooling (cond.) is shown by a black dotted line. The atmosphere expands in a transonic flow. A small amount of the absorbed energy (∼ 11%) is lost through free-free and Lyα emission.

does not proceed beyond an advection length of $0.27 \, R_{\mathrm{pl}}$. This is comparable to the grid resolution at the top of the atmosphere, but much higher than the resolution in the lower atmosphere, so that effects due to the advection of species are initially only resolved in the upper atmosphere. However, below $1.05 \, R_{\mathrm{pl}}$ velocities are low and the advective timescale is longer than the hydro-

gen recombination timescale. Advection of species can safely be neglected below this level. Furthermore, we manually reduced the advection length to 0.01 R_{pl} and did not find significant changes in the solution. We therefore conclude that the advection of neutral hydrogen into the upper atmosphere is resolved throughout this simulation.

3.4.4. Results

The atmosphere expands in a steady-state transonic flow that is directed from the hot Jupiter toward the host star. We find a steep density and temperature gradient within the first 0.2 R_{pl} (see Fig. 9). At 1.08 R_{pl} the atmosphere shows a temperature minimum with only 500 K at a pressure of 0.7 μbar; the density stratification below this point differs only slightly from an isothermal atmosphere with the same temperature (see Fig. 9 (a)). EUV radiation does not penetrate to this depth, but is mainly absorbed from 1.1 to 1.2 R_{pl}, where the temperature of the atmosphere strongly increases. In this pure hydrogen atmosphere free-free emission is the main radiative cooling agent below 1.08 R_{pl}, reemitting about 50% of the total heat input, up to 70% of which is provided by hydrogen line absorption at this depth. Hydrogen line emission, mainly Lyα radiation, dominates the radiative cooling from 1.08 to 2.0 R_{pl}, and recombination of hydrogen is the most efficient radiative cooling agent at higher altitudes.

Averaged over the atmosphere above the temperature minimum, 89% of the heat input is used for heating and acceleration of atmospheric gas, and eventually for lifting the material out of the gravitational potential well of the planet. The total energy gain is divided as follows: 77% of the radiative energy input is converted to gravitational potential energy, 17% to kinetic and 6% to internal energy. Note that we define the heating fraction as

$$f_{\mathrm{H}} = \frac{G_{\mathrm{R}} - L_{\mathrm{R}}}{G_{\mathrm{R}}}, \qquad (28)$$

here G_{R} is the actual heating produced by the absorption of radiation, not the energy of the absorbed radiation (see Eq. 8). In our hydrogen-only simulation, only free-free and Lyα emission decrease the radiative heating fraction significantly (see Fig. 9 (f)). The fraction approaches 1.0 in the upper atmosphere; however, emission by helium or metals is not included in this simulation. Especially line absorption and emission by metals can significantly affect the heating and cooling rates in the lower atmosphere.

Replacing the denominator in Eq.28 with the absorbed radiative energy gives the net heating efficiency, which is often used in hydrodynamic simulations of hot-Jupiter atmospheres to account for the fraction of energy that goes into ionizing hydrogen and also for not specifically included cooling agents. In this particular simulation, stellar emission is absorbed from 50 to 912 Å by the atmosphere (more than 50% absorption). This absorption produces 92% of the total heating rate; the remaining 8% are caused by hydrogen line absorption, mainly Lyα absorption. The heating efficiency in the XUV range is 0.71.

Thermal conduction does not play a significant role in the atmosphere since it is more than two orders of magnitude smaller than the main cooling agents at every point throughout the atmosphere (see Fig. 9 (e)). Comparing the structure from the initial settling phase without advection of species with our final results shows that the advection of neutral hydrogen into the upper atmosphere increases the average temperature from 3000 to 5500 K. Advecting neutrals into the otherwise highly ionized

region increases the heating rate because more ionization processes occur. This also boosts the heating fraction, as can be seen in Fig. 9. The final velocity exceeds the sonic speed of 10 km^{-1}.

Our results are in excellent agreement with the C3 model of Koskinen et al. (2013) for the atmospheric evaporation at the substellar point. Assuming a spherically symmetric atmosphere, we derive a mass-loss rate of $\dot{M} = 4\pi r^2 \rho v = 1.4 \times 10^{11}$ g s^{-1}, which is equal to 0.0023 M_{Jup} Ga^{-1}. This value is an upper limit since we simulated the substellar point with the highest mass-loss rate. For the surface averaged mass loss, a factor of 1/4 was used by Koskinen et al., which places our result just slightly below their values, ranging from $4 - 6.5 \times 10^{10}$ g s^{-1}. Within 5% accuracy, advection of species does not change the mass-loss rate because a slightly higher velocity in the advective simulation is canceled by a lower density.

Murray-Clay et al. (2009) were the first authors to include a model for Lyα cooling in the simulation of escaping planetary atmospheres. Their spatial distribution and total cooling rate compares well with our results. Lyα cooling leads to a lower peak temperature in the atmosphere and reduces the mass-loss rate (Koskinen et al. 2013). Note, however, that deeper in the atmosphere the density is high enough that collisional de-excitation dominates and absorption of Lyα radiation is a heating agent. About one quarter of the total cooling through Lyα radiation is counterbalanced by Lyα heating in the lower atmosphere. On the other hand, Murray-Clay et al. used a gray absorption scheme, which leads to a mass-loss rate lower by a factor of four (Koskinen et al. 2013). Such differences clearly prove the advantages of the detailed photoionization solver included in TPCI. Neglecting any significant cooling or heating agent affects the mass-loss rate, which crucially depends on the available energy. This becomes even more important when metals are included in the atmosphere and an increasing number of processes must be modeled.

Although the mass-loss rate does not change when the advection of species is included in the simulation, the advection of neutral hydrogen into the upper atmosphere is important for analyzing observational results. The Lyα absorption signal of the planet during transit does change significantly because of the higher neutral hydrogen column density. The high velocities of the expanding atmosphere are crucial to transport the neutral hydrogen into the upper atmosphere.

4. Discussion and conclusion

We have presented TPCI, which is an interface between the MHD code PLUTO and CLOUDY, an equilibrium photoionization solver. TPCI enables simulations of hydrodynamic steady-state and slowly evolving flows, including multiple physical effects such as gravity and thermal conduction. It simultaneously solves the equilibrium state of a gas or plasma under strong irradiation. The code is valid from cold molecular regions to fully ionized hot plasmas and computes the radiative transfer along 1D rays.

The presented test simulations prove the validity of the combined simulations. In the introduction we have established a number of requirements for TPCI. The interface has proven its capabilities in solving the ionization and microphysical state of gases for a wide range of densities and temperatures. The second test problem (see Sect. 3.2) demonstrates the simulation of gases including metals and shows effects of X-ray radiative transfer. Multidimensional simulations or magnetic fields have not been studied in our verification of the 1D scheme. In general, we find
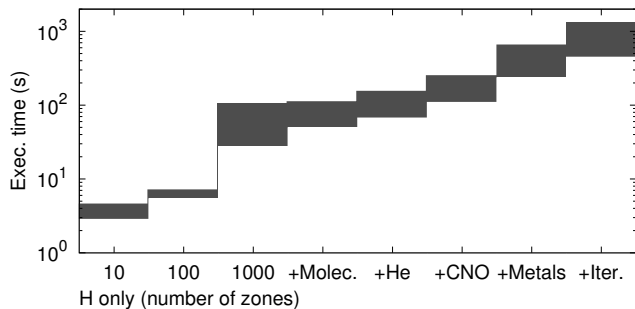
Fig. 10. Execution times of CLOUDY runs on local cpu with setups based on the hot-Jupiter simulation. Simulation times vary in the shaded range based on density and temperature. Each step increases the complexity of the simulation, starting with a simulation including only hydrogen and 10 zones in CLOUDY. In this case the execution time is dominated by the initialization of CLOUDY. The next steps are with 100 and 1000 zones. We then include step by step molecules, helium, carbon, nitrogen, and oxygen, and all 30 lightest elements. Finally, we iterate twice in CLOUDY over the complete domain to correct optical-depth effects.

that TPCI runs stably and reliably. The combination of the adaptable hydrodynamics code with a versatile radiative transfer and microphysics solver is generally applicable to photoevaporative flows and can for example be used to study the dynamics of H II regions or the evaporation of protoplanetary disks. Furthermore, CLOUDY is a powerful tool for spectral analysis, and observed spectra can be directly compared with results from the simulations.

One drawback in the use of TPCI is the computational effort of the detailed photoionization solver, which usually consumes almost all of the computational time. For the simulation of the test problems we used a few days to up to two months on a single 3.1 GHz processor. One-dimensional simulations are serial, so that simulations do not perform faster on clusters. In the search for hydrodynamic steady-state situations, the best call for reducing the computational effort is to find good initial conditions to speed up the convergence and to include more complex physics step by step from pre-converged simpler solutions.

Figure 10 shows execution times in single calls to the photoionization solver. The setup for the calls is based on the simulation of the hot-Jupiter atmosphere, but we used constant hydrogen number densities ranging from 10^5 to 10^{15} cm^{-3} and constant temperatures ranging from 1000 to 10 000 K. The actual execution times vary depending on the parameters. In a typical simulation of a hot-Jupiter atmosphere CLOUDY needs about 1000 zones for the adaptively adjusted grid, which means that execution times were about 100 s, but two iterations are needed to correctly compute the optical depth for the escape probability formalism. The settling phase of the simulation took about 10 000 calls to the photoionization solver, which explains the simulation time of about one month. For the advection of species, at least 30 iterations have to be made in the CLOUDY internal steady-state solver, but when starting from the previously converged simulation, about 200 calls to the photoionization solver suffice, which adds up to one day. In the future, the abundance of metals can be linearly increased during the simulation to prevent strong oscillation in the atmosphere and, thus, limit the CLOUDY calls to a minimum.

The convergence of the advection of species in the CLOUDY internal steady-state solver can cause problems in certain situations. The result is a solution where effects of the advection

of species are only resolved on scales larger than the advection length. One possible solution is to manually reduce the advection length to the needed accuracy, which increases the computational effort, however, because more iterations in CLOUDY are needed. Furthermore, advection can only be included in 1D simulations with flows toward the irradiating source. A possible solution would be to include passive scalar fields in PLUTO for every species and solve the advection by explicitly including source and sink terms, which could be retrieved from each call to the photoionization solver. This complicates the interface, however and necessitates more essential changes of the CLOUDY source code because the number densities of each species would have to be passed to CLOUDY and source and sink terms must be retrieved. Species include all ionization stages of the 30 lightest elements plus all included molecules.

The simulation of atmospheric evaporation in the well-studied hot Jupiter HD 209458 b demonstrates the capabilities of TPCI. The simulation of the hydrogen-only atmosphere shows significant differences compared to Murray-Clay et al. (2009) because the authors used a gray absorption scheme, or compared to Penz et al. (2008), who neglected Lyα cooling. Our atmosphere shows an excellent agreement with the corresponding model of Koskinen et al. (2013). We resolved a temperature minimum in the lower atmosphere because our simulation continues deeper into the atmosphere. Furthermore, we used a more comprehensive microphysics solver, which reveals significant cooling due to free-free emission in the lower atmosphere, which has previously been underestimated (Murray-Clay et al. 2009).

The increased accuracy in solving the absorption and emission processes is a clear advantage, and by using the well-tested CLOUDY code, we did not neglect any significant processes in our model. The total change in the mass-loss rate compared to the model of Koskinen et al. (2013) is lower than a factor of two in this pure hydrogen atmosphere, but larger differences can be expected when metals will be included. In the future, we will extend this initial test case to include molecules and metals and will investigate the effects of strong X-ray irradiation in the atmospheres of planets around active host stars.

References

Banks, P. M. & Kockarts, G. 1973, Aeronomy.
Bryan, G. L. & Norman, M. L. 1997, ArXiv Astrophysics e-prints [astro-ph/9710187]
Castor, J. I. 1970, MNRAS, 149, 111
Cecchi-Pestellini, C., Ciaravella, A., & Micela, G. 2006, A&A, 458, L13
Colella, P. & Woodward, P. R. 1984, Journal of Computational Physics, 54, 174
Courant, R., Friedrichs, K., & Lewy, H. 1928, Mathematische Annalen, 100, 32
Crossfield, I. J. M., Knutson, H., Fortney, J., et al. 2012, ApJ, 752, 81
Dale, J. E., Ercolano, B., & Clarke, C. J. 2007, MNRAS, 382, 1759
Dere, K. P., Landi, E., Mason, H. E., Monsignori Fossi, B. C., & Young, P. R. 1997, A&AS, 125, 149
Elitzur, M. 1982, Reviews of Modern Physics, 54, 1225
Elitzur, M., ed. 1992, Astrophysics and Space Science Library, Vol. 170, Astronomical masers
Ercolano, B., Barlow, M. J., Storey, P. J., & Liu, X.-W. 2003, MNRAS, 340, 1136
Ferland, G. J. 1979, MNRAS, 188, 669
Ferland, G. J., Korista, K. T., Verner, D. A., et al. 1998, PASP, 110, 761
Ferland, G. J., Porter, R. L., van Hoof, P. A. M., et al. 2013, Rev. Mexicana Astron. Astrofis., 49, 137
Frank, A. & Mellema, G. 1994, A&A, 289, 937
Fryxell, B., Olson, K., Ricker, P., et al. 2000, ApJS, 131, 273

García Muñoz, A. 2007, Planet. Space Sci., 55, 1426
Gottlieb, S. & Shu, C.-W. 1996, NASA CR-201591 ICASE Rep. 96-50
Henney, W. J., Arthur, S. J., Williams, R. J. R., & Ferland, G. J. 2005, ApJ, 621, 328
Jiang, G.-S. & Shu, C.-W. 1996, Journal of Computational Physics, 126, 202
Koskinen, T. T., Harris, M. J., Yelle, R. V., & Lavvas, P. 2013, Icarus, 226, 1678
Lammer, H., Selsis, F., Ribas, I., et al. 2003, ApJ, 598, L121
Landi, E., Del Zanna, G., Young, P. R., Dere, K. P., & Mason, H. E. 2012, ApJ, 744, 99
Le Teuff, Y. H., Millar, T. J., & Markwick, A. J. 2000, A&AS, 146, 157
Lightman, A. P. & White, T. R. 1988, ApJ, 335, 57
Mignone, A., Bodo, G., Massaglia, S., et al. 2007, ApJS, 170, 228
Mignone, A., Zanni, C., Tzeferacos, P., et al. 2012, ApJS, 198, 7
Montes, D., López-Santiago, J., Gálvez, M. C., et al. 2001, MNRAS, 328, 45
Morisset, C., Stasińska, G., & Peña, M. 2005, MNRAS, 360, 499
Morrison, R. & McCammon, D. 1983, ApJ, 270, 119
Murray-Clay, R. A., Chiang, E. I., & Murray, N. 2009, ApJ, 693, 23
O'Dell, C. R. 2001, ARA&A, 39, 99
O'Shea, B. W., Bryan, G., Bordner, J., et al. 2004, ArXiv Astrophysics e-prints [astro-ph/0403044]
Osterbrock, D. E. & Ferland, G. J. 2006, Astrophysics of gaseous nebulae and active galactic nuclei, ed. Osterbrock, D. E. & Ferland, G. J.
Owen, J. E., Ercolano, B., Clarke, C. J., & Alexander, R. D. 2010, MNRAS, 401, 1415
Penz, T., Erkaev, N. V., Kulikov, Y. N., et al. 2008, Planet. Space Sci., 56, 1260
Peters, T., Banerjee, R., Klessen, R. S., et al. 2010, ApJ, 711, 1017
Raga, A. C., Taylor, S. D., Cabrit, S., & Biro, S. 1995, A&A, 296, 833
Reale, F. & Orlando, S. 2008, ApJ, 684, 715
Rijkhorst, E.-J., Plewa, T., Dubey, A., & Mellema, G. 2006, A&A, 452, 907
Rosner, R., Tucker, W. H., & Vaiana, G. S. 1978, ApJ, 220, 643
Sanz-Forcada, J., Micela, G., Ribas, I., et al. 2011, A&A, 532, A6+
Schröter, S., Czesla, S., Wolter, U., et al. 2011, A&A, 532, A3+
Shapiro, P. R., Iliev, I. T., & Raga, A. C. 2004, MNRAS, 348, 753
Spitzer, L. 1978, Physical processes in the interstellar medium, ed. Spitzer, L.
Stone, J. M. & Norman, M. L. 1992, ApJS, 80, 753
Sutherland, R. S. & Dopita, M. A. 1993, ApJS, 88, 253
The Enzo Collaboration, Bryan, G. L., Norman, M. L., et al. 2013, ArXiv e-prints [arXiv:1307.2265]
Tian, F., Toon, O. B., Pavlov, A. A., & De Sterck, H. 2005, ApJ, 621, 1049
Toro, E. F., Spruce, M., & Speares, W. 1994, Shock Waves, 4, 25
Trammell, G. B., Arras, P., & Li, Z.-Y. 2011, ApJ, 728, 152
Tremblin, P. & Chiang, E. 2013, MNRAS, 428, 2565
Vidal-Madjar, A., Lecavelier des Etangs, A., Désert, J.-M., et al. 2003, Nature, 422, 143
Watson, A. J., Donahue, T. M., & Walker, J. C. G. 1981, Icarus, 48, 150
Wise, J. H. & Abel, T. 2011, MNRAS, 414, 3458
Woods, T. N. & Rottman, G. J. 2002, Solar Ultraviolet Variability Over Time Periods of Aeronomic Interest, ed. Mendillo, M., Nagy, A., & Waite, J. H., 221–+
Wright, J. T., Fakhouri, O., Marcy, G. W., et al. 2011, PASP, 123, 412
Yelle, R. V. 2004, Icarus, 170, 167

High-energy irradiation and mass loss rates of hot Jupiters in the solar neighborhood

M. Salz[1], P. C. Schneider[1], S. Czesla[1], J. H. M. M. Schmitt[1]

Hamburger Sternwarte, Universität Hamburg, Gojenbergsweg 112, 21029 Hamburg, Germany
e-mail: msalz@hs.uni-hamburg.de

ABSTRACT

Giant gas planets in close proximity to their host stars experience strong irradiation. In extreme cases photoevaporation causes a transonic, planetary wind and the persistent mass loss can possibly affect the planetary evolution. We have identified nine hot Jupiter systems in the vicinity of the Sun, in which expanded planetary atmospheres should be detectable through Lyα transit spectroscopy according to predictions. We use X-ray observations with *Chandra* and *XMM-Newton* of seven of these targets to derive the high-energy irradiation level of the planetary atmospheres and the resulting mass loss rates. We further derive improved Lyα luminosity estimates for the host stars including interstellar absorption. According to our estimates WASP-80 b, WASP-77 b, and WASP-43 b experience the strongest mass loss rates, exceeding the mass loss rate of HD 209458 b, where an expanded atmosphere has been confirmed. Furthermore, seven out of nine targets might be amenable to Lyα transit spectroscopy. Finally, we check the possibility of angular momentum transfer from the hot Jupiters to the host stars in the three binary systems among our sample, but find only weak indications for increased stellar rotation periods of WASP-77 and HAT-P-20.

Key words. X-rays: stars – stars: activity – planets and satellites: atmospheres – planets and satellites: physical evolution – planet-star interactions – binaries: general

1. Introduction

The discovery of giant gas planets in close proximity to their host stars brought the stability of these planets and their atmospheres into question. Orbiting as close as two stellar radii above the photosphere of the host star (Hebb et al. 2009), the so-called hot Jupiters and hot Neptunes are exposed to strong irradiation. In particular, the absorption of extreme ultraviolet (EUV) radiation ionizes hydrogen and heats the atmospheric gas. The resulting high temperatures of about 10 000 K can support a steady expansion of the atmosphere, which manifests itself in a planetary wind. In its formation this wind is not unlike the solar wind (Parker 1958; Watson et al. 1981). Smaller planets with low densities experience the strongest fractional mass loss and could lose their hydrogen and helium envelopes, evolving to hot Super-Earth like planets (Carter et al. 2012).

Indeed, expanded atmospheres have been confirmed around two hot Jupiters. In a study of the system HD 209458, Vidal-Madjar et al. (2003) discovered a 15% dimming in the line wings of the hydrogen Lyα line of the host star when transited by the hot Jupiter in the system, whereas the optical transit depth is only 1.5% (Henry et al. 2000; Charbonneau et al. 2000). To date, the presence of this upper atmosphere has been confirmed by several observations measuring excess absorption in H I, O I, C II, Si III, and Mg I lines (Vidal-Madjar et al. 2004; Ballester et al. 2007; Ehrenreich et al. 2008; Linsky et al. 2010; Jensen et al. 2012; Vidal-Madjar et al. 2013). In the second system, HD 189733, an expanded atmosphere was also confirmed by several observations (Lecavelier des Etangs et al. 2010, 2012; Jensen et al. 2012; Ben-Jaffel & Ballester 2013), and the system also exhibits an excess transit depth in X-rays (Poppenhaeger et al. 2013). Further tentative detections of excess absorption in transit obser-

vations of the systems WASP-12 (Fossati et al. 2010), 55 Cancri (Ehrenreich et al. 2012), and GJ 436 (Kulow et al. 2014) hint that expanded atmospheres could be a common feature in tightly bound gas giants.

Four of these five discoveries succeeded using Lyα transit spectroscopy. There are two reasons for this: First, the upper atmospheres of hot gas giants should consist mostly of hydrogen and helium, and second, the Lyα line dominates the UV spectrum of low mass stars despite interstellar absorption (France et al. 2013). Nevertheless, with today's instrumentation these types of investigations of exoplanetary atmospheres are only possible in close-by systems with strong Lyα emission.

Although the presence of expanded atmospheres is commonly accepted at least in the two standard cases, the origin of the Lyα absorption signal and the essential mass loss are not clear. Both can be affected by at least three processes, i.e., the planetary wind, the stellar wind, and the stellar radiation pressure. In general, the spectrally resolved absorption signal reveals the fraction of absorbed stellar emission and the absorption width. The transit depth can be explained by an opaque planetary atmosphere covering a certain fraction of the stellar disk. The absorption width of about 1 Å, corresponding to ± 100 km s^{-1}, can either be produced by a neutral hydrogen cloud with the given bulk velocity or by a static cloud with sufficient optical depth.

Koskinen et al. (2013a,b) support the idea that the escaping atmosphere produces a sufficient neutral hydrogen column density to explain the Lyα transit observations, although this wind proceeds with bulk velocities of only 10 km s^{-1}. The transit depth of their model atmosphere is consistent with the measured signal of HD 209458 b. However, the larger velocity offset of -200 km s^{-1} in the absorption signal of HD 189733 b (Lecavelier

Table 1. System parameters of the complete sample (see Sect. 2)

| System | Host star | | | | | | | | Planet | | | | | | | |
	Sp. type	T_{eff} (K)	V (mag)	$(B-V)$ (mag)	$(J-K)$ (mag)	d (pc)	P_{rot} (d)	Age (Ga)	R_{pl} (R_{jup})	M_{pl} (M_{jup})	ρ_{pl} (g/cm^{-3})	T_{eq} (K)	P_{orb} (d)	a (AU)	e	TD (%)
HAT-P-2	F8V	6300	8.7	0.46	0.19	114 ± 10	3.7 ± 0.4	0.4	1.1	8.9	7.3	1700	5.6	0.068	0.5	0.5
WASP-38	F8V	6200	9.5	0.48	0.29	110 ± 20	7.5 ± 1.0	1.0	1.1	2.7	2.1	1250	6.9	0.076	0	0.7
WASP-77	G8V	5500	10.3	0.75	0.37	93 ± 5	15.4 ± 0.4	1.7	1.2	1.8	1.3	1650	1.4	0.024	0	1.7
WASP-10	K5V	4700	12.7	1.15	0.62	90 ± 20	11.9 ± 0.9	0.6	1.1	3.2	3.1	950	3.1	0.038	0	2.5
HAT-P-20	K3V	4600	11.3	0.99	0.67	70 ± 3	14.6 ± 0.9	0.8	0.87	7.3	13.8	950	2.9	0.036	0	1.7
WASP-8	G8V	5600	9.8	0.82	0.41	87 ± 7	16.4 ± 1.0	1.6	1.0	2.2	2.6	950	8.2	0.080	0.3	1.3
WASP-80	K7-M0V	4150	11.7	0.94	0.87	60 ± 20	8.1 ± 0.8	0.2	0.95	0.55	0.73	800	3.1	0.034	0	2.9
WASP-43	K7V	4400	12.4	1.00	0.73	80 ± 30	15.6 ± 0.4	0.8	0.93	1.8	2.9	1350	0.8	0.014	0	2.6
WASP-18	F6IV-V	6400	9.3	0.44	0.28	99 ± 10	5.0 ± 1.0	0.7	1.3	10.2	10.3	2400	0.9	0.020	0	0.9
HD 209458	G0V	6065	7.7	0.58	0.28	50 ± 2	11.4	1.5	1.4	0.69	0.34	1450	3.5	0.047	0	1.5
HD 189733	K0-2V	5040	7.6	0.93	0.53	19	12.0 ± 0.1	0.7	1.1	1.1	0.96	1200	2.2	0.031	0	2.4
55 Cnc (b)	K0IV-V	5200	6.0	0.87	0.58	12	42.7 ± 2.5	6.7	—	0.80	—	700	14.6	0.113	0	—
GJ 436	M2.5V	3350	10.6	1.47	0.83	10	56.5	6.5	0.38	0.073	1.7	650	2.6	0.029	0.2	0.7

Notes. Columns are: name of the system, spectral type, effective temperature, visual magnitude, colors (SIMBAD or according to spectral type), distance, rotation period, and gyrochronological age of the host star (see Sect. 5); planetary radius, mass, density, equilibrium temperature (cited or $T_{eq} = T_{eff} \sqrt{R_{st}/2a}$), orbital period, semimajor axis, orbit eccentricity, and transit depth (TD).

References. The data were compiled using exoplanets.org (Wright et al. 2011) and the following publications: HAT-P-2: Bakos et al. (2007); van Leeuwen (2007); Pál et al. (2010), P_{rot} from v sin i, T_{eq} varies due to eccentricity (1250 to 2150 K); WASP-38: Barros et al. (2011); Brown et al. (2012); WASP-77: Maxted et al. (2013); WASP-10: Christian et al. (2009); Johnson et al. (2009); Smith et al. (2009), P_{rot} from LSP; HAT-P-20: Bakos et al. (2011), P_{rot} from LSP; WASP-8: Queloz et al. (2010); Cubillos et al. (2012), P_{rot} from LSP; WASP-80: Triaud et al. (2013), P_{rot} from v sin i; WASP-43: Hellier et al. (2011); WASP-18: Hellier et al. (2009); Pillitteri et al. (2014), P_{rot} from v sin i; HD 209458:Charbonneau et al. (2000); Henry et al. (2000); Torres et al. (2008); Silva-Valio (2008); HD 189733: Bouchy et al. (2005); Henry & Winn (2008); Southworth (2010); 55 Cnc: Butler et al. (1997); McArthur et al. (2004); Gray et al. (2003); Fischer et al. (2008); GJ 436: Butler et al. (2004); Knutson et al. (2011).

des Etangs et al. 2012) can probably not be explained with this model. Among others, Ekenbäck et al. (2010) argue that charge exchange between the fast ionized stellar wind and the neutral planetary wind creates the hydrogen population causing the Lyα absorption, but their model requires 40% of Jupiter's magnetic moment to reproduce the redshifted absorption. In principle radio observations could be used to determine the magnetic field strength of hot Jupiters, but most host stars have not been detected in radio observations so far (Sirothia et al. 2014). In particular, Lecavelier Des Etangs et al. (2011) presented observations with the Giant Metrewave Radio Telescope resulting in upper limits for the meter wavelength radio emission from HD 209458 and HD 189733. With certain assumptions, the nondetections indicate upper limits for the planetary magnetic field strength of only few times that of Jupiter. Regarding the field strength theoretical estimates are not particularly helpful either, as they predict values from insignificant to dominating field strength (Trammell et al. 2011). Furthermore, neutral hydrogen is also exposed to the radiation pressure from stellar Lyα emission, which can reach several times the gravitational acceleration of the host star (Bourrier & Lecavelier des Etangs 2013). In a collisionless regime, and with sufficient neutral hydrogen supply, radiation pressure can produce a neutral hydrogen population at velocity offsets of -100 km s^{-1}. Larger velocity shifts or redshifted absorption cannot be explained by radiation pressure.

Under certain circumstances photoevaporation, charge exchange, and radiation pressure can all affect the atmospheres of hot gaseous planets and especially mass loss rates. Since each mechanism depends on different system parameters, they should be distinguishable by comparing the absorption signals from dif-

ferent exoplanets. A common parameter of all three processes is the size of the expanded upper atmosphere, which is set by the gravitational potential of the planet and by the EUV irradiation. A planet of fixed size with a smaller mass produces not only a stronger planetary wind, but also has a larger interaction region for charge exchange and radiation pressure. Besides the atmospheric size, charge exchange is mainly affected by the temperature and velocity of the stellar wind (Holmström et al. 2008), whereas the radiation pressure primarily depends on the Lyα emission line strength of the host star (Bourrier & Lecavelier des Etangs 2013). While the two systems with secure detections of expanded atmospheres already show differences in their Lyα absorption signal (e.g., compare Vidal-Madjar et al. 2003; Lecavelier des Etangs et al. 2012), a larger sample of detections, increasing the phase space of system parameters, will eventually reveal correlations of the absorption signal with system parameters and help to identify the dominating processes in the atmospheres.

The X-ray luminosity of exoplanet hosts is a crucial parameter for both, estimating the mass loss rate of a hot gas giant and assessing the detectability of the expanded atmosphere. In the energy-limited case, the mass loss rate depends on the radiative energy input due to hydrogen ionizing emission of the host stars, however, EUV emission is mostly extinguished by interstellar absorption. Several methods exist to reconstruct this emission and particularly the X-ray luminosity is a robust and direct proxy (e.g., Sanz-Forcada et al. 2011), because both spectral ranges are formed in associated structures in the stellar atmospheres. Furthermore, X-rays constitute a significant fraction of the high-energy radiative output from active host stars like HD 189733

and Corot-2 (Pillitteri et al. 2010; Schröter et al. 2011; Sanz-Forcada et al. 2011). X-ray luminosities are also closely correlated with the Lyα luminosity of main-sequence stars (Linsky et al. 2013). Thus, they can be used to predict the signal in Lyα transit observations aimed at a detection of expanded atmospheres.

In an effort to increase the number of planets with detectable expanded atmospheres, we have identified a sample of nine hot gas giants in the vicinity of the Sun, where predictions yield strong Lyα emission amenable to transit spectroscopy. Here we report on our *Chandra* and *XMM-Newton* observations of seven targets without prior X-ray observations. The X-ray observations are used to determine the total high-energy irradiation of the planetary atmospheres. For this purpose, we compare three different methods to reconstruct the EUV emission of host stars. We present the first energy-limited mass loss rates based on observations. The improved Lyα luminosities of our targets in combination with estimates of interstellar absorption reveal the best targets for future transit spectroscopy campaigns. Finally, we assess the possibility of enhanced stellar rotation induced by tidal interactions with the close gas giants in three binary systems among our sample.

2. Target selection

To identify the most promising targets for Lyα transit spectroscopy among confirmed extrasolar planets we first selected hot, gaseous planets. The recent work by Marcy et al. (2014) has shown that the transition from rocky to gaseous planets with large amounts of volatile elements occurs at $\sim 2\,R_\oplus$. Therefore, we selected all planets with radii greater than $2\,R_\oplus$ and an orbital distance smaller than 0.1 AU to ensure high levels of irradiation. Planets with an optical transit depth smaller than 0.5% were also excluded to increase the contrast of the expected absorption signal.

In a second step, we predicted the strength of the Lyα emission line, using the following relation between effective temperature $T_{\rm eff}$, stellar rotation period $P_{\rm rot}$, and the Lyα line flux in $\mathrm{erg\,cm^{-2}\,s^{-1}}$ at 1 AU (Linsky et al. 2013):

$$\log\left(F_{\rm Ly\alpha}(1\,{\rm AU})\right) = \qquad\qquad (1)$$
$$\begin{cases} 0.37688 + 0.0002061\,T_{\rm eff} & \text{for } P_{\rm rot} = 3 - 10\,{\rm d}, \\ 0.48243 + 0.0001632\,T_{\rm eff} & \text{for } P_{\rm rot} = 10 - 25\,{\rm d}, \\ -1.5963 + 0.0004732\,T_{\rm eff} & \text{for } P_{\rm rot} > 25\,{\rm d}. \end{cases}$$

The stellar rotation periods were derived from the stellar radius and rotational velocity (see Sect. 2.1). Finally, we scaled the line flux with the stellar distance to obtain the flux at Earth (see Table 4). Interstellar absorption has a decisive effect on the observable strength and profile of the Lyα line. Because of considerable uncertainty in predicting the absorption, it is neglected in the selection process, but for the final targets we provide estimates in Sect. 4.2. The distance scaling ensures that the most promising systems are included.

Based on the anticipated Lyα flux, we ranked the preselected systems to find the most suitable targets for transit spectroscopy campaigns. The ranking order is mostly dominated by the distance of the host stars so that the most promising targets have distances less than 120 pc. Thus, they are probably contained in the Local Bubble of low-density, hot interstellar gas (Redfield & Linsky 2008). This further limits the uncertainty introduced by interstellar absorption. Among our final sample we accepted only targets with a Lyα flux exceeding 1/5 of the unab-
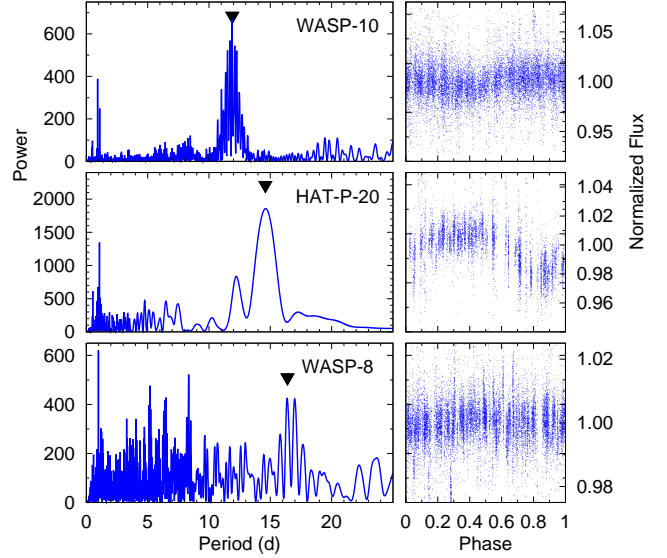
Fig. 1. Periodogram of the available stellar photometric data (SuperWASP) and the folded light curves, with the adopted stellar rotation periods marked by pointers. Periods with a power in excess of 30 occur with a rate of less than 1 in 10 000 by chance. Substructure of major period peaks is caused by period or phase shifts between different observing seasons. The 1 d period is prominent in all periodograms.

sorbed line flux from HD 209458 (Wood et al. 2005). Considering the remaining uncertainty in the prediction process, these targets can exhibit sufficiently strong Lyα lines for the detection of expanded atmospheres.

With this procedure we found 11 hot gas giants among all confirmed planets. As expected, the best-known systems, HD 189733 and HD 209458, lead the ranking. The three other systems with reported detections of absorption signals are not to be found in this target list. The distance of WASP-12 is too large for Lyα transit spectroscopy; 55 Cnc b is not transiting the host star, but only the expanded atmosphere has been found to undergo a grazing transit; and GJ 436 b is a slowly rotating host star with no certain detection of the equatorial rotational velocity used to derive estimates for the Lyα luminosity (Lanotte et al. 2014). 55 Cnc b and GJ 436 b have proven to be suitable targets for Lyα transit observations, thus, we included them in our analysis. The sample was scanned for previous X-ray observations: WASP-18 was not detected in a dedicated X-ray observation (Pillitteri et al. 2014) and WASP-43 has been analyzed by Czesla et al. (2013). The remaining seven host stars did not have any prior X-ray observation and unrestrictive *ROSAT* upper limits. The system parameters of our targets are summarized in Table 1.

2.1. Stellar rotation periods

Precise stellar rotation periods of the targets are needed to estimate the Lyα emission line strength. We compared published values with estimates based on the stellar rotational velocity and our own periodogram analysis of the host star's light curves (SuperWASP [1]). The adopted values are given in Table 1.

---

[1] http://www.superwasp.org/

Table 2. Details of the observations

Target	ObsID	Inst.	Start time (UT)	Duration (ks)	Start phase	Stop phase	Transit start phase
HAT-P-2	15707	C	2013-11-16 01:15	9.9	0.971	0.996	0.984
Wasp-38	15708	C	2014-01-18 07:52	9.9	0.984	1.004	0.986
Wasp-77	15709	C	2013-11-09 13:36	9.9	0.883	0.997	0.967
Wasp-10	15710	C	2013-11-15 07:31	9.9	0.786	0.830	0.985
Hat-P-20	15711	C	2013-11-24 17:33	9.9	0.699	0.749	0.987
Wasp-8	15712	C	2013-10-23 20:42	9.9	0.109	0.127	0.989
Wasp-80	0744940101	XMM	2014-05-15 20:13	15.5	0.718	0.783	0.986

Notes. 'C' is a *Chandra* ACIS-S observation, XMM is an *XMM-Newton* EPIC PN observation. Start and stop phase indicate the exposure duration in reference of the planetary orbit with the transit occurring at phase zero.

An initial estimate for the period can be derived from the stellar radius R_s and the equatorial rotational velocity v_{eq}:

$$P_{rot} = 2\pi R_s \times v_{eq}^{-1}, \qquad (2)$$

assuming that the inclination of the rotation axis is $90°$ — a reasonable assumption for most transiting systems. The rotational velocity and the stellar radius are available for most systems, and in the cases of WASP-80, HAT-P-2 and WASP-18 more precise rotation periods are not available.

WASP-38, WASP-77, WASP-10, HD 209458, HD 189733, 55 Cnc, and GJ 436 have published rotation periods based on photometric variability, which correspond well with the values derived from Eq. 2. The rotation period of WASP-43 was analyzed by Hellier et al. (2011).

We download the original photometric data of the available targets (HAT-P-2, WASP-10, HAT-P-20, WASP-8) from the SuperWASP archive and analyzed the light curves via a generalized Lomb-Scargle periodogram (LSP, Zechmeister & Kürster 2009) using the PyAstronomy package[2] to derive stellar rotation periods (see Fig.1). WASP-10 and HAT-P-20 show isolated peaks with high powers in the periodogram that agree with the $v \sin i$ based rotation periods within the errors. The analysis of HAT-P-2 remained inconclusive, so we reverted to the rotation period from Eq. 2.

The data of WASP-8 consist of two seasons with different major periods, which have false alarm probabilities of less than 10^{-4}. Only the period around 16.4 d is present in both seasons and shows a clear photometric variation in the phase folded light curve. The estimate from the stellar rotational velocity and the radius is about a factor of two larger, but the planet is in a retrograde orbit with a projected angle of $123°$ between the orbital and the stellar rotation axes (Queloz et al. 2010). Hence, the prior assumption of an inclination angle of $90°$ is probably invalid, and the photometric rotation period in combination with the $v \sin i$ indicate an inclination of the rotation axis with the line of sight of about $30°$.

3. Observations and data analysis

We observed six planet hosts with the *Chandra* X-ray observatory using 10 ks long exposures and WASP-80 with *XMM-Newton* for 16 ks (see Table 2). Three *Chandra* observations partially covered the planetary transit; the exposure of WASP-38 occurred completely within the transit of the hot Jupiter.

We analyzed the *Chandra* ACIS-S observations with the Chandra Interactive Analysis of Observations software package

[2] http://www.hs.uni-hamburg.de/DE/Ins/Per/Czesla/PyA/PyA/

Table 3. Optical Monitor results of WASP-80

Filter	Cen. Wavelength (nm)	Flux[a]	Mag.
U	344	5.4 ± 0.5	14.5
UVW1	291	1.5	16.0
UVM2	231	0.1	19.2
UVW2	212	< 0.04	< 20.3

Notes. The UVW2 filter did not yield a detection of the target. Count rate conversion for a K0V star (*XMM-Newton* User Handbook). The UVW1 and UVM2 conversion introduces a factor of two error and for UVW2 a factor of ten. Magnitudes were computed according to the fluxes. [a] (10^{-15} erg cm^{-2}s^{-1}Å^{-1})

(CIAO) 4.6, CALDB 4.5.9 (Fruscione et al. 2006). We extracted the source counts in a circular region with a radius of $2''$ and background counts in another circular region with a $25''$ radius placed in a source-free region close to the target position. The target coordinates at the observational epoch were obtained from the SIMBAD database, accounting for proper motion. For HAT-P-20, we used the proper motion from the UCAC4 catalog (Zacharias et al. 2013).

In Fig. 2 we show the source regions filtered for photon energies between $0.2 - 2$ keV, with the extraction regions marked by circles. We detected six host stars as X-ray sources (including the *XMM-Newton* observation, see below), only WASP-38 is a nondetection with zero photons at the source position. The centroids of the source counts in the *Chandra* pointings show offsets smaller than $0.5''$ from the nominal source positions, while the Proposers' Observatory Guide (Version 16) cites a one sigma pointing error of $0.6''$[3]. In the WASP-10 exposure, two photons were detected close to the source position, which shift the centroid by $1.1''$ if attributed to the target, but only 3% of the *Chandra* observations show a pointing error in excess of $1''$. The proper motion correction amounts to only $0.5''$ with a cited error of 10%. Accordingly, it is most likely that these are background photons, so they are not included in the analysis of WASP-10. In any case, the two photons do not have a large impact on the analysis.

WASP-80 was observed on May 15th, 2014, with all three detectors of the European Photon Imaging Camera (EPIC) on board of *XMM-Newton* in full frame mode with medium filters; more details about the telescope and the detectors can be found in the *XMM-Newton* User Handbook[4]. We also obtained four full frame images with the Optical Monitor (OM), each 1320 s

[3] http://cxc.harvard.edu/proposer/POG/
[4] http://xmm.esac.esa.int
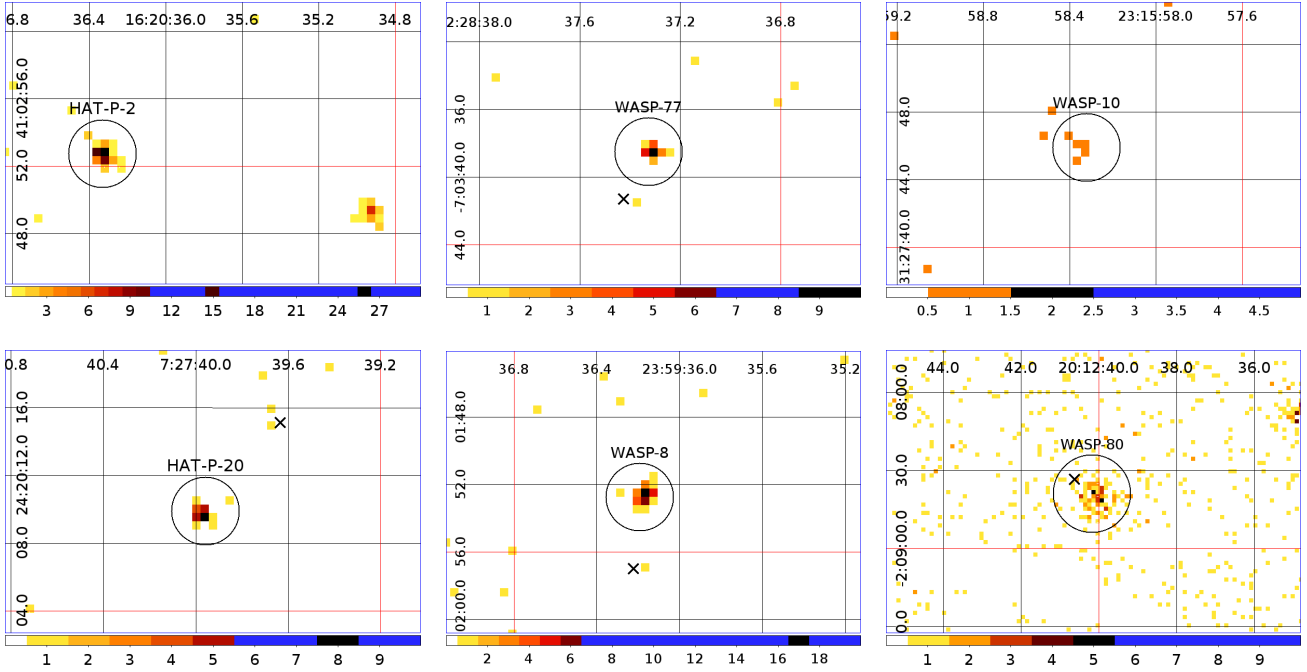
Fig. 2. Source regions filtered for soft X-ray emission $(0.2 - 2.0 \text{ keV})$. The target positions are marked by circles with a $2''/15''$ radius in the *Chandra/XMM-Newton* observations; the position of known companions is marked by crosses. In the panel of WASP-80, a nearby detected 2MASS source is also marked by a cross. The X-ray source close to HAT-P-2 is discussed in Sect. 3.1. Six out of seven targets have been detected as X-ray sources.

long with the filters U, UVW1, UVM2, and UVW2. The derived fluxes and magnitudes are given in Table 3. We reduced the data with the Scientific Analysis System (SAS 13.0.0) with the standard procedure and filters. The X-ray exposures are free of high background periods, so that no time filtering was applied. The source counts were extracted in a circular region with a radius of $15''$ and background counts were extracted from three circular regions on the same CCD, which were chosen with at least $30''$ distance to any recognizable X-ray source.

3.1. Binaries

WASP-8, WASP-77, and HAT-P-20 are known visual binary stars and the positions of the faint red companions (BD-07 436B, 2MASS J07273963+2420171, WASP-8 B) are marked in Fig. 2 by crosses. The relative position of the companions was obtained from images of the Two Micron All Sky Survey (2MASS, Skrutskie et al. 2006) and transfered to the X-ray images, assuming a common proper motion of the binaries. For the companion of HAT-P-20, the infrared colors J = 10.14, H = 9.44, and K = 9.22 from 2MASS indicate an M-type dwarf. The companions of WASP-77 and WASP-8 have spectral types of K5V and M, respectively (Maxted et al. 2013; Queloz et al. 2010).

The 2MASS images of all targets were screened for further close companions. Only WASP-80 shows a 2MASS source (2MASS 20124062-0208333) about 4 magnitudes darker at $9''$ distance, which is also marked in Fig. 2; the source is also clearly distinguishable in the OM exposure. The infrared colors indicate a late K to early M-type star, similar to the spectral type of WASP-80 (Triaud et al. 2013), which is not known to be a binary star. The magnitude difference at a similar spectral type suggests that the 2MASS detection is a background source.

In the exposure of HAT-P-2, we detected a soft X-ray source at a distance of $16''$ from the target, corresponding to 1800 AU at the distance of the HAT-P-2 (114 pc, van Leeuwen 2007). The 2MASS J-band yields no detection with an upper limit of 15.8 mag[5], hence a dwarf with a spectral type later than M5 would not be detected. Assuming the distance of HAT-P-2, the X-ray source has a luminosity of 2×10^{28} erg s^{-1}, whereas the maximal $L_X/L_{bol} = 10^{-3}$ in M-dwarfs results in 4×10^{27} erg s^{-1} (James et al. 2000) . The light curve excludes a strong flare and the gyrochronological age of HAT-P-2 (0.5 Ga in our analysis, 1.6 Ga in the more detailed analysis of Brown 2014) excludes increased activity due to a young age (< 100 Ma, Stelzer & Neuhäuser 2001). We conclude that this source is most likely a background object, possibly of extragalactic origin because HAT-P-2 does not lie in the galactic plane.

3.2. Light curve analysis

For our analysis of the high-energy irradiation of planetary atmospheres, we are interested in the mean coronal emission of the targets. Strong flares during the observations would result in unreasonably high luminosity estimates. The exposure time corrected X-ray light curves of the targets with 1 ks binning are shown in Fig. 3. We added the background subtracted counts of the three EPIC instruments for the light curve of WASP-80. No background correction is applied in the *Chandra* exposures. None of the observations shows a strong flare.

The count rate of WASP-80 declines significantly during the first 6 ks of the observation. The bottom panel of Fig. 3 shows the hardness ratio $(0.65 - 2.0/0.2 - 0.65 \text{ keV})$ of the target. The ratio decreases along with the count rate, indicating that this trend can be related to prolonged flaring activity at the exposure start.

---

[5] http://www.ipac.caltech.edu/2mass/overview/about2mass.html
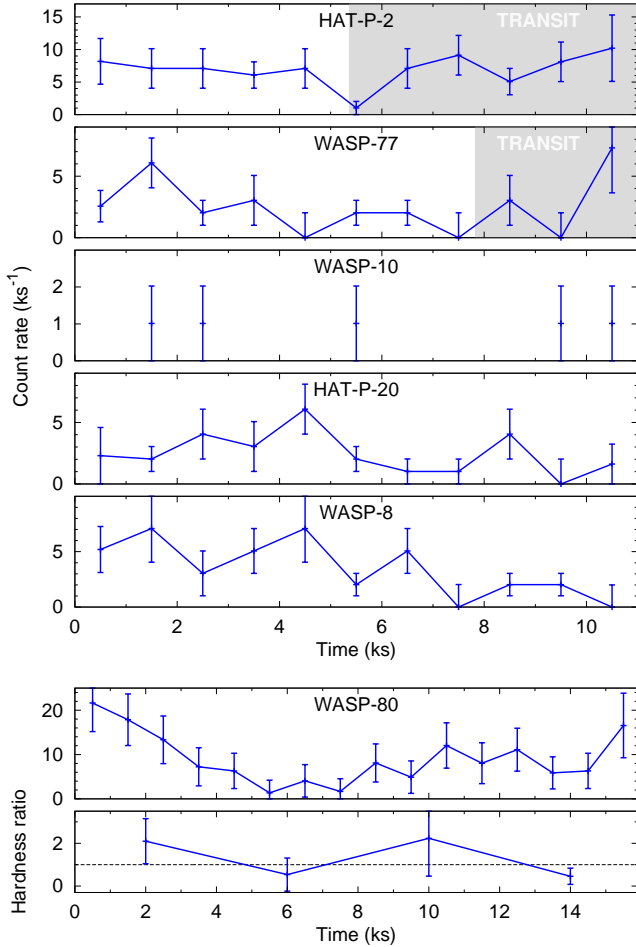
Fig. 3. X-ray light curves of the targets with a 1 ks binning. The *XMM-Newton* observation of WASP-80 is about 5 ks longer, and the count rate is the sum of all EPIC detectors; the error is given by the pipeline. In the *Chandra* observations, error bars represent the 1-sigma Poissonian uncertainty on the count rate. Planetary transits during observations are marked by shaded areas. The WASP-10 panel shows only the arrival times of the five source photons. The last panel depicts the hardness ratio $(0.65 − 2.0/0.2 − 0.65 \text{ keV})$ in the WASP-80 observation. No pronounced flare occurred during the observations.

However, the count rate around 6 ks is unusually low compared to the rest of the observation, so eventually we use the complete exposure to derive the mean X-ray flux of the target.

The observations of HAT-P-2 and WASP-77 partially cover the planetary transit. Individual X-ray exposures are not sensitive to the level of absorption expected from expanded atmospheres of hot Jupiters ($\sim 7\%$, Poppenhaeger et al. 2013). Nevertheless, the periods affected by the planetary transits are shaded in Fig. 3. Comparing the count rate during the transit with the pretransit rate, we derive an upper limit for the size of an X-ray opaque planetary atmosphere assuming a homogeneous X-ray surface brightness of the host star. For HAT-P-2 we have 31 in-transit counts with 32.7 counts expected, which corresponds to a maximum radius of an expanded atmosphere of 7.3 R_{pl}, and for WASP-77 5/5.5 in-transit/scaled out of transit counts were observed resulting in upper limit of 6.3 R_{pl} for the planetary atmosphere (95% confidence).

It is unlikely that the nondetection of WASP-38 is caused by an expanded planetary atmosphere that covers the complete stellar disk, because the atmosphere would have to be expanded over two stellar radii (24 R_{pl}), whereas usual estimates assume expansions by only a few planetary radii (e.g., Vidal-Madjar et al. 2003). Although, the derived upper limit for the X-ray luminosity of the host star is low, the value is consistent with predictions (see Table 4) and with other activity indicators (see Sect. 3.4).

3.3. Spectral analysis and X-ray luminosities

Spectra were extracted from source and background regions and analyzed with XSPEC V12.7.1 (Arnaud 1996). The three spectra from the individual cameras on board *XMM-Newton* were fitted in a joint analysis. We used the C-statistics, appropriate for low count rates (Cash 1979). According to the XSPEC guidelines, the data were binned to contain at least one photon per bin[6] with the exception of WASP-10, for which the five source counts were fitted using the unbinned data. We used an absorbed, one temperature, optically thin plasma emission model (APEC, Foster et al. 2012) with solar abundances (Grevesse & Sauval 1998). We added a second temperature component for WASP-80. In this case, the spectra contain sufficient source counts because of the longer exposure and a five times higher effective area at 1 keV of *XMM-Newton* compared with *Chandra*.

Since the absorption component of the model remained ill-constrained in the fitting procedure, we fixed the interstellar hydrogen column density using the source distance and an average interstellar hydrogen density of 0.1 cm^{-3} (Redfield & Linsky 2000). The resulting spectra and models are shown in Fig. 4, where the spectra were binned to a lower resolution for visualization. The inserts show the 1,2, and 3 sigma confidence contours of the two model parameters: plasma temperature and emission measure. These models are used to compute the X-ray fluxes in the 0.124 to 2.48 keV (5 to 100 Å) spectral range (see Table 4). The detected targets have mean coronal temperatures ranging from 2 to 9×10^6 K and their X-ray luminosities vary by one order of magnitude from 0.7 to 8×10^{28} erg s^{-1}.

The short X-ray exposures do not yield detections of the faint companions in the three binary systems. However, one or two photons are detected at the expected positions of the secondaries. Assuming similar coronal parameters for both components, we derive upper limits for the X-ray luminosity of the B components (95% confidence, see Table 5).

3.4. Optical observations

To check for activity indicators in the optical, we obtained quasi-simultaneous optical spectroscopy for WASP-38 and WASP-77. In particular, the spectra were taken with the "Heidelberg Extended Range Optical Spectrograph" (HEROS), mounted at the 1.2 m "Telescopio Internacional de Guanajuato, Robótico-Espectroscópico" (TIGRE) at La Luz observatory in Mexico (Schmitt et al. 2014). The spectra cover the $350 − 880$ nm range with only a small gap around 570 nm at a resolution of about 20 000.

We observed WASP-38 for 30 min, less than one hour after the X-ray exposure, and we observed WASP-77 twice, 5 h before and 11 h after the X-ray observation with each exposure lasting 45 min. Both the WASP-38 spectrum and the combined WASP-77 spectrum show a mean signal-to-noise ratio (SNR) of 25 in the blue channel, which is sufficient to derive the Mount Wilson

---

[6] http://heasarc.gsfc.nasa.gov/xanadu/xspec/
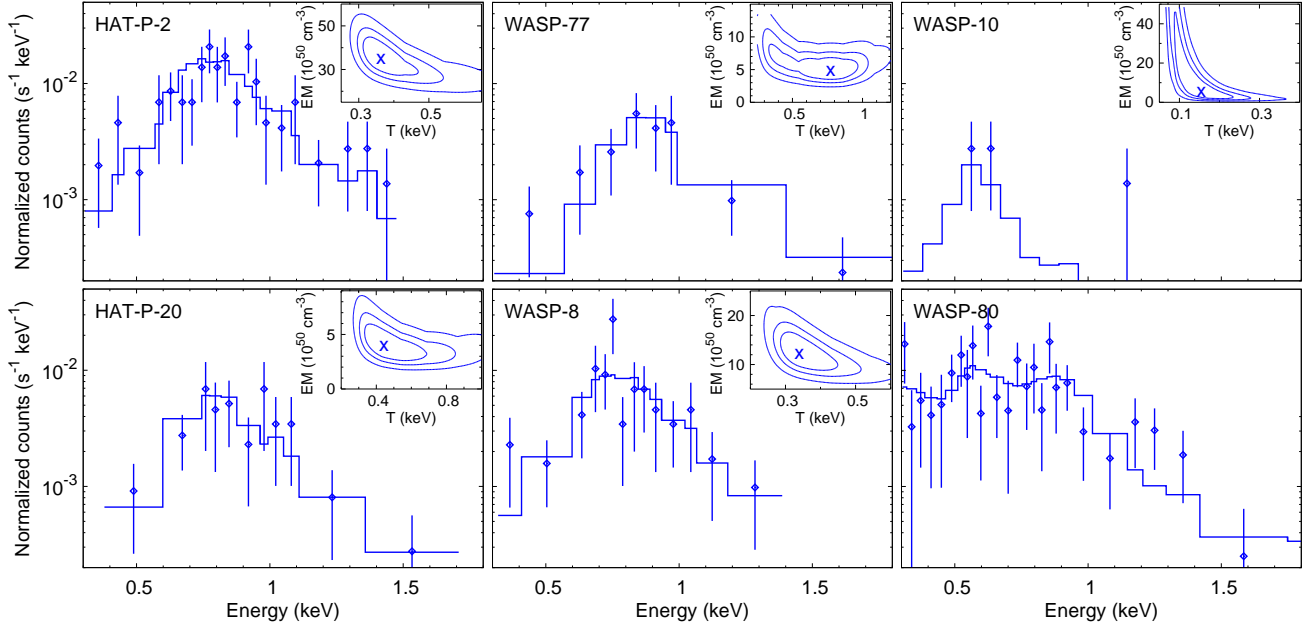
Fig. 4. X-ray spectra of the targets. The plasma emission models are depicted by the histograms and the source count rates by diamonds with error bars. The χ^2 contours for the 1, 2, and 3 σ confidence intervals of the model parameters are shown in the inserts. WASP-80 was fitted with a two temperature model; the contours of the four parameters are not shown. With the exception of WASP-10, which only has five source counts, the model parameters are well confined.

S-index (S MWO, Wilson 1978). We further converted S MWO into the chromospheric log R'_{HK} index, which represents the ratio of emission in the Ca II H and K emission lines and the stellar bolometric luminosity (Noyes et al. 1984; Rutten 1984).

For WASP-38, we obtained values of $S_{MWO} = 0.153 \pm 0.006$ and log $R'_{HK} = -4.87 \pm 0.04$, which are consistent with a basal chromospheric flux level and thus a low level of chromospheric activity (Mittag et al. 2013). This finding is also consistent with the absence of detectable X-ray emission during our observation. For WASP-77, we derived an S-index, S_{MWO}, of 0.338 ± 0.011, corresponding to a log R'_{HK} value of -4.57 ± 0.02. This indicates a moderate level of chromospheric activity clearly exceeding the basal level, which is, again, consistent with the detection of X-ray emission. Between the consecutive nights, we found no detectable variability in the Hα line, covered by the red spectral channel where the SNR is higher (~ 40).

4. Planetary irradiation and mass loss

While EUV emission ($100 < \lambda < 912$ Å) contributes about $\sim 90\%$ of the radiation power of hydrogen ionizing ($\lambda < 912$ Å) emission from inactive stars (Sanz-Forcada et al. 2011), above 400 Å it is completely absorbed by interstellar hydrogen. To derive estimates for the planetary mass loss rate, which crucially depends on the radiative energy input, we have to assess the EUV emission of the host stars.

4.1. Stellar EUV emission

Here, we compare three different methods to derive the EUV luminosity of dwarfs either based on the stellar rotation period, the X-ray luminosity, or the Lyα luminosity. The first method was introduced Lecavelier des Etangs (2007), who apply a relationship between the stellar equatorial rotation velocity and the stellar flux in the S2 bandpass of the Wide Field Camera on board
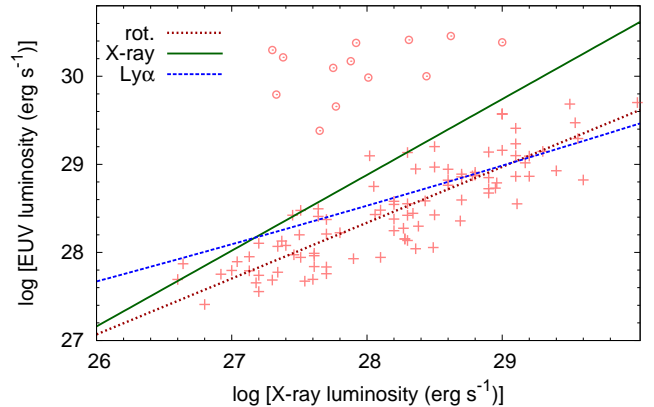
Fig. 5. Estimates of stellar EUV emission in the sample of Pizzolato et al. (2003) based on stellar rotation (red crosses), X-rays (green solid line) and Lyα emission (blue dashed line). A linear fit to the rotation based estimates is represented by a red dotted line. Circles indicate stars with rotation periods shorter than 1 d.

the *ROSAT* satellite (Wood et al. 1994). The flux in this band is further scaled to the full EUV range based on an average solar spectrum:

$$F_{EUV}(1 \text{ AU}) = 4.6 \left(\frac{v_{eq}}{2.0 \text{ km s}^{-1}} \right)^{1.4} \text{ erg cm}^{-2} \text{ s}^{-1} . \qquad (3)$$

Second, Sanz-Forcada et al. (2011) derive a relation between the X-ray (5 to 100 Å) and EUV luminosities of main-sequence stars,

$$\log L_{EUV} = (4.80 \pm 1.99) + (0.860 \pm 0.073) \log L_X . \qquad (4)$$

Their method is based on a sample of stars with a full reconstruction of the emission measure distribution from 10^4 to 10^7 K.

Table 4. Results from the analysis of the X-ray observations and the mass loss analysis for the host stars in the sample.

System	X-ray analysis					Mass-loss analysis							
	T $(10^6$ K$)$	EM^A	$F_X{}^B$	L_X $(10^{28}$ erg s$^{-1})$	L_X^{rot}	$\log L_{\mathrm{EUV}}$ (erg s^{-1})	$\log L_{\mathrm{Ly\alpha}}$ (erg s^{-1})	$F_{\mathrm{Ly\alpha}}{}^C$	$F_{\mathrm{Ly\alpha}}^{\mathrm{abs}D}$	$F_{\mathrm{XUV}}{}^E$	$\log \dot M$ (g s^{-1})	$\log \dot M^{\mathrm{rot}}$ (g s^{-1})	ΔM (%)
HAT-P-2	$4.2^{+1.4}_{-0.6}$	$35.8^{+10.3}_{-8.8}$	$5.2^{+0.5}_{-0.5}$	$8.2^{+1.7}_{-1.5}$	39.	28.9	29.0	6.5	$0.0 - 7.8$	1.3	9.52	9.79	0.004
WASP-38	—	—	<0.8	<1.1	9.4	<28.5	<28.7	<3.7	$<0.3 - 0.4$	<0.29	<9.42	9.74	0.008
WASP-77	$9.0^{+2.4}_{-5.9}$	$5.0^{+2.0}_{-1.6}$	$1.3^{+0.3}_{-0.2}$	$1.4^{+0.3}_{-0.3}$	2.1	28.6	28.8	5.6	$1.3 - 4.9$	3.3	10.85	10.3	0.29
WASP-10	$1.8^{+1.0}_{-1.8}$	$6.0^{+79.0}_{-6.0}$	$1.3^{+0.1}_{-1.3}$	$1.2^{+0.6}_{-1.2}$	1.8	28.6	28.7	5.7	$0.0 - 6.2$	1.2	9.90	9.47	0.01
HAT-P-20	$5.2^{+3.6}_{-1.4}$	$4.0^{+2.1}_{-0.4}$	$1.7^{+0.2}_{-0.4}$	$1.0^{+0.2}_{-0.2}$	1.1	28.5	28.7	8.9	$1.9 - 14.6$	1.2	9.22	8.75	0.001
WASP-8	$3.9^{+1.4}_{-0.7}$	$12.5^{+4.5}_{-3.9}$	$3.1^{+0.4}_{-0.6}$	$2.8^{+0.6}_{-0.7}$	1.9	28.7	28.9	8.0	$3.5 - 13.3$	0.46	9.53	8.90	0.01
WASP-80	$2.2^{+0.8}_{-0.9}$ $9.9^{+1.9}_{-1.9}$	$1.7^{+2.3}_{-0.6}$ $1.2^{+0.4}_{-0.4}$	$1.6^{+0.1}_{-0.2}$	$0.7^{+0.5}_{-0.5}$	1.6	28.5	28.7	10.8	$0.0 - 33.6$	1.1	10.54	10.3	0.29
WASP-43	—	—	—	$0.8^{+0.6}_{-0.3}$	0.76	28.5	28.7	6.2	$0.3 - 8.7$	6.6	10.84	10.1	0.21
WASP-18	—	—	—	<0.07	17.	<28.0	<28.3	<1.8	$<1.5 - 2.9$	<0.97	<9.36	10.3	0.001
HD 209458	—	—	—	<0.03	4.0	<27.8	28.6	15.	22	<0.11	<9.94	10.6	0.04
HD 189733	—	—	—	$1.5^{+0.5}_{-0.4}$	2.1	28.6	28.4	60.	190	2.1	10.73	10.2	0.28
55 Cnc (b)	—	—	—	0.04	0.31	27.7	28.1	65.	440	0.01	—	—	—
GJ 436	—	—	—	0.01	0.06	27.1	27.7	35.	50	0.06	8.92	8.78	0.18

Notes. Columns are: name of the system, coronal temperature and emission measure $^{(A)}$ $(10^{50}$ cm$^{-3})$; X-ray flux at Earth $^{(B)}$ (0.124-2.48 keV, 10^{-14} erg cm^{-2} s^{-1}); X-ray luminosity and predicted luminosity (Pizzolato et al. 2003); EUV luminosity (100-912 Å, Sanz-Forcada et al. 2011); reconstructed Lyα luminosity (Linsky et al. 2013); reconstructed Lyα flux at Earth $^{(C)}$ $(10^{-14}$ erg cm^{-2} s$^{-1})$; minimum and maximum Lyα flux at Earth after interstellar absorption $^{(D)}$ $(10^{-15}$ erg cm^{-2} s$^{-1})$; XUV flux at planetary distance $^{(E)}$ (<912 Å, 10^4 erg cm^{-2} s$^{-1})$; mass loss rate (Sanz-Forcada et al. 2011) and rotation based estimate (Ehrenreich & Désert 2011); and the last column is the total fractional mass loss of the planet in its lifetime (see text).

References. X-ray flux: WASP-43 (Czesla et al. 2013); WASP-18 (Pillitteri et al. 2014); HD 209458, HD 189733, 55 Cnc, and GJ 436 (Sanz-Forcada et al. 2011). Reconstructed Lyα flux: HD 209458 (Wood et al. 2005), HD 189733 (Bourrier & Lecavelier des Etangs 2013), 55 Cnc (Ehrenreich et al. 2012), and GJ 436 (France et al. 2013). Measured Lyα fluxes of HD 209458, HD 189733, and GJ 436 are mean integrated out-of-transit fluxes in the original HST data.

The plasma model is then folded with an atomic emission model to derive the spectral energy distribution. Third, Linsky et al. (2014) derive the EUV flux in several 100 Å wide bands on the basis of the Lyα flux. Their relations are based on intrinsic Lyα fluxes, EUVE measurements (<400 Å), and semiempirical models ($400 < \lambda < 912$ Å, Fontenla et al. 2014).

To establish a comparability of these three approaches, we use a sample of main-sequence stars from Pizzolato et al. (2003), which all have measured X-ray luminosities, known stellar rotation periods, and determined stellar masses. To apply the relation from Lecavelier des Etangs, we derive a stellar equatorial rotation velocity with the standard mass-radius relation for main-sequence stars (Lacy 1977) and then invert Eq. 2. The stellar Lyα luminosity is needed for the Linsky et al. method, but that luminosity is not available for the stars of Pizzolato. However, a close correlation between the X-ray and Lyα luminosities exists for main-sequence stars (Linsky et al. 2013),

$$\log L_{\mathrm{lya}} = 19.7 + 0.322 \log L_X . \qquad (5)$$

The equation is a linear fit to the K5 to F5 stars in the sample from Linsky et al. (2013). We can now use Eq. 5 to derive the Lyα luminosity, which is in turn utilized to compute the EUV flux. This method results in a second X-ray based estimate, and is valid for K5 to F5 stars. Among our sample, WASP-80, WASP-43, and especially GJ 436 have a later spectral types resulting in a larger uncertainty of the derived EUV luminosity.

Figure 5 shows the three estimates for the EUV luminosities of the Pizzolato et al. (2003) sample versus the X-ray luminosities. The rotation based estimates show the expected scatter, which reflects the accuracy of the correlation between X-ray emission and rotation period. For a better visualization, we show a linear fit to the rotation based estimates, leaving out stars with periods shorter than 1 d because they are in the saturated regime. Each method results in significantly different EUV luminosities. The best agreement occurs for inactive stars ($\log L_X = 27.2$), where the three correlations agree within a factor of 2.5, but for highly active stars the estimate of Sanz-Forcada et al. is about one order of magnitude higher than both other relations. The different results of the three approaches give an idea of the uncertainty in deriving stellar fluxes in this spectral range. The uncertainty is larger than the long-term variability expected for solar type stars. For example, in the Sun the chromospheric emission changes by up to 120% over one solar cycle (Woods et al. 2005), which is a factor of two smaller than the best agreement between the EUV estimates.

For the following mass loss analysis we use the relation from Linsky et al. (2014) to derive the EUV luminosity of the host stars in our sample (see Table 4). The relation is based on a detailed analysis of the EUV fluxes in eight spectral bands, and we consider the combination of observations and chromospheric models, validated on the basis of solar spectra, to be the best currently available option.

4.2. Improved Lyα flux estimates and interstellar absorption

Using Eq. 5, we derive improved estimates for the Lyα luminosities of our targets. The mean dispersion of this equation is a factor of two smaller than our initial estimates for the Lyα luminosities based on the spectral type and the stellar rotation period (see Sect. 2). We provide the new estimates in Table 4 along with the expected unabsorbed stellar flux at Earth. These values can be directly compared with the unabsorbed flux of HD 209458 ($F_{Ly\alpha} = 15 \times 10^{-14}$ erg cm^{-2} s^{-1}, Wood et al. 2005), where an expanded atmosphere has been unambiguously measured. However, interstellar absorption reduces the observable emission line strength at Earth. The absorption depends on the interstellar neutral hydrogen column density, on the relative velocity of the star compared to the moving interstellar clouds, and on the shape of the Lyα line.

The structure of the interstellar medium has been determined within 15 pc around the Sun (Redfield & Linsky 2008), but our targets are found at distances > 60 pc. Therefore, we use Na I measurements of interstellar absorption of stars with similar lines of sight as our targets to estimate the neutral hydrogen column density. From Table 1 of Welsh et al. (2010), with Na I absorption measurements along 1857 lines of sight, we select stars within 8° angular distance of our targets resulting in three lines of sight for WASP-80, for example, and up to 16 lines of sight for HAT-P-2. The column densities are scaled linearly from the distances of the stars of Welsh et al. to the distance of our targets and then converted into a hydrogen column density (Ferlet et al. 1985).

To evaluate the absorption, we constructed a mean Lyα line profile using a double Gaussian combining a narrow (130 km s^{-1}) and a broad (400 km s^{-1}) emission line component, which typically describes the line profile well (France et al. 2013). The line flux is normalized to the values derived from Eq. 1, with the broad component containing 15% of the flux. For main-sequence stars, the Lyα line profiles often show a double-peaked structure (Wood et al. 2005), which increases the detectable line flux compared to our estimates. The line width of stars also varies, imposing further uncertainty on the estimates (broader lines are less absorbed). The standard Lyα absorption cross section with a Voigt-profile is used for the absorption with a Doppler-width of 10 km s^{-1}. Deuterium absorption is included according to a Deuterium fraction in the Local Bubble of 1.56×10^{-5} (Wood et al. 2004). The relative velocity of the absorber is neglected because Welsh et al. (2010) did not publish the kinematics of the interstellar medium. This introduces an uncertainty of a few 10%, with absorbed fluxes up to 40% higher for relative velocities of up to ±50 km s^{-1}.

The absorbed line flux is computed for the minimum and maximum hydrogen column densities scaled from the surrounding measured lines of sight (see Table 4). With this procedure we take into account the uncertainty in the derived column densities due to inhomogeneous interstellar absorption, which is about an order of magnitude for most targets. For comparison, Table 4 also contains the measured line fluxes of the four stars with detected absorbtion signals. The limiting flux for the Space Telescope Imaging Spectrograph on board the Hubble Space Telescope is about 2.5×10^{-15} erg cm^{-2} s^{-1} (upper limit derived for GJ 1214, France et al. 2013). For most targets the estimates remain inconclusive. However, the derived line fluxes for WASP-38 and WASP-18 are too low for a detection because of the inactive state of the stars; these systems are thus not well suited for Lyα transit spectroscopy. Despite the large uncertainty in the absorbed Lyα flux of WASP-80, this is the closest target among

the sample and one of the most promising systems for follow-up campaigns.

4.3. Mass loss analysis

With the computed EUV fluxes, we can now determine the mass loss rates from the total radiative flux $F_{XUV} = F_X + F_{EUV}$, which impinges on the atmospheres (Erkaev et al. 2007; Sanz-Forcada et al. 2011)

$$\dot{M} = \frac{3\,\eta F_{XUV}}{4\,KG\,\rho_{pl}}\,. \tag{6}$$

Here, ρ_{pl} is the planetary density and G denotes the gravitational constant. We adopt a heating efficiency of $\eta = 0.15$, which accounts for the fraction of the radiative energy needed for ionization processes or lost through radiative cooling. This choice agrees with recent results from Shematovich et al. (2014), who find $\eta < 0.20$ in the atmosphere of HD 209458 b. Furthermore, it enables a direct comparison with the mass loss rates determined by Ehrenreich & Désert (2011), who utilized the stellar rotation based method from Lecavelier des Etangs (2007) to estimate the EUV fluxes (see Sect. 4). The parameter K is a reduction factor for the gravitational potential of the planet due to tidal forces (Erkaev et al. 2007). It is given by

$$K(\xi) = 1 - \frac{3}{2\xi} + \frac{1}{2\xi^3}\,, \tag{7}$$

with $\xi = r_{RL}/r_{pl} \approx (\delta/3)^{1/3}\lambda$, where $\delta = M_{pl}/M_{st}$ is planet to star mass ratio, and $\lambda = a/r_{pl}$ the ratio of the semimajor axis to the planetary radius. All results are summarized in Table 4.

The X-ray based mass loss rates of our targets are on average higher than the rotation based estimates from Ehrenreich & Désert, which corresponds to the expected offset due to the different methods of deriving the EUV irradiation. However, based on our measured irradiation levels, we find the mass loss rate of WASP-38 to be more than a factor of two lower and the value of WASP-8 a factor of four higher than the previous estimates. The mass loss rate of WASP-18 is even one order of magnitude lower than the stellar rotation based estimate.

We caution that these estimates are based on the assumption of energy-limited atmospheric escape, which in general provides an upper limit to the mass loss rate of a planet (Watson et al. 1981). Furthermore, for the heating efficiency, values ranging from 0.1 to 1.0 are used in literature (Ehrenreich & Désert 2011), although the recent study of Shematovich et al. (2014) for HD 209458 b somewhat restricts this unconfined parameter. This adds to a considerable source of uncertainty in the derivation of the high-energy irradiation (see Sect. 4). Hence, the mass loss rates must be viewed as order of magnitude estimates, but are more reliable than previous estimates without determination of the high-energy irradiation level (e.g., Ehrenreich & Désert 2011).

The current fractional mass loss of all planets in the sample is small. The close proximity and the small planetary masses of WASP-77, WASP-43, and WASP-80 result in the strongest mass loss rates on a par with the mass loss rate of HD 189733 b. WASP-80 loses 0.10% of its mass in 1 Ga, assuming constant stellar emission. Moreover, high-energy emission is up to a factor of 100 stronger in young stars (age < 100 Ma) (Ribas et al. 2005; Stelzer & Neuhäuser 2001). Assuming this high irradiation level for the first 100 Ma, the planet would have lost additional 0.28% of its mass. For our targets, we derive the total mass loss estimate by combining this value and applying the present

Table 5. Age estimates for the binary systems within our sample

System		Sp.T	Sep. (″)	log L_X (erg s^{-1})	A_{iso} (Ga)	A_{gyro} (Ga)	A_X (Ga)	h_{tide}/H_P
WASP-77	A	G8V	3.3	28.1	5.3	1.7	4.5	0.12
	B	K5V		< 27.5			> 8.9	
HAT-P-20	A	K3V	6.9	28.0	7	0.8	1.9	0.066
	B	M		< 27.4			> 1.7	
WASP-8	A	G8V	4.8	28.4	< 3.6	1.6	1.6	0.002
	B	M		< 27.6			> 1.5	

Notes. Columns are: system name and component, spectral type, separation of the components, X-ray luminosity, isochrone age Brown (2014); Bakos et al. (2011), gyrochronological age, age estimate based on the X-ray luminosity (Poppenhaeger & Wolk 2014), and height of the tidal bulge in reference to the photospheric scale height.

mass loss rate for the remaining lifetime (for the age estimates see Sect. 5). According to these values, six hot Jupiters have lost less than 0.01% of their masses through photoevaporation (see Table 4). Even if we conservatively assume an uncertainty as large as a factor 100 for the total mass loss estimates, these six planets cannot have lost more than 1% of their mass because of photoevaporation during their lifetime.

A final remark concerning photoevaporation: HAT-P-2 is the strongest X-ray source among our targets, but the mass loss rate is small because the planet is massive and has a comparatively large semimajor axis. Also the predicted mass loss rates of HAT-P-20 b and WASP-18 b are very small. These planets exhibit the highest densities in our sample. In general the formation of a hydrodynamic wind from such compact and massive objects is disputable. Hydrodynamic escape is only possible if the sonic point in the escape flow occurs before the exobase level is reached, otherwise radiative energy cannot be transformed into a bulk flow and only Jeans escape proceeds with a significantly lower mass loss rate (e.g., Tian et al. 2005). The compactness of HAT-P-2 b, HAT-P-20 b, and WASP-18 b may completely prevent the formation of a planetary wind.

5. Angular momentum transfer from hot Jupiters to their host stars

Giant gas planets in tight orbits raise substantial tidal bulges on their host stars (Cuntz et al. 2000). If the stellar rotation period is longer than the orbital period of the planet, it is possible that the tidal interaction induces a torque on the host star and reduces the stellar spin-down with age (Poppenhaeger & Wolk 2014). Based on measured X-ray luminosities Poppenhaeger & Wolk predict stellar ages of binaries, where the primary features a hot Jupiter in a close orbit. Binaries have the advantage of providing two individual age estimates for the system, and a younger age of the primary would indicate continuous angular momentum transfer from the hot Jupiter's orbital motion. Indeed, the two host stars with the strongest tidal interactions (HD 189733, CoRoT-2) in the study of Poppenhaeger & Wolk, suggest a significantly younger age of the hot Jupiter host compared with the secondary. In contrast three systems with smaller tidal interactions do not exhibit age differences.

The angular momentum transfer was also studied by Brown (2014), who analyzes the gyrochronological and isochrone ages of exoplanet hosts. Reduced spin-down of the host stars due to tidal interactions would appear as young gyrochronological ages

compared with the isochrone ages in hot Jupiter bearing systems. Brown found indications for a general age difference of 1.8 Ga between gyrochronological and isochrone age estimates, but no correlation with tidal interactions. However, the author does not exclude effects in individual systems. We use the mean of the three color based rotation-age relations from Brown (2014)[7] to derive gyrochronological age estimates for our targets (see Table 1).

For the three binaries among our targets we derive X-ray based age estimates, using the relationship from Poppenhaeger & Wolk (2014) . The upper limits for the X-ray luminosity of the secondaries provide lower limits for their ages. The strength of the tidal interactions can be assessed by the fractional height of the tidal bulges in reference to the photospheric pressure scale height h_{tide}/H_p (Cuntz et al. 2000). In addition, we provide the isochrone ages of the three targets from literature in Table 5.

For WASP-77 A, we derive an X-ray age of about 5 Ga and the B component should be older than 9 Ga. For HAT-P-20 A and B as well as for WASP-8 A and B, we derive ages of about 2 Ga with only slight differences, but the upper limits indicate that the B components seem to be about twice the age of the primaries. In contrast to WASP-8, WASP-77, and HAT-P-20 exhibit low X-ray luminosities compared with the rotation-based estimates. Their gyrochronological age estimates are consistently smaller than the X-ray based ages. The hot Jupiter WASP-77 b raises the highest relative tidal bulge on its host star, and this is the only system with an apparent age difference between the host star and the companion. The isochrone age of this system is consistent with the X-ray age of the secondary, which further supports an age difference between the two stellar companions. The age difference also exceeds the general offset of the isochrone age estimates of 1.8 Ga found by Brown. The same argument holds for HAT-P-20, but here the upper limit for the X-ray luminosity of the secondary does not reveal a significant age difference. There is no difference in the four age estimates of WASP-8, which exhibits the weakest tidal interactions. At this point the data do not provide strong evidence for a transfer of angular momentum from the hot Jupiters to the host stars.

6. Conclusion

We measured the X-ray luminosities of seven hot Jupiter hosts and determined the level of high-energy irradiation and the planetary mass loss rates. Additionally, the two previously analyzed targets and four systems with detected atmospheres are included in our discussion. According to our estimates, six of the eleven planets did not lose more than 1% of their mass as the result of a hydrodynamic planetary wind during their lifetime. In our sample, WASP-80 b, WASP-77 b, and WASP-43 b experience the strongest mass loss rates. Our improved Lyα flux estimates reveal that in seven of the nine systems expanded atmospheres could be detectable through Lyα transit spectroscopy by stacking a small number of transit observations. While WASP-80 b, WASP-77 b, and WASP-43 b are good targets because of their strong predicted mass loss rates, WASP-8 b is an interesting case because its higher mean density could locate the planet close to the transition from a strong photoevaporative wind to a stable atmosphere. We find only weak indications for an angular momentum transfer from the orbiting hot Jupiters to the host stars in the two binary systems with expected strong tidal interactions.

---

[7] For the two F-type stars we use the original relation from Barnes (2007) for the age relation based on $(B - V)$.

We conclude that currently the systems WASP-80, WASP-43, and WASP-77 represent the most promising candidates to search for absorption signals of the expanded atmospheres of hot Jupiters.

References

Arnaud, K. A. 1996, in Astronomical Society of the Pacific Conference Series, Vol. 101, Astronomical Data Analysis Software and Systems V, ed. G. H. Jacoby & J. Barnes, 17
Bakos, G. Á., Hartman, J., Torres, G., et al. 2011, ApJ, 742, 116
Bakos, G. Á., Kovács, G., Torres, G., et al. 2007, ApJ, 670, 826
Ballester, G. E., Sing, D. K., & Herbert, F. 2007, Nature, 445, 511
Barnes, S. A. 2007, ApJ, 669, 1167
Barros, S. C. C., Faedi, F., Collier Cameron, A., et al. 2011, A&A, 525, A54
Ben-Jaffel, L. & Ballester, G. E. 2013, A&A, 553, A52
Bouchy, F., Udry, S., Mayor, M., et al. 2005, A&A, 444, L15
Bourrier, V. & Lecavelier des Etangs, A. 2013, A&A, 557, A124
Brown, D. J. A. 2014, MNRAS, 442, 1844
Brown, D. J. A., Collier Cameron, A., Díaz, R. F., et al. 2012, ApJ, 760, 139
Butler, R. P., Marcy, G. W., Williams, E., Hauser, H., & Shirts, P. 1997, ApJ, 474, L115
Butler, R. P., Vogt, S. S., Marcy, G. W., et al. 2004, ApJ, 617, 580
Carter, J. A., Agol, E., Chaplin, W. J., et al. 2012, Science, 337, 556
Cash, W. 1979, ApJ, 228, 939
Charbonneau, D., Brown, T. M., Latham, D. W., & Mayor, M. 2000, ApJ, 529, L45
Christian, D. J., Gibson, N. P., Simpson, E. K., et al. 2009, MNRAS, 392, 1585
Cubillos, P., Harrington, J., Madhusudhan, N., et al. 2012, in AAS/Division for Planetary Sciences Meeting Abstracts, Vol. 44, AAS/Division for Planetary Sciences Meeting Abstracts, 103.08
Cuntz, M., Saar, S. H., & Musielak, Z. E. 2000, ApJ, 533, L151
Czesla, S., Salz, M., Schneider, P. C., & Schmitt, J. H. M. M. 2013, A&A, 560, A17
Ehrenreich, D., Bourrier, V., Bonfils, X., et al. 2012, A&A, 547, A18
Ehrenreich, D. & Désert, J.-M. 2011, A&A, 529, A136+
Ehrenreich, D., Lecavelier des Etangs, A., Hébrard, G., et al. 2008, A&A, 483, 933
Ekenbäck, A., Holmström, M., Wurz, P., et al. 2010, ApJ, 709, 670
Erkaev, N. V., Kulikov, Y. N., Lammer, H., et al. 2007, A&A, 472, 329
Ferlet, R., Vidal-Madjar, A., & Gry, C. 1985, ApJ, 298, 838
Fischer, D. A., Marcy, G. W., Butler, R. P., et al. 2008, ApJ, 675, 790
Fontenla, J. M., Landi, E., Snow, M., & Woods, T. 2014, Sol. Phys., 289, 515
Fossati, L., Haswell, C. A., Froning, C. S., et al. 2010, ApJ, 714, L222
Foster, A. R., Ji, L., Smith, R. K., & Brickhouse, N. S. 2012, The Astrophysical Journal, 756, 128
France, K., Froning, C. S., Linsky, J. L., et al. 2013, ApJ, 763, 149
Fruscione, A., McDowell, J. C., Allen, G. E., et al. 2006, in Society of Photo-Optical Instrumentation Engineers (SPIE) Conference Series, Vol. 6270, Society of Photo-Optical Instrumentation Engineers (SPIE) Conference Series
Gray, R. O., Corbally, C. J., Garrison, R. F., McFadden, M. T., & Robinson, P. E. 2003, AJ, 126, 2048
Grevesse, N. & Sauval, A. J. 1998, Space Sci. Rev., 85, 161
Hebb, L., Collier-Cameron, A., Loeillet, B., et al. 2009, ApJ, 693, 1920
Hellier, C., Anderson, D. R., Collier Cameron, A., et al. 2009, Nature, 460, 1098
Hellier, C., Anderson, D. R., Collier Cameron, A., et al. 2011, A&A, 535, L7
Henry, G. W., Marcy, G. W., Butler, R. P., & Vogt, S. S. 2000, ApJ, 529, L41
Henry, G. W. & Winn, J. N. 2008, AJ, 135, 68
Holmström, M., Ekenbäck, A., Selsis, F., et al. 2008, Nature, 451, 970
James, D. J., Jardine, M. M., Jeffries, R. D., et al. 2000, MNRAS, 318, 1217

Jensen, A. G., Redfield, S., Endl, M., et al. 2012, ApJ, 751, 86
Johnson, J. A., Winn, J. N., Cabrera, N. E., & Carter, J. A. 2009, ApJ, 692, L100
Knutson, H. A., Madhusudhan, N., Cowan, N. B., et al. 2011, ApJ, 735, 27
Koskinen, T. T., Harris, M. J., Yelle, R. V., & Lavvas, P. 2013a, Icarus, 226, 1678
Koskinen, T. T., Yelle, R. V., Harris, M. J., & Lavvas, P. 2013b, Icarus, 226, 1695
Kulow, J. R., France, K., Linsky, J., & Loyd, R. O. P. 2014, ApJ, 786, 132
Lacy, C. H. 1977, ApJS, 34, 479
Lanotte, A. A., Gillon, M., Demory, B.-O., et al. 2014, A&A, 572, A73
Lecavelier des Etangs, A. 2007, A&A, 461, 1185
Lecavelier des Etangs, A., Bourrier, V., Wheatley, P. J., et al. 2012, A&A, 543, L4
Lecavelier des Etangs, A., Ehrenreich, D., Vidal-Madjar, A., et al. 2010, A&A, 514, A72+
Lecavelier Des Etangs, A., Sirothia, S. K., Gopal-Krishna, & Zarka, P. 2011, A&A, 533, A50
Linsky, J. L., Fontenla, J., & France, K. 2014, ApJ, 780, 61
Linsky, J. L., France, K., & Ayres, T. 2013, ApJ, 766, 69
Linsky, J. L., Yang, H., France, K., et al. 2010, ApJ, 717, 1291
Marcy, G. W., Isaacson, H., Howard, A. W., et al. 2014, ApJS, 210, 20
Maxted, P. F. L., Anderson, D. R., Collier Cameron, A., et al. 2013, PASP, 125, 48
McArthur, B. E., Endl, M., Cochran, W. D., et al. 2004, ApJ, 614, L81
Mittag, M., Schmitt, J. H. M. M., & Schröder, K.-P. 2013, A&A, 549, A117
Noyes, R. W., Hartmann, L. W., Baliunas, S. L., Duncan, D. K., & Vaughan, A. H. 1984, ApJ, 279, 763
Pál, A., Bakos, G. Á., Torres, G., et al. 2010, MNRAS, 401, 2665
Parker, E. N. 1958, ApJ, 128, 664
Pillitteri, I., Wolk, S. J., Cohen, O., et al. 2010, ApJ, 722, 1216
Pillitteri, I., Wolk, S. J., Sciortino, S., & Antoci, V. 2014, A&A, 567, A128
Pizzolato, N., Maggio, A., Micela, G., Sciortino, S., & Ventura, P. 2003, A&A, 397, 147
Poppenhaeger, K., Schmitt, J. H. M. M., & Wolk, S. J. 2013, ApJ, 773, 62
Poppenhaeger, K. & Wolk, S. J. 2014, A&A, 565, L1
Queloz, D., Anderson, D. R., Collier Cameron, A., et al. 2010, A&A, 517, L1
Redfield, S. & Linsky, J. L. 2000, ApJ, 534, 825
Redfield, S. & Linsky, J. L. 2008, ApJ, 673, 283
Ribas, I., Guinan, E. F., Güdel, M., & Audard, M. 2005, ApJ, 622, 680
Rutten, R. G. M. 1984, A&A, 130, 353
Sanz-Forcada, J., Micela, G., Ribas, I., et al. 2011, A&A, 532, A6+
Schmitt, J. H. M. M., Schröder, K.-P., Rauw, G., et al. 2014, Astronomische Nachrichten, 335, 787
Schröter, S., Czesla, S., Wolter, U., et al. 2011, A&A, 532, A3+
Shematovich, V. I., Ionov, D. E., & Lammer, H. 2014, A&A, 571, A94
Silva-Valio, A. 2008, ApJ, 683, L179
Sirothia, S. K., Lecavelier des Etangs, A., Gopal-Krishna, Kantharia, N. G., & Ishwar-Chandra, C. H. 2014, A&A, 562, A108
Skrutskie, M. F., Cutri, R. M., Stiening, R., et al. 2006, AJ, 131, 1163
Smith, A. M. S., Hebb, L., Collier Cameron, A., et al. 2009, MNRAS, 398, 1827
Southworth, J. 2010, MNRAS, 408, 1689
Stelzer, B. & Neuhäuser, R. 2001, A&A, 377, 538
Tian, F., Toon, O. B., Pavlov, A. A., & De Sterck, H. 2005, ApJ, 621, 1049
Torres, G., Winn, J. N., & Holman, M. J. 2008, ApJ, 677, 1324
Trammell, G. B., Arras, P., & Li, Z.-Y. 2011, ApJ, 728, 152
Triaud, A. H. M. J., Anderson, D. R., Collier Cameron, A., et al. 2013, A&A, 551, A80
van Leeuwen, F., ed. 2007, Astrophysics and Space Science Library, Vol. 350, Hipparcos, the New Reduction of the Raw Data
Vidal-Madjar, A., Désert, J.-M., Lecavelier des Etangs, A., et al. 2004, ApJ, 604, L69
Vidal-Madjar, A., Huitson, C. M., Bourrier, V., et al. 2013, A&A, 560, A54
Vidal-Madjar, A., Lecavelier des Etangs, A., Désert, J.-M., et al. 2003, Nature, 422, 143
Watson, A. J., Donahue, T. M., & Walker, J. C. G. 1981, Icarus, 48, 150
Welsh, B. Y., Lallement, R., Vergely, J.-L., & Raimond, S. 2010, A&A, 510, A54
Wilson, O. C. 1978, ApJ, 226, 379
Wood, B. E., Brown, A., Linsky, J. L., et al. 1994, ApJS, 93, 287
Wood, B. E., Linsky, J. L., Hébrard, G., et al. 2004, ApJ, 609, 838
Wood, B. E., Redfield, S., Linsky, J. L., Müller, H.-R., & Zank, G. P. 2005, ApJS, 159, 118
Woods, T. N., Eparvier, F. G., Bailey, S. M., et al. 2005, Journal of Geophysical Research (Space Physics), 110, 1312
Wright, J. T., Fakhouri, O., Marcy, G. W., et al. 2011, PASP, 123, 412
Zacharias, N., Finch, C. T., Girard, T. M., et al. 2013, AJ, 145, 44
Zechmeister, M. & Kürster, M. 2009, A&A, 496, 577

Escaping atmospheres of hot gas planets in the solar neighborhood

Simulations of the hydrodynamic winds and predictions of the Lyα absorption signals

M. Salz[1], S. Czesla[1], P. C. Schneider[2,1], J. H. M. M. Schmitt[1]

[1] Hamburger Sternwarte, Universität Hamburg, Gojenbergsweg 112, 21029 Hamburg, Germany
e-mail: msalz@hs.uni-hamburg.de
[2] European Space Research and Technology Centre (ESA/ESTEC), Keplerlaan 1, 2201 AZ Noordwijk, The Netherlands

Submitted 16 March 2015

ABSTRACT

Absorption of high-energy irradiation in planetary thermospheres leads to the formation of planetary winds. In small gas planets the mass-loss rate resulting from strong winds can affect the evolution of the entire planet. We present 1D, spherically symmetric hydrodynamic simulations of the escaping atmospheres of 18 hot gas planets in the solar neighborhood to study the thermospheric escape and derive improved estimates of their mass-loss rates. Our sample includes only strongly irradiated planets, whose expanded atmospheres may be detectable via transit spectroscopy using current instrumentation. The simulations are performed with "the PLUTO-CLOUDY Interface", which couples a detailed photoionization solver with a general MHD code. We find that the tightly bound thermospheres of massive and compact planets such as HAT-P-2 b are hydrodynamically stable. Compact planets dispose of the radiative energy input through hydrogen line and free-free emission. Radiative cooling is still important in HD 189733 b, but it is small in planets with a low gravitational potential like GJ 436 b. Finally, we use our spherically symmetric atmospheres to estimate the expected Lyα absorption signals. Our simulations reproduce the observed trend of the Lyα absorption depth in the systems HD 209458 b, HD 189733 b, and GJ 436 b, and they are also consistent with the non-detection of the atmosphere of 55 Cnc e. According to our results, WASP-80 and GJ 3470 are currently the most prominent targets for observational follow-up.

Key words. methods: numerical – hydrodynamics – radiation mechanisms: non-thermal – planets and satellites: atmospheres – planets and satellites: dynamical evolution and stability

1. Introduction

Gas giants are ubiquitous among the known extrasolar planets, because they produce rather large transit signals that can be easily detected. Today, hot gas planets with semimajor axes smaller than 0.1 AU constitute more than 15 % of all verified planets (e.g., exoplanets.org, Wright et al. 2011). Such hot planets have been found as close as two stellar radii above the photosphere of their host stars (Hebb et al. 2009) and some of them also orbit highly active host stars in close proximity (Alonso et al. 2008; Schröter et al. 2011). This places their high-energy irradiation level as much as 10^5 times higher than the irradiation of Earth. The detection of gas planets in such extreme environments immediately raises questions about the stability of their atmospheres, about possible evaporation, and about the resulting lifetime of these planets (e.g., Schneider et al. 1998; Lammer et al. 2003).

In the case of close-in planets, the absorption of high-energy radiation causes temperatures of several thousand degrees in the planetary thermosphere[1] (e.g., Schneider et al. 1998); even at 1 AU the thermosphere of Earth is heated to up to 2000 K (e.g., Banks & Kockarts 1973). Under these conditions the upper atmospheric layers are likely unstable and expand continuously,

unless there is a confining outer pressure (Watson et al. 1981; Chassefière 1996). The formation of such a hydrodynamic planetary wind is similar to the early solar wind models by Parker (1958), with the major difference that the energy source for the wind is the external irradiation. Watson et al. (1981) also showed that under certain circumstances irradiated atmospheres undergo a more or less energy-limited escape, which simply means that the radiative energy input is completely used to drive the planetary wind. Naturally one has to account for the fact that the heating efficiency of the absorption is less than unity.

In the case of energy-limited escape the mass-loss rate is proportional to the XUV flux[2] impinging on the atmosphere and inversely proportional to the planetary density (Sanz-Forcada et al. 2011). Since the mass-loss rate depends only on the planetary density but not on its mass, small planets with low densities are more strongly affected by the fractional mass-loss rate. While for most detected hot gas planets the predicted mass-loss rates do not result in the loss of large fractions of their total mass over their lifetime (Ehrenreich et al. 2012), a complete evaporation of volatile elements is possible for smaller gas planets. Indeed this might be the reason for the possible lack of detected hot mini-Neptunes (Carter et al. 2012).

---

[1] Hot atmospheric layers of a planet where (extreme) ultraviolet radiation is absorbed.

[2] XUV stands for X-ray ($\lambda < 100$ Å) plus extreme ultraviolet radiation (EUV, $100 < \lambda < 912$ Å).

The existence of expanded thermospheres in hot gas planets was first confirmed in the exoplanet HD 209458 b, where Vidal-Madjar et al. (2003) found absorption of up to 15% in the line wings of the stellar hydrogen Lyα line during the transit of the hot Jupiter. Since the optical transit depth in this system is only 1.5% (Henry et al. 2000; Charbonneau et al. 2000), the excess absorption is most likely caused by a neutral hydrogen cloud around the planet. As Vidal-Madjar et al. also noted, the variability of solar-like stars is not sufficient to mimic this absorption signal. Although the Lyα emission of the Sun is strongly inhomogeneously distributed over the solar disk (e.g., see images from The Multi-Spectral Solar Telescope Array, MSSTA), this is only true for the line core, which is produced at temperatures of around 20 000 K in the solar chromosphere (Vernazza et al. 1973). The line wings originate much more deeply within the chromosphere at around 6000 to 7000 K. Emission at these temperatures is more homogeneously distributed over the solar disk, as seen for example by images in Hα or Ca ɪɪ K filters – lines that are produced at similar temperatures in the chromosphere. In analogy to the Sun, it is reasonable to assume that for solar-like stars the variability in the calcium line cores is also indicative of the variability in the wings of the Lyα line, where the planetary absorption is detected.

The variability of stars in the Ca ɪɪ H&K emission lines has been studied in detail for many stars (e.g. Vaughan et al. 1981). In particular, the inactive star HD 209458 shows a fractional standard deviation of only 1.0% over several years compared to the solar variation of 14.4% (Hall et al. 2007), and the short term variability is on the same order (using data from the California Planet Search program, Isaacson & Fischer 2010). For this star the variability in the Lyα line wings has been studied directly by Ben-Jaffel (2007), who found a variability of about 1% (with an uncertainty of 3%) in the three out-of-transit time bins. Compared to the Lyα absorption signal this is small, therefore, variability or spatial inhomogeneity of the stellar emission is unlikely to be the dominating source of the absorption signal seen during the planetary transit.

In the case of HD 209458 b the confidence in the detection of an expanded atmosphere was further increased by several transit observations, which revealed excess absorption in spectral lines of H ɪ, O ɪ, C ɪɪ, Si ɪɪɪ, and Mg ɪ (Vidal-Madjar et al. 2004; Ballester et al. 2007; Ehrenreich et al. 2008; Linsky et al. 2010; Jensen et al. 2012; Vidal-Madjar et al. 2013), although the detection of silicon was recently questioned (Ballester & Ben-Jaffel 2015). Today, only two additional systems exists with a comparable coverage of observations. In the more active host star HD 189733 excess absorption was detected in H ɪ, O ɪ, and possibly in C ɪɪ (Lecavelier des Etangs et al. 2010, 2012; Jensen et al. 2012; Ben-Jaffel & Ballester 2013) during the transit of the hot Jupiter. The superposition of several X-ray observations also shows an excess transit depth in this system (Poppenhaeger et al. 2013). In WASP-12 three observations confirmed the existence of an expanded atmosphere (Fossati et al. 2010; Haswell et al. 2012; Nichols et al. 2015). In addition, tentative detections of excess absorption were obtained in 55 Cancri and GJ 436 (Ehrenreich et al. 2012; Kulow et al. 2014).

2. Approach

2.1. Outline

Although observations show that an expanded atmosphere exists in at least the three planets HD 209458 b, HD 189733 b, and WASP-12 b, there is no generally accepted theory for the ob-

served absorption signals. The planetary atmospheres are affected by photoevaporation, by interactions with the stellar wind, by radiation pressure, and by planetary magnetic fields. All four processes also affect the absorption signals, for example, the observed signal of HD 209458 b has been explained by at least four different models (Koskinen et al. 2013b; Bourrier & Lecavelier des Etangs 2013; Ekenbäck et al. 2010; Trammell et al. 2014). In our view, one of the most promising ways to disentangle the different influences is to observe the planetary atmospheres in different systems with a wide parameter range (Fossati et al. 2015). Since all the processes depend on different parameters (e.g., Lyα emission line strength, stellar wind density and velocity, magnetic field strength) the comparison of absorption signals from different systems can reveal the dominating processes in the atmospheres.

In this context, we identified the most promising targets in the search for yet undetected expanded atmospheres. Here, we present coupled radiative-hydrodynamical simulations of the planetary winds in 18 of these systems. Our simulations were performed with "the PLUTO-CLOUDY Interface" (Salz et al. 2015a). In contrast to simple energy-limited estimates, our simulations identify the best targets for future transit observations with high certainty. The spherically symmetric simulations are comparable to the wind simulations in previous studies (e.g., Yelle 2004; Tian et al. 2005; García Muñoz 2007; Penz et al. 2008; Murray-Clay et al. 2009; Koskinen et al. 2013a), but for the first time we applied them to possible future targets. Furthermore, our use of a detailed microphysics solver is the most important improvement compared to previous simulations. Additionally, we used a detailed reconstruction of the planetary irradiation level in four spectral ranges for our simulations.

We first introduce our code and verify our assumptions (Sect. 3) and then compare the results for the different systems, explaining in detail the atmospheric structures (Sect. 4). We explain the transition from strong planetary winds in small planets to hydrodynamically stable thermospheres of compact, massive planets. Finally, we compute the Lyα absorption signals of the simulated atmospheres, which are used to identify the best targets for future transit spectroscopy campaigns (Sect. 5). It is important to note that this result remains unchanged, if the simulated spherical winds are not truly responsible for the measured absorption signals in Lyα line wings. This is because our simulations provide the amount of neutral hydrogen in the upper atmospheres, and despite the different theoretical interpretations of the absorption signals, the total measured Lyα absorption depth most strongly depends on the amount of neutral hydrogen in the expanded thermosphere. Thus, the strength of the absorption can be predicted, even if for example the interaction with the stellar wind shifts the absorption signal further into the Lyα line wings.

In principle, this interpretation can be misleading if the atmospheres are stabilized by some outer pressure. In particular, the stellar wind pressure could confine a planetary wind completely in the vicinity of the substellar point, because the ram pressure of the stellar wind can be large enough to suppress the formation of a planetary wind (Murray-Clay et al. 2009). However, closer to the terminator, hydrodynamic escape would still be ongoing, because the projected force of the stellar wind pressure in this direction is small. Also a strong planetary magnetic field can confine an atmosphere over fractions of the planetary surface, but open field lines will always exist, along which the escape flow can proceed unconfined (Trammell et al. 2014). Thus, a hydrodynamic wind as presented here, will certainly appear at least over fractions of the planetary surface. Trammell et al. argue that magnetically stabilized atmospheric regions cause sig-

nificant absorption in their simulations, but they neglect advection of neutral hydrogen and adiabatic cooling in their isothermal simulations. The high temperature and the high degree of ionization in static parts of an atmosphere (Watson et al. 1981) reduces the impact on the absorption signal. Therefore, we argue that the neutral hydrogen that is transported by the planetary wind into the upper atmosphere is also the main source for the measured Lyα absorption signals.

2.2. Target selection

Our target selection has been described in Salz et al. (2015b). Basically, we select targets, where expanded atmospheres can be detected by Lyα transit spectroscopy. We predict the Lyα luminosity of all host stars based on their X-ray luminosity, and if not available, based on spectral type and stellar rotation period using the relations presented by Linsky et al. (2013). We further select only transiting systems with an orbital separation < 0.1 AU to ensure high levels of irradiation. Note that this is not necessarily a boundary for hydrodynamic escape. Earth-sized planets can harbor escaping atmospheres at even smaller irradiation levels, because their atmospheres are relatively weakly bound as a result of the small planetary mass; this was already studied by Watson et al. (1981) for Earth and Venus. While we selected only planets with a transit depth > 0.5% in Salz et al. (2015b), we drop this criterion here, because recent observations indicate that also small planets can produce large absorption signals (Kulow et al. 2014). This extends our sample further toward planets with smaller masses and increases the phase space of system parameters.

Finally we limit the sample by selecting only planets with a Lyα flux stronger than 1/5 of the reconstructed flux of HD 209458 b. Considering the remaining uncertainties of the scaling relations and of the predicted interstellar absorption, these targets are potentially bright enough for transit spectroscopy.

In total we find 18 suitable targets (see Table 1), all located within 120 AU, since the stellar distance has a strong impact on the detectability. This probably places the targets within the Local Bubble of hot ionized interstellar material (Redfield & Linsky 2008), limiting the uncertainty introduced by interstellar absorption. As expected, systems with detected absorption signals (HD 189733, HD 209458, GJ 436) also lead the ranking according to our estimates. 55 Cnc e is also among the top targets, but for this planet an expanded atmosphere was not detected (Ehrenreich et al. 2012). We add three further targets to the list, which do not strictly fulfill our selection criteria: WASP-12 is too distant for Lyα transit spectroscopy, but excess absorption was measured in metal lines (Fossati et al. 2010). The distance of CoRoT-2 is too large, but the host star is extremely active (Schröter et al. 2011), which makes the system interesting. 55 Cnc b does not transit its host star, but a grazing transit of an expanded atmosphere has been proposed (Ehrenreich et al. 2012).

This finally leaves us with 21 planets in 20 systems. We present simulations for 18 of these targets. We did not simulate the atmospheres of WASP-38 b and WASP-18 b, because they host stable thermospheres (see Sect. 4.6). 55 Cnc b was not simulated, because the radius is unknown in this non-transiting planet; the radius is an important input parameter for our simulations.

2.3. Reconstruction of the XUV flux and the SED

One of the main input parameters for our simulations is the irradiation strength and the spectral energy distribution (SED) of the host stars. Therefore, we first explain our reconstruction of the stellar SED, before going into details about the simulations.

Clearly, the strength of a planetary wind crucially depends on the available energy, which is mostly supplied by the EUV emission of the host stars, but X-rays also contribute a large fraction of the high-energy emission of active host stars like CoRoT-2 (Schröter et al. 2011). Interstellar absorption extinguishes EUV emission even from close-by targets so that observations cannot be used to determine the irradiation level in this spectral range. The upper atmosphere, which is simulated here, is mostly translucent to FUV, NUV, and optical emission, except for line absorption as shown by the observations (see Introduction). However, the simulations presented here include only hydrogen and helium (H+He), hence, any absorption beyond the Lyα line is negligible in terms of radiative heating. In the bottom panel of Fig. 1, we anticipate the transmitted spectrum in the simulation of the atmosphere of HD 209458 b to justify this statement. The absorption from 10 to 912 Å is clearly visible as well as the transmission of the optical emission, and furthermore the complete extinction of the Lyα line.

The reconstruction of the SED must be sufficiently accurate in the spectral range up to and including the Lyα line. For this purpose, we developed a piecewise reconstruction, which is mainly based on the prediction of the EUV luminosity of late type dwarfs by Linsky et al. (2014). Note that several methods exist to predict the EUV luminosity of stars (Salz et al. 2015b). The results of these methods differ by up to one order of magnitude for active stars, which directly translates into the uncertainty of the mass-loss rates in the simulations.

The reconstruction of the SEDs is split into four spectral regions and for each range we need a spectral shape and a luminosity to assemble the full SED. The derived luminosities for each spectral range are given in Table. 3.

1. For the X-ray spectrum (0 to 100 Å) we use a 2 or 4×10^6 K plasma emission model from CHIANTI (Dere et al. 1997, 2009) for inactive or active host stars respectively (active: $L_X > 10^{28}\,\mathrm{erg\,s^{-1}}$). The SED is normalized to the observed X-ray luminosities of the host stars. Only if observations are unavailable, we use an estimate based on the stellar rotation period and the stellar mass (Pizzolato et al. 2003). The models are computed with a low resolution (bin width = 10 Å) adapted to the resolution in the EUV range. The absorption of X-rays causes ionization and line absorption is negligible in this spectral range at the given densities. Thus, the presence of emission lines is irrelevant in the X-ray regime and the low resolution is sufficient.
2. For the hydrogen Lyα emission line of the host stars a Gaussian with a FWHM of 4 Å is used. The irradiation strength is normalized according to the host star's total Lyα luminosity. Only for four host stars the luminosity has been reconstructed based on HST observations. For most of the targets the Lyα luminosity is predicted based on the X-ray luminosity following Linsky et al. (2013). The width of the Lyα line is adapted to the resolution of our photoionization solver. This essentially affects only the strength of the radiation pressure as discussed in Sect. 4.8.
3. For the EUV range (100 Å to ∼ 912 Å) the luminosity of the host stars is predicted based on the Lyα luminosity given by step 2 (Linsky et al. 2014). For most targets this procedure

Table 1. System parameters of the complete sample (see Sect. 2.2). Sorted according to the strength of the simulated mass loss.

System	Host star								Planet							
	Sp. type	$T_{\rm eff}$ (K)	V (mag)	$B-V$ (mag)	$J-K$ (mag)	d (pc)	$P_{\rm rot}$ (d)	Age (Ga)	$R_{\rm pl}$ ($R_{\rm jup}$)	$M_{\rm pl}$ ($M_{\rm jup}$)	$\rho_{\rm pl}$ (g cm^{-3})	$T_{\rm eq}$ (K)	$P_{\rm orb}$ (d)	a (AU)	e	TD (%)
WASP-12	G0V	6300	11.6	0.57	0.29	380	37.5	13.2	1.8	1.4	0.32	2900	1.1	0.023	0.05	1.4
GJ 3470	M1.5	3600	12.3	1.17	0.81	29	20.7 ± 0.2	1.2	0.37	0.044	1.1	650	3.3	0.036	0	0.57
WASP-80	K7-M0V	4150	11.9	0.94	0.87	60	8.1 ± 0.8	0.2	0.95	0.55	0.73	800	3.1	0.034	0	2.9
HD 149026	G0IV	6150	8.1	0.61	—	79	11.5	1.2	0.65	0.36	1.6	1440	2.9	0.043	0	0.29
HAT-P-11	K4V	4750	9.5	1.19	0.60	37	29.2	2.9	0.42	0.083	1.3	850	4.9	0.053	0.2	0.33
HD 209458	G0V	6065	7.6	0.58	0.28	50	11.4	1.5	1.4	0.69	0.34	1320	3.5	0.047	0	1.5
55 Cnc (e)	K0IV-V	5200	6.0	0.87	0.58	12	42.7 ± 2.5	6.7	0.19	0.026	4.2	1950	0.7	0.015	0	0.045
GJ 1214	M4.5	3050	14.7	1.73	0.97	13	44.3 ± 1.2	3.4	0.24	0.020	1.9	550	1.6	0.014	0	1.3
GJ 436	M2.5V	3350	10.6	1.47	0.83	10	56.5	6.5	0.38	0.073	1.7	650	2.6	0.029	0.2	0.70
HD 189733	K0-2V	5040	7.6	0.93	0.53	19	12.0 ± 0.1	0.7	1.1	1.1	0.96	1200	2.2	0.031	0	2.4
HD 97658	K1V	5100	7.7	0.86	0.47	21	38.5 ± 1.0	6.6	0.21	0.025	3.4	750	9.5	0.080	0.06	0.085
WASP-77	G8V	5500	10.3	0.75	0.37	93	15.4 ± 0.4	1.7	1.2	1.8	1.3	1650	1.4	0.024	0	1.7
WASP-43	K7V	4400	12.4	1.00	0.73	80	15.6 ± 0.4	0.8	0.93	1.8	2.9	1350	0.8	0.014	0	2.6
CoRoT-2	G7V	5650	12.6	0.85	0.47	270	4.5 ± 0.1	0.1	1.5	3.3	1.5	1550	1.7	0.028	0.01	2.8
WASP-8	G8V	5600	9.9	0.82	0.41	87	16.4 ± 1.0	1.6	1.0	2.2	2.6	950	8.2	0.080	0.3	1.3
WASP-10	K5V	4700	12.7	1.15	0.62	90	11.9 ± 0.9	0.6	1.1	3.2	3.1	950	3.1	0.038	0.05	2.5
HAT-P-2	F8V	6300	8.7	0.46	0.19	114	3.7 ± 0.4	0.4	1.2	8.9	7.3	1700	5.6	0.068	0.5	0.52
HAT-P-20	K3V	4600	11.3	0.99	0.67	70	14.6 ± 0.9	0.8	0.87	7.3	13.8	950	2.9	0.036	0.01	1.6
WASP-38	F8V	6200	9.4	0.48	0.29	110	7.5 ± 1.0	1.0	1.1	2.7	2.1	1250	6.9	0.076	0.03	0.69
WASP-18	F6IV-V	6400	9.3	0.44	0.28	99	5.0 ± 1.0	0.7	1.3	10.2	10.3	2400	0.9	0.020	0.01	0.92
55 Cnc (b)	K0IV-V	5200	6.0	0.87	0.58	12	42.7 ± 2.5	6.7	—	0.80	—	700	14.6	0.113	0	—

Notes. Explanation of the columns: name of the system, spectral type, effective temperature, visual magnitude, colors (SIMBAD), distance, stellar rotation period, gyrochronological age according to Brown (2014) or mean of the three color based age estimates from the same author, planetary radius, mass, density, equilibrium temperature or where cited average dayside brightness temperature, orbital period, semimajor axis, orbit eccentricity, and transit depth.

References. The data were compiled using exoplanets.org (Wright et al. 2011) and the following publications: HAT-P-2: Bakos et al. (2007); van Leeuwen (2007); Pál et al. (2010), $P_{\rm rot}$ from v sin i, $T_{\rm eq}$ varies due to eccentricity (1250 to 2150 K); WASP-38: Barros et al. (2011); Brown et al. (2012); WASP-77: Maxted et al. (2013); WASP-10: Christian et al. (2009); Johnson et al. (2009); Smith et al. (2009), $P_{\rm rot}$ from (Salz et al. 2015b); HAT-P-20: Bakos et al. (2011), $P_{\rm rot}$ from (Salz et al. 2015b); WASP-8: Queloz et al. (2010); Cubillos et al. (2012), $P_{\rm rot}$ from (Salz et al. 2015b); WASP-80: Triaud et al. (2013), $P_{\rm rot}$ from v sin i; WASP-43: Hellier et al. (2011); WASP-18: Hellier et al. (2009); Pillitteri et al. (2014), $P_{\rm rot}$ from v sin i; HD 209458:Charbonneau et al. (2000); Henry et al. (2000); Torres et al. (2008); Silva-Valio (2008), dayside brightness temperature from Spitzer observation (Crossfield et al. 2012); HD 189733: Bouchy et al. (2005); Henry & Winn (2008); Southworth (2010) , dayside brightness temperature from Spitzer observation (Knutson et al. 2007); GJ 1214: Charbonneau et al. (2009); Berta et al. (2011); Narita et al. (2013); GJ 3470: Bonfils et al. (2012); Biddle et al. (2014); GJ 436: Butler et al. (2004); Knutson et al. (2011); 55 Cnc: Butler et al. (1997); McArthur et al. (2004); Gray et al. (2003); Fischer et al. (2008); HAT-P-11: Bakos et al. (2010); HD 149026: Sato et al. (2005), $P_{\rm rot}$ from v sin i, dayside brightness temperature from Spitzer observation (Knutson et al. 2009); HD 97658: Howard et al. (2011); Henry et al. (2011); WASP-12: Hebb et al. (2009), $P_{\rm rot}$ upper limit from v sin i, dayside brightness temperature from HST WFC3 observation (Swain et al. 2013); CoRoT-2: Alonso et al. (2008); Lanza et al. (2009); Schröter et al. (2011).

reverts back to an X-ray based estimate, because the Lyα luminosity is based on the X-ray luminosity. If a measurement of the Lyα luminosity is available, we obtain two predictions for the EUV luminosities (X-ray and Lyα based) and use the average. The shape of the SED is taken from an active or inactive solar spectrum (Woods & Rottman 2002), depending on the activity of the host star. This shape is continued to a connecting point with the photospheric blackbody, where we use a visual best fit for the connection point between 1500 to 4000 Å. Certainly the spectral shape of the host stars will differ from the solar type emission, however, only the relative strength of broader ranges is relevant, because the radiation causes ionization and the presence of spectral lines is unimportant (except for the He II Lyα see below).

4. For the remaining part of the spectrum we choose a blackbody according to the host star's effective temperature. This range does not affect the simulations, but can be used to check absorption in the hydrogen Balmer lines for example.

Our approach does not include a prediction of the He II Lyα line (304 Å), which accounts for 20% of the EUV emission in the solar spectrum. The use of the solar SED shape introduces another error at this point (private communication Linsky). While a more detailed reconstruction of the SEDs is conceivable, it certainly has a smaller effect on the results than the uncertainty on the overall EUV luminosity of the host stars.

Figure 1 shows the reconstructed SEDs for the host stars. The total XUV irradiation is a factor of 200 stronger for CoRoT-2 b than in GJ 436 b. In these two systems X-rays contribute 60% and 30% of the total energy of hydrogen ionizing radiation. Also the relative Lyα emission line strength varies strongly for the individual targets. HD 209458 shows powerful Lyα emission given
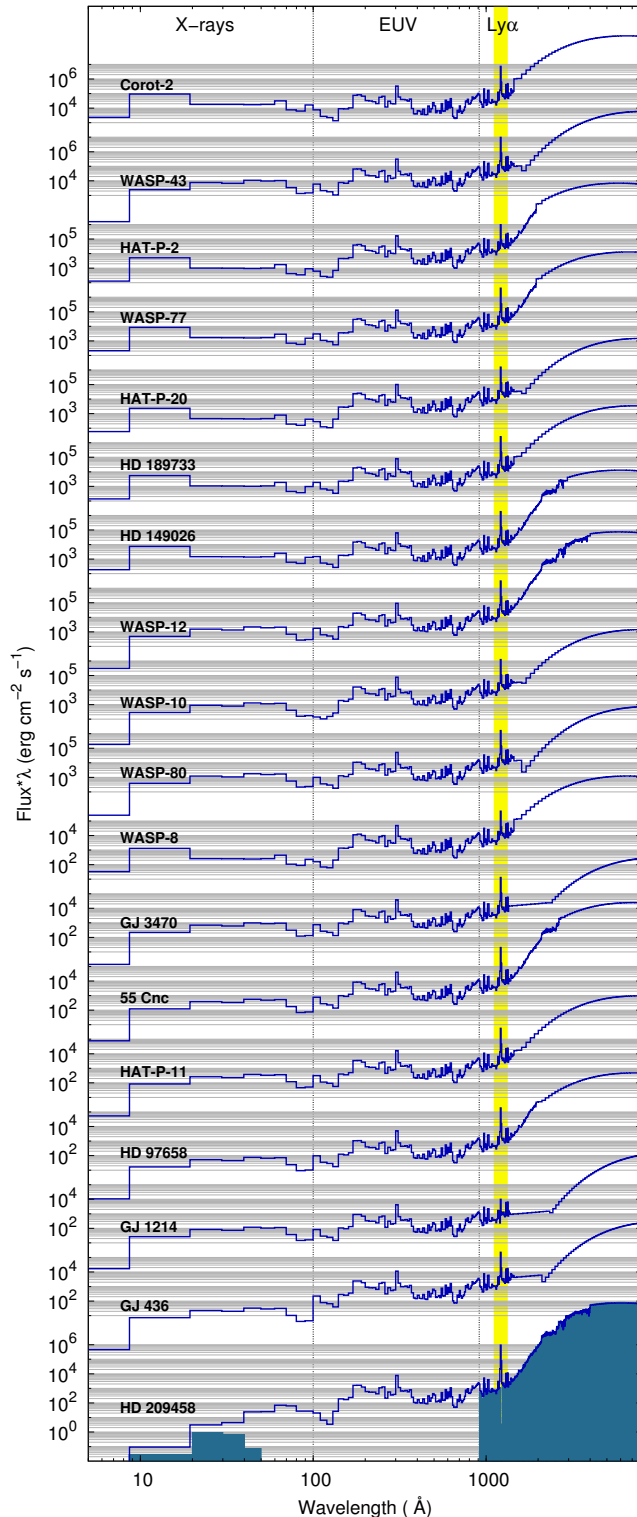
Fig. 1. Reconstructed stellar flux sorted from top to bottom according to the irradiation level at the planetary distance. HD 209458 b is plotted separately at the bottom, because we also show the transmitted radiation (shaded region), which would be absorbed below our simulation region. The shape of the SEDs is similar, but the XUV irradiation strength drops by more than two orders of magnitude from CoRoT-2 to GJ 436.

the inactive state of the host star. In contrast, the upper limit for GJ 1214 derived by France et al. (2013) is extremely low (see Fig. 1).

3. Simulations

3.1. Overview

We simulate the hydrodynamically expanding atmospheres of 18 hot gas planets in spherically symmetric, 1D simulations. Absorption and emission, and the corresponding heating and cooling is solved self-consistently using a microphysics solver, which incorporates most elementary processes from first principles. The computational effort for the presented simulations is difficult to quantify, because they were often restarted to handle individual issues. In total, we estimate that the computational effort corresponds to a continuous run over 6 months on 25 3.1/3.6 GHz CPUs, which equals ~ 300 000 hours on a standard 1 GHz CPU. The simulations were performed on several standard workstations.

The structure of this section is as follows. We introduce the code (3.2) used for the simulations and explain the numerical setup (3.3). We verify the convergence of the simulations (3.4). Resolution and boundary effects are investigated in Sect. 3.5 to 3.7. The impact of metals and molecules on the results is checked in Sect. 3.8. We conclude this section with an overview of the uncertainties that generally affect 1D simulation such as ours both from a numerical and observational point of view (3.9).

3.2. Code

We use our photoionization-hydrodynamics simulation code "the PLUTO-CLOUDY Interface" (TPCI) for the simulations of the escaping planetary atmospheres (Salz et al. 2015a). The interface couples the photoionization solver CLOUDY to the magnetohydrodynamics code PLUTO. This allows simulations of steady-state photoevaporative flows. PLUTO is a versatile MHD code that includes different physical phenomena, among others, gravitational acceleration and thermal conduction (Mignone et al. 2007, 2012). Our interface introduces radiative heating and cooling as well as radiative acceleration from CLOUDY in PLUTO. CLOUDY solves the microphysical state of a gas under a given irradiation in a static density structure (Ferland et al. 1998, 2013). The user can choose to include all elements from hydrogen to zinc and CLOUDY then solves the equilibrium state regarding the degree of ionization, the chemical state, and the level populations in model atoms. Radiative transfer is approximated by the escape probability mechanism (Castor 1970; Elitzur 1982). We include the impact of the advection of species on the equilibrium state as described in Salz et al. (2015a).

The use of CLOUDY is one of the main improvements compared with previous models of escaping planetary atmospheres, because it not only solves the absorption of ionizing radiation in detail, but also the emission of the gas. Previous studies have either chosen a fixed heating efficiency for the absorbed radiation to account for a general radiative cooling effect or they specifically included individual radiative cooling agents like Lyα cooling (e.g., Murray-Clay et al. 2009; Koskinen et al. 2013a). With such an approach it is impossible to find radiative equilibrium, because not all relevant microphysical processes are included. Therefore, these simulations can only be used for strongly escaping atmospheres, where radiative cooling has a minor impact, but not for almost stable thermospheres, which are close the radiative equilibrium. TPCI resolves this issue and can be used to sim-

ulate the transition from rapidly escaping atmospheres, where the radiative energy input is virtually completely used to drive the hydrodynamic wind, all the way to a situation with a hydrostatic atmospheres, where the absorbed energy is re-emitted.

3.3. Simulation setup

We simulate the expanding planetary atmospheres on a spherical, 1D grid. A uniform setup is chosen for all simulations. The planetary atmosphere is irradiated from the top. We simulate the substellar point, which results in a maximal outflow rate because of the high irradiation level at this point. Forces due to the effective gravitation potential in the rotating two-body system are included as well as radiation pressure. Thermal conduction is considered in a simplified manner by adding the thermal conductivity coefficients of an electron plasma and of a neutral hydrogen gas (Salz et al. 2015a).

Our simulations have several input parameters, which are fixed by observations, i.e., the planetary mass and radius, the semimajor axis, and the stellar mass. Additionally, we need to know the irradiating SED (see Sect. 2.3). The last two required parameters are not well defined: First, the temperature in the lower atmosphere, which is close to the equilibrium temperature but with a considerable uncertainty (see Sect. 3.6); and second, the boundary density, which reflects how deep our simulations proceed into the lower atmosphere (see Sect. 3.7). Fortunately, these two parameters have no strong impact on the outcome, therefore, the resulting atmosphere is unique for every planet and we do not need to sample a parameter space.

The simulated atmospheres consist of hydrogen and helium only; metals or molecules are neglected in our current simulations (see Sect. 3.8). CLOUDY solves a plane parallel atmosphere, allowing radiation to escape in both directions toward the host star and toward the lower atmosphere. We double the optical depth at the bottom of the atmosphere to ensure that radiation does not escape freely into a vacuum in this direction. We further use a constant microturbulence of 1 km s^{-1}, which is adapted to the conditions close to our lower boundary; the microturbulence has little impact on the overall atmospheric structure.

A stretched grid with 500 grid cells spans the range from 1 to 15 planetary radii (in some simulation up to $12 \, R_{\text{pl}}$). The resolution is increased from $2 \times 10^{-4} \, R_{\text{pl}}$ to $0.22 \, R_{\text{pl}}$ at the top boundary. We emphasize the high resolution at the lower boundary, which is not always visible in figures showing the complete atmospheres. The photoionization solver runs on an independent grid, which is autonomously chosen and varies throughout the simulation progress. It uses 600 to 900 grid cells. The resolution in the dense atmosphere at the lower boundary can be up to a factor ten higher than in the hydrodynamic solver.

The number of boundary conditions that are fixed are two at the bottom (density, pressure) and none at the top boundary. This is the correct choice for a subsonic inflow and a supersonic outflow (e.g. Aluru et al. 1995). The bottom boundary condition is anchored in the lower atmosphere at a density of 10^{14} cm^{-3}. This is sufficient to resolve the absorption of the EUV emission, which is mostly absorbed in atmospheric layers with a density of about 10^{11} cm^{-3}. Furthermore, we fix the pressure according to the equilibrium temperature of the planets (see Table 1). This results in pressures around 14 dyn cm^{-2} equivalent to 14 μbar. The velocity in the boundary cell is adapted at each time step according to the velocity in the first grid cell. However, we allow only inflow, setting the boundary velocity to zero otherwise. This choice dampens oscillations that appear in simulations with
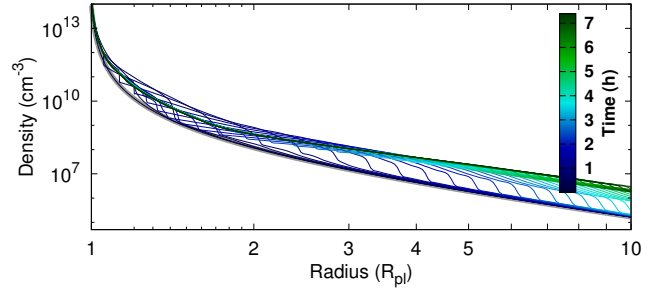
Fig. 2. Convergence of the atmosphere of WASP-80. The density structure is plotted versus the radius. The initial structure is indicated by a thick gray line, the time evolution is given by the color scheme.

steep density gradients at the lower boundary. The impact of the lower boundary conditions on the outcome of the simulations is discussed in Sect. 3.6 and 3.7.

The chosen numerical setup of the PLUTO code is a third order Runge-Kutta integrator (Gottlieb & Shu 1996), with the weighted essentially non-oscillatory finite difference scheme (WENO3 , Jiang & Shu 1996) for interpolation and the Harten, Lax and van Leer approximate Riemann solver with contact discontinuity (HLLC, Toro et al. 1994). The radiative source term is not included in the Runge-Kutta integrator, but a simple forward Euler time stepping is used.

3.4. Convergence and initial conditions

All simulations were started from the same initial conditions, which are adjusted to an atmosphere with a medium mass-loss rate. Every atmosphere undergoes a series of shock waves in the first few hours (of real time). This is depicted in Fig. 2 for the density structure in the atmosphere of WASP-80 b. Two shock waves propagate from the lower atmosphere (left-hand side) into the upper atmosphere (right-hand side), increasing the average density in the thermosphere by a factor of ten. The depicted 7 h evolution in the atmosphere corresponds to less than 10^{-3} of the final converging time. The final steady-state does not depend on the chosen initial conditions.

The convergence of the simulations was analyzed by checking the mass-loss rate and the temperature structure. We define a system specific time scale as

$$t_{\text{sys}} = \frac{R_{\text{pl}}}{v_{\text{pl}}} \qquad (1)$$

and choose $v_{\text{pl}} = 1 \text{ km s}^{-1}$ is a typical velocity scale in the planetary thermospheres. 1000 of such time steps correspond to between half a year and four years in the systems. This time is sufficient for atmospheric material to propagate at least once through the computational domain. We ensured that the temperature structure and the total mass-loss rate have converged to a level of 0.1 on this time scale. Individual simulations were advanced a factor of 10 longer and did not show any significant further changes.

3.5. Resolution effects

We have checked that the chosen resolution does not affect the results of our simulations. The resolution of the stretched grid at the lower boundary has been increased in three steps by factors of two in the simulations of HD 209458 b and HD 189733 b.

HD 189733 b has a steeper density gradient in the lower atmosphere and is more challenging for the numerical solver. Decreasing the resolution leads to larger oscillations in the atmospheres, which remain after the convergence of the simulations as defined above. They do not affect the time averaged density, temperature, or velocity structure and, therefore, also not the mass-loss rate (fractional change of the mass-loss rate $\Delta \dot{M}/\dot{M} < 10^{-2}$).

The remaining oscillations are larger in the atmosphere of HD 189733 b as compared with HD 209458 b, hence, atmospheres with lower mass-loss rates are affected more strongly by such oscillations. The oscillations are numerical artifacts coming from two sources. First, the small acceleration of the planetary wind in the lower atmospheres results from a slight imbalance of the gravitational force and the force due to the hydrostatic pressure gradient. Subtraction of these large forces results in a small value, which is prone to numerical inaccuracy. Increasing the resolution results in better estimates of the pressure gradient, which in turn reduces the errors and thus the oscillations. The second source of oscillations in the lower atmosphere of planets with a small mass-loss rate is a consequence of these atmospheric layers being almost in radiative equilibrium. When the microphysics solver is called within TPCI the best level of equilibrium between radiative heating and cooling is about 10^{-2}. This results in small transient heating and cooling events in regions of radiative equilibrium. Hence, oscillations are induced.

In some cases the oscillations are large enough to be seen in our figures. If this is the case, we present time averaged structures. The convergence to the steady-state as defined above is unaffected by these oscillations, but the accuracy of the final atmospheric structure is worse than in simulations without oscillations. This is one reason for our conservative convergence level of 10%. Furthermore, the computational effort of the individual simulation is increased by the oscillations.

The independence of the mass-loss rates on the resolution distinguishes our simulations from those of Tian et al. (2005). The mass-loss rates in their simulations depended on the chosen number of grid points. However, the authors used a Lax-Friedrich solver with a higher numerical diffusion compared with the more advanced Godunov-type scheme with the approximate HLLC Riemann solver. Tian et al. identified the numerical diffusion to be responsible for the dependency of their mass-loss rates on the resolution, which is consistent with our findings.

3.6. Boundary temperature

The temperature at the lower boundary is one of the free parameters in our simulations. It corresponds to a temperature in the lower atmosphere of the planet at a certain height. Basically, the equilibrium temperature T_{eq} of the planet provides a simple approximation for this temperature (with zero albedo, e.g., Charbonneau et al. 2005):

$$T_{eq} = T_{eff} \sqrt{R_{st}/2a} \,. \tag{2}$$

Here, T_{eff} is the effective temperature of the host star, R_{st} is the stellar radius, and a is the semimajor axis of planetary orbit. In some cases measurements of the average dayside brightness temperatures are available from infrared transit observations (see Table 1). However, neither the equilibrium temperature nor the brightness temperature necessarily represents the temperature at the atmospheric height, which corresponds to the lower boundary of our simulations. Detailed radiative transfer models are another method to obtain an accurate temperature structure for the
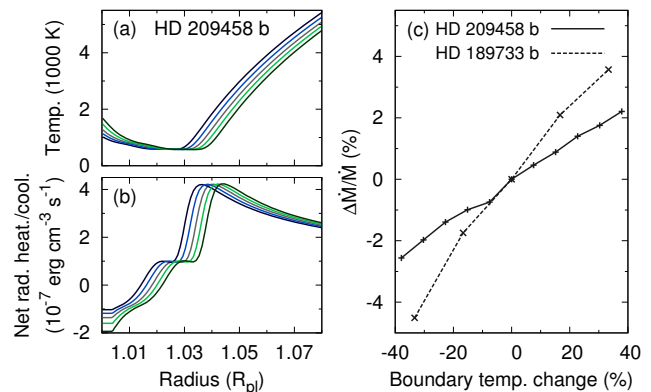
Fig. 3. Influence of the temperature at the lower boundary on the mass-loss rates. Temperature structure (a) and the heating rate (b) in the lower atmosphere of HD 209458 b are shown along with the change in the mass-loss rate (c) in the planets HD 209458 b and HD 189733 b. The color scheme in panels (a) and (b) indicates the boundary temperature from −400 K (blue) to +400 K (green). A higher boundary temperature results in a slightly higher mass-loss rate.

lower atmosphere, but such models only exist for well studied systems like HD 209458 b. Even for this planet, Koskinen et al. (2013a) conclude that despite several different observations and models the temperature structure in the lower atmosphere is uncertain.

Fortunately, we do not need to know the temperature at the lower boundary with high precision. To verify this, we tested the impact of this temperature on our results. In the simulations of the atmospheres of HD 209458 b and HD 189733 b, which have boundary temperatures of 1320 K and 1200 K respectively, we increased and decreased the temperature in steps of 100 K/200 K. Figure 3 shows that increasing the boundary temperature slightly expands the planetary atmosphere, which increases the mass-loss rate. The change in the mass-loss rate scales linearly with the change of the boundary temperature over the tested range. The overall impact is small: A change of 40% in the boundary temperature causes the mass-loss rate to change by less than 5%. Our results are comparable to those of Murray-Clay et al. (2009), who tested a wider range for the lower boundary temperature. This result is not surprising, because the gain in advected energy due to a 1000 K temperature change is about a factor ten smaller than the total radiative energy input. The change in the mass-loss rate is about twice as strong in the simulation of HD 189733 b, because a temperature minimum occurs in the atmosphere of HD 209458 b, which better decouples the simulation from the boundary conditions, because radiative processes have more time to dispose of additional energy.

Even considerable changes in the lower boundary temperature affect the total mass-loss rates in our simulations by less than 10%. With respect to the uncertainty on other parameters, especially the irradiation level, we can neglect the effect at this point.

3.7. Boundary density

The density at the lower boundary is another free parameter in our simulations. Changing the boundary density has a larger effect on the mass-loss rate than changing the boundary temperature. This is a result of a slight inconsistency in the setup of our simulations. The density at the lower boundary is a density that
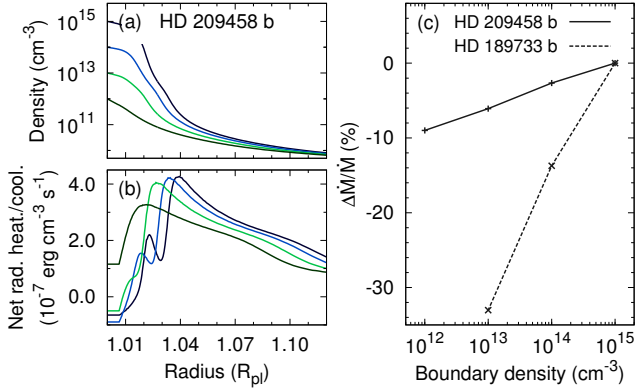
Fig. 4. Influence of the density at the lower boundary on the mass-loss rates. The density (a) and the heating rate (b) in the lower atmosphere of HD 209458 b are depicted. Panel (c) shows the change in the mass-loss rate in the two test simulations (HD 209458 b, HD 189733 b). The color scheme indicates the boundary density ranging from 10^{12} cm^{-3} (green) to 10^{15} cm^{-3} (blue). Reducing the boundary density by two orders of magnitude decreases the mass-loss rate by less than 40%.

is reached at a certain height above the planetary photosphere[3]. However, our simulation setup always starts at 1 R_{pl}. If we start with a density two orders of magnitude smaller, this layer is located higher up in the planetary atmosphere; the change in height is about 0.025 R_{pl} in the case of HD 209458 b. In the spherical simulation the irradiated area of the grid cells increases with R_{pl}^2, thus, a similar volume heating rate gives a total heating larger by 5%, which in turn affects the mass-loss rate. This effect is depicted in Fig. 4, which shows that the density structures of the individual simulations almost merge in the upper thermosphere of HD 209458 b, but larger differences occur in the lower atmosphere. These would be mitigated if we had started the simulations with a lower boundary density at the correct heights, e.g., in the simulation with a boundary density of 10^{13} cm^{-3} at 1.025 R_{pl}. In the simulation with a boundary density of 10^{12} cm^{-3} a significant fraction of the XUV radiation passes through our atmosphere without being absorbed in the computational domain.

For HD 189733 b the impact of the boundary density on the mass-loss rate is larger. Decreasing the boundary density to 10^{12} cm^{-3} causes a discontinuity in the density structure from the boundary cell to the first grid point, and the total mass-loss rate is reduced by 60%. We confirmed that none of the presented simulations is affected by such a density discontinuity. Our standard simulation has a density of 10^{14} cm^{-3} at the lower boundary. The uncertainty in the correct height of this atmospheric layer above the planetary photosphere induces an error on the mass-loss rates less than 50%, consistent with the results of Murray-Clay et al. (2009). We also note that the observationally determined planetary radii are usually not accurate to the level of one percent.

3.8. Metals and Molecules

Our current simulations only include the chemistry of hydrogen and helium. Including metals substantially increases the computational load and will be studied for individual systems in the future. To justify that we can neglect metals in this study, we anticipate results from a test simulation of the atmosphere of HD 209458 b including metals. We find that the temperature

---

[3] Since a gas planet has no surface, we refer to the outer most layer that is opaque to optical light as photosphere.

Table 2. Uncertainties on the result of the simulations.

Source	Trend[A]	Impact	Ref.
Three dimensional structure[B]	(−)	× 4	1
Irradiation strength	(±)	× 3	2
Magnetic fields	(−)	× 3	3
Metals	(−)	× 2	
Molecules[C] (H$_2$)	(−)	× 2	
Stellar wind	(−)	uncert.	4
Boundary density	(±)	50%	
Temperature in lower atmosphere	(±)	10%	

Notes. [A] A negative trend indicates that the effect will reduce the simulated mass loss rates. [B] Our mass-loss rates are reduced by this factor and the remaining uncertainty is smaller. [C] Only moderately irradiated smaller planets host molecular winds.

References. Phenomena without reference are discussed in the text. (1) Stone & Proga (2009); (2) Salz et al. (2015b); (3) Trammell et al. (2014); (4) Murray-Clay et al. (2009).

structure of the lower atmosphere (< 1.05 R_{pl}) is dominated by line heating and cooling of metals, but the temperature in this region has only a small effect on the mass-loss rate (see Sect. 3.6). The mass-loss rate is reduced by a factor of two because of line cooling in the thermosphere (one of the strongest lines is Ca II at 7306 Å). Hence, metals have an effect on the results, which is likely smaller than the uncertainty in the EUV irradiation level (Salz et al. 2015b).

Metals also efficiently absorb X-rays, which increases the available energy. Strongly expanded thermospheres like in HD 209458 b are opaque to X-rays longward of 25 Å, but more compact atmosphere are only opaque longward of 60 Å in our simulations (defined as 50% absorption). Including metals shifts these cutoff values to approximately 10 and 20 Å. In the case of our most active host star CoRoT-2 metals would increase the absorbed energy in the planetary atmosphere by 13%.

We also disable the formation of molecules in CLOUDY. This choice is unphysical, because photodissociation of H$_2$ would occur close to the lower boundary (Koskinen et al. 2013a). Molecules strongly affect the temperature structure of the lower atmospheres, but the impact of this temperature structure on the mass-loss rate is quite small (see Sect. 3.6). Furthermore, planets with a moderate irradiation level can host a molecular outflow. A detailed study of this phenomenon is beyond the scope of this paper, but we performed a test simulation of one of the planets with the smallest irradiation level, GJ 1214 b, including molecules in the planetary atmosphere. The simulation shows an H$_2$ fraction of 10 to 25% in the thermosphere of the planet and H$^-$ is a significant cooling agent. The mass-loss rate is reduced by 15%, thus, our simulations without molecules remain valid as long as hydrogen is the major constituent of the atmospheres.

3.9. Overview of the uncertainty budget

One-dimensional simulations of the planetary winds are subject to several uncertainties. These are introduced by observational limitations and by the simplifications of the 1D model. We provide a short overview and estimate the impact of probably the most important effects that are neglected (see Table 2).

The largest uncertainty is introduced by neglecting the 3D structure of the system geometry, however, Stone & Proga (2009) have shown that 1D models produce valid estimates for the planetary mass-loss rates, if the irradiation is handled cor-

rectly. In Salz et al. (2015b) we indicated that the irradiation level of hot gas planets is uncertain, because the EUV spectral range is completely absorbed by interstellar hydrogen and different reconstruction methods differ by up to a factor of 10. Most recently, Chadney et al. (2015) revised one of the methods, reducing the differences for active stars, nevertheless, we adopt a conservative error estimate of a factor of 3 for the EUV reconstruction. Magnetic fields have been studied for example by Trammell et al. (2014), who stated that the field strength of hot Jupiters is uncertain, but if the planets host sufficiently strong fields, the outflow can be suppressed over larger fractions of the planetary surface. The impact of metals and molecules on the wind has been explained in the previous section. A planetary wind will also interact with the stellar wind, which in principle can suppress the formation of a wind at least on the dayside of the planet (Murray-Clay et al. 2009). Finally, related to our simulations, the boundary conditions introduce a smaller uncertainty on the resulting mass-loss rates.

4. Results

4.1. Overview

We now present the simulated atmospheres of 18 planets. The atmospheres of HD 209458 b and HD 189733 b are compared in Sect. 4.2, where we explain in detail the individual processes affecting the planetary atmospheres. The complete sample of planets is presented and compared in Sect. 4.3, where the impact of individual system parameters on the planetary atmospheres is investigated. We then compute the mass-loss rates (4.4), explain the case of WASP-12 b (4.5), identify stable thermospheres (4.6), consider the ram pressure of the planetary winds (4.7), and estimate the strength of the radiation pressure (4.8).

4.1.1. Heating fraction versus heating efficiency

For the analysis of our simulations we define the heating fraction as

$$\text{heating fraction} = \frac{\text{rad. heating} - \text{rad. cooling}}{\text{rad. heating}}. \quad (3)$$

Note that the heating fraction differs from the often used heating efficiency, which is defined as:

$$\text{heating eff.} = \eta = \frac{\text{rad. heating} - \text{rad. cooling}}{\text{absorbed rad. energy}}. \quad (4)$$

Here, the denominator holds the total energy contained in the absorbed radiative flux. The difference of the two definitions is mainly the energy that is used to ionize hydrogen and helium; this energy fraction is not available for heating the planetary atmosphere. Equation 3 excludes this fraction of the radiative energy input, hence, the heating fraction approaches one as radiative cooling becomes insignificant, and it is zero in radiative equilibrium. The heating efficiency is also zero in radiative equilibrium, but it never reaches a value of one.

4.2. Structure of the escaping atmospheres

To understand the general behavior of escaping planetary atmospheres, we compare two examples: HD 209458 b and HD 189733 b. For HD 209458 b we also juxtapose a simulation with only hydrogen as constituent (H-only). In Fig. 5 we show the density, temperature, velocity, and specific heating rate
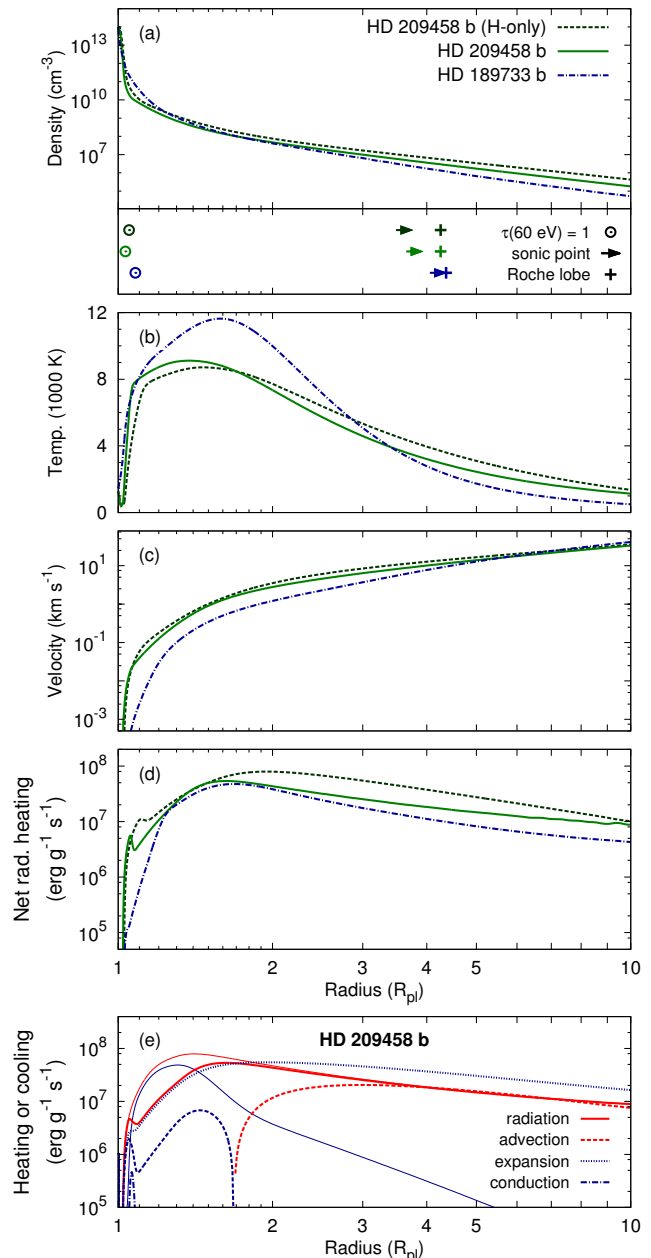
Fig. 5. Atmospheres of HD 209458 b and HD 189733 b. For HD 209458 b both a hydrogen-only and a hydrogen and helium simulation are shown. We plot the density, temperature, velocity, and the specific heating rate. The symbols in the lower panel (a) indicate the $\tau(60\,\text{eV}) = 1$ levels (circles), the sonic points (arrows), and the Roche lobe heights (plus signs), with the order of the planets according to the legend. Panel (e) shows the individual heating (red) and cooling (blue) agents in the H+He atmosphere of HD 209458 b. Radiative heating (red) and cooling (blue) are displayed individually by the thin solid lines and the thick solid line gives the net radiative heating rate.

throughout the atmospheres in the three simulations. Panel (e) further shows individual heating and cooling terms in the atmosphere of HD 209458 b with hydrogen and helium (H+He). Finally, Fig. 6 splits the radiative heating and cooling terms into the most important agents. In all our figures the right-hand side of the plot is the top of the atmosphere, while the left-hand side
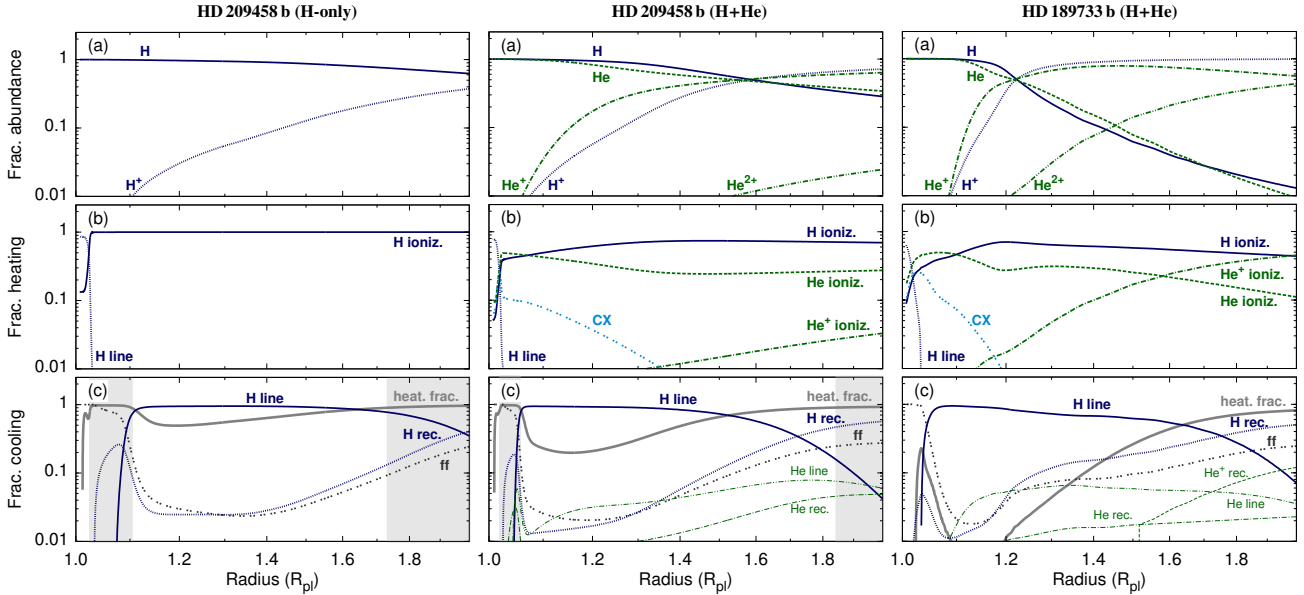
Fig. 6. Abundances and heating/cooling agents in the atmospheres of HD 209458 b (H-only), HD 209458 b (H+He), and HD 189733 b. Panels (a) depict the fractional abundances in the three atmospheres, (b) show the contribution of individual radiative heating agents to the total heating rates, and (c) show the same for the cooling rates. In panel (c) we also show the heating fraction by the solid thick gray line. Regions with little radiative cooling are shaded (heating fraction > 0.9). We show the atmospheres up to 2 R_{pl}. The atmosphere of HD 189733 b shows weak oscillations. Labels are: hydrogen and helium line cooling/heating (H/He line); ionization heating of hydrogen, helium, or ionized helium (H/He/He$^+$ ioniz.); charge transfer between neutral hydrogen and ionized helium (CX); recombination cooling of hydrogen, helium, or ionized helium (H/He/He$^+$ rec.); free-free emission (ff); and heating fraction (heat. frac.).

is the lower boundary, which is located in the denser atmosphere close to the planetary photosphere.

The general structure of all planetary atmospheres is similar. The density in the atmospheres decreases with height; the density gradient in the thermosphere is shallow due to the high temperature, which results from the absorption of stellar XUV emission. The high temperature further leads to a persistent expansion of the atmospheric gas, which accelerates the atmosphere against the gravitational force of the planet. The initial velocity is small ($\sim 10^{-5}$ km s^{-1}) at the lower boundary, but reaches the sonic point within the simulation box, and the atmospheric material exits the simulated region as a supersonic wind. Thus, we simulate the transonic hydrodynamic planetary winds.

4.2.1. Atmosphere of HD 209458 b

First, we focus on the atmosphere of HD 209458 b, which is depicted by the green solid lines in Fig. 5. Panel (a) shows that the density decreases from the boundary density of 10^{14} to 10^5 cm^{-3}. The extent of the Roche lobe for HD 209458 b is 4.2 R_{pl} above the substellar point and the sonic point is reached at 3.5 R_{pl}. The optical depth for EUV photons (60 eV) reaches one at a height of 1.04 R_{pl}. This height corresponds well with the atmospheric layer that experiences the maximum volume heating rate in atmospheres with little radiative cooling.

Panel (b) in Fig. 5 shows that the absorption of XUV emission around the height of 1.04 R_{pl} increases the temperature. This raises the atmospheric scale height and the density gradient becomes more shallow above this height. The temperature reaches a maximum of 9100 K. The bulk velocity strongly increases along with the temperature in the lower atmosphere (see panel (c)).

Panel (d) shows the net specific radiative heating rate throughout the atmosphere. We plot the specific heating rate, which is the heating rate per gram of material, because it clearly shows where the atmospheric material gains most of the energy for the escape. The net heating rate has a maximum close to the temperature maximum, but declines above 1.6 R_{pl} where the atmosphere is more strongly ionized. There is a distinct dip in the net heating rate at 1.15 R_{pl}, which is caused by hydrogen line cooling. This can be seen in panel (e), where we show the pure radiative heating and cooling rates as thin, solid lines. Subtracting the radiative cooling rate from the heating rate gives the net radiative heating rate (solid thick line), which is displayed in panel (d) and (e). Between 1.05 and 1.8 R_{pl} about 45% of the radiative heating produced by the absorption of XUV radiation is counterbalanced by hydrogen line emission, mainly Lyα cooling.

In panel (e) we further compare the radiative heating rate to the hydrodynamic energy sources and sinks. In the atmosphere of HD 209458 b the advection of internal energy is a heat sink below 1.7 R_{pl}, but acts as a heat source above this level, providing 50% of the energy in the upper thermosphere. The adiabatic expansion of the gas is a heat sink throughout the atmosphere. This term stands for the energy, which is converted into gravitational potential and kinetic energy. It now becomes clear why the temperature decreases in the upper thermosphere: Radiative heating becomes inefficient due to a high degree of ionization, but the adiabatic cooling term remains large. Therefore, the advected thermal energy is used to drive the expansion of the gas. Panel (e) also shows cooling due to thermal conduction, which is largest where the temperature increases most strongly, but it is not relevant in any of the simulations.

In Fig. 6 the H+He atmosphere of HD 209458 b is depicted in the middle column. Panel (a) shows the fractional abundances.

Ionized hydrogen is the major constituent above 1.6 R_{pl} (H/H$^+$ transition layer). This correlates with the height above which the radiative heating declines. The He/He$^+$ transition occurs slightly below. Panel (b) shows the individual radiative heating agents. Ionization of hydrogen is the most important heating agent, but also ionization of helium contributes throughout the atmosphere. Ionization of He$^+$ to He^{2+} contributes less than 10% of the heating rate in this atmosphere and is most important above the Roche lobe (not depicted in Fig. 6). Charge exchange between H and He$^+$ is a heat source when hydrogen is weakly ionized.

Panel (c) of Fig. 6 shows the cooling agents and the heating fraction. Where the total radiative cooling rate is small ($< 10\%$ of the heating rate) the plot is shaded. The most important cooling agent is hydrogen line cooling between 1.06 and 1.7 R_{pl} (see the discussion of Fig. 5 (e) above). Beyond 1.8 R_{pl} radiative cooling is small; the main cooling agents in this region are hydrogen recombination and free-free emission of electrons. Only at the bottom of the atmosphere ($< 1.02 R_{pl}$) free-free emission is stronger than the heating rate. At this level hydrogen line heating is the main energy source, because ionizing radiation has been absorbed in higher atmospheric layers. The specific cooling at this height is negligible. Helium contributes less than 10% to the radiative cooling rate in the atmosphere of HD 209458 b.

While our simulation shows that HD 209458 b produces a strong, transonic wind as a result of the absorption of XUV radiation, it also demonstrates that the hot atmosphere re-emits a significant fraction of the radiative energy input mostly by Lyα line emission in lower thermospheric layers.

4.2.2. The H-only atmosphere and the H/H$^+$ transition layer

If the atmosphere of HD 209458 b consisted of hydrogen only, the general structure would be similar to an atmosphere including hydrogen and helium (see Fig. 5). However, an H-only atmosphere of HD 209458 b produces a slightly stronger planetary wind. On average, including helium in our simulations decreases the mass-loss rate by a factor of two. Since the involved Lyα cooling is important for all atmospheres, we will explain the difference here in more detail.

Including helium increases the mean molecular weight of the atmosphere, therefore, a higher temperature is needed to sustain the atmospheric density structure. The higher temperature in turn, increases the cooling rate by increasing the collisional excitation of hydrogen. Lyα cooling is proportional to the occupation number of the second level; the relative occupation number can be approximated using the Boltzmann factor (exp $-h\nu/kT$). Lyα radiation mainly escapes from a depth around 1.15 R_{pl}, where the temperatures are about 8000 and 8500 K in the H-only and H+He simulations respectively. The higher temperature in the H+He simulation raises the occupation number of the second level by a factor of two, which results in the increased cooling rate. A comparison of the left and the middle columns in Fig. 6 (c) shows this as a decrease in the heating fraction at this height from 50% to 20% (solid, thick, gray line).

The H/H$^+$ transition in the H-only simulation occurs at a height of 2.3 R_{pl} in contrast to 1.6 R_{pl} in the H+He simulation. This higher transition layer results from the stronger mass-loss rate, because more neutral hydrogen is advected into the thermosphere. Additionally, the shift of the transition layer further reduces the Lyα cooling rate by increasing the neutral hydrogen column density above the Lyα emission layer.

Koskinen et al. (2013a) found the H/H$^+$ transition to occur at 3.4 R_{pl} in the atmosphere of HD 209458 b compared to our 1.6 R_{pl}. The height of the transition layer depends on the cool-

ing in the lower thermosphere as seen by the comparison of the H-only and H+He simulations. This was also noted by Koskinen et al.; they compared their results with those of Yelle (2004), who found strong H$_3^+$ cooling and a transition layer height of 1.7 R_{pl}. Koskinen et al. argued that H$_3^+$ is probably not formed if metals are present in the atmosphere, but this argument does not hold for Lyα cooling. Unfortunately, the considerable uncertainties in all of these simulations (see Table 2) do not allow a final statement regarding the transition layer height in the atmosphere of HD 209458 b.

4.2.3. Impact of the gravitational potential on the mass loss: HD 189733 b versus HD 209458 b

Comparing the atmospheres of HD 189733 b and HD 209458 b, one finds three major differences: The atmosphere of HD 189733 b is hotter, the expansion velocity is smaller below the Roche lobe, and the net radiative heating is also smaller (see Fig. 5). The maximum temperature in the atmosphere of HD 189733 b is 2600 K higher than in HD 209458 b. This is not only caused by the XUV irradiation, which is 16 times higher than for HD 209458 b, but also by a weaker planetary wind with less adiabatic cooling. The atmosphere still reaches the sonic point, but just below the Roche lobe, above which the material is accelerated freely toward the stellar surface (see the gravitational potential in Fig. 10). The temperature decreases more strongly in the upper thermosphere, because the degree of ionization is high and only little radiative heating remains.

In the case of HD 189733 b it is remarkable that the simulated wind is weaker in terms of the total mass-loss rate although the irradiation level is higher than in HD 209458 b. The weaker wind is a result of increased radiative cooling, which actually depends on the depth of the gravitational potential well of the planet. This can be demonstrated with a thought experiment: Let us start with a planet that hosts a strong wind and only weak radiative cooling. What happens if we increase the mass of the planet?

- The first reaction will be a contraction of the atmosphere, because the gravitational acceleration was increased. However, we only slightly increase the planetary mass, so that the upward flux of the planetary wind does not collapse but only becomes weaker.
- The smaller mass flux has two effects: First, the adiabatic cooling decreases, because a smaller velocity means that the atmospheric expansion proceeds slower. This causes a higher atmospheric temperature. Second, the advection of neutral hydrogen into the upper atmosphere is weaker, which shifts the ionization front closer to the planetary surface.
- The increased temperature partially counterbalances the higher gravity and prevents the atmosphere to contract further, but it also increases radiative cooling (Lyα and free-free emission). Lyα cooling is further increased by the now smaller neutral hydrogen column density above the emission layer, which increases the escape probability.
- The radiative cooling reduces the available energy for driving the planetary wind.
- The outflow settles at a lower mass-loss rate and the resulting atmosphere is hotter and more strongly ionized.

If the radiative cooling did not increase with the temperature, the down settling of the atmosphere would be a transient effect and the mass-loss rate be restored to the original value. The atmosphere of a massive planet is more tightly bound, therefore, it is hotter and experiences stronger radiative cooling. This implies a

smaller heating efficiency. Of course, we can drive this thought experiment further by again increasing the mass of the hypothetical planet. At a certain mass the radiative energy input will be completely re-emitted by a hot and more compact thermosphere, which explains the transition from a strong planetary wind to a stable hydrostatic atmosphere.

The intermediate case is precisely what occurs in the atmosphere of HD 189733 b. Most of the EUV photons are absorbed at a height of 1.08 R_{pl}. While the heating fraction is close to unity at this height in the atmosphere of HD 209458 b, in HD 189733 b it is only 10 to 20%, which results in only weak acceleration of the planetary wind. Hydrogen and helium are mainly ionized above 1.2 R_{pl} and helium is doubly ionized above 2.1 R_{pl} (see Fig. 6). The overall structure of the heating and cooling agents is similar to the atmosphere of HD 209458 b, but shifted toward smaller heights. Ionization of He$^+$ to He^{2+} is the main radiative heating agent above 2.0 R_{pl}. However, the total radiative heating in the upper thermosphere (> 2.3 R_{pl}) is small compared to the advected energy. Therefore, the upper thermosphere of HD 189733 b is cooler than that of HD 209458 b.

4.3. The atmospheres of hot gas planets in comparison

We can now compare the atmospheres of our sample of hot gas planets. HAT-P-2 b, HAT-P-20 b, WASP-8 b, and WASP-10 b are excluded, because these compact planets host stable thermospheres (see Sect. 4.6). In the following, we discuss how the atmospheres depend on system parameters such as irradiation level, planetary density, or the planetary gravitational potential. We either compare two planets, which differ mostly in a single system parameter, or we compare two subsamples, for which we divide our systems loosely at a gravitational potential of $\log -\Phi_G = 13.0$. The cut allows us to explain differences in the atmospheres of high-potential and low-potential planets, which we use as a short term for the strength of the gravitational potential per unit mass.

The atmospheres of the complete sample of planets are shown in Fig. 7, which is split into two columns: low-potential planets are depicted in the left-hand column and high-potential planets in the right-hand column. In the figure each subsample is ordered with respect to the mass-loss rate. GJ 3470 b has the strongest mass-loss rate among the low-potential planets and WASP-12 b is its counterpart among the high-potential planets. HD 97658 b and CoRoT-2 b are the planets with the smallest mass-loss rates among the subsamples. The general behavior of all atmospheres follows our explanations in Sect. 4.2. The density decreases with height, the temperature reaches several thousand degrees maximally and decreases in the upper thermosphere, and all atmospheres reach a sonic point between 3 and 5 R_{pl}, except for the atmosphere of WASP-12 b (see Sect. 4.5).

4.3.1. Atmospheric temperature and the H/H$^+$ transition layer

A comparison of both columns in Fig. 7 shows that high-potential planets have a lower average density in the thermosphere. The temperature maximum always occurs between 1.3 and 3 R_{pl} in the atmospheres, and rises from low-potential (2700 K in GJ 1214 b) to high-potential planets (16 600 K in CoRoT-2 b). The level of irradiation only weakly affects the maximal temperature in the atmospheres, e.g., the irradiation level of WASP-12 b is 16 times higher than in HD 209458 b, but the maximal temperature is only about 2 % higher. In this case,

strong adiabatic cooling lowers the thermospheric mean temperature.

Super-Earth sized planets have atmospheres that are almost completely neutral throughout our simulation box. As the planets become more massive and compact, the H/H$^+$ transition layer moves closer to the planetary surface (see Fig. 7 (d)), which is mainly a result of the higher temperature in the thermospheres of high-potential planets. To some degree the irradiation strength also affects the height of the transition layer, which can be demonstrated by comparing GJ 436 b with HAT-P-11 b. Both planets have similar densities and gravitational potentials. Despite the stronger planetary wind of HAT-P-11 b, the H/H$^+$ transition occurs at a height of 3.7 R_{pl} in its thermosphere compared to 7.8 R_{pl} in GJ 436 b. Thus, the higher XUV irradiation level of HAT-P-11 b shifts the transition layer to smaller heights. The almost neutral atmospheres of GJ 1214 b and HD 97658 b result from a combination of weakly bound and cool atmospheres with moderate XUV irradiation levels. These two thermospheres would also contain a significant fraction of H$_2$, which is neglected here (see the discussion about molecules in Sect. 3.8).

The specific heating rate is more homogeneously distributed throughout the thermospheres of low-potential planets (see Fig. 7 (e)), which is a result of a higher neutral hydrogen fraction in their atmospheres. In contrast, the upper thermospheres of WASP-77 b, WASP-43 b, and CoRoT-2 b experience negligible amounts of radiative heating, because both hydrogen and helium are almost completely ionized. For example, the fractional abundance of He^{2+} is > 0.99 above 2 R_{pl} in CoRoT-2 b.

4.3.2. Approaching radiative equilibrium: the effect of the gravitational potential

The $\tau(60\,\text{eV}) = 1$ layer always occurs between 1.03 and 1.15 R_{pl} for all planets[4]. The planetary wind is strongly accelerated at this height in low-potential planets, but planets with a higher potential ($\log -\Phi_G > 13.2$) show almost no acceleration in this atmospheric layer (see Fig. 7 (c)). Their atmospheres are more gradually accelerated between 1.1 and 2 R_{pl}. The small amount of acceleration in the lower thermospheres of high-potential planets is a result of strong radiative cooling. Consider, for example, CoRoT-2 b with the strongest irradiation among our sample. This planet experiences the smallest net radiative heating rate. Below 1.3 R_{pl} the atmosphere is close to radiative equilibrium (see Fig. 7 (f)), so that Lyα and free-free emission re-emit almost the complete radiative energy input of 1.55×10^5 erg cm^{-2} s^{-1}. Radiative cooling of these two cooling agents becomes more and more important going from planets with a low gravitational potential to high-potential planets.

Lyα cooling starts to re-emit larger fractions of the energy input at a height around 1.2 R_{pl} in the atmospheres of WASP-80 b and HD 149026 b (see panels (f) in Fig. 7). This cooling is not present in the smallest planets, and only becomes important once the atmospheres are heated to more than 8000 K. For example, at a temperature of 5000 K the collisional excitation of the second level in hydrogen is reduced by a factor of 7000, thus, Lyα cooling can be neglected. In high-potential planets the $\tau(60\,\text{eV}) = 1$ layer occurs close to the bottom of the Lyα emission layer. As a result, in HD 209458 b 80% of the absorbed energy delivered by these photons is re-emitted, in HD 189733 b 98% is re-emitted and in WASP-43 b this fraction increases to about 99.9%.

---

4   We need to keep in mind, that we plot the atmospheres versus the planetary radius, thus, the true size of the simulation box for WASP-12 is almost ten times larger than for 55 Cnc e.
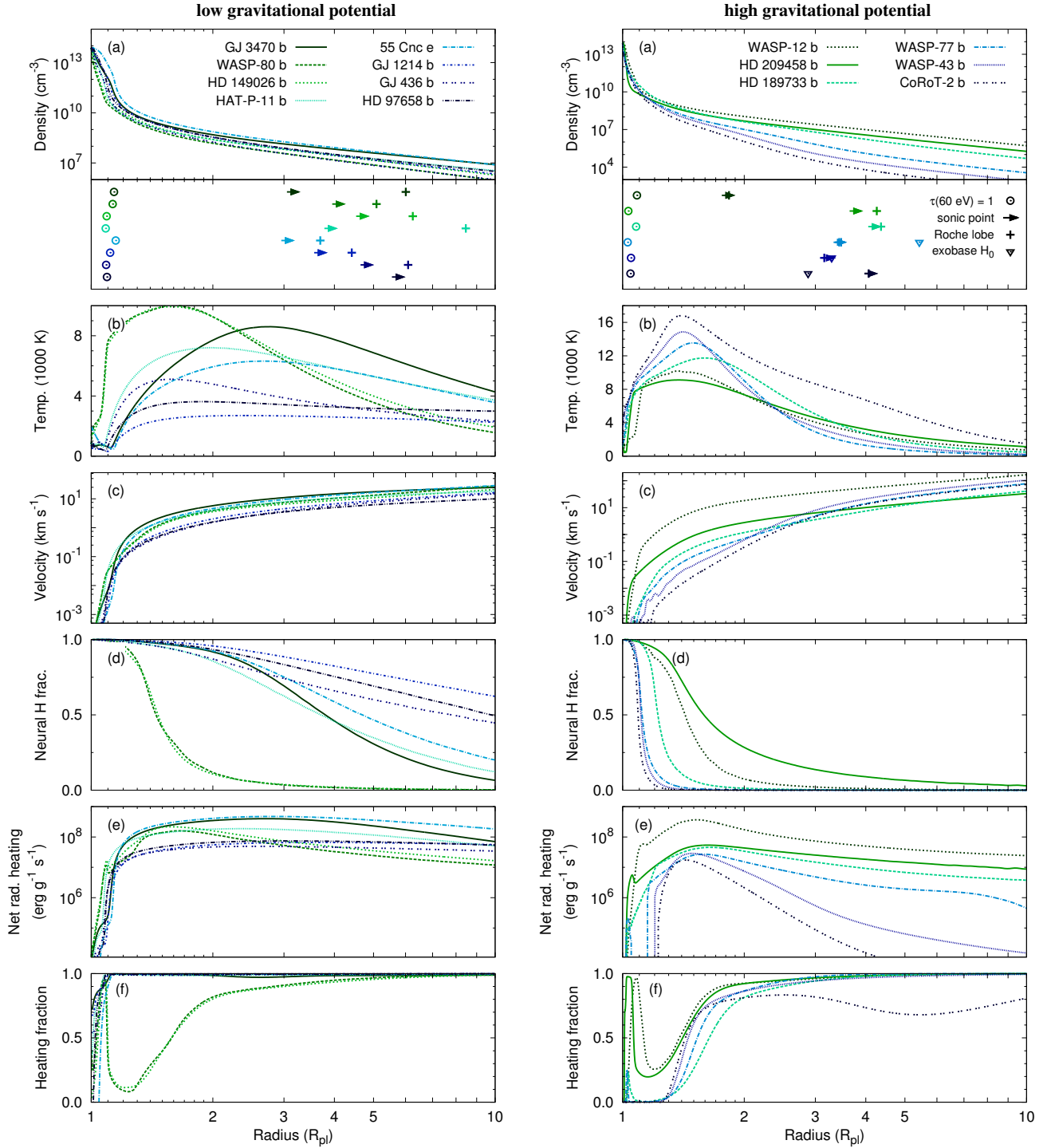
Fig. 7. Atmospheres of the planets in the sample. Low-potential planets are shown on the left-hand side and high-potential planets on the right-hand side. Time averaged profiles are shown for high-potential planets. Symbols in the lower panel (a) are the same as in Fig.5; additionally the height where the atmospheres become collisionless for neutral hydrogen are marked (triangles). On each side the planets are sorted from high (GJ 3470 b/WASP-12 b) to low (HD 97658 b/CoRoT-2 b) mass-loss rates, which is also referenced by a color scheme from green to blue.

Radiation with higher energies penetrates deeper into the atmospheres and heats the atmosphere of HD 209458 b below the Lyα emission layer. Free-free emission, the second major cooling agent, is weak in the atmosphere of HD 209458 b, which is reflected by a heating fraction of almost one around $1.04\,R_{\mathrm{pl}}$.

This leads to heating and acceleration of the planetary wind by stellar irradiation with photon energies higher than 60 eV. The heating below the Lyα emission layer becomes less important in the atmosphere of HD 189733 b and the heating fraction is reduced to 0.001 for WASP-43 b, which is a result of increased

free-free emission in hot, lower atmospheric regions. This temperature increase of the dense atmospheric layers close to the lower boundary in massive and compact planets can be seen in panel (b) of Fig. 7.

4.4. Mass loss rates

In the simulations we evaluate the mass-loss rates using the formula $\dot{M}^{sim} = 1/4 \times 4\pi R^2 \rho v$. The additional factor of $1/4$ results from averaging the irradiation over the planetary surface. In our spherical simulation the planet is irradiated from all sides, but in reality only the dayside is illuminated. The difference of the spherical surface and the surface of the planetary dayside disk is $1/4$. The factor is also supported by two-dimensional simulations (Stone & Proga 2009). A sorted list of the calculated mass-loss rates is provided in Table 3. We also provide two more mass loss columns: $\dot{M}$ is the fractional mass loss per Ga, and $\dot{M}_Y^{tot}$ is an estimate for the total, fractional mass loss during the first 100 Ma after formation of the planetary system. This value is derived by linearly scaling the mass loss according to the expected irradiation from the young host star. The XUV emission is derived in the same fashion as before, but assuming average X-ray luminosities for young stars from Stelzer & Neuhäuser (2001), i.e., G-type $\log L_X \approx 29.7$, K-type $\log L_X \approx 29.5$, and M-type $\log L_X \approx 29.0$.

In general, the mass-loss rates are most strongly affected by the gravitational potential, the irradiation level and by the planetary density. The effect of the gravitational potential is directly visible in Fig. 7, looking at the low thermospheric densities of high-potential planets, while the velocities do not differ by much compared to low-potential planets. The impact of the irradiation level can be demonstrated by coming back to our comparison of GJ 436 b with HAT-P-11 b. HAT-P-11 b experiences a five times higher irradiation level and its wind is 4.4 times stronger. The effect of the planetary density on the mass-loss rates can be seen by comparing HD 149026 b and WASP-80 b, which both have almost the same gravitational potential. The irradiation of HD 149026 b is almost twice as strong as in WASP-80 b, but the mass-loss rate is lower. This is a result of the higher planetary density.

Our simulations show that none of the planets is currently unstable. For WASP-12 b this contradicts earlier mass loss estimates (see Sect. 4.5). Among our sample 55 Cnc e is highly interesting, because the planetary density of 4 g cm^{-3} suggests that the planet must consist of a significant amount of volatiles ($\sim 20\%$, Gillon et al. 2012). Our calculated mass-loss rate would erode this amount of volatiles in 23 Ga. Furthermore, the planet may have lost 5 % of its initial mass at young ages. We caution that these results are based on hydrogen dominated atmospheres. The planetary composition has most likely been altered over the lifetime of 55 Cnc e and although the planet can maintain an atmosphere over long timescales, large amounts volatiles are lost in the planetary wind.

4.5. The extreme case of WASP-12 b

WASP-12 b is an exception among all simulated planets. Its extreme proximity of only 2 stellar radii above the stellar photosphere reduces the size of the Roche lobe to only 1.8 R_{pl} above the substellar point. The gravitational potential of the planet is reduced by a factor of $K = 0.28$. This causes the strongest mass-loss rate among the planets in our sample, which is, however, 10 000 times weaker than the proposed mass loss of Li et al.

(2010) and still 400 times weaker than value of Lai et al. (2010). In this case a multidimensional simulation can result in a higher mass-loss rate, because of the elongated shape of the planetary Roche lobe. The Roche lobe height perpendicular to the star-planet axis is $2/3 \times 1.8$ R_{pl} = 1.2 R_{pl} (Li et al. 2010), which results in a gravitational reduction factor of $K = 0.04$. However, this cannot explain the differences of our result and the published values.

For their mass loss estimates, both Li et al. and Lai et al. derived a density of 3×10^{-12} g cm^{-3} at 1.2 R_{pl} and assume a bulk flow with the speed of sound. The density in our simulation decreases more strongly with height, due to a temperature minimum of 1200 K at 1.02 R_{pl}, resulting in a density that is a factor of 100 lower. Thus, the authors assumption of an isothermal atmosphere with a temperature of 3000 K is incorrect. Furthermore the sound speed is reached at the L1 point and at 1.2 R_{pl} it is a factor 10 lower than the sound speed. These two effects cause the large differences between our simulated mass-loss rate and the estimates of Li et al. (2010) and Lai et al. (2010). While according to Li et al. the planet would have a lifetime of only 10 Ma, our simulation results in less than 1 % mass loss per Ga. In respect to the planetary mass loss, this resolves the problem of the small chance to discovering the planet in a brief period of its lifetime.

4.6. Exobase and stable thermospheres

Hydrodynamic simulations are only valid as long as collisions are frequent enough and a Maxwellian velocity distribution is maintained. This is not always true in planetary atmospheres because of the exponential density decrease with height. At a certain height collisions become too infrequent and atmospheric particles move without collisions on parabolic or hyperbolic paths. This height is called the exobase. Energetic atoms from the tail of the Maxwellian velocity distribution can escape from the exobase, a process called Jeans escape. Jeans escape appears on all planetary bodies, but the escape rates are quite small. For expanded thermospheres of hot gas planets Jeans escape is typically one order of magnitude smaller than hydrodynamic escape (Tian et al. 2005). Thus, hydrodynamic escape is the dominant escape process, if the hydrodynamic approximation is valid. We verify the validity of the hydrodynamic simulations in retrospect by determining the height of the exobase, which is defined as the height above which the collision probability for atmospheric constituents is unity in the outward direction (e.g., Tian et al. 2005).

The exobase height crucially depends on the collision cross-section. For planetary atmospheres a typical collision cross-section often used is $\sigma = 3.3 \times 10^{-15}$ cm^2 (Chamberlain 1963; Hunten 1973; Tian et al. 2005; García Muñoz 2007). The calculations of Dalgarno (1960) confirm that this value also holds for collisions of neutral hydrogen, $\sigma = 4.3 \times 10^{-15}$ cm^2. However, some authors argue for a collisionless regime closer to the planetary photosphere. They use an H-H collision cross-section of only $\sigma = 3 \times 10^{-17}$ cm^2 (Ekenbäck et al. 2010; Bourrier & Lecavelier des Etangs 2013), which places the exobase deeper in the atmosphere. However, the atmospheres of these close-in planets are always highly ionized at the exobase level. Thus, charge exchange between H-H$^+$ with a cross-section of $\sigma \sim 2 \times 10^{-15}$ cm^2 (Ekenbäck et al. 2010) becomes the dominant process for determining the height at which neutral hydrogen enters a collisionless regime. Note that the cross-section for proton-proton scattering is yet a factor of 100 larger (e.g. Spitzer 1978;

Table 3. Irradiation of the planets and results from the simulations. Ranking according to the simulated mass-loss rates.

System	$\log L_X$ (erg s^{-1})	Ref.	$\log L_{Ly\alpha}$ (erg s^{-1})	$\log F_{Ly\alpha}{}^c$	Ref.	$\log L_{EUV}$ (erg s^{-1})	$\log F_{XUV}{}^d$	$\log -\Phi_G$ (erg g^{-1})	$\log \dot{M}^{sim}$ (g s^{-1})	$\dot{M}$ (‰ Ga^{-1})	$\dot{M}_Y^{tot}$ (‰)	Lyα abs. (%)
WASP-12 b	< 27.58	7	< 28.58	< −14.66	12	< 28.35	< 4.26	13.14	11.64	5.2	19.7	51.6
GJ 3470 b	27.63	7	28.60	−12.41	12	28.37	3.89	12.33	10.66	17.3	12.5	25.4
WASP-80 b	27.85	1	28.67	−12.97	12	28.46	4.03	13.02	10.57	1.2	1.7	21.7
HD 149026 b	28.60	7	28.91	−12.97	12	28.80	4.29	13.00	10.43	1.3	1.0	6.0
HAT-P-11 b	27.55	7	28.57	−12.65	12	28.33	3.51	12.55	10.29	3.9	8.0	13.5
HD 209458 b	< 26.40	4	28.77	−12.70	8	< 27.84	< 3.06	12.96	10.27	0.5	5.5	20.1
55 Cnc e	26.65	4	28.06	−11.98	11	27.66	3.87	12.41	10.14	8.8	49.5	2.1
GJ 1214 b	25.91	5	< 25.69	< −14.62	10	26.61	2.93	12.19	9.68	4.0	19.0	25.7
GJ 436 b	25.96	4	27.65	−12.46	10	27.14	2.80	12.54	9.65	1.0	4.7	18.8
HD 189733 b	28.18	4	28.43	−12.22	9	28.61	4.32	13.26	9.60	0.1	0.1	9.6
HD 97658 b	27.22	7	28.46	−12.26	12	28.19	2.98	12.33	9.47	2.0	5.8	3.5
WASP-77 b	28.13	1	28.76	−13.26	12	28.59	4.51	13.42	8.79	< 0.1	—	3.4
WASP-43 b	27.88	2	28.68	−13.21	12	28.48	4.82	13.54	8.03	< 0.1	—	4.1
CoRoT-2 b	29.32	6	29.14	−13.80	12	29.13	5.19	13.61	7.63	< 0.1	—	4.1
WASP-8 b	28.45	1	28.86	−13.10	12	28.73	3.66	13.57	*5.0*	< 0.1	—	1.6
WASP-10 b	28.09	1	28.74	−13.24	12	28.57	4.08	13.73	*2.7*	< 0.1	—	—
HAT-P-2 b	28.91	1	29.01	−13.19	12	28.94	4.12	14.14	*< 5.9*	< 0.1	—	—
HAT-P-20 b	28.00	1	28.72	−13.05	12	28.53	4.08	14.18	*< 4.5*	< 0.1	—	—
WASP-38 b	< 28.04	1	< 28.73	< −13.43	12	< 28.55	< 3.46	13.65	—	—	—	—
WASP-18 b	< 26.82	3	< 28.34	< −13.74	12	< 28.02	< 3.99	14.16	—	—	—	—
55 Cnc b	26.65	4	28.06	−11.98	11	27.66	2.14	—	—	—	—	—

Notes. Explanation of the columns: planetary name, X-ray luminosity (0.124-2.48 keV), Lyα luminosity (Linsky et al. 2013), Lyα flux at Earth neglecting interstellar absorption $^{(c)}$ (erg cm^{-2} s^{-1}) , EUV lum. (100-912 Å, Linsky et al. 2014), XUV flux at planetary distance $^{(d)}$ (< 912 Å, erg cm^{-2} s^{-1}) , mass-loss rate from the simulations ($1/4 \times 4\pi R^2 \rho v$), total fractional mass loss in parts per thousand per Ga, fractional cumulative mass loss during first 100 Ma in parts per thousand, integrated Lyα absorption signal (±200 km s^{-1}, optical transit depth is not subtracted).

References. (1) Salz et al. (2015b); (2) Czesla et al. (2013); (3) Pillitteri et al. (2014); (4) Sanz-Forcada et al. (2011); (5) Lalitha et al. (2014); (6) Schröter et al. (2011); (7) prediction based on rotation period and mass (Pizzolato et al. 2003); (8) Wood et al. (2005); (9) Bourrier & Lecavelier des Etangs (2013); (10) France et al. (2013); (11) Ehrenreich et al. (2012); (12) rotation based prediction from (Linsky et al. 2013).

Murray-Clay et al. 2009), so that the ionized wind stays collisional to even larger heights above the planetary photosphere.

The exobase level as defined by Tian et al. (2005) is marked in all plots of the simulated atmospheres, if it is inside the simulated region. For most of our planets the hydrodynamic simulations are valid within the simulation box. In the atmospheres of CoRoT-2 b, WASP-43 b, and WASP-77 b neutral hydrogen decouples from the ionized species between 2.8 and 5.5 R_{pl} (see Fig. 7). The atmosphere of HD 189733 b becomes collisionless for neutral hydrogen at a height of 12 R_{pl}. Neutral hydrogen above this height can be accelerated out of the ionized planetary wind by radiation pressure in the Lyα line. Nevertheless, the thermospheres are collisional for ionized particles. Above 2 R_{pl} ionization of He$^+$ is the main heat source for the wind of CoRoT-2 b. This ion is coupled to H$^+$ and electrons, thus, an ionized planetary wind can form.

More importantly, we find that the atmospheres of the massive and compact planets HAT-P-2 b, HAT-P-20 b, WASP-10 b, and WASP-8 b become collisionless before the atmospheric gas is significantly accelerated. Figure 8 shows this for WASP-8 b. The EUV radiation is absorbed deep in the thermosphere, but does not lead to strong acceleration because of efficient radiative cooling. The density gradient is steep and the atmosphere becomes collisionless for neutral hydrogen at 1.7 R_{pl} and for protons at 3.0 R_{pl}. The strongest acceleration takes place above these layers, where the hydrodynamic simulation is invalid and internal energy cannot be converted into a bulk flow. The simulations of these four planets result in very low mass-loss rates (< 3 × 10^5 g s^{-1}), but these are unphysical and cannot be interpreted as valid predictions. Even if we consider the uncertainties
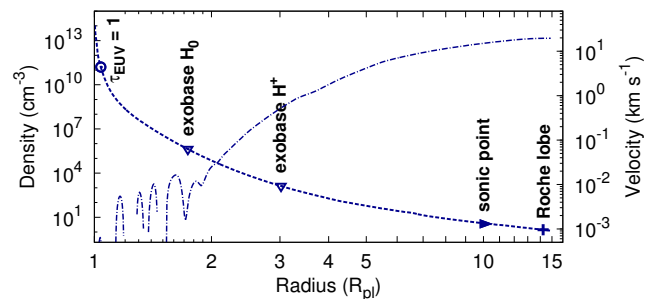
Fig. 8. Mean density and velocity structure in the hydrodynamic simulation of the atmosphere of WASP-8 b. The density is depicted by the dashed line and the velocity by the dash-dotted one. The atmospheric layer where the bulk EUV emission is absorbed is marked by a circle. The triangles mark the radii, where the atmosphere becomes collisionless for neutral hydrogen and protons. The arrow marks the sonic point and the plus sign the Roche lobe size. Oscillations are visible in the velocity structure of the lower atmosphere. The hydrodynamic simulation is only valid below the exobase at 3 R_{pl}. This planet hosts a stable and compact thermosphere.

in our simulations, we conclude that these planets do not support a hydrodynamic wind, but rather compact and stable thermospheres. WASP-38 b and WASP-18 b are similarly compact and massive as WASP-10 b or WASP-8 b, thus, these two hot Jupiters also host stable thermospheres. Naturally, these thermospheres are again subject to Jeans escape and non-thermal escape processes like ion pick-up.
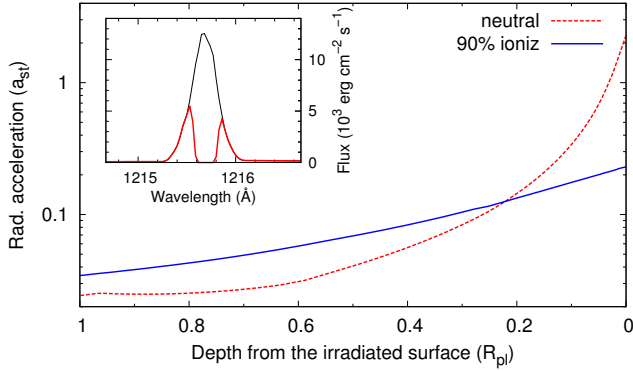
Fig. 9. Radiative acceleration due to Lyα absorption in an upper atmospheric layer of the atmospheres of HD 209458 b. The acceleration is given in units of the stellar gravitational acceleration. A neutral (dashed, red) and a 90% ionized atmosphere (solid, blue) are compared. The insert shows the Lyα flux at the distance of the planet (thin) and the transmitted flux behind this atmospheric layer (thick line). Only in a neutral atmosphere the radiative acceleration can exceed the stellar gravity.

4.7. Ram pressure of the winds

In general, the atmospheres of the compact planets WASP-77 b, WASP-43 b, and CoRoT-2 b are collisional and a planetary wind can form. However, the ram pressures of the planetary winds are only between 0.2 and 0.01 pbar at the sonic point. If we compare these values to a stellar wind pressure of about 10 pbar for a hot Jupiter at 0.05 AU (Murray-Clay et al. 2009), it is most likely that these planetary thermospheres are confined over a large fraction of the planetary surface. Thus, if a hydrodynamic escape exists, the mass-loss rates will be even smaller than the results from our simulations. The same argument holds for HD 189733 b with a ram pressure of only 0.8 pbar at the sonic point. In contrast, the wind of HD 209458 b has a ram pressure of 5 pbar and that of WASP-80 b has already 17 pbar. The wind of WASP-80 b is probably strong enough to blow against the stellar wind pressure over the full dayside of the planet. The ram pressures of the other planets range from 8 pbar (GJ 436 b) to 500 pbar (WASP-12 b).

4.8. Radiation pressure

The absorption of stellar Lyα emission by neutral hydrogen in a planetary atmosphere leads to an acceleration that can exceed the stellar gravitational attraction. If neutral hydrogen is transported beyond the planetary Roche lobe and if it is in a collisionless regime, it can be accelerated to velocities of about 100 km s^{-1} (Bourrier & Lecavelier des Etangs 2013). However, our hydrodynamic simulations show that escaping atmospheres stay collisional to large distances above the planetary photosphere (see Fig. 7). Hence, when considering radiation pressure, we must take into account that neutral hydrogen is coupled to the ionized planetary wind through charge exchange. This reduces the radiation pressure according to the ionization fraction of the atmosphere.

Radiation pressure is included in our simulations, but in the standard simulations the resolution of the SED does not resolve the Lyα line. While the line flux is correct, the peak is about a factor 10 too small, which is essentially equivalent to neglecting the radiation pressure. To evaluate the relevance of this effect, we performed a test of the radiative acceleration with a simplified CLOUDY simulation of a hydrogen cloud with a density of 10^5 cm^{-3}, which is approximately the density at the top of the

atmosphere of HD 209458 b. We ran the test with a fixed ionization fraction of zero and 90%, using the same SED as in the standard simulation, but with an increased resolution at the Lyα line to fully resolve the central emission line strength.

Figure 9 shows the resulting radiative acceleration. The neutral atmosphere experiences 2.5 times the gravitational acceleration of the host star at the upper most layers of the atmosphere. Shadowing effects lead to a rapid decrease in the acceleration below the irradiated surface. In principle neutral hydrogen could be accelerated away from the planetary thermosphere, which is consistent with the results from Bourrier & Lecavelier des Etangs (2013). However, the upper atmosphere of HD 209458 b is about 90% ionized and collisional. This reduces the radiative acceleration by a factor of ten as depicted in Fig. 9. In the escaping atmosphere of HD 209458 b the radiative acceleration reduces the gravitational attraction of the host star only slightly. The radiation pressure in the Lyα line is more than a factor of 30 smaller than the ram pressure of the planetary wind at the Roche lobe of HD 209458 b. The wind from the dayside of the planet cannot be stopped by radiation pressure, it will rather collide with the stellar wind as described in the previous section.

HAT-P-11 b and HD 97658 b experience the strongest radiative acceleration due to a favorable combination of the distance from the host star, the host star's Lyα luminosity, and the neutral hydrogen fraction in the upper thermosphere. In a thin layer (width < 0.5 R_{pl}) at the top of the simulated atmosphere these two planets experience a radiative acceleration of half the gravitational acceleration of the host star. The reduced stellar attraction close to our upper boundary does not affect the structure of the thermospheres below 14 R_{pl}. In all other systems the radiative acceleration is less than a tenth of the gravitational acceleration of the host star.

In summary, acceleration due to radiation pressure in the Lyα line can be neglected in the studied systems. It only reduces the effective stellar gravitational attraction in the uppermost thermospheric layers. The small amount of neutral hydrogen, which reaches the collisionless regime in the simulations of HD 189733 b, WASP-77 b, WASP-43 b, and CoRoT-2 b is irrelevant for the absorption signals produced in transit observations (see Sects. 5.2 and 5.3).

5. Predicted absorption signals

5.1. Method

The simulated systems were selected based on a prediction of the host stars' Lyα fluxes at Earth, so that all host stars are potentially bright enough to detect the planetary atmospheres. We now use the spherically symmetric atmospheres to calculate the Lyα absorption signals to find the most promising targets for transit spectroscopy. We emphasize that when we talk about Lyα absorption by planetary atmospheres, the actual physical process is scattering of photons into different lines of sight. Absorption of Lyα with collisional de-excitation occurs only deep in the simulated atmospheres. We do not account for any emission or line transfer in the computation of the absorption signal, or for scattering of photons into our line of sight. Essentially our treatment is a single scattering approximation. We further assume a homogeneous brightness of the stellar disk in Lyα emission. This approximation is likely valid for emission in the Lyα line wings at least for solar-like stars (see Introduction).

To compute the absorption we interpolate the spherical atmosphere onto a Cartesian grid with a resolution of 201 cells. We select all rays above the planetary surface; the Lyα trans-
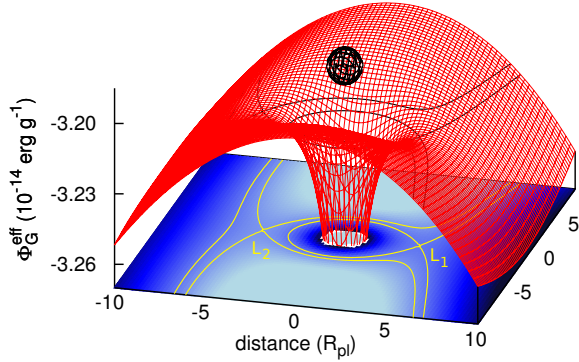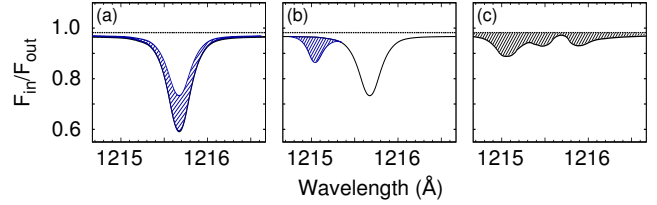
Fig. 10. Effective gravitation potential in HD 209458 b. The size of the planet is depicted by the black sphere. The position of the host star is toward the right-hand side. The height of the Roche lobe in our simulation corresponds to the position of the L_1 Lagrange point. The spherically symmetric approximation for the potential becomes invalid above the Roche lobe.

Fig. 11. Formation of the measured Lyα absorption signals. (a) Absorption of an unperturbed spherical atmosphere with the absorption from unbound hydrogen marked. (b) Absorption after interaction with the stellar wind; the absorption of unbound hydrogen is shifted into the line wing. (c) Measured absorption signal after interstellar absorption and convolution with the instrumental line spread function.

mission in a single ray is given by the product of the absorption in each cell, with the absorption in the individual cell computed according to the local density, temperature, and tangential velocity. We use the standard Lyα absorption cross-section with a Voigt-profile. The Doppler width is given by the sum of the local thermal and turbulent widths; the latter is given by the speed of sound. Deuterium absorption is included with a deuterium fraction of (D/H) = 2.2×10^{-5} according to measurements from Jupiter (Lellouch et al. 2001). This is slightly higher than the deuterium fraction of (D/H) = 1.56×10^{-5} in the Local Bubble (Wood et al. 2004). The absorption of each ray is weighted with the fractional area of the stellar disk that a ring with the given height above the planetary photosphere covers. The resulting transmission signal is folded with the line spread function for the $52'' \times 0.1''$ aperture of the Space Telescope Imaging Spectrograph on board the Hubble Space Telescope. This reduces the sharpness of the predicted absorption signals and provides results comparable with measurements. The procedure is similar to the description in Koskinen et al. (2010), but we do not include interstellar absorption (see below).

We calculate the absorption from the lower boundary to the height of the Roche lobe and for the complete simulated atmosphere (up to a height of 15 R_{pl}). Fig. 10 depicts the effective gravitational potential in the rotating two-body system of HD 209458 b and its host star. The spherical approximation of our simulation is only valid within the Roche lobe indicated by the inner yellow line. At larger heights, the effective gravitational potential strongly favors material flows toward or away from the host star. The twofold approach in the computation of the absorption signals follows the idea that the absorption signal from below the Roche lobe is the signal of the unperturbed planetary wind, which can be approximated by the spherical simulations. The signal of the full atmospheres shows the complete absorption of all neutral hydrogen transported into the thermosphere and beyond the Roche lobe.

The excess absorption by unbound neutral hydrogen will be shifted to larger velocity offsets by the non-spherical gravitational potential and by an interaction with the stellar wind. The two colliding winds are in a collisional regime, as simulated for example by Tremblin & Chiang (2013). They form an interaction region, where hot stellar protons are mixed with cold neutral hydrogen from the planetary wind. Charge exchange produces a hot neutral hydrogen population. Strong turbulence in the inter-

action region increases the width of the absorption signal and the material also reaches high velocity offsets. Thus, the excess absorption of unbound neutral hydrogen is shifted into the line wings. This radial velocity shift is depicted in Fig. 11 (a) and (b). Panel (c) depicts the signal after the line core has been absorbed by interstellar hydrogen, which is how we would see the signal from Earth. Only by shifting the excess absorption caused by unbound hydrogen into the line wing, it becomes detectable, otherwise it would be extinguished by interstellar absorption. Note that the only source for neutral hydrogen is the simulated planetary wind; the total number of neutral hydrogen atoms is not affected by charge exchange. For the sake of completeness, we note that the absorption signal does not necessarily depend linearly on the amount of neutral hydrogen in the thermosphere. If neutral hydrogen is shifted in velocity space, the shift of a small additional absorption signal in the line center can result in a deeper absorption signal in the line wing, but this effect is beyond the scope of our model.

5.2. Comparison with measured absorption signals

First, we compare the computed absorption signals to the measurements in HD 209458 b, HD 189733 b, GJ 436 b, and to the non-detection in 55 Cnc e. For this purpose we analyzed the available data from the targets and show our simulated absorption signals in comparison with the measured absorption in Fig. 12. Only for HD 209458 b we show the transmission spectrum from the detailed analysis of Ben-Jaffel (2008). The figure also contains the stellar in- and out-of-transit Lyα line profiles, as well as our calculated transmission images. In general, the calculated transmission images correlate with the absorption signals as follows: The deep absorption in the line center is produced by the thin, extended atmospheric layers, which are partially transparent in the transmission images, but cover a large fraction of the stellar disk. The dense, lower atmospheric layers absorb most of the Lyα radiation also in the line wings, but they cover only a smaller fraction of the stellar disk. Our results for 55 Cnc e are given in Fig. 13 along with the measurements by Kulow et al. (2014).

The integrated absorption signals (± 200 km s^{-1}) are provided in Table 4. Most of the absorption occurs in the line center, where interstellar absorption extinguishes the signal. However, we do not include interstellar absorption in the prediction of the absorption signals, because according to our model the measured absorption signals in the line wings is proportional to the excess absorption by unbound neutral hydrogen (see Fig. 11). The computed absorption depth reproduces the observed trend (see Table 4): We derive large absorption signals for HD 209458 b and GJ 436 b, where large signals were measured; in HD 189733 b
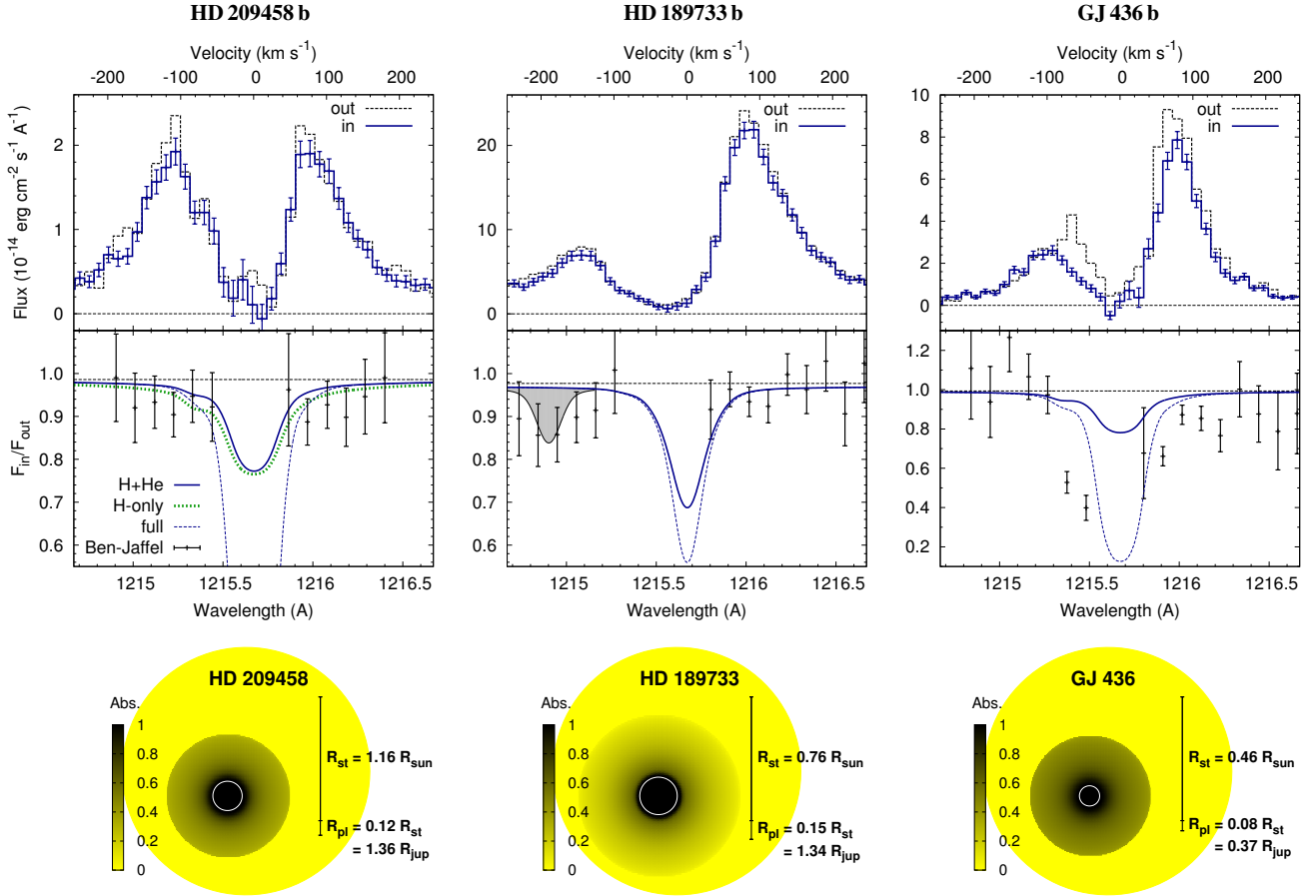
Fig. 12. Comparison of the measured Lyα absorption signals with the absorption resulting from our simulations. The upper panels show the in- and out-of-transit Lyα line profiles; the middle panels show the flux ratio binned by a factor of two. Computed transmission images are depicted at the bottom; the size of the atmospheres is given by the height of the Roche lobe. System names are provided in the figure. The central part of the Lyα line affected by geocoronal emission is not shown in the middle panels. For HD 209458 b we show the flux ratio from a detailed analysis by Ben-Jaffel (2008); for HD 189733 b and GJ 436 we rely on our own data reduction, which is consistent with the discovery papers (Lecavelier des Etangs et al. 2012; Kulow et al. 2014). The horizontal dashed lines represent the optical transit depth; solid thick lines show the absorption from the atmosphere below the Roche lobe; the dashed thin lines depict the absorption from the complete simulated atmosphere. For the system HD 209458 b we also depict the absorption from the Roche lobe of the H-only simulation by the green dotted line. The middle panel of HD 189733 b also contains the excess absorption from unbound neutral hydrogen shifted by $-180\,\mathrm{km\,s^{-1}}$ (filled, gray curve).

the measured and simulated absorption signals are smaller; and for 55 Cnc e the non-detection agrees with the results from the simulations. Since our simulations were not fitted to the measured absorption signals, but are based on measurements and assumptions with considerable uncertainties, we cannot expect a better agreement with our results.

The middle panel in the left-hand column of Fig. 12 shows the absorption signal of HD 209458 b, which is measured in the blue and in the red line wings. The absorption has been discussed in detail by Murray-Clay et al. (2009) and by Koskinen et al. (2013a). HD 209458 b is the only system, where the absorption signal can be solely explained by a spherical atmosphere, depending on the height of the H/H$^+$ transition layer. With an ionization front at a height of 1.4 R_{pl}, Murray-Clay et al. cannot reproduce the measured absorption, but in the model of Koskinen et al. the transition occurs at a height of 3.4 R_{pl} and, thus, their predicted absorption fits the transit observation. Our simulation results in an H/H$^+$ transition layer at a height of 1.6 R_{pl}, which again does not produce sufficient absorption. However, a twice as strong planetary wind already shifts the ionization front

to 2.3 R_{pl} as seen in our H-only simulation (see Sect. 4.2). The absorption signal of the H-only atmosphere produces a better fit to the measured absorption, but still remains insufficient (see Fig. 12). The fact that a relatively small change in the atmosphere (see Sect. 4.2.2) decisively affects the absorption signal renders it difficult to decide whether a spherically expanding atmosphere causes the absorption signal, or if significant additional absorption by unbound neutral hydrogen is required.

Our simulation further results in large amounts of unbound hydrogen, which cause additional absorption mostly in the line center (depicted by the dashed line in the middle panel in the left-hand column of Fig. 12). Because of interstellar absorption this component is not directly observable. However, our model is based on the assumption that the stellar wind partially shifts the absorption of unbound hydrogen into the line wings. In relation to GJ 436 b, we would expect stronger absorption in the blue line wing and a cometary tail like structure; however, nothing alike has been observed. There are several possibilities to explain these differences. Our estimate for the XUV irradiation level is potentially too low for this system. A higher irradiation

Table 4. Absorption signals from observations and simulations.

System	opt. TD (%)	Measured Lyα abs. (%)	Simulated Lyα abs. (%)	Ref.
GJ 436 b	0.7	22.9 ± 4.8	19	3
HD 209458 b	1.5	8.4 ± 2.0	20	1
HD 189733 b[A]	2.4	2.9 ± 1.4	9.6	2
55 Cnc e	0.05	0.7 ± 1.0	2.1	4

Notes. The columns are: planet name, optical transit depth (TD), measured absorption (range of ±200 km s^{-1}, excluding geocoronal contamination), predicted absorption of the full atmosphere in the range of ±200 km s^{-1}. [A] The absorption signal of HD 189733 b is only significant in the blue line wing.

References. (1) Ben-Jaffel (2008); (2) Lecavelier des Etangs et al. (2012); (3) Kulow et al. (2014); (4) Ehrenreich et al. (2012).

Fig. 13. Simulated Lyα transmission for 55 Cnc e. Symbols are the same as in Fig. 12. The transit data is from Ehrenreich et al. (2012). The non-detection of a planetary absorption signal agrees with the result from our simulation.

level causes a stronger but also more ionized planetary wind and, thus, reduces the amount of unbound neutral hydrogen. Also a partially confined atmosphere or a weak interaction with the stellar wind could be responsible for the different measured absorption signals of HD 209458 b and GJ 436 b.

In the case of HD 189733 b it is impossible to explain the spectral shape of the measured absorption signal with a spherically expanding atmosphere. The absorption of HD 189733 b is found at radial velocity shifts of up to −250 km s^{-1} and around +100 km s^{-1} (see Fig. 12). Even considering all uncertainties, a spherical wind will not produce sufficient absorption at such high line shifts. The absorption signal from our simulation is narrow compared with the signal of HD 209458 b. This is caused by the highly ionized planetary wind driven by strong XUV irradiation. The low-density neutral hydrogen in the upper thermosphere absorbs only close to the line center. The excess absorption of unbound neutral hydrogen is almost sufficient to explain the signal, detected in the line wing, when shifted by −180 km s^{-1} (see Fig. 12).

For GJ 436 b we show the absorption in the post-transit observation, which is larger than the in-transit absorption (Kulow et al. 2014). This feature indicates a cometary tail like structure. The absorption of the atmosphere below the Roche lobe is too weak to explain the measured absorption signal. Nevertheless, there is sufficient unbound neutral hydrogen to explain the observation as indicated by the dashed line in Fig. 12. In contrast to HD 189733 b, the radial velocity shift of the measured signal is smaller.

Excess absorption was not detected during the transit of 55 Cnc e (Ehrenreich et al. 2012). There is a weak signal in the blue line wing, but the false alarm probability is 89%. The absorption produced by the simulated escaping atmosphere including unbound hydrogen is maximally 8% in the line center. Although the planet does host a strong wind, the simulated absorption signal remains small, mainly because the planet is very small compared to its host star, but also because the ionization fraction in the thermosphere is higher as a result of the strong irradiation. In principle, this signal could have been detected, if it was completely shifted into the line wing. However, also the simulated signal is close to the detection limit and, considering the uncertainties of our approach, the simulations agree with the observations. It is unfortunate that the wind of one of the most strongly affected planets in terms of the fractional mass loss (see
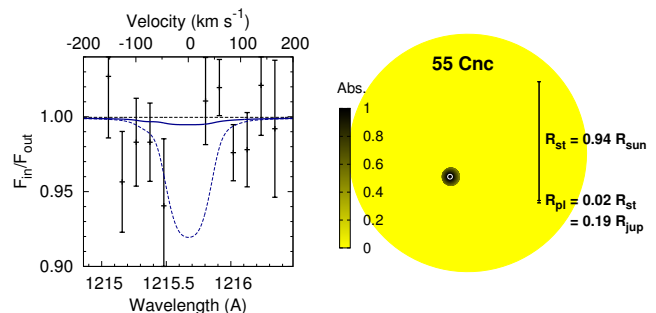
Sect. 4.4) is probably not detectable with today's instrumentation.

The direct comparison of the absorption signals in the systems HD 209458 b, HD 189733 b, and GJ 436 b reveals remarkable differences in the spectral shapes of the absorption signals. While our 1D models reproduce the trend of the measured absorption depth in the systems, the key to a better understanding of the planetary winds lies in the ability to explain the different spectral shapes.

5.3. Absorption signals from nearby systems

Figures 14 & 15 show the calculated absorption signals and the transit images for all planets of our sample; Table 3 provides the integrated absorption signals in the range of ±200 km s^{-1}. We must keep in mind that although the absorption is depicted in the line center, where interstellar absorption would extinguish any planetary signal, we expect that a fraction of the absorption of unbound hydrogen is shifted into the line wings just as in the detected absorption signals of HD 189733 b and GJ 436 b.

The low-potential planets produce deeper absorption signals, because they host more expanded neutral atmospheres and unbound neutral hydrogen causes strong additional absorption. All of the low-potential planets qualify for Lyα transit measurements in terms of the expected absorption signal. WASP-80 b is one of the most promising systems in the search for yet undetected expanded atmospheres. The planet's size is large compared to its host star and the Roche lobe has an extend of 0.85 R_{st}. Thus, the planetary atmosphere can almost cover the complete host star. This results in the strongest predicted absorption signal with a depth of 0.64 not including excess absorption of unbound hydrogen.

The simulated absorption signal of GJ 3470 b is even stronger than that of WASP-80 b if unbound hydrogen is included. For this planet we speculate that strong absorption in the post-transit phase may be present. Although GJ 1214 b also produces a large absorption signal, the host star was not detected in a Lyα observations with the Hubble Space Telescope (France et al. 2013), so that the absorption cannot be measured in this line with current instrumentation.
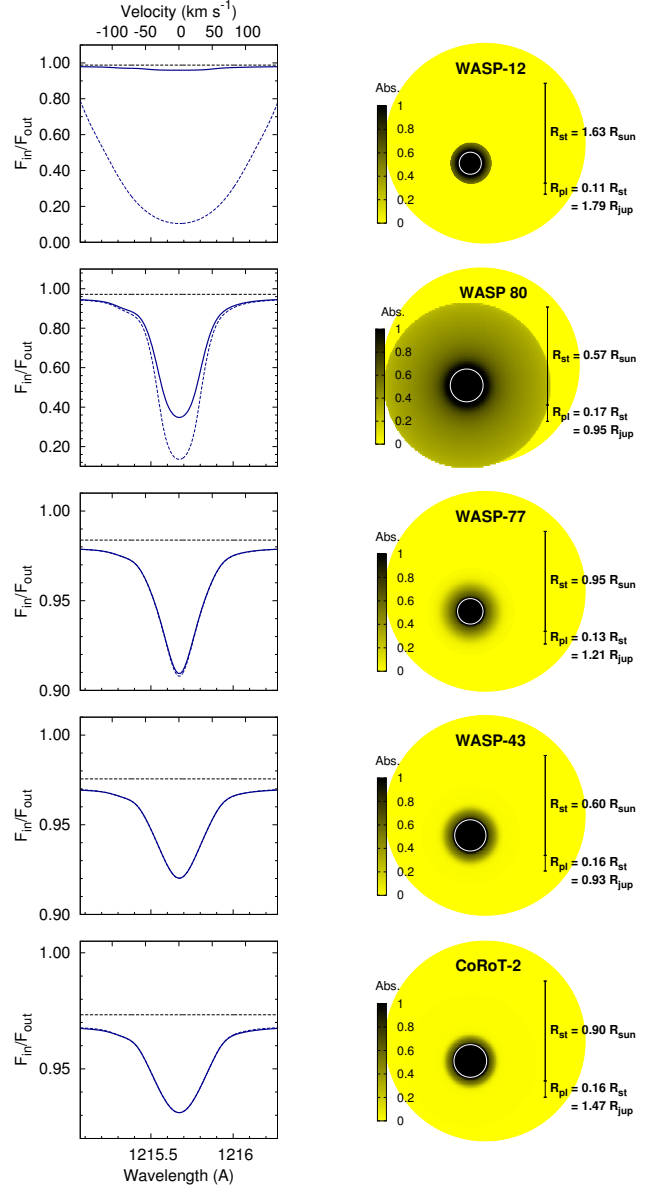
HD 97658 b produces the smallest total absorption signal of the low-potential planets due to the unfavorable planet to star size ratio. We do not predict absorption of unbound hydrogen for this planet, because the Roche lobe is larger than our simulation box. Our computed signal is about twice as strong as that of 55 Cnc e, which in principle could be detected with the HST.
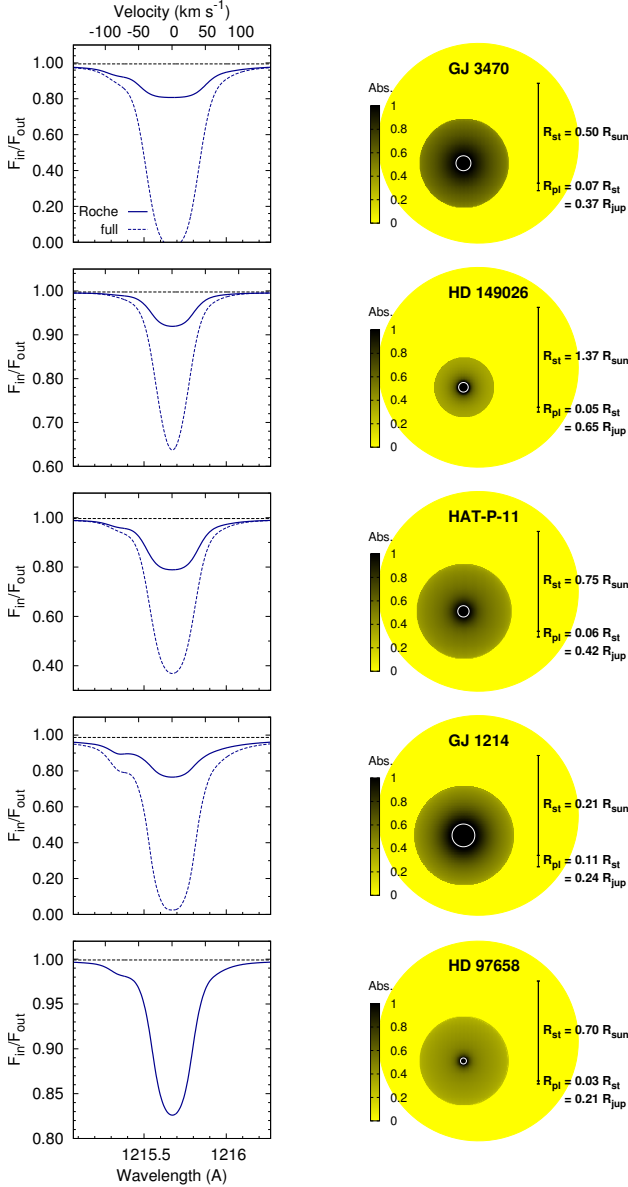
Fig. 14. Simulated Lyα transmission for low-potential planets. For each system we show the absorption in the Lyα line from below the Roche lobe (solid line) and from unbound hydrogen (dashed, blue). Black dashed lines indicate the optical transit depth. The calculated transmission image is depicted next to the spectrum for each system. The mass-loss rate decreases from top to bottom.

Fig. 15. Simulated Lyα transmission spectra and images for high-potential planets plus WASP-80 b (same as Fig. 14). With the exception of WASP-12 b (see text) and WASP-80 b, these planets produce small absorption signals. WASP-80 b produces the strongest absorption signal of all planets.

This super-Earth is highly interesting, because it could be the closest proxy to the young Venus, enshrouded in a dense protoatmospheric hydrogen envelope, where the evaporation process can be measured. The mass of this planet is only 8 Earthmasses and the irradiation level is similar to that of Venus at a solar age of 100 Ma ($\sim$1000 erg cm^{-2} s^{-1}, Ribas et al. 2005)

The large mass-loss rate of WASP-12 b results in strong absorption of unbound hydrogen. The absorption width is caused by velocities of up to 100 km s^{-1} in the upper thermosphere. In principle, the strong absorption agrees with the detection of excess absorption in metal lines (Fossati et al. 2010), but Lyα emission cannot be measured in this system due to its large distance.

In the atmospheres of WASP-43 b, WASP-77 b, or CoRoT-2 b neutral hydrogen remains confined within the Roche lobe. The predicted excess absorption for these three planets, subtracting the optical transit depth, is more than a factor of four weaker than the signals in HD 209458 b or HD 189733 b. This amount of absorption cannot be measured with the HST.

5.4. Absorption signals of stable thermospheres

So far, we did not further analyze the atmospheres of HAT-P-2 b, HAT-P-20 b, WASP-10 b, and WASP-8 b, because our hydrodynamic simulations are not valid in their collisionless ther-
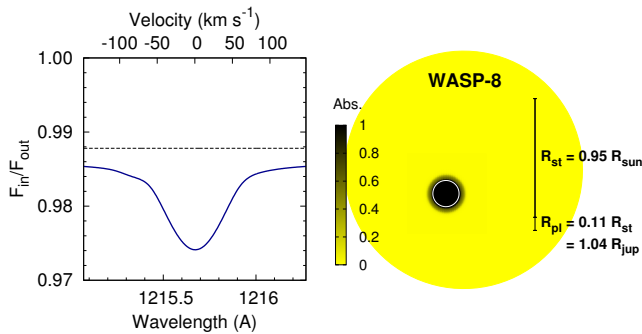
Fig. 16. Simulated Lyα transmission for WASP-8 b (same as Fig. 14). The neutral part of thermosphere is only slightly expanded and cannot be detected in transit observations.

mospheres (see Sect. 4.6). Nevertheless, below $2\,R_{pl}$ the atmospheres are collisional, nearly static, and essentially in radiative equilibrium. Thus, we can use these compact stable thermospheres to predict the Lyα absorption signals of hot gas planets with hydrodynamically stable atmospheres. As an example, we show the absorption signal of WASP-8 b (see Fig. 16). The planets only have slightly expanded neutral atmospheres, because the temperatures are high in stable thermospheres without adiabatic cooling. The thermospheres produce about 1% of excess absorption in the Lyα line, which is not detectable with today's instrumentation. The same applies to WASP-18 b and WASP-38 b (see Sect. 4.6).

6. Conclusion

We present coupled photoionization-hydrodynamics simulations of the planetary winds from hot gas planets in the solar neighborhood. The most promising candidates in terms of Lyα transit spectroscopy were selected for the simulations, which were performed with our TPCI code. We have explained the behavior of the escaping atmospheres in detail with a focus on the differences between winds from small planets and massive, compact planets. The use of a detailed microphysics solver including radiative cooling has proven to be crucial for the results presented here. In particular, we find a transition from strong winds in planets with a low gravitational potential to stable atmospheres in high-potential planets. The transition occurs due to strong radiative cooling in hot, compact thermospheres of high-potential planets. Radiative cooling is weak in smaller planets, because adiabatic cooling in the rapidly expanding atmospheres efficiently reduces the thermospheric temperatures. In our simulations of hydrogen and helium atmospheres, Lyα and free-free emission are the most important cooling agents. Specifically, we found stable thermospheres in the planets HAT-P-2 b, HAT-P-20 b, WASP-8 b, WASP-10 b, WASP-38 b, and WASP-18 b.

Lyα absorption signals of the spherically symmetric atmospheres are presented. The comparison with the measured absorption in HD 209458 b, GJ 436 b, HD 189733 b, and also the non-detection in 55 Cnc e shows that the decreasing trend in the absorption depth of these four systems is reproduced by our simulations. Spherically expanding atmospheres do not explain the measured radial velocity shifts of the absorption signals. Since our simulations have shown that radiation pressure is negligible in the hydrodynamically escaping atmospheres, we agree with Murray-Clay et al. (2009) that the colliding planetary and stellar winds are most likely responsible for the line shifts. Charge exchange in an interaction region can create a hot, strongly turbulent population of neutral hydrogen with a large velocity offset (Holmström et al. 2008; Tremblin & Chiang 2013). Nevertheless, our simulated planetary winds provide the amount of neutral hydrogen in the thermospheres and, thus, determine the total amount of absorption.

We showed that, in general, planets with a smaller gravitational potential produce larger absorption signals, because their atmospheres are more expanded and contain more neutral hydrogen. The comparison of planets with stable atmospheres and planets hosting strong winds further shows that escaping atmospheres are essential for the detection of Lyα absorption signals. If the atmospheres of hot gas planets were confined by an outer pressure, the mean temperatures would rise higher due to the lack of adiabatic cooling. Such atmospheres are strongly ionized and produce only little Lyα absorption.

Progress in this field requires on one hand multidimensional simulations including stellar and planetary winds, as well as the charge exchange process. On the other hand, a broader observational basis is essential to understand the influences of system parameters on the absorption signals. Based on the predicted strong absorption signals, WASP-80 b and GJ 3470 b are the most promising targets in the search for yet undetected expanding atmospheres.

References

Alonso, R., Auvergne, M., Baglin, A., et al. 2008, A&A, 482, L21
Aluru, N., Law, K., Raefsky, A., Pinsky, P., & Dutton, R. 1995, Computer Methods in Applied Mechanics and Engineering, 125, 187
Bakos, G. Á., Hartman, J., Torres, G., et al. 2011, ApJ, 742, 116
Bakos, G. Á., Kovács, G., Torres, G., et al. 2007, ApJ, 670, 826
Bakos, G. Á., Torres, G., Pál, A., et al. 2010, ApJ, 710, 1724
Ballester, G. E. & Ben-Jaffel, L. 2015, ArXiv e-prints [arXiv:1503.01621]
Ballester, G. E., Sing, D. K., & Herbert, F. 2007, Nature, 445, 511
Banks, P. M. & Kockarts, G. 1973, Aeronomy.
Barros, S. C. C., Faedi, F., Collier Cameron, A., et al. 2011, A&A, 525, A54
Ben-Jaffel, L. 2007, ApJ, 671, L61
Ben-Jaffel, L. 2008, ApJ, 688, 1352
Ben-Jaffel, L. & Ballester, G. E. 2013, A&A, 553, A52
Berta, Z. K., Charbonneau, D., Bean, J., et al. 2011, ApJ, 736, 12
Biddle, L. I., Pearson, K. A., Crossfield, I. J. M., et al. 2014, MNRAS, 443, 1810
Bonfils, X., Gillon, M., Udry, S., et al. 2012, A&A, 546, A27
Bouchy, F., Udry, S., Mayor, M., et al. 2005, A&A, 444, L15
Bourrier, V. & Lecavelier des Etangs, A. 2013, A&A, 557, A124
Brown, D. J. A. 2014, MNRAS, 442, 1844
Brown, D. J. A., Collier Cameron, A., Díaz, R. F., et al. 2012, ApJ, 760, 139
Butler, R. P., Marcy, G. W., Williams, E., Hauser, H., & Shirts, P. 1997, ApJ, 474, L115
Butler, R. P., Vogt, S. S., Marcy, G. W., et al. 2004, ApJ, 617, 580
Carter, J. A., Agol, E., Chaplin, W. J., et al. 2012, Science, 337, 556
Castor, J. I. 1970, MNRAS, 149, 111
Chadney, J. M., Galand, M., Unruh, Y. C., Koskinen, T. T., & Sanz-Forcada, J. 2015, Icarus, 250, 357
Chamberlain, J. W. 1963, Planet. Space Sci., 11, 901
Charbonneau, D., Allen, L. E., Megeath, S. T., et al. 2005, ApJ, 626, 523
Charbonneau, D., Berta, Z. K., Irwin, J., et al. 2009, Nature, 462, 891
Charbonneau, D., Brown, T. M., Latham, D. W., & Mayor, M. 2000, ApJ, 529, L45
Chassefière, E. 1996, J. Geophys. Res., 1012, 26039
Christian, D. J., Gibson, N. P., Simpson, E. K., et al. 2009, MNRAS, 392, 1585
Crossfield, I. J. M., Knutson, H., Fortney, J., et al. 2012, ApJ, 752, 81
Cubillos, P., Harrington, J., Madhusudhan, N., et al. 2012, in AAS/Division for Planetary Sciences Meeting Abstracts, Vol. 44, AAS/Division for Planetary Sciences Meeting Abstracts, 103.08

Czesla, S., Salz, M., Schneider, P. C., & Schmitt, J. H. M. M. 2013, A&A, 560, A17

Dalgarno, A. 1960, Proceedings of the Physical Society, 75, 374

Dere, K. P., Landi, E., Mason, H. E., Monsignori Fossi, B. C., & Young, P. R. 1997, A&AS, 125, 149

Dere, K. P., Landi, E., Young, P. R., et al. 2009, A&A, 498, 915

Ehrenreich, D., Bourrier, V., Bonfils, X., et al. 2012, A&A, 547, A18

Ehrenreich, D., Lecavelier des Etangs, A., Hébrard, G., et al. 2008, A&A, 483, 933

Ekenbäck, A., Holmström, M., Wurz, P., et al. 2010, ApJ, 709, 670

Elitzur, M. 1982, Reviews of Modern Physics, 54, 1225

Ferland, G. J., Korista, K. T., Verner, D. A., et al. 1998, PASP, 110, 761

Ferland, G. J., Porter, R. L., van Hoof, P. A. M., et al. 2013, Rev. Mexicana Astron. Astrofis., 49, 137

Fischer, D. A., Marcy, G. W., Butler, R. P., et al. 2008, ApJ, 675, 790

Fossati, L., Bourrier, V., Ehrenreich, D., et al. 2015, ArXiv e-prints [arXiv:1503.01278]

Fossati, L., Haswell, C. A., Froning, C. S., et al. 2010, ApJ, 714, L222

France, K., Froning, C. S., Linsky, J. L., et al. 2013, ApJ, 763, 149

García Muñoz, A. 2007, Planet. Space Sci., 55, 1426

Gillon, M., Demory, B.-O., Benneke, B., et al. 2012, A&A, 539, A28

Gottlieb, S. & Shu, C.-W. 1996, NASA CR-201591 ICASE Rep. 96-50

Gray, R. O., Corbally, C. J., Garrison, R. F., McFadden, M. T., & Robinson, P. E. 2003, AJ, 126, 2048

Hall, J. C., Lockwood, G. W., & Skiff, B. A. 2007, AJ, 133, 862

Haswell, C. A., Fossati, L., Ayres, T., et al. 2012, ApJ, 760, 79

Hebb, L., Collier-Cameron, A., Loeillet, B., et al. 2009, ApJ, 693, 1920

Hellier, C., Anderson, D. R., Collier Cameron, A., et al. 2009, Nature, 460, 1098

Hellier, C., Anderson, D. R., Collier Cameron, A., et al. 2011, A&A, 535, L7

Henry, G. W., Howard, A. W., Marcy, G. W., Fischer, D. A., & Johnson, J. A. 2011, ArXiv e-prints [arXiv:1109.2549]

Henry, G. W., Marcy, G. W., Butler, R. P., & Vogt, S. S. 2000, ApJ, 529, L41

Henry, G. W. & Winn, J. N. 2008, AJ, 135, 68

Holmström, M., Ekenbäck, A., Selsis, F., et al. 2008, Nature, 451, 970

Howard, A. W., Johnson, J. A., Marcy, G. W., et al. 2011, ApJ, 730, 10

Hunten, D. M. 1973, Journal of Atmospheric Sciences, 30, 1481

Isaacson, H. & Fischer, D. 2010, ApJ, 725, 875

Jensen, A. G., Redfield, S., Endl, M., et al. 2012, ApJ, 751, 86

Jiang, G.-S. & Shu, C.-W. 1996, Journal of Computational Physics, 126, 202

Johnson, J. A., Winn, J. N., Cabrera, N. E., & Carter, J. A. 2009, ApJ, 692, L100

Knutson, H. A., Charbonneau, D., Allen, L. E., et al. 2007, Nature, 447, 183

Knutson, H. A., Charbonneau, D., Cowan, N. B., et al. 2009, ApJ, 703, 769

Knutson, H. A., Madhusudhan, N., Cowan, N. B., et al. 2011, ApJ, 735, 27

Koskinen, T. T., Harris, M. J., Yelle, R. V., & Lavvas, P. 2013a, Icarus, 226, 1678

Koskinen, T. T., Yelle, R. V., Harris, M. J., & Lavvas, P. 2013b, Icarus, 226, 1695

Koskinen, T. T., Yelle, R. V., Lavvas, P., & Lewis, N. K. 2010, ApJ, 723, 116

Kulow, J. R., France, K., Linsky, J., & Loyd, R. O. P. 2014, ApJ, 786, 132

Lai, D., Helling, C., & van den Heuvel, E. P. J. 2010, ApJ, 721, 923

Lalitha, S., Poppenhaeger, K., Singh, K. P., Czesla, S., & Schmitt, J. H. M. M. 2014, ApJ, 790, L11

Lammer, H., Selsis, F., Ribas, I., et al. 2003, ApJ, 598, L121

Lanza, A. F., Pagano, I., Leto, G., et al. 2009, A&A, 493, 193

Lecavelier des Etangs, A., Bourrier, V., Wheatley, P. J., et al. 2012, A&A, 543, L4

Lecavelier des Etangs, A., Ehrenreich, D., Vidal-Madjar, A., et al. 2010, A&A, 514, A72+

Lellouch, E., Bézard, B., Fouchet, T., et al. 2001, A&A, 370, 610

Li, S.-L., Miller, N., Lin, D. N. C., & Fortney, J. J. 2010, Nature, 463, 1054

Linsky, J. L., Fontenla, J., & France, K. 2014, ApJ, 780, 61

Linsky, J. L., France, K., & Ayres, T. 2013, ApJ, 766, 69

Linsky, J. L., Yang, H., France, K., et al. 2010, ApJ, 717, 1291

Maxted, P. F. L., Anderson, D. R., Collier Cameron, A., et al. 2013, PASP, 125, 48

McArthur, B. E., Endl, M., Cochran, W. D., et al. 2004, ApJ, 614, L81

Mignone, A., Bodo, G., Massaglia, S., et al. 2007, ApJS, 170, 228

Mignone, A., Zanni, C., Tzeferacos, P., et al. 2012, ApJS, 198, 7

Murray-Clay, R. A., Chiang, E. I., & Murray, N. 2009, ApJ, 693, 23

Narita, N., Fukui, A., Ikoma, M., et al. 2013, ApJ, 773, 144

Nichols, J. D., Wynn, G. A., Goad, M., et al. 2015, ArXiv e-prints [arXiv:1502.07489]

Pál, A., Bakos, G. Á., Torres, G., et al. 2010, MNRAS, 401, 2665

Parker, E. N. 1958, ApJ, 128, 664

Penz, T., Erkaev, N. V., Kulikov, Y. N., et al. 2008, Planet. Space Sci., 56, 1260

Pillitteri, I., Wolk, S. J., Sciortino, S., & Antoci, V. 2014, ArXiv e-prints [arXiv:1406.2620]

Pizzolato, N., Maggio, A., Micela, G., Sciortino, S., & Ventura, P. 2003, A&A, 397, 147

Poppenhaeger, K., Schmitt, J. H. M. M., & Wolk, S. J. 2013, ApJ, 773, 62

Queloz, D., Anderson, D. R., Collier Cameron, A., et al. 2010, A&A, 517, L1

Redfield, S. & Linsky, J. L. 2008, ApJ, 673, 283

Ribas, I., Guinan, E. F., Güdel, M., & Audard, M. 2005, ApJ, 622, 680

Salz, M., Banerjee, R., Mignone, A., et al. 2015a, accepted for publication in A&A

Salz, M., Schneider, P. C., Czesla, S., & Schmitt, J. H. M. M. 2015b, ArXiv e-prints [arXiv:1502.00576]

Sanz-Forcada, J., Micela, G., Ribas, I., et al. 2011, A&A, 532, A6+

Sato, B., Fischer, D. A., Henry, G. W., et al. 2005, ApJ, 633, 465

Schneider, J., Rauer, H., Lasota, J. P., Bonazzola, S., & Chassefiere, E. 1998, in Astronomical Society of the Pacific Conference Series, Vol. 134, Brown Dwarfs and Extrasolar Planets, ed. R. Rebolo, E. L. Martin, & M. R. Zapatero Osorio, 241–+

Schröter, S., Czesla, S., Wolter, U., et al. 2011, A&A, 532, A3+

Silva-Valio, A. 2008, ApJ, 683, L179

Smith, A. M. S., Hebb, L., Collier Cameron, A., et al. 2009, MNRAS, 398, 1827

Southworth, J. 2010, MNRAS, 408, 1689

Spitzer, L. 1978, Physical processes in the interstellar medium

Stelzer, B. & Neuhäuser, R. 2001, A&A, 377, 538

Stone, J. M. & Proga, D. 2009, ApJ, 694, 205

Swain, M., Deroo, P., Tinetti, G., et al. 2013, Icarus, 225, 432

Tian, F., Toon, O. B., Pavlov, A. A., & De Sterck, H. 2005, ApJ, 621, 1049

Toro, E. F., Spruce, M., & Speares, W. 1994, Shock Waves, 4, 25

Torres, G., Winn, J. N., & Holman, M. J. 2008, ApJ, 677, 1324

Trammell, G. B., Li, Z.-Y., & Arras, P. 2014, ApJ, 788, 161

Tremblin, P. & Chiang, E. 2013, MNRAS, 428, 2565

Triaud, A. H. M. J., Anderson, D. R., Collier Cameron, A., et al. 2013, A&A, 551, A80

van Leeuwen, F., ed. 2007, Astrophysics and Space Science Library, Vol. 350, Hipparcos, the New Reduction of the Raw Data

Vaughan, A. H., Preston, G. W., Baliunas, S. L., et al. 1981, ApJ, 250, 276

Vernazza, J. E., Avrett, E. H., & Loeser, R. 1973, ApJ, 184, 605

Vidal-Madjar, A., Désert, J.-M., Lecavelier des Etangs, A., et al. 2004, ApJ, 604, L69

Vidal-Madjar, A., Huitson, C. M., Bourrier, V., et al. 2013, A&A, 560, A54

Vidal-Madjar, A., Lecavelier des Etangs, A., Désert, J.-M., et al. 2003, Nature, 422, 143

Watson, A. J., Donahue, T. M., & Walker, J. C. G. 1981, Icarus, 48, 150

Wood, B. E., Linsky, J. L., Hébrard, G., et al. 2004, ApJ, 609, 838

Wood, B. E., Redfield, S., Linsky, J. L., Müller, H.-R., & Zank, G. P. 2005, ApJS, 159, 118

Woods, T. N. & Rottman, G. J. 2002, Solar Ultraviolet Variability Over Time Periods of Aeronomic Interest, ed. Mendillo, M., Nagy, A., & Waite, J. H., 221–+

Wright, J. T., Fakhouri, O., Marcy, G. W., et al. 2011, PASP, 123, 412

Yelle, R. V. 2004, Icarus, 170, 167

LETTER TO THE EDITOR

Energy-limited escape revised

The transition from strong planetary winds to stable thermospheres[*]

M. Salz[1], P. C. Schneider[2,1], S. Czesla[1], J. H. M. M. Schmitt[1]

[1] Hamburger Sternwarte, Universität Hamburg, Gojenbergsweg 112, 21029 Hamburg, Germany
e-mail: msalz@hs.uni-hamburg.de
[2] European Space Research and Technology Centre (ESA/ESTEC), Keplerlaan 1, 2201 AZ Noordwijk, The Netherlands

ABSTRACT

Gas planets in close proximity to their host stars suffer from mass loss, which can affect the evolution of smaller planets. The energy-limited concept is generally used to derive estimates for such mass losses. Our new photoionization hydrodynamics simulations of the thermospheres of hot gas planets show that the energy-limited escape concept is only valid for planets with a gravitational potential smaller than $\log_{10}(-\Phi_G) < 13.10$ erg g^{-1}, because in these planets the radiative energy input is almost completely used to drive the planetary wind. In massive and compact planets with $\log_{10}(-\Phi_G) \gtrsim 13.6$ erg g^{-1}, the atmospheres are more tightly bound and most of the radiative energy input is re-emitted through hydrogen line and free-free emission. Between these two values the heating efficiency declines as a power law. Furthermore, the mass-loss rates of smaller planets are enhanced, because they host strongly expanded atmospheres, thus, exposing a larger surface to stellar irradiation. Scaling laws for the heating efficiency and the expansion radii are presented depending on the gravitational potential of the planet and on the irradiation level. Our scaling laws correct errors of several orders of magnitude in the mass-loss rate estimates of gas planets. The revised energy-limited escape concept can be used to derive estimates for the mass-loss rates of super-Earth-sized planets as well as massive hot Jupiters.

Key words. methods: numerical – hydrodynamics – radiation mechanisms: non-thermal – planets and satellites: atmospheres – planets and satellites: dynamical evolution and stability

1. Introduction

More than 30 years ago Watson et al. (1981) demonstrated that planetary atmospheres may become hydrodynamically unstable when exposed to strong high-energy irradiation. Therefore, the discovery of hot Jupiters (Mayor et al. 1995) soon raised the question about the stability of their atmospheres. Lammer et al. (2003) were among the first to demonstrate the decisive role of extreme ultraviolet (EUV) and X-ray irradiation for the dynamics of hot-Jupiter atmospheres. In particular, the impact of high-energy radiation heats the planetary thermosphere through ionization and subsequent thermalization of the radiative energy, which then initiates a process of continuous thermospheric expansion. Thus, a planetary wind is launched, powered by the stellar high-energy emission.

Today, the impact of atmospheric mass loss on the evolution of hot Jupiters is believed to be small, because the fractional mass loss remains moderate throughout the planetary lifetime (e.g., Ehrenreich et al. 2012). However, photoevaporative mass loss may play a more decisive role for the evolution of smaller gas or terrestrial planets, whose atmospheres are less tightly bound. In particular, we demonstrated that planets like 55 Cnc e may lose their complete reservoir of volatiles over a planetary lifetime, eventually leaving only a rocky super-Earth-type core behind (Salz et al. 2015b). Hence, photoevaporative mass loss may be among the crucial factors determining the distribution of small, close-in planets versus semimajor axis.

Expanded planetary thermospheres, likely undergoing hydrodynamic escape, have been reported for the five systems HD 209458 b, HD 189733 b, WASP-12 b, 55 Cancri b, and GJ 436 b (Vidal-Madjar et al. 2003; Lecavelier des Etangs et al. 2010; Fossati et al. 2010; Ehrenreich et al. 2012; Kulow et al. 2014). In the literature, the mass-loss rates of these planets or of larger samples are often estimated by assuming energy-limited escape.

2. Energy-limited escape

The energy-limited concept is based on an energy budget consideration, treating the planetary thermosphere as a closed system (e.g., Erkaev et al. 2007). In this context, the planetary mass-loss rate is given by the fraction of the radiative energy input and the total specific energy gain of the evaporated atmospheric material. The total energy is the sum of the potential, kinetic and thermal energies, and for example, the specific potential energy gain is given by the difference between the potential energy per unit of matter at the Roche lobe height and at the planetary photosphere. The same holds for the specific kinetic and thermal energy gain. The radiative energy input is given by the stellar high-energy flux times the area of the planetary disk times a heating efficiency. This heating efficiency specifies the fraction of the radiative energy, which is available for atmospheric heating. In particular, ionization processes consume a certain part of the radiative energy input; furthermore, recombinations and collisional excitations cause radiative cooling, which also reduces the available energy. For example, Shematovich et al. (2014) found a height

---

[*] Appendices are available in electronic form.

dependent heating efficiency between 0.1 and 0.25 in a detailed study of the thermosphere of HD 209458 b. In the literature, values from 0.1 to 1.0 have been adopted for this essential factor.

2.1. The energy-limited escape equation

In the energy-limited approach the kinetic and thermal energy gain is neglected, which results in the following equation for the planetary mass-loss rate $\dot{M}$ (e.g., Erkaev et al. 2007; Sanz-Forcada et al. 2010):

$$\dot{M}_{el} = \frac{3 \beta^2 \eta F_{XUV}}{4 K G \rho_{pl}} .$$ (1)

Here, ρ_{pl} is the mean planetary density and G the gravitational constant. F_{XUV} stands for irradiating X-ray plus EUV flux; $\beta = R_{XUV}/R_{pl}$ is a correction factor for the size of the planetary disk, which absorbs XUV radiation; R_{XUV} is the radius, where the bulk XUV radiation is absorbed. Equation 1 is sometimes given with a factor of β^3 (e.g., Baraffe et al. 2004; Sanz-Forcada et al. 2010), but we favor[1] β^2 (Watson et al. 1981; Lammer et al. 2003; Erkaev et al. 2007). η is the heating efficiency and K is the potential energy reduction factor introduced by Erkaev et al. (2007), which accounts for the finite size of the planetary Roche lobe,

$$K(\xi) = 1 - \frac{3}{2\xi} + \frac{1}{2\xi^3} \quad \text{with} \quad \xi = \left(\frac{M_{pl}}{3M_{st}}\right)^{1/3} \frac{a}{R_{pl}}.$$ (2)

Here, M_{pl} and M_{st} are the planetary and stellar masses, a is the semimajor axis of the planetary orbit and R_{pl} is the planetary radius.

2.2. Problems of the original energy-limited escape concept

Energy-limited escape is either used for upper limits of planetary mass-loss rates, or for order of magnitude estimates by choosing an appropriate heating efficiency. There are however three deficiencies, which may cause substantial errors. The first problem is the use of a constant heating efficiency for the absorption of XUV radiation. This determines the amount of energy that is used to drive the planetary wind, and thus, it directly affects the mass-loss rate. We show below that the heating efficiencies vary by several orders of magnitude in different atmospheres. The second problem is the unknown size of the planetary atmosphere that absorbs XUV radiation; a larger atmosphere absorbs more radiation and undergoes a stronger expansion. This increases the mass-loss rates of smaller gas planets by up to a factor of ten. The third problem is the general assumption of hydrodynamic escape, which is only valid if the planetary thermosphere is collisional up to the Roche lobe height, because radiative heating cannot be converted into a bulk acceleration above the exobase, where the planetary atmosphere becomes collisionless. The energy-limited concept cannot be used to estimate mass-loss rates from hydrodynamically stable thermospheres.

---

[1] The equation contains R_{pl}^3, as seen by the density in the denominator, but one of the radii is introduced by the gravitational potential. Correcting the gravitational potential with β implies that the atmospheric material escapes from the XUV absorption radius and not from the photosphere. However, the energy to lift material from the photosphere to the XUV absorption radius must also be accounted for.

3. Simulations: The transition from hydrodynamic winds to stable thermospheres

Salz et al. (2015b) presented simulations of 18 hot gas planets in the solar neighborhood, using 1D spherically symmetric simulations of the substellar point, which include the chemistry of hydrogen and helium. The simulations were carried out with "The PLUTO-CLOUDY Interface" (TPCI, Salz et al. 2015a). TPCI is an interface between the MHD code PLUTO (Mignone et al. 2012) and the photoionization solver CLOUDY (Ferland et al. 2013). The use of a detailed photoionization solver liberates us from assuming a fixed heating efficiency, which has been done in previous models of escaping atmospheres (e.g., Koskinen et al. 2013). Since CLOUDY solves the relevant microphysical processes from first principles, we can use our simulations to derive the heating efficiency in the individual planetary atmospheres. TPCI can be applied to rapidly escaping atmospheres, where the radiative energy input is "completely" used to drive the hydrodynamic wind, but also to hydrostatic atmospheres, where the absorbed energy is re-emitted.

Salz et al. (2015b) found that the thermospheres of massive and compact planets differ decisively from those of smaller planets. For this paper, we have performed six additional simulations of hypothetical planets, i.e., two planets at the orbital distance of HD 209458 b with 2.5 and 5 times the planetary mass, and four planets at the distance of WASP-10 b with 1/10, 1/5, 1/3, and 1/2 of the planetary mass. Other system parameters like the irradiation strength or the planetary radius are set to the original values of HD 209458 b and WASP-10 b.

Figure 1 shows our simulations of the escaping atmospheres of the planets at the orbital distance of WASP-10 b. As we go from small to high planetary masses, the density in the thermosphere decreases, the temperature increases, and the wind velocity decreases. The higher temperature in the thermosphere causes enhanced radiative cooling, which is dominated by Lyα cooling above $\sim$1.1 R_{pl} and by free-free emission below. The heating efficiency decreases as radiative cooling becomes more important (see Fig. 1 (f)). This reduces the available energy for accelerating the planetary wind, which is the reason for the lower velocities in the thermospheres of the more massive planets. The lower velocity results in reduced adiabatic cooling, which also increases the temperature in the thermosphere. As a second effect of the smaller velocity, less neutral hydrogen is advected into the upper thermospheres. Thus, a weaker planetary wind shifts the transition height from H to H$^+$ closer to the planetary photosphere.

The atmosphere of WASP-10 b with the true planetary mass of $M_{pl} = 3.2\,M_{jup}$ is collisionless above 1.44 R_{pl}. The acceleration below the exobase is insufficient to drive a transonic wind. Our simulation is not valid above the exobase; it results in a mass loss rate of 500 g s^{-1}, which is unphysical, however. If we compute the mass-loss rate according to Jeans escape at the exobase (Lecavelier des Etangs et al. 2004) we derive a value of only 0.6 g s^{-1}. The true mass-loss rate is between the two values. An approach combining the hydrodynamic and kinetic description would provide a more precise estimate (e.g., Yelle 2004), but this is beyond the scope of this paper. Anyway, non-thermal escape rates may be even larger than both values (e.g., Lammer et al. 2013). We call the thermospheres of planets with such negligibly small thermal mass-loss rates hydrodynamically stable.

4. The revised energy-limited escape

As we have seen in the example of WASP-10 b, massive and compact gas giants host stable thermospheres. The energy-
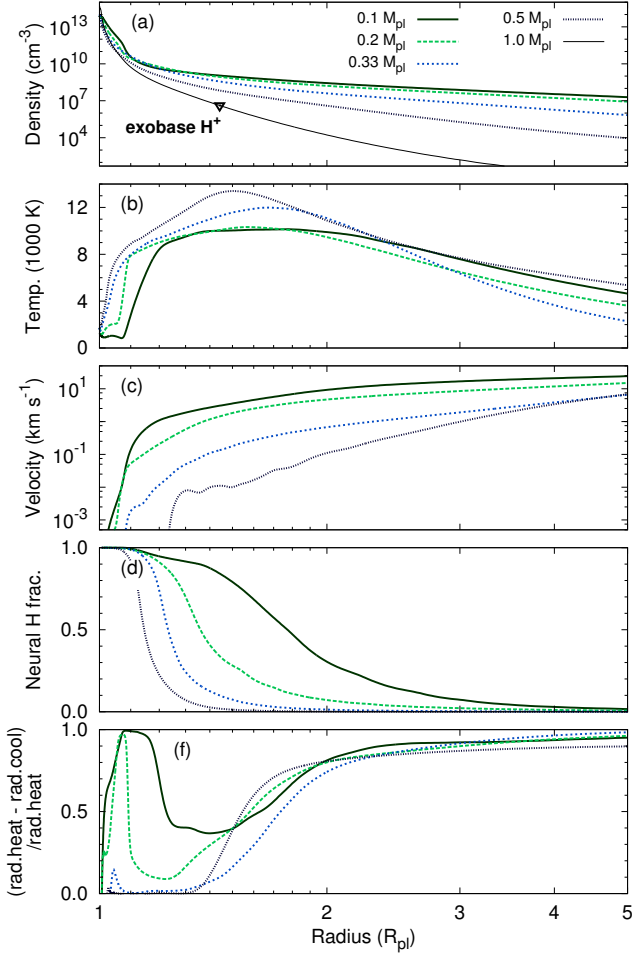
Fig. 1. Atmospheres of WASP-10 b with increasing planetary mass: density (a), temperature (b), velocity (c), neutral hydrogen fraction (d), and heating fraction (f). We only plot the density for the 1 M_{pl} atmosphere, because the our simulation is not valid above the exobase.

limited escape concept with a fixed heating efficiency is therefore not valid for such planets. We compute the expansion radii and the heating efficiencies for all simulations presented by Salz et al. (2015b) plus our new simulations and derive scaling laws for the two factors. The values are provided in Table A.1.

4.1. Atmospheric expansion

To evaluate Eq. 1 it is important to know the size of the XUV absorbing planetary atmosphere, because it determines the amount of available energy. From the simulations we define the mean XUV absorption radius R_{XUV} as

$$R_{XUV}^2 = \int_{R_{pl}}^{R_{Rl}} r^2 h(r)\, dr \left/ \int_{R_{pl}}^{R_{Rl}} h(r)\, dr \right., \qquad (3)$$

with the Roche lobe height R_{Rl} and the local heating rate $h(r)$. Mathematically, the total radiative heating produced by the absorption of the complete XUV flux in a thin layer at R_{XUV}, is equivalent to the distributed heating in the simulations.

The calculated R_{XUV} increase with decreasing gravitational potential, and, to a smaller extent, a higher irradiation level causes the thermospheres to expand. We use singular value de-

composition (SVD) to find the best fitting plane in the three-dimensional space spanned by the gravitational potential, Φ_G, the irradiating XUV flux, F_{XUV}, and the expansion radii in units of planetary radii, β. This results in the scaling law

$$\log_{10}(\beta) = \max\left(-0.375 \log_{10}(-\Phi_G) + 0.044 \log_{10}(F_{XUV}) + 4.92,\, 0.0\right). \qquad (4)$$

The fit is shown in Fig. B.1. The atmospheric expansion can be neglected for massive hot Jupiters, but in the range of super-Earth-sized planets the expansion causes increased mass-loss rates by a factor of ten.

4.2. Correction for the heating efficiency

The heating efficiency is not directly available in our simulations. We use a comparison of the energy-limited mass-loss rates and the simulated mass-loss rates to derive the effective heating efficiency in the individual simulations

$$\eta_{eff} = \dot{M}_{sim}/\dot{M}_{el}. \qquad (5)$$

Physically, our effective heating efficiency is not a true heating efficiency for the absorption of XUV radiation in gas, because it accounts for the fraction of the radiative energy input, which is converted into kinetic and internal energy. Therefore, the use of η_{eff} in Eq. 1 takes back the assumption of the energy-limited concept that the kinetic and thermal energy gain can be neglected and reconciliates the derived mass-loss rates with the fundamental energy budget consideration introduced in Sect. 2.

Our definition of η_{eff} is also affected by several minor factors, which influence the mass-loss rates in the simulations. For example, not the complete stellar XUV radiation is absorbed, but up to 10% of the radiative energy is transmitted through the lower boundary (X-rays up to ∼ 20 Å). In contrast, we also find small amounts of hydrogen line heating, especially Lyα line heating in the denser atmosphere close to the lower boundary. Additionally, our boundary conditions slightly affect the mass-loss rates. The combined relative uncertainty on the simulated mass-loss rates is less than 50 % (see Table 2 in Salz et al. 2015b).

The mass-loss rates are evaluated according to $\dot{M}_{sim} = 1/4 \times 4\pi R^2 \rho v$; the additional factor of 1/4 results from averaging the irradiation over the planetary surface. The energy-limited mass-loss rates are calculated from Eq. 1 with a heating efficiency of $\eta = 1.0$ (system parameters are provided in Table 1 of Salz et al. (2015b)). We use the β factors from the previous section for the energy-limited escape rates, which ensures that the energy budget is the same in both mass-loss evaluations.

The effective heating efficiencies reach a maximal value of 0.13. The most compact planet where we still find a planetary wind, CoRoT-2 b, has a heating efficiency of only $10^{-4.7}$. Figure 2 shows the effective heating efficiencies plotted versus the gravitational potential; planets with stable atmospheres are not included (WASP-8, WASP-10, HAT-P-2, HAT-P-20). While the heating efficiency is constant for planets with $\log_{10}(-\Phi_G) < 13.1$ erg g^{-1}, it rapidly declines for planets with larger gravitational potentials. We fitted this dependency with a piecewise linear model in log space. Using $v = \log_{10}(-\Phi_G)$, we obtain

$$\log_{10}(\eta_{eff}) = \begin{cases} -1.11 & \text{for } v \le 13.10, \\ -1.11 - 7.05\,(v - 13.10) & \text{for } 13.10 < v < 13.6. \end{cases} \qquad (6)$$
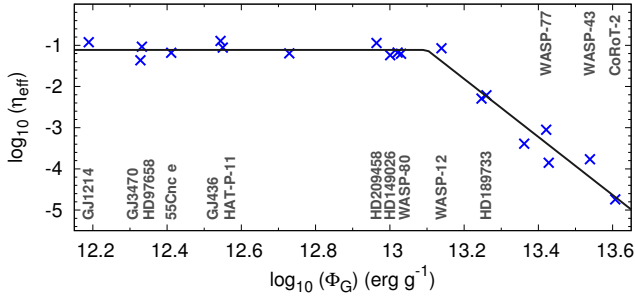
Fig. 2. Effective heating efficiencies in the simulations. The solid line is the fitted broken power law. Planets are labeled, except for the new artificial planets with changed planetary masses.

Fig. 3. System parameters covered by our simulations. The heating efficiency is referenced by the color scheme. We indicate regions of strong planetary winds, intermediate winds, and stable atmospheres with red, yellow, and blue background colors. The dotted line shows a 1 Ga evaporation border for a Jupiter-mass planet. The new series of simulations are indicated by black dashed lines.

On average the maximum effective heating efficiency in the simulated atmospheres is $\eta_{\mathrm{eff}}^{\mathrm{max}} = 0.077$. We emphasize that, according to our definition, η_{eff} is exclusively intended for the use in escaping planetary atmospheres. The atmosphere of HD 209458 b has an effective heating efficiency of $\eta_{\mathrm{eff}} = 0.11$. On average the kinetic and thermal energy gain contribute 24 % to the total energy gain in our simulations. This boosts the true heating efficiency in HD 209458 b to 0.15. This result agrees well with the derived heating efficiency from Shematovich et al. (2014) of between 0.1 and 0.25. These authors found secondary ionizations and excitations due to photoelectrons to be an important energy sink. Our photoionization solver includes these processes[2], which explains the agreement between the results derived with the different approaches.

4.3. Range of validity for the revised energy-limited escape

In Fig. 3 we show the system parameters covered by our simulations, which indicates the range of validity for our scaling laws. Here, planets with stable thermospheres are included. A hydrodynamic planetary wind does not exist for planets with a gravitational potential energy in excess of $\log_{10}(-\Phi_{\mathrm{G}}) \gtrsim 13.6 \mathrm{\ erg\ g}^{-1}$ independent of the irradiation level. In an intermediate region from $13.3 < \log_{10}(-\Phi_{\mathrm{G}}) < 13.6 \mathrm{\ erg\ g}^{-1}$ hydrodynamic escape can exist, but is easily suppressed by a stellar wind pressure over large fractions of the planetary surface (Salz et al. 2015b). None of the simulated planets is currently unstable because of its mass-loss rate, as indicated by the evaporation border for a Jupiter-mass planet in Fig. 3.

5. Conclusion

Based on TPCI simulations of the escaping thermosphere of hot gas planets we find a transition from strong winds in planets with a low gravitational potential to stable atmospheres in massive and compact planets. This transition is a result of strong radiative cooling in the hot thermospheres of massive hot Jupiters. Planets with a gravitational potential larger than $\log_{10}(-\Phi_{\mathrm{G}}) \gtrsim 13.6 \mathrm{\ erg\ g}^{-1}$ cannot host hydrodynamically escaping atmospheres. The energy-limited escape concept is valid for planets with $\log_{10}(-\Phi_{\mathrm{G}}) < 13.10 \mathrm{\ erg\ g}^{-1}$, using an effective heating efficiency of $\eta_{\mathrm{eff}} = 0.077$. For planets between these two

---

[2]   Auger electrons plus ionizations from suprathermal electrons are described in Ferland et al. (1998). References regarding excitation by non-thermal particles in CLOUDY are given by Ferland et al. (2013). For example, Lyα excitation by suprathermal electrons contributes 5% to the total Lyα cooling rate in the atmosphere of HD 209458 b.

values we derived a scaling law for the heating efficiency. The mass-loss rates of smaller planets are additionally increased by significantly expanded atmospheres. We presented a scaling law for the expansion radii depending on the gravitational potential and the irradiation level.

In practice, we suggest to derive the atmospheric expansion and the effective heating efficiency with Eqs. 4 & 6 for a planetary atmosphere; these can be used in Eq. 1 to estimate the resulting mass-loss rate. This procedure improves the energy-limited escape concept to include the effects of strong radiative cooling in compact and hot atmospheres and the increased absorption of the expanded atmospheres of smaller planets. The revised energy-limited escape corrects errors of several orders of magnitude in the mass-loss estimates and is valid for all planets ranging from super-Earth-sized to massive hot Jupiters providing the atmospheres are hydrogen and helium dominated.

References

Baraffe, I., Selsis, F., Chabrier, G., et al. 2004, A&A, 419, L13
Ehrenreich, D., Bourrier, V., Bonfils, X., et al. 2012, A&A, 547, A18
Erkaev, N. V., Kulikov, Y. N., Lammer, H., et al. 2007, A&A, 472, 329
Ferland, G. J., Korista, K. T., Verner, D. A., et al. 1998, PASP, 110, 761
Ferland, G. J., Porter, R. L., van Hoof, P. A. M., et al. 2013, Rev. Mexicana Astron. Astrofis., 49, 137
Fossati, L., Haswell, C. A., Froning, C. S., et al. 2010, ApJ, 714, L222
Koskinen, T. T., Harris, M. J., Yelle, R. V., & Lavvas, P. 2013, Icarus, 226, 1678
Kulow, J. R., France, K., Linsky, J., & Loyd, R. O. P. 2014, ApJ, 786, 132
Lammer, H., Chassefière, E., Karatekin, Ö., et al. 2013, Space Sci. Rev., 174
Lammer, H., Selsis, F., Ribas, I., et al. 2003, ApJ, 598, L121
Lecavelier des Etangs, A., Ehrenreich, D., Vidal-Madjar, A., et al. 2010, A&A, 514, A72+
Lecavelier des Etangs, A., Vidal-Madjar, A., McConnell, J. C., & Hébrard, G. 2004, A&A, 418, L1
Mayor, M., Queloz, D., Marcy, G., et al. 1995, IAU Circ., 6251, 1
Mignone, A., Zanni, C., Tzeferacos, P., et al. 2012, ApJS, 198, 7
Salz, M., Banerjee, R., Mignone, A., et al. 2015a, accepted for pub. in A&A
Salz, M., Czesla, S., Schneider, P. C., & Schmitt, J. H. M. M. 2015b, subm. A&A
Sanz-Forcada, J., Micela, G., Ribas, I., et al. 2011, A&A, 532, A6+
Sanz-Forcada, J., Ribas, I., Micela, G., et al. 2010, A&A, 511, L8+
Shematovich, V. I., Ionov, D. E., & Lammer, H. 2014, A&A, 571, A94
Vidal-Madjar, A., Lecavelier des Etangs, A., Désert, J.-M., et al. 2003, Nature, 422, 143
Watson, A. J., Donahue, T. M., & Walker, J. C. G. 1981, Icarus, 48, 150
Yelle, R. V. 2004, Icarus, 170, 167

Table A.1. Irradiation of the planets, energy-limited mass-loss rates, and results from the simulations. Ranking according to simulated mass loss.
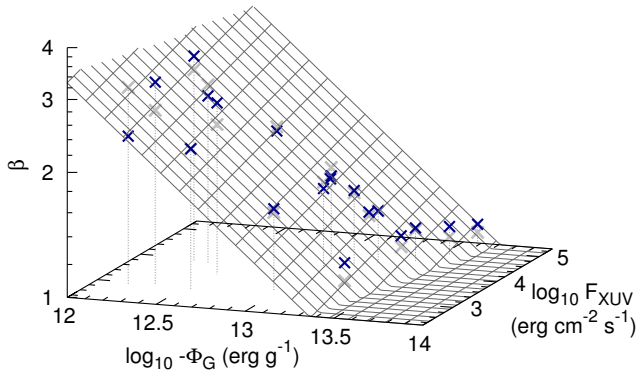
System	$\log_{10}(F_{\mathrm{XUV}})^d$ (erg g^{-1})	$\log_{10}(-\Phi_{\mathrm{G}})$ (erg g^{-1})	R_{XUV} (R_{pl})	$\log_{10}(\dot{M}_{\mathrm{el}})$ (g s^{-1})	$\log_{10}(\dot{M}_{\mathrm{sim}})$ (g s^{-1})	$\log_{10}(\eta_{\mathrm{eff}})$
WASP-12 b	< 4.26	13.14	1.50	12.71	11.64	−1.07
GJ 3470 b	3.89	12.33	3.13	12.02	10.66	−1.36
WASP-80 b	4.03	13.00	1.55	11.75	10.57	−1.18
HD 149026 b	4.29	13.00	1.60	11.67	10.43	−1.24
HAT-P-11 b	3.51	12.55	2.59	11.35	10.29	−1.06
HD 209458 b	< 3.06	12.96	1.57	11.21	10.27	−0.94
55 Cnc e	3.87	12.41	2.53	11.32	10.14	−1.18
GJ 1214 b	2.93	12.19	2.27	10.60	9.68	−0.92
GJ 436 b	2.80	12.54	2.18	10.55	9.65	−0.90
HD 189733 b	4.32	13.26	1.34	11.81	9.60	−2.21
HD 97658 b	2.98	12.33	3.08	10.51	9.47	−1.04
WASP-77 b	4.51	13.42	1.20	11.84	8.79	−3.05
WASP-43 b	4.82	13.54	1.17	11.80	8.03	−3.77
Corot-2 b	5.19	13.61	1.13	12.37	7.63	−4.74
WASP-8 b	3.66	13.57	1.13	10.82	*5.0*	*−5.82*
WASP-10 b	4.08	13.73	1.15	10.90	*2.7*	*−8.21*
HAT-P-2 b	4.12	14.14	< 1.12	10.87	*< 5.9*	*< −5.5*
HAT-P-20 b	4.08	14.18	< 1.12	10.37	*< 4.5*	*< −6.4*
artificial planets						
HD 209458 b (2.5)	3.06	13.36	1.20	10.53	7.14	−3.39
HD 209458 b (5.0)	3.06	13.66	1.10	10.12	*2.0*	*−8.12*
WASP-10 b (0.1)	4.08	12.73	2.05	12.55	11.35	−1.20
WASP-10 b (0.2)	4.08	13.03	1.61	11.99	10.78	−1.21
WASP-10 b (0.33)	4.08	13.25	1.36	11.59	9.30	−2.29
WASP-10 b (0.5)	4.08	13.43	1.21	11.29	7.44	−3.85

Notes. Explanation of the columns: name of the system, XUV flux at planetary distance $^{(d)}$ (< 912 Å, erg cm^{-2} s^{-1}, see Salz et al. (2015b)) , gravitational potential of the planet, bulk XUV absorption radius in the simulations, energy-limited mass-loss rate (Sanz-Forcada et al. 2011), mass-loss rate from the simulations ($1/4 \times 4\pi R^2 \rho v$), effective heating efficiency (see text). Mass-loss rates and effective heating efficiencies of hydrodynamically stable atmospheres are printed in italics.

Appendix A: System parameters

The parameters are provided in Table A.1.

Appendix B: Atmospheric expansion

Fig. B.1. Mean XUV absorption radii in the simulations. Our fit is given by the plane.

Acknowledgements

Eidesstattliche Versicherung

Hiermit erkläre ich an Eides statt, dass ich die vorliegende Dissertationsschrift selbst verfasst und keine anderen als die angegebenen Quellen und Hilfsmittel benutzt habe.

_____	_____
Ort, Datum	Unterschrift